Magnetic structures of the lithium orthophosphates and the study of the Bragg glass phase of vortex matter

Toft-Petersen, Rasmus

Publication date:
2011

Document Version
Publisher's PDF, also known as Version of record

Magnetic structures of the lithium orthophosphates and the study of the Bragg glass phase of vortex matter

by Rasmus Toft-Petersen

Supervisors: Niels Hessel Andersen
and Asger Bech Abrahamsen

Risø National Laboratory, DTU

19th of October 2011

Contents

1 Magnetic structures of the lithium orthophosphates - introduction 3

1.1 The magnetic structures of the Lithium-Ortho-Phosphates 3

2 Elements of Crystallography and Magnetism 5

2.1 Magnetism 5

2.1.1 The one electron atom 5

2.1.2 Many-electron atoms 6

2.1.3 Crystal field effects: level splitting, orbital quenching and anisotropy 11

2.1.4 Exchange interaction 15

2.1.5 Super-exchange interaction 16

2.1.6 Dzyaloshinsky-Moriya interaction and anisotropic exchange 19

2.2 Crystallography 21

2.2.1 Irreducible representations of the symmetry group 22

2.2.2 Irreducible basis vectors and the quadratic spin Hamiltonian 27

2.2.3 Symmetry and the Dzyaloshinsky-Moriya interaction 28

3 Neutron Scattering 31

3.1 Properties of the neutron 31

3.1.1 Basic properties 31

3.1.2 Nuclear interactions 32

3.1.3 Magnetic interactions 34

3.2 Scattering from ordered systems 38

3.2.1 Bragg's law and reciprocal space 43

3.3 Neutron instrumentation 45

3.3.1 Neutron sources 45

3.3.2 General concepts and components 46

3.3.3 Two-axis diffractometers - TriCS 47

3.3.4 Cold triple-axis spectrometers - FLEX and RITA-II 48

3.3.5 Small angle neutron scattering - SANS-II 49

3.3.6 Magnetic form factor 50

3.3.7 Lorentz factor 50

4 Field- and temperature-induced magnetic phase transitions in $LiNiPO_4$ 53

4.1 Experimental setup - RITAII 55

4.2 Evidence of a low temperature spiral and a second order transition to a linearly polarized structure 55

4.3 Experimental setup - FLEX 57

4.3.1 Alignment problems 57

4.4 Evidence of high field commensuration of the magnetic structure 59
4.5 Magnetization measurements 62
4.6 $(\mu_0 H, T)$ phase diagrams of $LiNiPO_4$ 64
4.7 Spin excitations in the high field spiral phase 65
4.8 Magnetoelectricity in the high field spiral phase 69

5 Continuous spin flop and bicritical fluctuations in isotropic $LiMnPO_4$ 71
5.1 Introduction 71
5.2 The TriCS experiment - continuous spin flop and structure determination 72
5.2.1 Experimental details 72
5.2.2 Flopped structure determined using key peaks 73
5.2.3 Structural refinement of the TriCS data 75
5.3 Magnetization measurements 78
5.4 Magnetic phase diagram and bicriticality in $LiMnPO_4$ 79
5.4.1 Experimental details 80
5.4.2 The ordering phase boundary 80
5.4.3 The phase diagram 81
5.4.4 Criticality at the flop field H_b 83

6 Zero field spin structure and field induced spin canting in anisotropic $LiCoPO_4$ 87
6.1 Introduction 87
6.1.1 Calculations done by Jens Jensen 89
6.2 Zero field spin structure - the TriCS experiment 89
6.2.1 Experimental setup 89
6.2.2 Simplification of the possible structure using key peaks 90
6.2.3 Refinement of the zero field magnetic structure of $LiCoPO_4$ 92
6.3 Magnetic structure of $LiCoPO_4$ in field applied along a 95
6.3.1 Dzyaloshinsky-Moriya interaction in $LiCoPO_4$ 98
6.4 Possible additional DM mechanisms in $LiCoPO_4$ 98
6.4.1 Removal of mirror plane - possible DM interactions 99
6.4.2 Possible causes of weak ferromagnetism 102
6.4.3 Hamiltonians that cause spin rotations 102
6.4.4 Possible DM interactions in applied fields along magnetoelectrically active axes 103
6.5 Field induced magnetic phase transition for fields applied along b 107
6.5.1 The first RITA-II experiment for fields applied along b using a vertical 15 T cryomagnet 107
6.5.2 The RITA-II experiment with an 11 T horizontal field cryomagnet 109

7 The study of the Bragg glass phase of vortex matter - introduction 113

8 Conventional superconductivity and the Bragg glass phase of vortex matter 115

8.1 BCS theory of superconductivity . . . 115
8.1.1 Non-interacting electron gas . . . 115
8.1.2 Interaction between electrons and fermi-liquids . . . 116
8.1.3 Attractive potential . . . 117
8.1.4 Phonon coupling . . . 118
8.1.5 The BCS gap function . . . 121
8.2 Ginzburg-Landau theory of superconductivity . . . 124
8.2.1 The Ginzburg-Landau differential equations . . . 125
8.2.2 Domain wall energy . . . 126
8.2.3 The linearized Ginzburg-Landau equation and the Abrikosov vortex state . 127
8.3 Forces acting on and between flux lines . . . 129
8.3.1 Structure of an isolated vortex . . . 130
8.3.2 Interaction between flux lines . . . 131
8.3.3 Intermediate mixed state . . . 132
8.3.4 Flux line pinning . . . 133
8.4 Collective properties of the vortex lattice: The Bragg glass theory and proposed phase diagrams . . . 134
8.4.1 Phenomenological description of the elasticity . . . 135
8.4.2 Larkin-Ovchinnikov theory . . . 135
8.4.3 Bragg glass theory . . . 137
8.4.4 Predictions of Bragg glass theory . . . 140
8.4.5 Proposed phase diagrams . . . 143

9 Reverse Monte Carlo simulation of the vortex lattice in superconducting Vanadium 145

9.1 Experimental details . . . 145
9.1.1 Setup geometry . . . 145
9.1.2 The vanadium sample used in this work . . . 148
9.1.3 Magnetic form factor of a flux line . . . 149
9.2 Reverse Monte Carlo refinement . . . 149
9.2.1 The RMC code used for analyzing the high resolution rocking curves . . . 152
9.3 The vortex lattice of superconducting Vanadium . . . 155
9.3.1 The SANS-II experiment in May 2008 . . . 156
9.3.2 Initial analysis of the rocking curves with high statistics . . . 164
9.3.3 Problems with the simulations - Simulated Annealing . . . 169
9.3.4 The intrinsic finite size problem . . . 172
9.3.5 Results of the simulations . . . 173

9.3.6 The SANS-II experiment in December 2010 180
9.3.7 Field dependence of the rocking curve intensities at higher temperatures . . 181
9.3.8 The high statistics rocking curve at high field and high temperature 184
9.3.9 VSM magnetization measurements 186
9.3.10 Interpretation of the flux line phase diagram 189

10 Concluding remarks **191**
10.1 Magnetic structures of the lithium orthophosphates 191
10.2 The study of the Bragg glass phase of vortex matter 192

11 References **193**

12 List of publications - Rasmus Toft-Petersen **198**

A Selected MATLAB-scripts **199**
A.1 Rocking curve convoluted fitting function 199

B SA results for the unaltered 180 mT rocking curve **201**

Acknowledgements

During my time at Risø (and the PSI) I have received invaluable help and guidance from numerous people. First and foremost I would like to express my gratitude to my supervisor, Niels Hessel Andersen, from whom I have learned a lot. Due to Niels' dedication to physics and his helpfulness, I have always had someone to spar with and learn from on more occasions than I could reasonably expect. It is mainly due to Niels that the whole course of the project went without any other problems than those relating to physics. I owe thanks to Thomas B. S. Jensen as well for getting me started on the lithium-ortho-phosphates. Thomas put a lot of energy into getting me out on the instruments, has provided invaluable theoretical support and has been great company during beam time. Thanks to Asger Bech Abrahamsen for getting me into the flux line business, and for help and guidance throughout the project. Even though Asger has been busy with other projects, he as always spent more time on my problems than he actually had once the discussion got going. Mark Laver has been a major help both with the RMC problems piling up at the end of the project and in helping me tackle the many problems and pitfalls accompanying the examination of vortex lattices, in the limited time I had available. Both Asger and Mark set high beam-time standards both with regards to competence, effort and spirit.

Thanks to Niels B. Christensen for helping with several experiments, scientific writing and general physics advice. I also owe Bente Lebech and Oksana Zaharko a huge thanks for helping me with the refinements of the magnetic structures; their advice and help has been invaluable. Thanks to Kim Lefmann for allowing me to use the student beam time on RITA-II, and for all the help and encouragement that followed. Peter Willendrup and Erik Knudsen have willingly helped with any problem regarding computing for which I am grateful. Christoph Niedermayer has been a great help during my first couple of beam times; helping me to deal with the avalanche of rookie mistakes made while keeping up the good mood. Michel Kenzelmann has given valuable theoretical advice regarding magnetoelectrics, for which I am grateful. I would like to thank David Vaknin of Ames Laboratory - whom I have never met - and his crew for providing all the crystals and for a fruitful collaboration.

I would also like to thank my fellow students Jacob Larsen, Linda Udby and Jari I Hjøllum, for fruitful discussions. Thanks to my mother - Vibeke Toft-Petersen - for weeding out the worst lingual mistakes in the thesis and to the rest of my family - Jørgen, Marie and Søren - for always showing an interest in the project even though it is kind of a niche by any comparison. Lastly, I would like to thank my girlfriend Kirstina for support and being loads of fun, but most of all for *not* caring about physics. Kirstina reminds me that there are other things to care about than physics, which has been needed at times.

Preface

This thesis represents the work done during my three years of Ph.D study. The first year of my study was mainly used on an attempt to discover new nitride materials. This proved to be an interesting path but immensely difficult, as making nitrides by means of solid state reactions in furnaces put relentless requirements to both equipment and experience. Due to this fact and the fact that I am a physicist, the focus naturally changed at the end of the first year from the nitrides towards the examination of magnetically ordered materials using neutron scattering. Thomas B. S. Jensen was a major part of this shift, as it was his work on $LiNiPO_4$ that formed the basis for a re-examination of $LiNiPO_4$ and the other lithium-ortho-phosphates, especially $LiCoPO_4$ and $LiMnPO_4$. Many of the tools and considerations done by him were directly applicable to the open questions in these two compounds. The very first neutron scattering experiment I made as a SANS-experiment on superconducting Vanadium. The analysis of that data required knowledge about vortex lattices generally and knowledge about Reverse Monte Carlo (RMC) specifically, which was obtained sporadically parallel to the work done on the lithium-ortho-phosphates. Thus, nine months before the end of my contract I had four more or less finished minor projects which I found interesting and had invested time in. This thesis is an attempt to wrap it all up.

Since this thesis describes work done on four magnetic systems, concerning two different subjects in magnetism, it ended up being rather long. As the scope of the thesis broadened, I began to fear that this might cause a lack of depth and detail. To avoid this, I decided to put some of the important theoretical concepts and derivations in my thesis as the best way for me to achieve understanding of a subject is to write everything down in my own way. Therefore, the theoretical chapters contain many details; which is mainly for my own sake. These detailed theoretical chapters are chapters 2, 3 and 8; they contain only textbook material, written down as I understand it. Any experienced reader, who feels confident in the subjects of magnetism, crystallography, neutron scattering, superconductivity and vortex matter may safely skim or even skip these chapters; they contain no new information. However, I hope that more unexperienced readers may find these chapters useful as a supplement to the theoretical textbooks, if stumbling upon the subjects of this thesis in their own work.

The thesis is organized as follows: First, a short introduction to magnetoelectric materials end especially the lithium-ortho-phosphates is given. The introduction is followed by a detailed account of the relevant magnetic interactions as well as a short account of the crystallographic and group theoretical concepts needed for an analysis of the neutron data. Next, a detailed account is given of the theory of neutron scattering which is the main experimental method used in this thesis. After these textbook chapters, the work done on the lithium-ortho-phosphates is described in three separate chapters concerning the work done on $LiNiPO_4$, $LiMnPO_4$ and $LiCoPO_4$, respectively.

The part of the thesis concerning the investigation of a possible Bragg glass phase in superconducting Vanadium is a little shorter. The introduction is followed by a short account of BCS theory, Ginzburg-Landau theory and Bragg glass theory. This is succeeded by a chapter describing the special experimental SANS setup, a description of the RMC principle and at last ending with an analysis of the rocking curve intensities as well as the RMC refinement of high resolutions rocking curves.

1 Magnetic structures of the lithium orthophosphates - introduction

Since this thesis concerns two subjects in which the only common denominator is the subject of magnetism and the use of neutron scattering as the central experimental method, the introduction will be divided into two parts concerning each subject separately.

1.1 The magnetic structures of the Lithium-Ortho-Phosphates

A ferroic material is a material that spontaneously exhibits a static and switchable order parameter. For instance, a ferromagnetic material can be statically magnetized, with iron being the most obvious example. The electric counterpart to the ferromagnetic materials are the ferroelectric materials which can be statically polarized; there is an electric polarization density within the material giving rise to a static surface charge perpendicular to the polarization vector. On very rare occasions, a material exhibits both ferromagnetism and ferroelectricity *spontaneously* (without external applied fields of any kind) - these materials are called the *multiferroics*. On less rare occasions, is is possible to *induce* one ferroic property by influencing the other ferroic state with an applied field. Good example of such materials are the *magnetoelectric* materials, where an applied magnetic field induces a polarization and an applied electric field induced a magnetization. Figure 1 illustrates the proper nomenclature when the ferroic order parameters in question are magnetic and electric

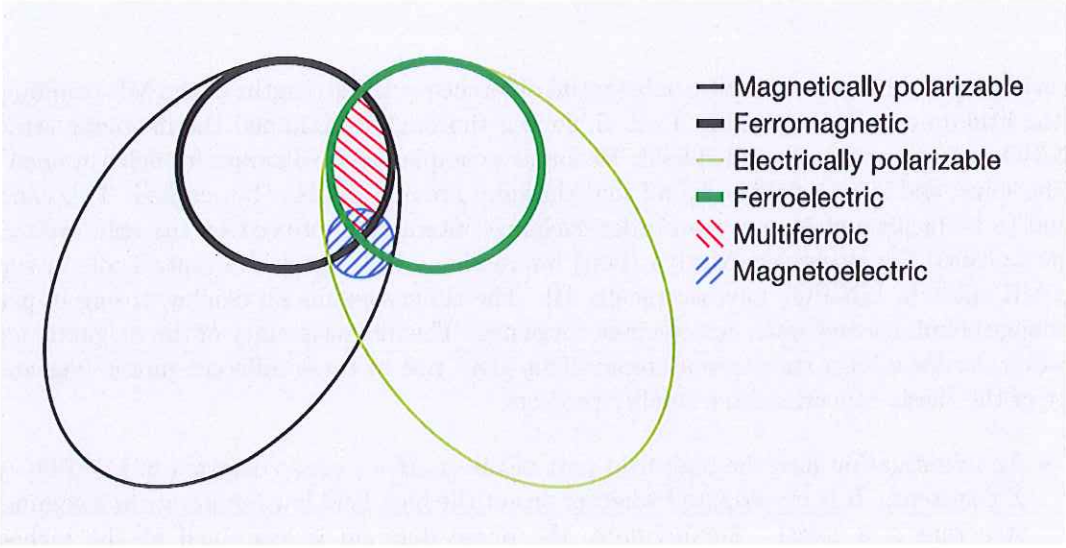

Figure 1: An illustration of the nomenclature of multiferroics and magnetoelectrics. True multiferroics exhibits both a spontaneous magnetization and spontaneous electric polarization. The magnetoelectrics on the other hand are defined by the *coupling* between the two order parameters; the spontaneous presence of any of the order parameters is thus not a necessary condition.

The *lithium-ortho-phosphates* - $LiMPO_4$, where M = Mn, Fe, Co or Ni - are isostructural orthorhombic (space group *Pnma* - $a \approx 10.1$ Å, $b \approx 5.9$ Å and $c \approx 4.7$ Å) magnetoelectric materials that neither show significant spontaneous magnetization nor electric polarization. These materials all order *antiferromagnetically* below temperatures ranging from 21 K (Co) to 50 K (Fe). Applying a magnetic field along certain crystallographic directions (either a, b or c) induces an electric

polarization. The coupling is linear following the formula

$$P_i = \alpha_{ij} H_j, \tag{1}$$

where $i, j = a, b, c$ and α_{ij} are components of the linear magnetoelectric tensor $\boldsymbol{\alpha}$. The magnetoelectric coupling in the compounds examined in this thesis have the following form

$$\boldsymbol{\alpha}_{LiCoPO_4} = \begin{pmatrix} \cdot & \bullet & \cdot \\ \bullet & \cdot & \cdot \\ \cdot & \cdot & \cdot \end{pmatrix} \quad \boldsymbol{\alpha}_{LiNiPO_4} = \begin{pmatrix} \cdot & \cdot & \bullet \\ \cdot & \cdot & \cdot \\ \bullet & \cdot & \cdot \end{pmatrix} \quad \boldsymbol{\alpha}_{LiMnPO_4} = \begin{pmatrix} \bullet & \cdot & \cdot \\ \cdot & \bullet & \cdot \\ \cdot & \cdot & \bullet \end{pmatrix},$$

where the large dots mark the non-zero components. There is a difference in the form of the magnetoelectric tensor of the three compounds, originating from the nature of the magnetic ion. These differences are significant. Table 1 shows the characteristics of the magnetic ions in the three compounds examined in this thesis; the meaning of which will be explained in the following chapters.

Magnetic ion	Electron conf.	L	S	Spin orientation	$\Delta g/g$	$\lvert\alpha_{max}\rvert$ [s/m]
Mn^{2+}	$[Ar]3d^5$	0	5/2	a	0	$2 \cdot 10^{-5}$
Ni^{2+}	$[Ar]3d^8$	3	1	c	0.1	$4 \cdot 10^{-5}$
Co^{2+}	$[Ar]3d^7$	2	3/2	b	0.3	$7 \cdot 10^{-4}$

Table 1: Characteristics of the magnetic ions in the three lithium ortho-phosphates examined in this thesis. The spin and orbital quantum numbers are found using Hund's rules without taking the crystal surroundings into account. The spin orientations are found in the literature [1, 2]. $\Delta g/g$ determines the strength of higher-order exchange couplings induced by the spin-orbit coupling - explained in the text. The maximum strengths of the ME-effect are found in [3].

As evident in table 1 there are also substantial difference in the strengths of the ME-couplings found in the lithium-ortho-phosphates. T. B. S. Jensen thoroughly examined the magnetic structure in $LiNiPO_4$ in both zero and applied field. He found a complex phase diagram for fields applied parallel to the spins, and in zero field he found that the spins are not co-linear but canted. This canting was found to be facilitated by a second order exchange interaction induced by the spin orbit coupling - the so-called Dzyaloshinsky-Moriya (DM) interaction - which played a central role in explaining the ME effect in $LiNiPO_4$ microscopically [4]. The three systems all display strong in-plane (ab) exchange couplings and weak out-of-plane couplings. The dimensionality of the magnetic moments, however, varies a lotin the three systems. This gives rise to three different phase diagrams. This part of the thesis concerns three smaller projects:

- An investigation into the high field part of the $(\mu_0 H, T)$ phase diagram of $LiNiPO_4$ (pseudo-XY system). It is investigated whether or not the high field low temperature incommensurate structure is a spiral. Furthermore, the phase diagram is examined at the highest fields available for neutron scattering - 17.3 tesla. The spin waves has been measured in the hgih field incommensurate phase.
- An examination of the magnetic phase diagram of the isotropic $LiMnPO_4$ (Heisenberg system) for fields applied along the spin direction, which exhibits a spin flop transition, using both neutron scattering and magnetization measurements.
- Having obtained evidence for a DM interaction in $LiNiPO_4$ this interaction is expected to be stronger in $LiCoPO_4$ (pseudo-Ising system). The magnetic structure has been examined in both zero and applied field in search for both DM and higher order interactions. Furthermore, an attempt is made to establish the magnetic phase diagram for fields applied along the easy direction as well.

2 Elements of Crystallography and Magnetism

In this section, the necessary concepts and results for understanding the lithium-ortho-phospates are described. Some crystallographic concepts are very useful, since the symmetries present in ordered systems has profound consequences for the physics contained in these system, as will be evident. Since this part of the thesis deals with magnetic structures and interactions the necessary elements of the theory of magnetism will be presented in some detail. Results from non-relativistic quantum mechanics found in [5, 6] will be used without reference in this section.

2.1 Magnetism

All charged particles exhibit a magnetic dipole moment, since they have intrinsic angular momentum, namely spin. The electrons exhibit the largest magnetic dipole moment of the particles constituting atoms, since they are the lightest of the particles constituting matter and $\mu = -g_e \frac{e\hbar}{2m_e} \mathbf{S}_e$. Because of this, usual magnetic topics only concerns magnetism of electrons, and this thesis is no exception. Electrons are fermions, obeying the Pauli principle, stating that any multi electron wave function are antisymmetric with respect to two-electron exchange, or identically that no two identical fermions can occupy the same quantum state. This principle lies at the heart of atomic physics and magnetism. In the following, atomic units are used so that $\hbar = 1$, $c = 1$, $e = 1$, $m_e = 1$ (the mass of the electron) and $4\pi\varepsilon_0 = 1$.

2.1.1 The one electron atom

As is well known, the atom consists of a nucleus, where positively charged protons are glued together with the neutral neutrons by the strong nuclear force overcoming the coulomb repulsion between protons, surrounded by the negatively charged electrons. The neutral atom has an equal number of protons and electrons, the latter of which are bound by the coulomb potential of the nucleus ([7]):

$$V(r) = -\frac{Z}{r}, \tag{2.2}$$

where Z is the atomic number and r is the distance from the electron to the nucleus. The eigenstates for a single electron bound by this potential are found by solving the time-independent Schrödinger equation for hydrogen atoms:

$$\left[\frac{-\hbar}{2m_{cm}}\nabla^2 - \frac{Z}{r}\right]\Psi(\mathbf{r}) = E\Psi(\mathbf{r}) \tag{2.3}$$

where $m_{cm} = \frac{M}{1+M}$ is the reduced mass of the system (M is the mass of the nucleus expressed in terms of the electron mass), E is the eigenstate energy and $\Psi(\mathbf{r})$ is the spatial electronic wave function. For one electron atoms, the Schrödinger-equation can be solved exactly:

$$\Psi_{n,l,m}(r,\phi,\theta) = R_{nl}(r)Y_{lm}(\theta,\phi), \tag{2.4}$$

Where $R_{nl}(r)$ and $Y_{lm}(\theta,\phi)$ are the radial and orbital parts of the wave function respectively ([7], [5]). This separation of the radial and angular part of the wave function is possible due to the coulomb potential being spherically symmetric. R_{nl} is a sum of polynomials with $n - l$ terms, n being the convenient *principal quantum number* and l the well known quantum number describing the eigenvalue of the $\hat{L}^2$ operator. The principal quantum number denotes the energy levels of the hydrogenic atom which are

$$E_n = -\frac{Z^2\mathbb{R}}{n^2}, \tag{2.5}$$

where $\mathbb{R}$ is the well known Rydberg constant which is the ionization energy of hydrogen in its ground state. For any given energy level with principal quantum number n, it must hold that $l \leq n-1$. The last good quantum number describing the spatial wave function of hydrogenic atoms are the well known eigenvalue of the $\hat{L}_z$-operator - the magnetic quantum number m describing the projection of the angular momentum vector onto the arbitrarily chosen z-axis. For any given value of l, m can assume $2l+1$ values. Thus, the energy eigenvalues E_n of the hydrogenic atoms are n^2-fold degenerate, $2n^2$-fold degenerate if spin is included. The radial part of the wave function depends on n and l, and the spherical part - described by the spherical harmonics - depends on l and m. The values for angular momenta have been given letter names: s for $l=0$, p for $l=1$, d for $l=2$ and f for $l=3$. For $l>0$, the electronic distributions assume drop-like shapes with different symmetries.

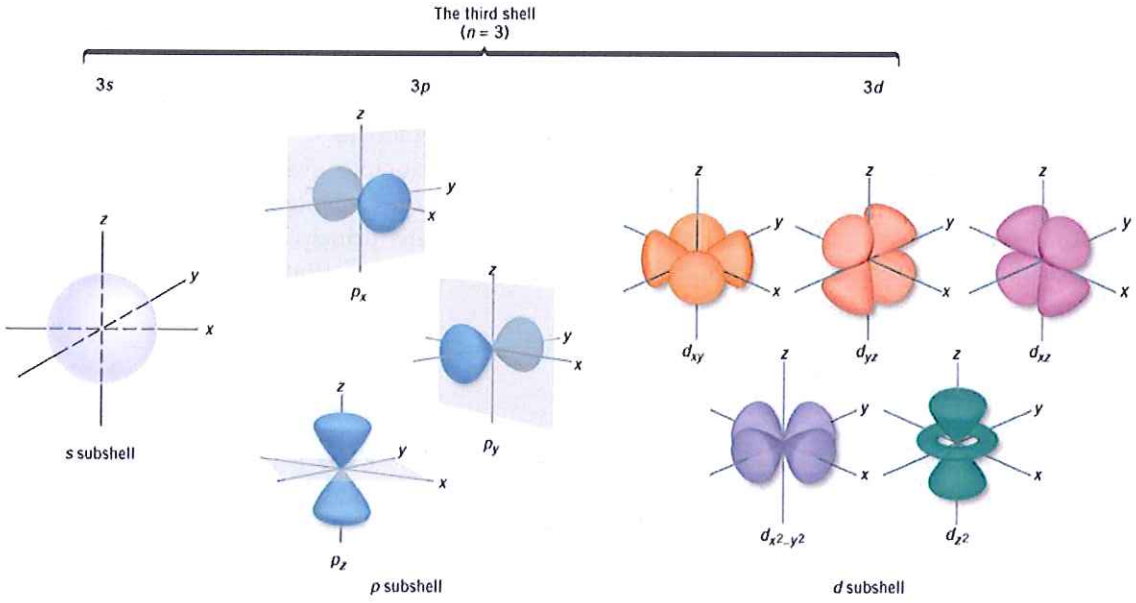

Figure 2: The spatial distribution of an electron in the orbitals possible with principal quantum number (n = 3). Picture from http://www.sci.uidaho.edu/Chem101/Links.htm

The possible spatial electron distributions for $n = 3$ are shown in figure 2. This constitutes the simplest possible model for hydrogenic atoms, without taking any of the many perturbations shown to have an effect into account. These perturbations include relativistic kinematic effects, spin-orbit-interactions ($\hat{\mathbf{L}} \cdot \hat{\mathbf{S}}$), the exotic Lamb shift (electronic coupling to the ground state of the quantized electromagnetic field) and the hyperfine shifts/splittings (nuclear spin, finite nuclear size and eventual electric quadrupole effects). Nevertheless, this basic model form the basis of atomic physics.

2.1.2 Many-electron atoms

In the following, only the electron-nucleus interaction, the electron-electron interaction and the electron spin-orbit coupling will be considered; all other (and smaller) perturbations are neglected. Initially including only the electron-electron interaction, the Hamiltonian for an N-electron atom will be [7]:

$$\mathcal{H} = \sum_{i=1}^{N} \left[-\frac{1}{2}\nabla^2 - \frac{Z}{r_i} \right] + \sum_{i<j=1}^{N} \frac{Z}{r_{ij}} \tag{2.6}$$

This is the general atomic coulomb Hamiltonian. It is evident from the time-independent Schödinger equation - $\mathcal{H}\Psi = E\Psi$ - that the wave function cannot be separated into a radial and spherical part, due to the inter-electronic potential. In describing the field felt by the Nth electron, assume that the main effect of the $N-1$ other electrons is to screen the nuclear charge, reducing the effective charge of the nucleus. If this is true, the inter-electronic interaction can be described as being mainly spherical symmetrical with a small non-spherical correction. This is the basic assumption in the theoretical treatment of many-electron atoms - one that builds a bridge between the many-electron system and the simple hydrogenic systems - called the *central field approximation.* The residual part of the potential due to the inter-electron couplings is not spherically symmetric, but can now be assumed to be small, and hence qualifying as a small perturbation subject to perturbation-theory. Then, the spherically symmetric part of the potential acting on any electron has the form

$$V_{cf}(r) = -\frac{Z}{r_i} + S(r), \tag{2.7}$$

where $S(r)$ is the spherically symmetric part of the inter electronic interaction.The Hamiltonian can now be written as follows:

$$\mathcal{H} = \left[\sum_{i=1}^{N}\left(-\frac{1}{2}\nabla^2 + V_{cf}(r_i)\right)\right] + \left[\sum_{i<j=1}^{N}\frac{Z}{r_{ij}} - \sum_i S(r_i)\right] \tag{2.8}$$

$$= \mathcal{H}_{cf} + \mathcal{H}_1 \tag{2.9}$$

The wave functions satisfying the time-independent Schödinger-equation for the spherically symmetric Hamiltonian $\mathcal{H}_{cf}$, can now be separated into a radial and a spherical part. The single-electron orbitals can be found by solving

$$\left[-\frac{1}{2}\nabla^2 + V_{cf}(r_i)\right]u_{nlm}(\mathbf{r}) = E_{nl}u_{nlm}(\mathbf{r}), \quad \text{where}$$

$$u_{nlm}(\mathbf{r}) = R^{cf}_{nl}(r)Y_{lm}(\theta,\phi). \tag{2.10}$$

The radial parts of the single-electron wave functions differ from their hydrogenic counterparts, but the spherical part must be the same - namely the spherical harmonics. The multi-electron solution of the time-dependent Schödinger can be written as follows:

$$\mathcal{H}_{cf}\Psi_c = \left[\sum_{i=1}^{N}\left(-\frac{1}{2}\nabla^2 + V_{cf}(r_i)\right)\right]\Psi_c$$

$$= E_c\Psi_c, \quad \text{where}$$

$$\Psi_c = \prod_{i=1}^{N} u_{n_i l_i m_i}(\mathbf{r}_i). \tag{2.11}$$

The multi-electron eigenfunctions in the central field are products of all the single electron eigenfunctions, and the eigen energy is the sum of the single electron eigen energies. Besides the three central field quantum numbers nlm, another very important quantum number needs to be included in the model, namely the additional *spin* magnetic quantum number. Since the central field Hamiltonian does not depend on spin orientation, the spin eigenfunctions can easily be incorporated into the single electron central field orbitals:

$$u_{nlm_l m_s}(\mathbf{r},\mathbf{s}) = R^{cf}_{nl}(r)Y_{lm_l}(\theta,\phi)\chi^{1/2}_{m_s}. \tag{2.12}$$

When including spin, the wave functions proposed in equation 2.11 are not adequate, since they are not anti-symmetric with respect to exchange of any two electrons. Let α_i be the four quantum

numbers n_i, l_i, m_{li}, and m_{si}. An antisymmetric multi electron wave function can be written as a determinant known as the *Slater determinant*:

$$\Psi_c(\mathbf{r}_1,\mathbf{s}_1,\mathbf{r}_2,\mathbf{s}_2,...,\mathbf{r}_N,\mathbf{s}_N) = \begin{vmatrix} u_{\alpha_1}(\mathbf{r}_1,\mathbf{s}_1) & u_{\alpha_2}(\mathbf{r}_1,\mathbf{s}_1) & \dots & u_{\alpha_N}(\mathbf{r}_1,\mathbf{s}_1) \\ u_{\alpha_1}(\mathbf{r}_2,\mathbf{s}_2) & u_{\alpha_2}(\mathbf{r}_2,\mathbf{s}_2) & \dots & u_{\alpha_N}(\mathbf{r}_2,\mathbf{s}_2) \\ \vdots & \vdots & \ddots & \vdots \\ u_{\alpha_1}(\mathbf{r}_N,\mathbf{s}_N) & u_{\alpha_2}(\mathbf{r}_N,\mathbf{s}_N) & \dots & u_{\alpha_N}(\mathbf{r}_N,\mathbf{s}_N) \end{vmatrix}. \quad (2.13)$$

The eigenfunctions of the central field Hamiltonian are of this form. Note, that if two electrons are in the same state, that is if $\alpha_i = \alpha_j$ for some i, j, then two columns in the determinant are the same, and the wave function is 0. Hence, *no two electrons can occupy the same state.* Thus, only two electrons can be in a $n = 1$ state, and only if they have different spins. The energy levels depend on the principal quantum number n and are $2n^2$-fold degenerate - each of these bundles of states with the same energy are called *shells.* For each value of n there is a maximum l-value of $n-1$, just as in the case of hydrogenic atoms. For each of these l-values there are $2(2l+1)$ possible magnetic states, including spin. These magnetic bundles of states are called *sub shells.* The first few shells and sub shells with lowest quantum numbers have been given letter names, see table 2.

-	0	1	2	3	4	5	6
n	-	K	L	M	N	O	P
l	s	p	d	f	g	h	-

Table 2: Shell- and sub shell names.

Due to the Pauli principle, the electrons in many-electron atoms cannot all occupy the same lowest energy state, the shells are filled from the ground state upwards in energy. This is the empirical fact that is the basis for all chemical phenomena. As previously mentioned, the central field Hamiltonian is not adequate for describing many electron atoms. At least two perturbations need to be accounted for: $\mathcal{H}_1$ and the spin-orbit coupling. The spin-orbit coupling is coupling between the orbital angular momentum of the electron and the spin angular momentum - stemming from the magnetic interaction *and* interactions due to precession. Including these interactions, the many-electron Hamiltonian can be written as:

$$\mathcal{H} = \mathcal{H}_{cf} + \left[\sum_{i<j=1}^{N} \frac{Z}{r_{ij}} - \sum_i S(r_i)\right] + \left[\sum_{i=1}^{N} \eta(r_i)\hat{\mathbf{l}}_i \cdot \hat{\mathbf{s}}_i\right] \quad (2.14)$$

$$= \mathcal{H}_{cf} + \mathcal{H}_1 + \mathcal{H}_2 \quad \text{where}$$

$$\eta(r_i) = \frac{1}{2}\frac{1}{r_i}\frac{dV_{cf}(r_i)}{dr_i} \quad (2.15)$$

It can be shown that the contribution to $\mathcal{H}_2$ from filled shells vanishes (intuitively it makes sense, since every l-state has two electrons with opposite spins). In order for perturbation theory to work, the two perturbations of the central field Hamiltonian, $\mathcal{H}_1$ and $\mathcal{H}_2$, must not have equal strength. It is assumed that $\mathcal{H}_2 << \mathcal{H}_1$, which is only the case when the atomic number Z is small or intermediate, as $\mathcal{H}_2$ scales with Z^4 ([7]).

Degeneracy removal by the electron correlation Hamiltonian $\mathcal{H}1$

The fact that the electrons are correlated as evident in the perturbation Hamiltonian $\mathcal{H}_1$, removes some of the $2n^2$ degeneracy of the principal quantum states. Intuitively, the electrons want to be as far away from each other as possible to lower the energy of $\mathcal{H}_1$, thereby favoring some configurations of angular momenta within the unfilled shell. It can be shown that the perturbed

Hamiltonian $\mathcal{H}_{cf}+\mathcal{H}_1$ commutes with both the total orbital angular momentum and the total spin angular momentum:

$$[\mathcal{H}_{cf}+\mathcal{H}_1, \mathbf{L}^2]=0, \quad [\mathcal{H}_{cf}+\mathcal{H}_1, \mathbf{S}^2]=0 \quad \text{and} \quad [\mathcal{H}_{cf}+\mathcal{H}_1, \mathbf{J}^2]=0, \quad \text{where}$$
$$\mathbf{L}=\sum_{i=1}^{N}\mathbf{l}_i, \quad \mathbf{S}=\sum_{i=1}^{N}\mathbf{s}_i \quad \text{and} \quad \mathbf{J}=\mathbf{L}+\mathbf{S} \tag{2.16}$$

Thus, both L and S are good quantum numbers. For any closed shell $S=L=0$, which means that only the unfilled shells are relevant in determining the total spin and orbital angular momentum of the possible electron configurations. In determining the possible values of L and S one needs to use the rules of addition of angular momenta found in textbooks ([6]), but one also needs to take the Pauli principle into account for electrons belonging to the same sub shell. This will not be elaborated here. The eigenstates of the Hamiltonian can be denoted $|\gamma LSM_LM_S\rangle$, where M_L and M_S are projections of the total angular momenta onto the z-axis and γ is an additional quantum number analogous to the principal quantum number. These states have $(2L+1)(2S+1)$ degeneracy, stemming from the fact that an isolated atom has no preferred direction of the angular momentum vector and hence the energy levels are independent of M_L and M_S. The calculation of the ground state configuration and the energy levels of the allowed configurations is no easy task. There are empirically based rules though, called *Hunds rules* ([7, 8]), determining (in many cases) the ground state configuration of angular momenta of a given atom. The first two rules can be intuitively understood on the grounds of the electronic coulomb repulsion expressed in $\mathcal{H}_1$:

- **Hunds 1st rule:** In the unfilled shell, first arrange the configuration of angular momenta to maximize the spin quantum number S. As the Pauli principle prevents electrons with parallel spins to be in the same place, this will minimize $\mathcal{H}_1$.
- **Hunds 2nd rule:** After maximizing S, maximize L. Electrons in orbits parallel to one-another can more easily maximize the distance between them, avoiding coulomb repulsion.

After treating the correlation term of the multi-electron Hamiltonian, the next step is to treat the weaker spin orbit term.

Degeneracy removal by the spin-orbit Hamiltonian $\mathcal{H}_2$

The spin-orbit coupling is the coupling between the orbital and spin angular momenta of a single electron, favoring the spin direction to be anti-parallel to the orbital angular momentum vector. This will remove some of the $(2L+1)(2S+1)$-degeneracy of the sub shells described previously. The term $\mathcal{H}_2$ in the many-electron Hamiltonian written in equation 2.15 commutes with the total orbital angular momentum squared $\mathbf{L}^2$, the total spin angular momentum squared $\mathbf{S}^2$ and with the square of the total atomic angular momentum $\mathbf{J}^2=(\mathbf{L}+\mathbf{S})^2$ However, $\mathcal{H}_2$ *does not* commute with the magnetic operators L_i nor S_i $(i=x,y,z)$, the only good magnetic quantum number is J_i. Since $\mathcal{H}_1 >> \mathcal{H}_2$ the splitting caused by the spin-orbit term will be much smaller than that caused by the correlation term. Hence, different LS-multiplets will not mix due to the spin-orbit perturbation. Therefore, the spin-orbit splitting of each state can be evaluated separately. It can be proved (done in [7]) that within each LS multiplet,

$$\mathcal{H}_2=\lambda_{LS}\mathbf{L}\cdot\mathbf{S}, \quad \text{where} \quad \mathbf{L}=\sum_i \mathbf{l}_i, \quad \mathbf{S}=\sum_i \mathbf{s}_i, \tag{2.17}$$

and where λ_{LS} is specific for the multiplet. It is worth noting that configurations with either $S=0$ or $L=0$ will not be split as $\mathbf{L}\cdot\mathbf{S}$ will be zero. Recalling that $\mathbf{J}^2$ is

$$\mathbf{J}^2=\mathbf{L}^2+2\mathbf{L}\cdot\mathbf{S}+\mathbf{S}^2,$$

and switching to the convenient basis $|\gamma LSJM_J\rangle$ the spin orbit energy shift can be evaluated as

$$\begin{aligned}\langle\gamma LSJM_j|\mathcal{H}_2|\gamma LSJM_j\rangle &= \frac{\lambda_{LS}}{2}\langle\gamma LSJM_j|\mathbf{J}^2-\mathbf{L}^2-\mathbf{S}^2|\gamma LSJM_j\rangle \\ &= \frac{\lambda_{LS}}{2}\left[J(J+1)-L(L+1)-S(S+1)\right]. \end{aligned} \tag{2.18}$$

Using the rules of addition of angular momenta, the possible values of J are $|L-S|, |L-S|+1, ..., L+S$. Therefore, the number of values are $2S+1$ if $L \geq S$ and $2L+1$ if $L < S$. The difference between energy levels is $E(J)-E(J-1) = \lambda_{LS}J$, which is dependent on λ_{LS}. Therefore, depending on the sign of λ_{LS} either the state with maximum or minimum value of J will be the ground state. The sign of λ_{LS} depends on whether the sub shell is less than half filled or more than half filled (precisely half filled results in the state not being split). This results in *Hunds 3rd rule*, or

- **Lande's interval rule:** The state with $J = |L-S|$ will be the ground state if there is a single open sub shell that is less than half filled. If the sub shell is more than half filled, the state with $J = L+S$ will be the ground state.

Even when including $\mathcal{H}_2$ there is no preferred direction in space, so each of these split states still retains a $J(J+1)$-degeneracy representing the possible M_J quantum numbers. A level scheme of the atomic splitting of a p-orbital is shown in figure 3.

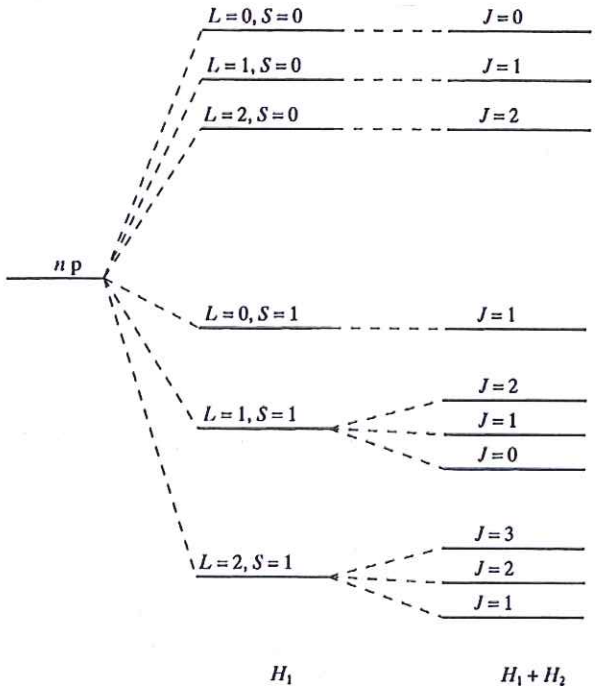

Figure 3: The splitting of the principal multi-electron atomic states. The perturbation accounted for in the Hamiltonian is shown below. Picture modified from [7].

This concludes the treatment of the free atom. When atoms are bound in crystal structures, a wide range of magnetic effects and interactions is possible, some of which will be described in the following.

2.1.3 Crystal field effects: level splitting, orbital quenching and anisotropy

The lithium ortho-phosphates are systems with ionic molecular bonds, where an electron transference occurs. There is a permanent transference of charge between the atoms and with localized valence electrons. The system is held together by the coulomb force between the ions. Thus, every ion in the crystal is subjected to an electrostatic field caused by the surrounding ions. The effect of this crystal field is stronger than the spin-orbit coupling in case of the transition metals ([9]), so the crystal field perturbs the Hamiltonian $\mathcal{H}_{cf} + \mathcal{H}_1$ causing a splitting of the LS-multiplets. The ionization state of the magnetic transition metal ions in LiMPO$_4$ is M^{2+}, and the unfilled shell is 3d ($n = 3$, $l = 2$). In the following, it is assumed that the crystal field is too weak to mix the LS ground state with higher energy multiplets; it is assumed that the crystal field Hamiltonian can be diagonalized within the LS-multiplet subspace. An illustration of the difference in coulomb energy of different $3d$ orbitals can be seen in figure 4a. It is clear that given the p-orbitals of the surrounding oxygen atoms, the $d_{x^2-y^2}$ orbital has a higher coulomb energy than the d_{xy}. When describing the crystal field, a simplifying assumption is that the anions surrounding the transition metal ion can be viewed as point charges not overlapping with the orbitals of the $3d$ orbitals (a very crude assumption only valid to first order). The electrostatic crystal field potential and the corresponding perturbation Hamiltonian for the transition metal ions can be written as:

$$V_{crystal}(\mathbf{r}) = \sum_i \frac{e_i}{|\mathbf{r} - \mathbf{R}_i|} \quad \text{and} \quad \mathcal{H}_{crystal} = -e \sum_{j=1}^{N} V_{crystal}(\mathbf{r}_j), \tag{2.19}$$

where $\mathbf{R}_i$ are the position vectors of the surrounding ions with charge e_i, and N is the number of electrons occupying the unfilled shell of the transition metal ion subject to the crystal field. The transition metal ions in the lithium ortho-phosphates sit slightly displaced from the center of an oxygen octahedron (see figure 4). When evaluating the effects of the crystal field, it is useful to expand the crystal field potential in terms of spherical harmonics - called the *multipole expansion.* This allows for a direct application of the symmetry properties of the crystal to the crystal field potential to exclude the terms forbidden by symmetry arguments. Switching to spherical coordinates - $\mathbf{R}_i \to (R_i, \theta_i, \phi_i)$ and $\mathbf{r} \to (r, \theta, \phi)$ - the crystal field potential can be written as follows:

$$\begin{aligned} V_{crystal}(r, \phi, \theta) &= \sum_l \sum_{m=-l}^{l} K_{lm} r^l P_l^{|m|}(\cos\theta) e^{im\phi} \quad \text{where} \\ K_{lm} &= \frac{(l - |m|)!}{(l + |m|)!} \sum_i \frac{e_i}{R_i^{l+1}} P_l^{|m|}(\cos\theta_i) e^{im\phi_i} \end{aligned} \tag{2.20}$$

where $P_l^{|m|}$ is the Legendre polynomial. The terms describe the coupling of the crystal field - which are described by K_{lm} - with the electrons in the unfilled shell of the magnetic ion of increasing order in the multipole expansion. The term for $l = 0$ is $V_0 = \sum_i e_i/R_i$ and is simply the constant coulomb potential of a charge sitting in the position of the magnetic ion. It is a constant term, not depending on the angular distribution of the electrons and hence it does not cause any splitting L-multiplet. If one takes the spherical harmonics as tensor operators, one can use the Wigner-Eckart theorem to obtain the selection rules ([6]):

$$\langle l'm'|Y_q^k|lm\rangle \neq 0 \quad \text{only when} \quad q = m' - m \quad \text{and} \quad |l' - l| \leq k \leq l' + l \tag{2.21}$$

Thus, for a d electron with $l = 2$ the maximum value of l in the sum of equation 2.20 is 4. This is equivalent of saying that higher multipole orders than four cannot perturb $3d$ charge distributions. Due to the time-reversal symmetry of the crystal field, only terms with even l are finite. Furthermore, if the crystal field expressed with the magnetic ion in the origin has inversion symmetry, only terms with even m persists. Thus - in the presence of inversion symmetry - only the terms V_2 and

V_4 are relevant in the multipole expansion for the crystal field surrounding a transition metal ion. The values of K_{lm} depend on the symmetry of the field. In case of perfect cubic symmetry (the metal ion sitting in the center of the octahedron), it can be shown that only V_4 is non-zero. This causes a splitting of the $3d$ orbitals into different multiplets depending on the number of electrons in the unfilled shell (see figure 4 c) for the case of Fe^{2+} splitting into a triplet and a doublet). However, in the lithium orthophosphates the octahedron is not perfect but irregular, giving rise to a non-zero V_2 component. Furthermore, the oxygen octahedron is only the dominant part of the crystal field, there are other ions in the crystal playing a smaller part, and thus the symmetry of the crystal as a whole - which in the case of the lithium orthophosphates is much lower than cubic - determines the splitting. The consequence of these facts is that the $3d$ multiplet will split into a number of non-degenerate singlets.

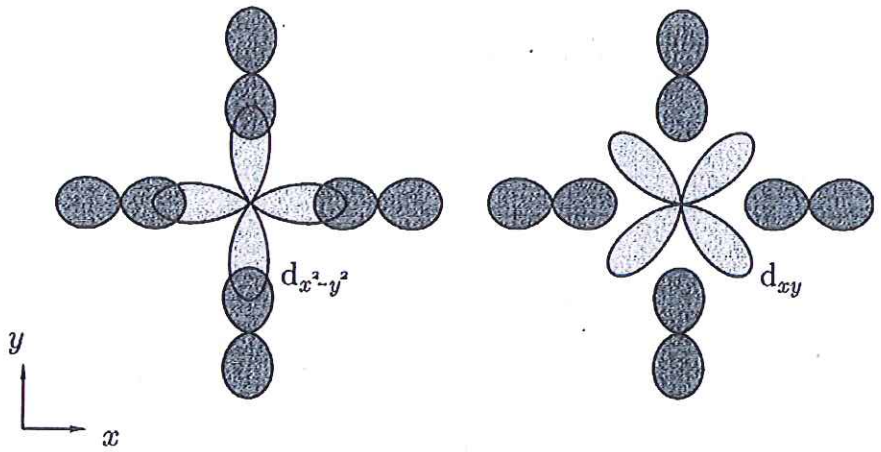

(a) Projection of the electron distribution of a transition metal ion surrounded by oxygen ions onto an xy-plane.

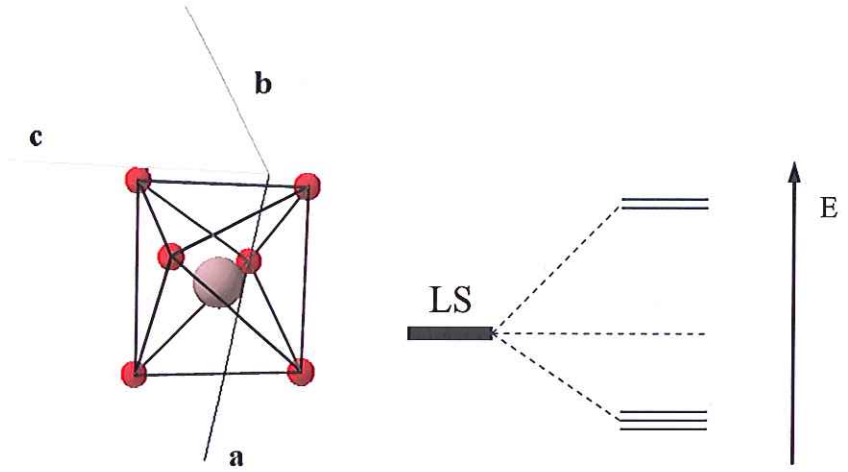

(b) The oxygen octahedron surrounding the M^{2+}-ion in LiMPO$_4$

(c) Splitting of a Fe^{2+} $L = 2, S = 2$ state due to a perfect octahedral crystal field

Figure 4: a) Examples of charge distribution of the d-shell transition metal electrons surrounded by p-shell electrons from the four oxygen atoms in the same plane. b) The actual position of the transition metal ion (brown) slightly displaced within an oxygen (red) octahedron. c) Example of crystal field splitting of an $(3d)^6$ state of an Fe^{2+}-ion.

Orbital quenching

The electrostatic potential produced by the static position of electric charges is invariant with respect to time-reversal and is therefore described by a real function. As the crystal field Hamiltonian $\mathcal{H}_{crystal}$ is real, the eigenfunctions of this Hamiltonian in the subspace spanned by the LS multiplet must be real. However, the orbital angular momentum operator is purely imaginary: $\hat{\mathbf{L}} = i\hbar(\mathbf{r} \times \boldsymbol{\nabla})$. Therefore, the expectation value of $\hat{\mathbf{L}}$ must be purely imaginary, but since $\hat{\mathbf{L}}$ is hermitian the expectation value must also be real. Thus, following must hold:

$$\langle n|\hat{\mathbf{L}}|n\rangle = \langle n|\hat{\mathbf{L}}|n\rangle^* = -\langle n|\hat{\mathbf{L}}|n\rangle = 0 \tag{2.22}$$

This only holds for the diagonal matrix elements. The ground state of the crystal field Hamiltonian has been argued to be non-degenerate in the previous section. Therefore, the expectation value of the angular momentum operator is zero:

$$\langle 0|\hat{\mathbf{L}}|0\rangle = 0 \tag{2.23}$$

This is known as *orbital quenching*. It follows from the low symmetry of the crystal field splitting that the $3d$ orbitals form non-degenerate singlets. However, the spin-orbit coupling can restore some of the quenched orbital angular momentum as this perturbation will mix some of the crystal field singlets. Furthermore, this will result in preferred directions in space (single ion anisotropy) as will be elaborated in the following section.

Spin-orbit term: Single ion anisotropy and induced orbital momentum

Both the spin-orbit term and the Zeeman energy resulting from an applied magnetic field $\mathbf{H}$ is treated as a perturbation of the crystal field Hamiltonian $\mathcal{H}_0 = \mathcal{H}_{cf} + \mathcal{H}_1 + \mathcal{H}_{crystal}$. Using equation 2.17, the Hamiltonian is

$$\mathcal{H} = \mathcal{H}_0 + \mathcal{H}_{so} + \mathcal{H}_{zeeman} = \mathcal{H}_0 + \lambda_{LS}\mathbf{L}\cdot\mathbf{S} + \mu_B\mathbf{H}\cdot(2\mathbf{S}+\mathbf{L})\,. \tag{2.24}$$

In the previous section the splitting of different spatial orbitals due to the crystal field splitting was examined. The potential consisted only of coulomb repulsion between different static charges positioned in space, and hence the potential was only dependent of the spatial coordinates of the electrons. Hence, the Hilbert space of the unperturbed electron states can be considered as a product space between the spatial space and the spin space, as they are independent. In the following, only the spatial part of the unperturbed electronic wave functions are included in the matrix elements of the perturbation calculation, leaving the spins as operators to obtain a spin-Hamiltonian. Since the orbital angular momentum is quenched to first order in the ground state, the first order ground state energy change is

$$\Delta E_{so}^{(1)} = 2\mu_B\mathbf{H}\cdot\mathbf{S}, \tag{2.25}$$

which is merely the Zeeman energy of the quenched ground state. When taking the perturbation to second order, the ground state is mixed with the crystal field states with higher energy and finite

orbital angular momentum yielding the second order energy shift:

$$\begin{aligned}
\Delta E_{so}^{(2)} &= \sum_{k\neq 0} \frac{|\langle 0|\mathcal{H}_{so}|k\rangle|^2}{E_0 - E_k} \\
&= \sum_{k\neq 0} \frac{1}{E_0 - E_k} \left(\sum_{\nu} \lambda \langle 0|L_\nu S_\nu|k\rangle + 2\langle 0|H_\nu S_\nu|k\rangle + \langle 0|H_\nu L_\nu|k\rangle \right) \\
&\times \left(\sum_{\mu} \lambda \langle k|L_\mu S_\mu|0\rangle + 2\langle k|H_\mu S_\mu|0\rangle + \langle k|H_\mu L_\mu|0\rangle \right) \\
&= -\sum_{\mu\nu} \left[\lambda^2 \Lambda_{\mu\nu} S_\mu S_\nu + 2\lambda \mu_B \Lambda_{\mu\nu} H_\mu S_\nu + \mu_B^2 \Lambda_{\mu\nu} H_\mu H_\nu \right], \quad \text{where} \qquad (2.26) \\
\Lambda_{\mu\nu} &\equiv \sum_{k} \frac{\langle 0|L_\mu|n\rangle\langle n|L_\nu|0\rangle}{E_k - E_0}. \qquad (2.27)
\end{aligned}$$

In the above equation μ and ν represent Cartesian coordinates while E_k and $|k\rangle$ are eigen energies and eigenstates of the crystal field Hamiltonian. The fact that the spin is left as an operator and only the orbital parts of the wave functions are considered makes equation 2.27 particularly simple as terms of the form $\langle n|H_\mu S_\nu|0\rangle$ vanish as $\langle n|0\rangle = 0$. The sum of the first and second order expansion of the spin-orbit/Zeeman perturbation *of the ground state* can now be written as a spin Hamiltonian:

$$\mathcal{H}_{so} = -\sum_{\mu\nu} \left[2\mu_B H_\mu \left(\delta_{\mu\nu} - \lambda \Lambda_{\mu\nu} \right) S_\nu - \lambda^2 S_\mu \Lambda_{\mu\nu} S_\nu - \mu_B^2 H_\mu \Lambda_{\mu\nu} H_\nu \right] \qquad (2.28)$$

The first term of this ground state Hamiltonian is an effective Zeeman energy, with the g-factor replaced by an *effective g-tensor*:

$$g_{\mu\nu} \equiv 2\left(\delta_{\mu\nu} - \lambda \Lambda_{\mu\nu} \right). \qquad (2.29)$$

Thus, the tensor $\Lambda_{\mu\nu}$ describes the orbital moment induced by the spin-orbit interaction. In $LiNiPO_4$ for instance, the effective g-value for the magnetic moment of the Ni^{2+} ion is 2.2 even though the quenched ground state has $S = 1$ ([4]). The second term in equation 2.28 is the *single ion anisotropy Hamiltonian*, which described the splitting of the $(2S+1)$-fold degeneracy caused by the spin-orbit interaction giving a preferred spin direction in space. For simplicity, it is assumed that the Cartesian axes x, y and z coincide with the principal axes of the crystal system, and that the $\Lambda_{\mu\nu}$ can be diagonalized. Using the basis for diagonalization, the anisotropy term $\mathcal{H}_{aniso} = -\lambda^2(\Lambda_x S_x^2 + \Lambda_y S_y^2 + \Lambda_z S_z^2)$ can be expressed as follows:

$$\begin{aligned}
\mathcal{H}_{aniso} &= \frac{-\lambda^2}{3} \left(\Lambda_x + \Lambda_y + \Lambda_z \right) S(S+1) \\
&- \frac{\lambda^2}{3} \left(\Lambda_z - \frac{1}{2}(\Lambda_x + \Lambda_y) \right) \left[3S_z^2 - S(S+1) \right] - \frac{\lambda^2}{2} \left(\Lambda_x - \Lambda_y \right) \left(S_x^2 - S_y^2 \right) \\
&= DS_z^2 + E(S_x^2 - S_y^2), \qquad (2.30)
\end{aligned}$$

where the constant terms involving only $2S+1$ have been discarded since these terms only describe the total spin of the ground state. The term DS_z^2 splits the ground state into doubly degenerate levels with $S_z = \pm S, \pm(S-1), ..., \pm 1/2$. In case of integer S there is a non-degenerate level with $S_z = 0$. As $S_x^2 - S_y^2 = 1/2(S_+ S_+ + S_- S_-)$ the term $E(S_x^2 - S_y^2)$ has finite matrix elements with $\Delta S_z = \pm 2$. This can only happen in case of integer spin; therefore this term will only lift the double degeneracy in case of integer spin, where $\mathcal{H}_{aniso}$ is non-diagonal in the basis of eigenfunctions to the S_z-operator. In case of half-odd integer S, $\mathcal{H}_{aniso}$ splits the eigenstates of S_z into doublets called *Kramers doublets*. These degeneracies are lifted by an external field. The

third term in 2.28 describes a second order Zeeman energy for orbital angular momentum, and gives rise to an anisotropy of the magnetic susceptibility. It will be given no further attention here. The effects described in this section arise solely because of the crystallographic surroundings of a single magnetic ion. However, in many cases the magnetic ions in a crystal can interact with one another in several different ways, causing correlated magnetism in a macroscopic crystal. Some of these interactions will be described in the following.

2.1.4 Exchange interaction

Consider two identical transition metal magnetic ions in proximity to one another, with localized $3d$ valence electrons as is the case in the lithium orthophosphates. The electronic wave function of two d-orbital single-electron-states occupying the two ions are denoted $\Psi(\mathbf{r}_1)$ and $\Psi(\mathbf{r}_2)$. The expectation value of the coulomb potential $V_C = \frac{1}{r_{12}}$ is the inner product

$$\langle \Psi(\mathbf{r}_1)\Psi(\mathbf{r}_2)|V_C|\Psi(\mathbf{r}_1)\Psi(\mathbf{r}_2)\rangle = \frac{1}{2}\int\int \Psi(\mathbf{r}_1)^*\Psi(\mathbf{r}_2)^*\frac{1}{r_{12}}\Psi(\mathbf{r}_2)\Psi(\mathbf{r}_1)dx_1dx_2 \tag{2.31}$$

where x denotes both the three spatial coordinates and the spin state. Let $\phi_{nm}(\mathbf{r})$ denote a complete set of orthonormal one-electron wave functions of the nth atom with magnetic quantum number m and let χ_s be the spin wave function. The electron wave function $\Psi(\mathbf{r})$ can be regarded as a Fermi field in the second quantization. Thus, the Hamiltonian is expressed in terms of electron state creation and annihilation operators, $\Psi(\mathbf{r})$ and $\Psi^\dagger(\mathbf{r})$, which themselves are expanded in terms of annihilation and creation operators for the localized orthogonal electron states $\phi_{nm}(\mathbf{r})$

$$\begin{aligned}
\Psi(\mathbf{r}) &= \sum_{nms} a_{nms}\phi_{nm}(\mathbf{r})\chi_s \\
\Psi^\dagger(\mathbf{r}) &= \sum_{nms} a^\dagger_{nms}\phi^*_{nm}(\mathbf{r})\chi^*_s, \quad \text{where} \qquad (2.32)\\
\{a_{nms}, a^\dagger_{n'm's'}\} &= \delta_{nn'}\delta_{mm'}\delta_{ss'} \quad \text{and} \quad \{a^\dagger_{nms}, a^\dagger_{n'm's'}\} = \{a_{nms}, a_{n'm's'}\} = 0. \qquad (2.33)
\end{aligned}$$

The nature of the single electron states $\phi_{nm}(\mathbf{r})$ are briefly discussed in [10]. They are the so-called *Wannier functions*, convenient because Wannier functions localized on different lattice sites are orthogonal. Equation 2.33 states the usual conditions for fermion creation and annihilation operators. Substituting equation 2.32 directly into equation 2.31 gives the second quantized Hamiltonian of the coulomb interaction between two electrons :

$$\begin{aligned}
\mathcal{H}_C &= \frac{1}{2}\sum_{\substack{n_1,m_1\\s_1}}\sum_{\substack{n_2,m_2\\s_2}}\sum_{\substack{n_3,m_3\\s_3}}\sum_{\substack{n_4,m_4\\s_4}}\langle n_1m_1, n_2m_2|\frac{1}{r_{12}}|n_3m_3, n_4m_4\rangle \\
&\times\ a^\dagger_{n_1m_1s_1}a^\dagger_{n_2m_2s_2}a_{n_3m_3s_2}a_{n_4m_4s_1}. \qquad (2.34)
\end{aligned}$$

The term where all n are equal describes the coulomb-interaction between electrons belonging to the same atom. In an ionic crystal, a crude assumption only valid till first order is that *each electron is localized on its respective ion, not being able to switch to another ion.* The d-orbitals are safely assumed to be non-degenerate, so when evaluating the expectation value of $\mathcal{H}_C$ in the ground state, only the two terms with $n_1 = n_3$ and $n_2 = n_4$ or $n_2 = n_3$ and $n_1 = n_4$ are non-zero. This is because only the number operator $n_{nms} = a^\dagger_{nms}a_{nms}$ for a given state leaves the state it operates on unchanged, giving a non-zero expectation value. Thus, the two terms are

$$\begin{aligned}
\mathcal{H}_C &= \frac{1}{2}\sum_{n_1,m_1,n_2,m_2}\sum_{s_1s_2}\langle n_1m_1n_2m_2|\frac{1}{r_{12}}|n_2m_2n_1m_1\rangle a^\dagger_{n_1m_1s_1}a_{n_1m_1s_1}a^\dagger_{n_2m_2s_2}a_{n_2m_2s_2} \\
&- \frac{1}{2}\sum_{n_1,m_1,n_2,m_2}\sum_{s_1s_2}\langle n_1m_1n_2m_2|\frac{1}{r_{12}}|n_1m_1n_2m_2\rangle a^\dagger_{n_1m_1s_1}a_{n_1m_1s_2}a^\dagger_{n_2m_2s_2}a_{n_2m_2s_1}. \qquad (2.35)
\end{aligned}$$

The terms in equation 2.35 are the product of two distinct number operators, and merely describe the coulomb interaction between two electrons on different sites with arbitrary spin. The terms in equation 2.35, however, annihilate an electron on site 2 with the spin of the electron on site 1 and create an electron on this site with the spin of the electron on site 2, and equivalently on site 1. This term describes the effects of spin *exchange* (not to be confused with exchange of the electrons themselves), originating from the properties of the Fermi operators which are equivalent of the Pauli exclusion principle. The diagonal part of this exchange Hamiltonian lowers the energy of the system with parallel spins compared to the case with anti-parallel spins. The spin operators can be expressed using the single electron creation and annihilation operators:

$$\begin{aligned} s_{nm-z} &= \frac{1}{2}\left(a^\dagger_{nm\uparrow}a_{nm\uparrow} - a^\dagger_{nm\downarrow}a_{nm\downarrow}\right) \\ s_{nm-x} + is_{nm-y} &= a^\dagger_{nm\uparrow}a_{nm\downarrow} \\ s_{nm-x} - is_{nm-y} &= a^\dagger_{nm\downarrow}a_{nm\uparrow} \end{aligned} \tag{2.36}$$

Using these identities the exchange Hamiltonian can be rewritten in a very interpretable way (done in [9]), denoting the matrix element in equation 2.35 $J^{m_1m_2}_{n_1n_2}$:

$$\begin{aligned} \mathcal{H}_E &= -\sum_{\substack{n_1n_2\\m_1m_2}} J^{m_1m_2}_{n_1n_2}\left(\frac{1}{2} + 2\mathbf{s}_{n_1m_1}\cdot\mathbf{s}_{n_2m_2}\right) \\ &= C - \sum_{\substack{n_1n_2\\m_1m_2}} J^{m_1m_2}_{n_1n_2}\left(2\mathbf{s}_{n_1m_1}\cdot\mathbf{s}_{n_2m_2}\right) \end{aligned} \tag{2.37}$$

The sign of the matrix elements $J^{m_1m_2}_{n_1n_2}$ can be evaluated by expanding the coulomb potential in its Fourier series:

$$V_C = \frac{1}{r_{12}} = \frac{1}{(2\pi)^3}\sum_k \frac{1}{k^2}e^{i\mathbf{k}\cdot(\mathbf{r}_1-\mathbf{r}_2)} \tag{2.38}$$

Inserting this Fourier expansion into the expression for $J^{m_1m_2}_{n_1n_2}$ gives

$$\begin{aligned} J^{m_1m_2}_{n_1n_2} &= \frac{1}{(2\pi)^3}\sum_k \frac{1}{k^2}\int \phi^*_{n_1m_1}(\mathbf{r}_1)\phi_{n_2m_2}(\mathbf{r}_1)e^{i\mathbf{k}\cdot\mathbf{r}_1}d\mathbf{r}_1 \\ &\times \int \phi^*_{n_2m_2}(\mathbf{r}_2)\phi_{n_1m_1}(\mathbf{r}_2)e^{i\mathbf{k}\cdot\mathbf{r}_2}d\mathbf{r}_2 \\ &= \frac{1}{(2\pi)^3}\sum_k \frac{1}{k^2}\left|\int \phi^*_{n_1m_1}(\mathbf{r})\phi_{n_2m_2}(\mathbf{r})e^{i\mathbf{k}\cdot\mathbf{r}}d\mathbf{r}\right|^2 > 0. \end{aligned} \tag{2.39}$$

As evident, $J^{m_1m_2}_{n_1n_2}$ is always positive. In this model, the spins are therefore preferred to be parallel, lowering the exchange energy. The Pauli principle forbids electrons with parallel spins to be in the same place, and in analog to Hunds 1st rule, the coulomb energy will be lowered when the spins are parallel. This picture, however, is much too simple to account for the large variety of magnetic interactions observed in nature. A few more interactions are needed, also in the case of the lithium orthophosphates.

2.1.5 Super-exchange interaction

In ionic crystals the electrons are described as localized on their respective ions. This description is valid when comparing ionic insulators to metals in which some of the valence electrons are free to move throughout the crystal as a whole. In case of completely localized electrons, an interaction Hamiltonian preferring parallel spins was derived in the previous section. However, the orbital

overlap between two magnetic ions with an unmagnetic ion in between, is able to facilitate a probability of electrons jumping between lattice sites, and in that case the exchange interaction becomes a bit more subtle. Assume that there is only one valence electron pr. ion. Suppose that some electrostatic crystal field described by the Hamiltonian $\mathcal{H}_c$ allows for an electron to jump from ion n to ion n' with a small probability described by the Hamiltonian

$$\mathcal{H}_{kin} = \sum_{nn's} b_{n\to n'}^{m\to m'} a_{n's}^{\dagger} a_{ns} \tag{2.40}$$

$$b_{n\to n'}^{m\to m'} = \int \phi_{m'}(\mathbf{r}-\mathbf{R}_{n'})\mathcal{H}_c\phi_m(\mathbf{r}-\mathbf{R}_n)d\mathbf{r}. \tag{2.41}$$

The suffix n on the wave functions ϕ has been dropped because it is implied by the position vectors $\mathbf{R}_n$ and $\mathbf{R}_{n'}$. Since this process involves an actual displacement of the average position of the electron, the Hamiltonian is kinematic. An electrostatic field Hamiltonian is isotropic in spin space, and hence the total spin is a constant of motion; the spin cannot be flipped during this process of electron transference. By introducing this transference probability one introduces the possibility of two electrons being on the same atom, which has a coulomb energy cost called U (this is independent on indices n and n' as each ion is identical). In ionic insulators such as the lithium orthophosphates the electrons are not free to move throughout the crystal; they are localized. Hence the kinetic term in equation 2.40 must be much smaller than the energy cost of two electrons being on the same ion, otherwise the electrons would be mobile. Therefore, when evaluating a Hamiltonian of general coulomb repulsion between electrons on a lattice (equation 2.34) and when including the kinetic term in equation 2.40, the ground state must be the state with one electron localized on each ion (also justified in [10]). The coulomb energy between electrons on different ions is omitted, since this term is a constant coulomb energy of the ground state and only serves to effectively make the barrier U smaller ([10]). Setting all the n's in equation 2.34 equal and omitting the sum over lattice sites gives the coulomb energy of 2 electrons being on the same site

$$\begin{aligned}\mathcal{H}_U &= \frac{1}{2}\sum_{\substack{m_1m_2\\m_3m_4}}\sum_{s_1s_2}\langle nm_1, nm_2|\frac{1}{r_{12}}|nm_3, nm_4\rangle \\ &\times\ a_{nm_1s_1}^{\dagger}a_{nm_2s_2}^{\dagger}a_{nm_3s_2}a_{nm_4s_1}.\end{aligned} \tag{2.42}$$

It is assumed that the localized electron orbitals are non-degenerate in m, which is justified by the effects of the crystal field. In principle the electron on ion n can jump to an orbital on ion n' with a higher energy, but the lowest energy term will be that of the electron jumping to the same ground state orbital. However, the Pauli principle requires the spins to be anti-parallel for two electrons to occupy the same ground state to be possible. Setting all m's equal in 2.42, taking a sum over lattice sites and including the kinetic Hamiltonian gives the so-called *Hubbard Hamiltonian:*

$$\mathcal{H}_{Hub} = \sum_{nn's} b_{n\to n'}^{0\to 0} a_{n's}^{\dagger}a_{ns} + U\sum_n a_{n\uparrow}^{\dagger}a_{n\uparrow}a_{n\downarrow}^{\dagger}a_{n\downarrow} \tag{2.43}$$

where $U = \int\int |\phi_{n0}(\mathbf{r}_1)|^2 1/r_{12}|\phi_{n0}(\mathbf{r}_2)|^2 d\mathbf{r}_1 d\mathbf{r}_2$. As the kinetic term is much smaller than the repulsive term, this kinetic term can be treated as a perturbation of the repulsive Hamiltonian. Since the ground state has one d electron pr. ion the matrix element operator $\langle 0|b_{n\to n'}^{0\to 0}|0\rangle$ is equal to $b_0\delta_{nn'}$, which does not move any electrons. Therefore, the problem reduces to that described in section 2.1.4. So even though the exchange term is not included in equation 2.43, the first order shift in energy can be said to be the sum of Nb_0, where N is the number of lattice sites, and b_0 is the expectation value of the direct exchange term in equation 2.37 in the ground state. The second order process of one electron jumping from ion n to n' after which one of the two electron on ion n' returns to ion n. In the simple picture of considering only the ground state, this is only allowed

for anti-parallel spins due to the Pauli principle. The energy shift of this process can be calculated to be ([9])

$$\Delta E^{(2)} = -\sum_{\substack{nn' \\ ss'}} \frac{|b^{0\to 0}_{n\to n'}|^2}{U} a^\dagger_{ns'} a_{n's'} a^\dagger_{n's} a_{ns}. \tag{2.44}$$

Expressing the fermion ladder operators in terms of spin operators - as in the case with direct exchange - using equations 2.36, gives an interpretable form of the second order energy shift:

$$\Delta E^{(2)} = -\sum_{nn'} \frac{|b^{0\to 0}_{n\to n'}|^2}{U} \left(\frac{1}{2} - 2\mathbf{s}_n \cdot \mathbf{s}_{n'}\right). \tag{2.45}$$

For parallel spins, $(1/2 - 2\mathbf{s}_n \cdot \mathbf{s}_{n'}) = 0$ as it should. The electron jump matrix elements $b^{m\to m'}_{n\to n'}$ are non-zero mostly only between nearest neighbor or next-nearest neighbor lattice sites. The physics of this second order exchange term favoring anti-parallel spins is the following: Neighboring electrons with anti-parallel spins are able to delocalize - and hence minimize their kinetic energy - by sharing space with their respective neighbors. This sharing is usually mediated by some anion between the two magnetic ions, that allows the electrons to jump via overlapping orbitals. Electrons with parallel spins have to stay on their respective ions. However, this is not necessarily true if the ground state is degenerate, or if the other orbitals have energies very close to the ground state. Including the possibility of electrons jumping to other orbitals than the ground state, and omitting any constant contributions, the sum of the energy shifts from both the first and second order exchange terms between pairs of electrons is ([9]):

$$\Delta E_{exch} = -2\sum_{mm'} J^{mm'}_{n_1 n_2} \mathbf{s}^m_{n_1} \cdot \mathbf{s}^{m'}_{n_2} + 4\sum_{mm'} \frac{|b^{m\to m'}_{n_1\to n_2}|^2}{U} \mathbf{s}^m_{n_1} \cdot \mathbf{s}^{m'}_{n_2} \tag{2.46}$$

The problem is complicated further by the fact that more than one electron is occupying the unfilled d-shell in most cases. In treating this complication, the orbital dependence of the inter-electron coupling is assumed negligible as well as the significance of the off-diagonal matrix elements in $m \to m'$ of the coulomb-Hamiltonian in 2.34. The cost of having n electrons on the same atom, can therefore be simplified to be U for every pair of electrons interacting with each other at the lattice point. Assume that there are n electrons in the unfilled shell of each ion in the ground state. The number of electron pairs are then given by $n(n-1)/2$. The energy cost of moving one electron from one ion to another is therefore

$$\Delta E = U\left(\frac{n(n+1)}{2} + \frac{(n-1)(n-2)}{2} + n(n-1)\right) = U, \tag{2.47}$$

which is the same as with one electron pr. ion. It is assumed that the LS multiplet $\mathbf{S}$ is determined from Hunds 1st rule where the unpaired electrons on a given ion have parallel spins, such that

$$\mathbf{s}^m = \frac{1}{2S}\mathbf{S}. \tag{2.48}$$

The exchange energy between a pair of ions can now be written in terms of a single exchange constant:

$$\Delta E_{exch} = -2J_{n_1 n_2} \mathbf{S}_{n_1} \cdot \mathbf{S}_{n_2}, \quad \text{where} \quad J_{n_1 n_2} = \frac{1}{(2S)^2} \sum_{mm'} \left(J^{mm'}_{n_1 n_2} - 2\frac{|b^{m\to m'}_{n_1\to n_2}|^2}{U}\right). \tag{2.49}$$

This exchange constant depends on the surrounding ions as well as the conditions under which the electron transfer occurs, called the *exchange path*. The transfer can go through an intermediate single ion or a whole chain of ions, and hence exchange couplings can be very complicated theoretically. An important point is that the exchange constant $J_{n_1 n_2}$ can be both positive and negative, favoring either parallel or anti-parallel spin orientation of the ion pair considered.

2.1.6 Dzyaloshinsky-Moriya interaction and anisotropic exchange

In section 2.1.3 an orbital momentum induced by the spin-orbit coupling was described. The spin orbit interaction can cause exotic exchange interactions as well. Within the multiplet split by the crystal field, the spin orbit-interaction and the exchange interaction can be treated as a perturbation of the two-ion system ([9])

$$\mathcal{H}' = \lambda \mathbf{L}_1 \cdot \mathbf{S}_1 + \lambda \mathbf{L}_2 \cdot \mathbf{S}_2 + V_{exch}. \tag{2.50}$$

When both the spin-orbit and the exchange interaction are included a second order process involving both these interactions is allowed. Consider the four processes in which ion 1 is excited from the ground state g_1 to some state n_1 by the spin-orbit interaction, after which the exchange interaction acts between ion 1 and 2 and de-excites ion 1. This same process can happen on ion 2 (g_2 and n_2). The two additional second order processes in which the exchange interaction excites the ion in question and the spin orbit-interaction deexcites the ion should be included as well; four processes in total. To evaluate the energy shift resulting from this perturbation, second-order perturbation theory is used. The goal is to describe the magnetic interaction resulting from processes involving both the exchange coupling and the spin-orbit coupling, processes in which one ion is excited and de-excited by the same interaction are of no interest as they are treated in sections 2.1.3 and 2.1.5. Thus keeping only the terms in $|\langle g_1 g_2|\mathcal{H}'|n_1 g_2\rangle|^2$ and $|\langle g_1 g_2|\mathcal{H}'|n_1 g_2\rangle|^2$ involving both interactions, results in a second order shift in energy of

$$\begin{aligned}\Delta E_0^{(2)} &= -\lambda\Bigg(\sum_{n_1}\frac{\langle g_1|\mathbf{L}_1\cdot\mathbf{S}_1|n_1\rangle\langle n_1 g_2|V_{exch}|g_1 g_2\rangle + \langle g_1 g_2|V_{exch}|n_1 g_2\rangle\langle n_1|\mathbf{L}_1\cdot\mathbf{S}_1|g_1\rangle}{E_{n_1}-E_{g_1}} \\ &+ \sum_{n_2}\frac{\langle g_2|\mathbf{L}_2\cdot\mathbf{S}_2|n_2\rangle\langle g_1 n_2|V_{exch}|g_1 g_2\rangle + \langle g_1 g_2|V_{exch}|g_1 n_2\rangle\langle n_2|\mathbf{L}_2\cdot\mathbf{S}_2|g_2\rangle}{E_{n_2}-E_{g_2}}\Bigg).\end{aligned} \tag{2.51}$$

As in the case with the perturbation calculation of the single ion anisotropy from the spin-orbit perturbation, the unperturbed electron state space is a product space of the orbital space and the spin space. Therefore, a spin Hamiltonian can be written from the second order energy shift by using only the orbital part of the wave function in the matrix elements, leaving the spins as operators. This results in the equalities

$$\langle n_1 g_2|V_{exch}|g_1 g_2\rangle = J(n_1 g_2, g_1 g_2)\mathbf{S}_1\cdot\mathbf{S}_2 \quad \text{and} \quad \langle n_1|\mathbf{L}_1\cdot\mathbf{S}_1|g_1\rangle = \langle n_1|\mathbf{L}_1|g_1\rangle\cdot\mathbf{S}_1, \tag{2.52}$$

where $J(n_1 g_2, g_1 g_2)$ is the exchange integral taken from equation 2.49. Using the additional fact the $\mathbf{L}$ is purely imaginary, the spin Hamiltonian of the so-called *Dzyaloshinsky-Moriya* (DM) interaction can thus be written as ([9])

$$\begin{aligned}\mathcal{H}_{DM} &= 2\lambda\sum_{\mu}\Bigg\{\sum_{n_1}\frac{J(n_1 g_2, g_1 g_2)\langle g_1|\mathbf{L}_{1\mu}|n_1\rangle[S_{1\mu},(\mathbf{S}_1\cdot\mathbf{S}_2)]}{E_{n_1}-E_{g_1}} \\ &+ \sum_{n_2}\frac{J(g_1 n_2, g_1 g_2)\langle g_2|\mathbf{L}_{2\mu}|n_2\rangle[S_{2\mu},(\mathbf{S}_1\cdot\mathbf{S}_2)]}{E_{n_2}-E_{g_2}}\Bigg\},\end{aligned} \tag{2.53}$$

where μ represents Cartesian coordinates and $[S_{i\mu},(\mathbf{S}_1\cdot\mathbf{S}_2)]$ $(i=1,2)$ is a commutator. The relation $[\mathbf{S}_1,(\mathbf{S}_1\cdot\mathbf{S}_2)] = -i\mathbf{S}_1\times\mathbf{S}_2$ reveals the nature of the DM interaction as equation 2.53 can be rewritten as

$$\mathcal{H}_{DM} = \mathbf{D}\cdot(\mathbf{S}_1\times\mathbf{S}_2), \quad \text{where} \tag{2.54}$$

$$\mathbf{D} = -2i\lambda\Bigg(\sum_{n_1}\frac{\langle g_1|\mathbf{L}_1|n_1\rangle}{E_{n_1}-E_{g_1}}J(n_1 g_2, g_1 g_2) - \sum_{n_2}\frac{\langle g_2|\mathbf{L}_2|n_2\rangle}{E_{n_2}-E_{g_2}}J(g_1 n_2, g_1 g_2)\Bigg). \tag{2.55}$$

Two important features of this interaction are that $\mathbf{D}$ is antisymmetric with respect to ion exchange, and that the DM interaction - when present - favors perpendicular spin pairs. Thus, when an exchange or super-exchange coupling - favoring either parallel or anti-parallel spins - co-exists with the DM interaction in a given compound there will be a competition between them. When dealing with (partially) quenched transition metal ions in low symmetry surroundings, the DM interaction is the weaker interaction which serves to slightly cant the spins away from the co-linear directions preferred by the exchange interaction. The strength of the DM interaction can be estimated to be $\frac{\Delta g}{g} \cdot b$ [11], where b is the electron transference matrix element mentioned previously which is proportional to the strength of the super-exchange interaction. The fact that the DM interaction is an antisymmetric two-ion interaction puts some restraints on which systems and magnetic ions can even exhibit a DM-interaction, as will be evident in section 2.2.3.

Anisotropic exchange

In principle higher order terms in the spin orbit coupling can be considered, in which more than one process induced by the $\mathbf{L} \cdot \mathbf{S}$ term is involved. However, the strength of these terms will decrease heavily upon increasing the order. Here, only the term which is second order in the spin orbit coupling (DM can be considered to be first order in the spin-orbit coupling) is considered called *anisotropic exchange*. The term is treated in [9, 11] and is on the following form:

$$\mathcal{H}_{AE} = \sum_{ij} \mathbf{S}_i \cdot \mathcal{T}_{ij}^{(2)} \cdot \mathbf{S}_j, \tag{2.56}$$

where $\mathcal{T}_{ij}^{(2)}$ is a tensor of rank 2, describing the coupling between the spins on ionic positions i and j. This coupling can be anisotropic and couple different spin components. The strength is very difficult to calculate especially in the many-electron case, but it can be estimated to be of the order $(\frac{\Delta g}{g})^2 b$, which is a fraction of the strength of the DM interaction in most cases.

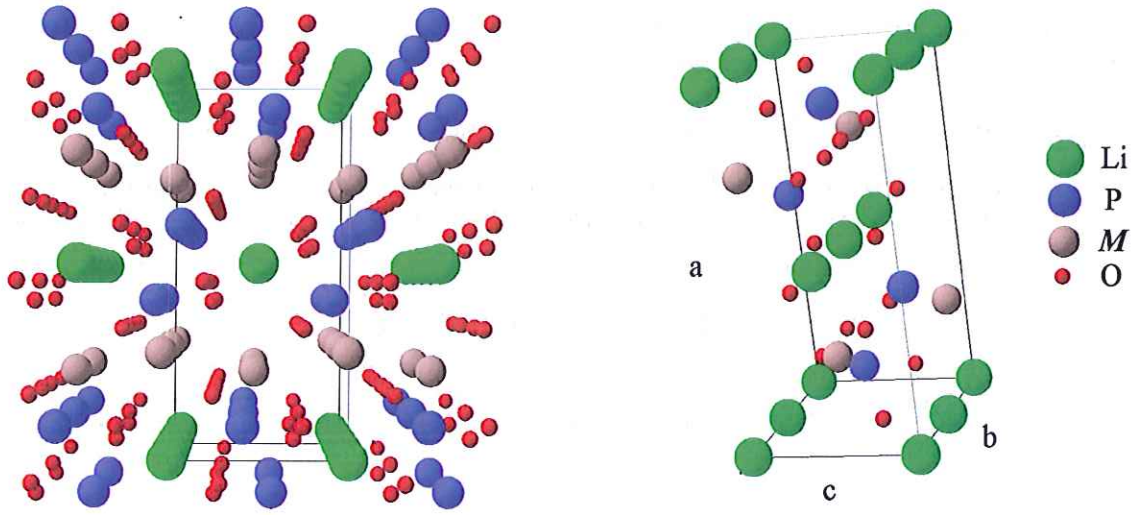

(a) LiMPO$_4$ viewed along the high symmetry b direction (b) The LiMPO$_4$ unit cell with four formula units

Figure 5: The structure of the lithium orthophosphates as determined from powder x-ray experiments ([12, 13, 14]).

2.2 Crystallography

Solid states of matter consist of a systematic arrangement of the huge number of constituent atoms in a repeating pattern in all three dimensions. These systems are described by their symmetries. A symmetry is defined as geometrical operation on a system that leaves the system unaltered or *invariant* while preserving the distances between all points of the body. The directions for which there are translational symmetry are all possible axes for a coordinate system useful to describe the system. Three linearly independent axes can be arbitrarily chosen among these directions, with the distances of translation as choice of unit lengths. This unit length is usually chosen as the minimal distance for translational symmetry along a given direction (in some cases a multiple of these distances if convenient). This essentially describes a box of atoms of which infinitely many identical boxes are closely packed in all three crystallographic directions to describe the system. This box with unit volume is known as the *unit cell.* The unit cell of the lithium-ortho-phosphates is shown in figure 5.

The shape of any unit cell has to be one which is able to voidlessly fill three dimensional space when stacked. Therefore only, certain symmetries are possible. For instance, a unit cell with 5-fold rotational symmetry is not allowed simply because the unit cells cannot be stacked to voidlessly fill three dimensional space (this is somewhat analogous to the problem of mapping the globe on a rectangular piece of paper - the two geometries are in different classes). For any given compound, the symmetry elements of the structure comprises a group. A group is a mathematical set with a defined operation between elements, which satisfies the following criteria:

- **Identity:** The group G must contain an identity element e such as $\forall g \in G : e \cdot g = g$.
- **Associativity:** $\forall g_1, g_2, g_3 \in G : (g_1 \cdot g_2) \cdot g_3 = g_1 \cdot (g_2 \cdot g_3)$.
- **Inverse:** All elements in the group must possess an inverse element within that group: $\forall g \in G \; \exists \; g^{-1} \in G : g^{-1}g = e$
- **Closure:** The result of any two elements operating on each other must remain within the group: $\forall g_1, g_2 \in G : g_1 \cdot g_2 \in G$

The operation defined in the group is not necessarily commutative; if it is, the group is said to be *Abelian.* Upon further analysis of the possible structures which are able to fill space, there are 230 unique *space groups* in total, each containing a different set of symmetry elements. Obvious symmetry elements are any translation of integer lattice units - $\mathrm{T} = n\mathrm{a} + m\mathrm{a} + l\mathrm{c}$, the number of which are infinite for an infinitely large crystal. These are the trivial symmetry elements, and they are not included in the space groups - although they are still there of course. More significant are the crystallographic *point groups*, which are the groups of symmetries which take at least one lattice point onto itself. These are the *inversions* - $(x, y, z) \rightarrow (-x, -y, -z)$ - the *mirror planes* - $(x, y, z) \rightarrow (x, -y, z)$ - or the *rotations* - $(x, y, z) \rightarrow (x, -y, -z)$. In many cases the symmetries are point group symmetries combined with a small translation of a given fraction of a unit cell. For instance, a so-called *2-fold screw axis* is a 180° rotation around an axis followed by a translation. One can use the International Tables for Crystallography[1] to find the symmetry elements of a given group. Excluding the lattice translations the set of symmetry elements of the

[1] http://it.iucr.org/

lithium orthophosphates - G - are as given below:

$$
\begin{aligned}
1 &: \text{Identity} \\
&(x,y,z) \rightarrow (x,y,z) && (2.57)\\
2'_x &: \text{2-fold screw axis at } (x,0.25,0.25) \\
&(x,y,z) \rightarrow (x+0.5,0.5-y,0.5-z) && (2.58)\\
2'_y &: \text{2-fold screw axis at } (0,y,0) \\
&(x,y,z) \rightarrow (-x,0.5+y,-z) && (2.59)\\
2'_z &: \text{2-fold screw axis at } (0.25,0,z) \\
&(x,y,z) \rightarrow (0.5-x,-y,0.5+z) && (2.60)\\
I &: \text{Inversion in } (0,0,0) \\
&(x,y,z) \rightarrow (-x,-y,-z) && (2.61)\\
m_{xz} &: \text{Mirror plane at } y=0.25 \\
&(x,y,z) \rightarrow (x,0.5-y,z) && (2.62)\\
m'_{xy} &: \text{Glide plane at } z=0.25 \text{ with glide vector } (0.5,0,0) \\
&(x,y,z) \rightarrow (x+0.5,y,0.5-z) && (2.63)\\
m'_{yz} &: \text{Glide plane at } x=0.25 \text{ with glide vector } (0,0.5,0.5) \\
&(x,y,z) \rightarrow (0.5-x,y+0.5,z+0.5) && (2.64)
\end{aligned}
$$

The symmetry group of the lithium orthophosphates is thus $G \otimes G_{\mathbf{T}}$, where $G_{\mathbf{T}}$ is the group of integer lattice translations - $G_{\mathbf{T}} = \{T_{\mathbf{T}} | \mathbf{T} = n\mathbf{a} + m\mathbf{b} + l\mathbf{c}\}$. The primes in equations 2.59-2.64 denote that the symmetry element is a combination of a point group symmetry element and a finite translation, and therefore does *not* leave any point fixed. The point group from which the symmetries above is generated is called $D_{2h} = \{1, 2_x, 2_y, 2_z, I, m_{xy}, m_{yz}, m_{xz}\}$. The unprimed elements are thus 2-fold rotation axes and mirror planes, respectively. The crystallographic point group can also be said to contain the *macroscopic symmetry elements*, which are the operations that can be seen from a macroscopic point of view. A translation of a few lattice units is microscopic operations not noticeable on a macroscopic scale. It is thus the point group that determines the possible macroscopic physical properties, such as birefringence, pyroelectricity or magnetoelectricity. For instance, zero field electric polarization is forbidden in the lithium orthophosphates because of the mirror planes and especially the inversion symmetry in D_{2h}. That some of the mirror planes has to be followed by a microscopic translation in order to actually be a symmetry does not change this physical situation. Furthermore, in order to have magnetoelectricity, these symmetries must be broken upon applying a field.

2.2.1 Irreducible representations of the symmetry group

The symmetry of the crystal system has a profound significance when describing and determining the magnetic structure. As neutron scattering experiments are always interpreted in the framework of reciprocal space, the mathematical description of the magnetic structure is best done in terms of the Fourier transform of the spin operators. In all the lithium ortho-phosphates there are four magnetic ions in the unit cell situated on the $4c$ position in the $Pnma$ space group:

$$
\begin{aligned}
\mathbf{r}_1 &= (0.25+\varepsilon, 0.25, 1-\delta) \\
\mathbf{r}_2 &= (0.75+\varepsilon, 0.25, 0.5+\delta) \\
\mathbf{r}_3 &= (0.75-\varepsilon, 0.75, \delta) \\
\mathbf{r}_4 &= (0.25-\varepsilon, 0.75, 0.5-\delta), && (2.65)
\end{aligned}
$$

where δ and ε are displacements specific to the magnetic ion in question. The relevant spin operators are the ones describing each Cartesian component j of the spin of each magnetic ion i in the n'th unit cell $S_{ij}(\mathbf{R}_n) = S_j(\mathbf{R}_n + \mathbf{r}_i)$ for $i = 1,2,3,4$ and $j = x,y,z$. $\mathbf{R}_n$ is the position vector of the n'th unit cell. The Fourier transforms of the spin operators are

$$S_{ij}(\mathrm{k}) = \frac{1}{N}\sum_{n=1}^{N} S_{ij}(\mathbf{R}_n)e^{i\mathrm{k}\cdot\mathbf{R}_n}, \quad i = 1,2,3,4 \text{ and } j = x,y,z. \tag{2.66}$$

If the magnetic unit cell is the same as the crystallographic unit cell, there are only 12 degrees of freedom in the magnetic system completely determining the magnetic structure. This is the so-called *commensurate* or *uniform* case, where Fourier transformed spin components are only non-zero in case of $\mathrm{k} = (0,0,0)$. Then the Fourier transformed spin operator is just the average Cartesian spin component on the given site. If there is a modulation of said spin component along a particular direction k_{ic}, a phase factor $e^{i\mathrm{k}\cdot\mathbf{R}_n}$ is merely multiplied onto the spin component. So in case of a single k structure, the 12 Fourier transformed spin components are only non-zero when $\mathrm{k} = \mathrm{k}_{ic}$. In both cases the structure can be completely and uniquely described by the 12 Fourier transformed spin components and hence the spin space is spanned by these basis vectors *in both cases.*

The basic objective achieved by using the co-called *representation group theory* is to find a convenient set of basis vectors for the vector space spanned by the twelve Fourier transformed spin operators. This basically means 12 different spin structures or spin symmetries that transform in a simple manner when applying the symmetry operations in G, and where as many basis vectors as possible transform identically under *all* the symmetry operations in the symmetry group. This is advantageous in two different ways:

- The spin Hamiltonian has to be invariant under the symmetry operations of $G \otimes G_{\mathbf{T}}$. This is simply a consequence of the indistinguishableness of the two physical situations before and after the application of the symmetry operation (which holds by definition). As will be elaborated later, any Hamiltonian quadratic in spins (as all the Hamiltonians treated in 2.1), will have terms consisting of products between basis vectors transforming identically.
- The irreducible basis vectors facilitates a much easier interpretation of neutron data. Using these basis vectors, chances are that different points in reciprocal space reflect a single spin symmetry or basis vector, rather than a mix of basis vectors. This enables one to say a lot about the magnetic structure from just a few peaks, both those that show magnetic scattering and those that do not. This will be a fundamental tool for analyzing the neutron scattering data presented in this work.

The set of all the linear operations in the space spanned by the 12 Fourier transformed spin operators can be expressed by 12×12 matrices, and can be shown to form a group which could be called $L(S)$. By expressing a certain relation between $L(S)$ and G in a clever way, the group $L(S)$ can be said to *represent* G. Such a relation is called a *homomorphy*:

> *A single valued mapping* $\Gamma : G \to G'$ *between two groups* G *and* G' *is said to be a* **homomorphy** *if* $\forall g_1, g_2 \in G: \ \Gamma(g_1 g_2) = \Gamma(g_1)\Gamma(g_2)$. (2.67)

Thus, a homomorphy can be said to produce an image of the group G in G'. The definition of a representation as used in analyzing magnetic structures is as follows:

> *Given the vector space* S *and the group* G*, the group of linear operations on* S *-* $L(S)$*- is a* **representation** *of the group* G *with the* **representation space** S *if there exists a homomorphy* $\Gamma : G \to L(S)$. (2.68)

When dealing with crystallographic problems, the vector space $L(S)$ can always represent the symmetry group G. The usefulness of the representation lies in *reducing the representation.* Since there are 12 magnetic degrees of freedom in the lithium orthophosphates, a representation $\Gamma(g)$ of any element g from the symmetry group G must be a 12×12 matrix. Reducing the representation is done by changing the basis of the representation space S ($|1\rangle - |12\rangle \rightarrow |1'\rangle - |12'\rangle$), so the representations $\Gamma(g)$ has the same block matrix form for all group elements $g \in G$, for instance:

$$\Gamma(g) = \begin{bmatrix} x_{1,1} & \dots & x_{1,12} \\ \vdots & \ddots & \vdots \\ x_{12,1} & \dots & x_{12,12} \end{bmatrix} \rightarrow \left[\begin{array}{cc|ccc|cc|c|c} a_{11} & a_{12} & 0 & 0 & 0 & 0 & 0 & \dots & 0 \\ a_{21} & a_{22} & 0 & 0 & 0 & 0 & 0 & \dots & 0 \\ \hline 0 & 0 & b_{11} & b_{12} & b_{13} & 0 & 0 & \dots & 0 \\ 0 & 0 & b_{21} & b_{22} & b_{23} & 0 & 0 & \dots & 0 \\ 0 & 0 & b_{31} & b_{32} & b_{33} & 0 & 0 & \dots & 0 \\ \hline 0 & 0 & 0 & 0 & 0 & c_{11} & c_{12} & \dots & 0 \\ 0 & 0 & 0 & 0 & 0 & c_{21} & c_{12} & \dots & 0 \\ \hline \vdots & \vdots & \vdots & \vdots & \vdots & \vdots & \vdots & \ddots & 0 \\ 0 & 0 & 0 & 0 & 0 & 0 & 0 & \dots & f_{11} \end{array}\right]. \quad (2.69)$$

This reduction means that the representation space S has been divided into subspaces $S_1, S_2, ..., S_j$ spanned by these new basis vectors. In the rather arbitrary example above, the first subspace is spanned by $|1'\rangle - |2'\rangle$, the second subspace by $|3'\rangle - |5'\rangle$ and so forth. Hence, any symmetry element is represented in each subspace of the representation space, for instance:

$$\Gamma_1(g) = \begin{bmatrix} a_{11} & a_{12} \\ a_{21} & a_{22} \end{bmatrix} \in L(S_1), \quad \text{or} \quad \Gamma_2(g) = \begin{bmatrix} b_{11} & b_{12} & b_{13} \\ b_{21} & b_{22} & b_{23} \\ b_{31} & b_{32} & b_{33} \end{bmatrix} \in L(S_2). \quad (2.70)$$

If the reduced representation can not be reduced further - if the subspaces of the representation space can not be reduced further - the representation is said to be *irreducible.* Obtaining the irreducible representations is equivalent to obtaining the simplest way of representing the symmetry group of the system in question, in the group of linear operations on the vector space spanned by the magnetic degrees of freedom. This is done by finding the smallest subspaces of the representation space that represent the symmetry group by virtue of the groups of linear operations on said subspaces. This tedious point is illustrated in figure 6.

There are two useful points to be made about the irreducible representations, which are not shown here (shown in [15]):

- Any vector within the representation subspace of a given irreducible representation, is transformed into the same subspace when acted upon by any of the symmetry elements in G
- If the symmetry group G is Abelian, then the number of irreducible representations equals the number of symmetry elements in G

The irreducible representations has been calculated manually in an instructive way for the lithium orthophosphates in [15] in case of $\mathbf{k} = (0,0,0)$ and $\mathbf{k}_{ic} = (0, k_{ic}, 0)$. They can also be calculated using the program BasIReps - available on the Internet within the FullProf suite. One needs the space group of the material, the number and positions of the magnetic ions and the propagation vector. The two cases - the commensurable and incommensurable - are treated below.

The commensurate case - $\mathbf{k} = (0,0,0)$

Since G is Abelian and has eight group elements, there are eight irreducible representations in the commensurate case. The basis functions spanning the representation subspaces of these irreducible

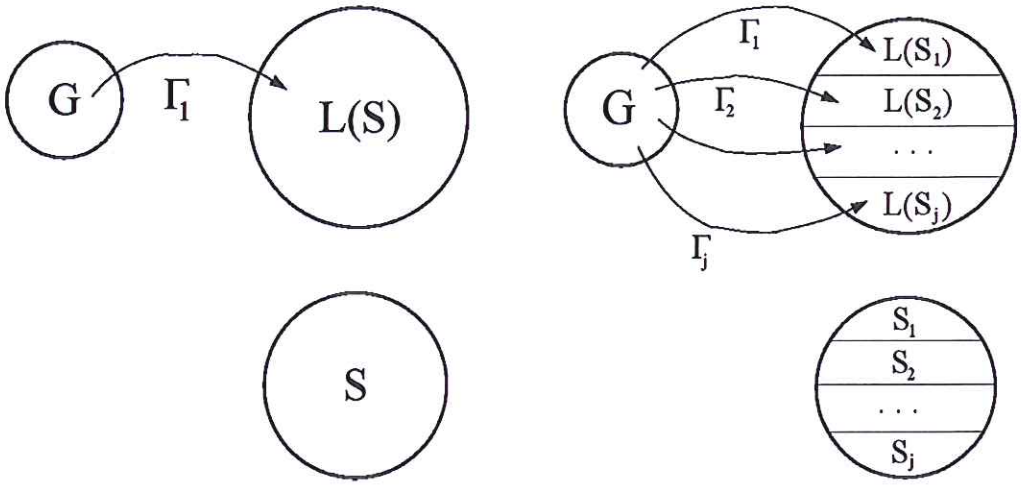

(a) The symmetry group G represented by the group of linear operations on S, $L(S)$

(b) The symmetry group G represented by several subspaces of $L(S)$ generated by several subspaces of the representation space S

Figure 6: An illustration of the concept of irreducible representations.

representations are all on the following form:

$$\begin{aligned} A_j &= S_{1j}(0) - S_{2j}(0) - S_{3j}(0) + S_{4j}(0), \\ C_j &= S_{1j}(0) + S_{2j}(0) - S_{3j}(0) - S_{4j}(0), \\ G_j &= S_{1j}(0) - S_{2j}(0) + S_{3j}(0) - S_{4j}(0) \quad \text{and} \\ F_j &= S_{1j}(0) + S_{2j}(0) + S_{3j}(0) + S_{4j}(0), \\ &\text{where} \quad j = x, y, z. \end{aligned} \tag{2.71}$$

It is worth noticing that the basis vectors are *collective* spin structures for the whole system with one polarization; having 4 magnetic ions in the unit cell, there are three possible antiferromagnetic structures and one ferromagnetic structure for any given polarization. The irreducible vectors are exactly these. The magnetic structure of the lithium ortho-phosphates has been roughly determined in [1, 16] to be a C-type structure with polarization along a for $LiMnPO_4$, along b for $LiCoPO_4$ and along c for $LiNiPO_4$. If one shifts the crystallographic unit cell by $(-0.25, -0.25, 0)$ and removes all but the magnetic transition metal ion, the magnetic ions sits only slightly displaced from a face-centered orthorhombic structure. Using this cell it is easy to depict the irreducible basis structures - see figure 7.

As evident, the established C-type structure is an antiferromagnetic structure consisting of ferromagnetic planes in the ac-plane alternating in polarization along the b direction. The eight irreducible representations, and how the basis vectors transform under the symmetry operations in G are given in table 3 (reproduced from [15]).

In table 3 it is worth noticing that the irreducible representations with basis vectors along y have only one basis vector. This is due to the fact that there is a high symmetry mirror plane perpendicular to the b-axis. It is also evident that A and C or F and G type structures are in the same representation subspaces, while A and G or F and C are not.

The incommensurate case - $\mathbf{k}_{ic} = (0, k_{ic}, 0)$

In case of the magnetic structure being an incommensurate modulated one along b - with ordering wave vector $\mathbf{k}_{ic} = (0, k_{ic}, 0)$ - the symmetry group forming the basis for the irreducible representa-

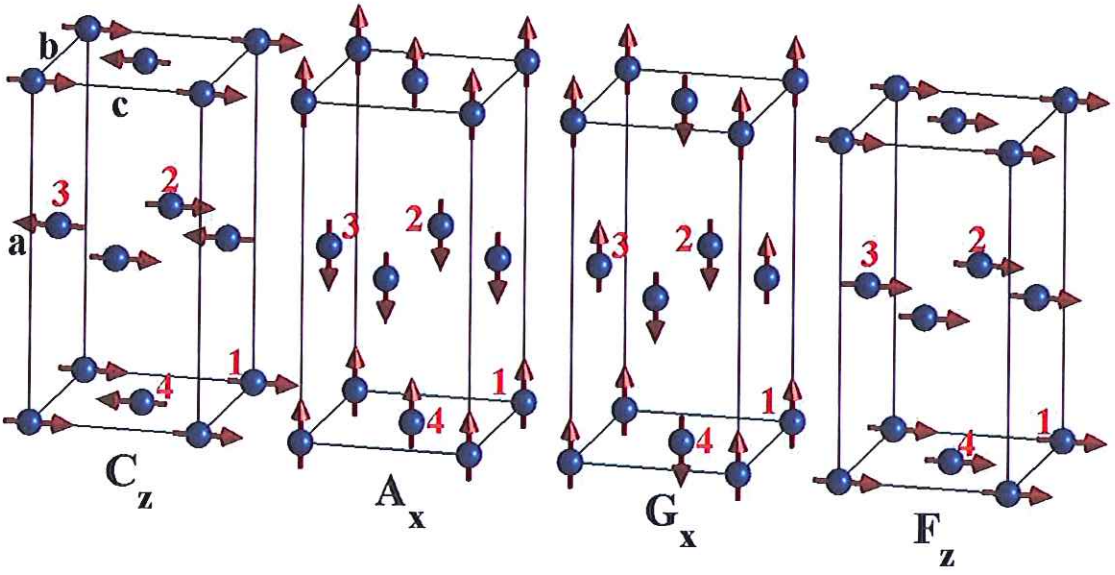

Figure 7: Four of the twelve commensurate irreducible basis structures related to the three AFM symmetry classes (A, G and C) and the ferromagnetic class (F). Only one of the three possible polarizations (x, y, z) is shown for each one of the four different classes.

	1	$2'_x$	$2'_y$	$2'_z$	I	m'_{xy}	m_{xz}	m'_{yz}	Basis vectors
Γ_1	1	1	1	1	1	1	1	1	G_y
Γ_2	1	1	-1	-1	1	-1	-1	1	F_x, G_z
Γ_3	1	-1	1	-1	1	-1	1	-1	F_y
Γ_4	1	-1	-1	1	1	1	-1	-1	G_x, F_z
Γ_5	1	1	1	1	-1	-1	-1	-1	C_x, A_z
Γ_6	1	1	-1	-1	-1	1	1	-1	A_y
Γ_7	1	-1	1	-1	-1	1	-1	1	A_x, C_z
Γ_8	1	-1	-1	1	-1	-1	1	1	C_y

Table 3: The eight irreducible representations of the symmetry group excluding translations in the lithium orthophosphates and how they transform under the symmetry operations of G. The basis vectors for the representation space of each irreducible representation is given as well.

tions is greatly reduced, as only the symmetries leaving k_{ic} invariant are considered. This is due to the fact that the relevant spin operators are the 12 operators $S_{ij}(\mathrm{k}_{ic})$ where $i = 1, 2, 3, 4$ and $j = x, y, z$. Wanting to stay within this representation vector space $S_{\mathrm{k}_{ic}}$, symmetry operations altering k_{ic} are discarded. As the modulation is along b, the symmetry elements reversing the sign of y also reverse the sign of k_{ic} and should not be considered. Thus, the group of symmetry elements leaving k_{ic} invariant is

$$G_{\mathrm{k}_{ic}} = \left\{1, 2'_y, m'_{xy} m'_{yz}\right\}, \tag{2.72}$$

which is known as the *little group of* k_{ic}. In the incommensurate case, the basis vectors have been calculated in [15] to be

$$\begin{aligned} A_j &= S_{1j}(\mathrm{k}_{ic}) - S_{2j}(\mathrm{k}_{ic}) - \beta S_{3j}(\mathrm{k}_{ic}) + \beta S_{4j}(\mathrm{k}_{ic}), \\ C_j &= S_{1j}(\mathrm{k}_{ic}) + S_{2j}(\mathrm{k}_{ic}) - \beta S_{3j}(\mathrm{k}_{ic}) - \beta S_{4j}(\mathrm{k}_{ic}), \\ G_j &= S_{1j}(\mathrm{k}_{ic}) - S_{2j}(\mathrm{k}_{ic}) + \beta S_{3j}(\mathrm{k}_{ic}) - \beta S_{4j}(\mathrm{k}_{ic}) \quad \text{and} \\ F_j &= S_{1j}(\mathrm{k}_{ic}) + S_{2j}(\mathrm{k}_{ic}) + \beta S_{3j}(\mathrm{k}_{ic}) + \beta S_{4j}(\mathrm{k}_{ic}), \\ &\text{where} \quad j = x, y, z \quad \text{and} \quad \beta = e^{i\pi k_{ic}} \end{aligned} \tag{2.73}$$

The little group $G_{\mathrm{k}_{ic}}$ is Abelian, and therefore there are only 4 irreducible representations since there are only four elements in the little group. These representations and their transformation properties are listed in table 4.

	1	$2'_y$	m'_{xy}	m'_{yz}	Basis vectors
Γ_1	1	β	1	β	A_x, G_y, C_z
Γ_2	1	$-\beta$	1	$-\beta$	F_z, G_x, A_y
Γ_3	1	β	-1	$-\beta$	F_y, C_x, A_z
Γ_4	1	$-\beta$	-1	β	F_x, C_y, G_z

Table 4: The four irreducible representations of the little group $G_{\mathrm{k}_{ic}}$ in the lithium orthophosphates and how they transform under the symmetry operations of $G_{\mathrm{k}_{ic}}$. The basis vectors for the representation space of each irreducible representation is given.

Even though the ordering wave vector differs (and hence the basis vectors), comparing table 3 and 4 reveals that removing symmetries from the group to be represented results in fewer irreducible representations containing a larger number of basis vectors. This has physical consequences, as becomes evident in the next section.

2.2.2 Irreducible basis vectors and the quadratic spin Hamiltonian

The space of all single ion spin operators is spanned by the irreducible basis vectors, both in the commensurate and the incommensurate case. It is therefore possible to write any quadratic spin Hamiltonian - notice that all the Hamiltonians mentioned in 2.1 are quadratic in spin - as a sum of products of irreducible basis vectors

$$\mathcal{H}_s = \sum_{ij} \kappa_{ij} \gamma_i^\dagger \gamma_j \tag{2.74}$$

$$\text{where } \gamma_i \in \Gamma_i,\ \gamma_j \in \Gamma_j \tag{2.75}$$

and where κ_{ij} is some coupling constant. Is is easily seen from tables 3 and 4 that if $\Gamma_i \neq \Gamma_j$, then it is possible to find a symmetry element under which the two basis vectors in the term in question transform differently. That would change the sign of that particular term in the Hamiltonian, and hence the Hamiltonian would not be invariant under the symmetries of the system which it is required to be by definition. Therefore, any term consists of products between basis vectors *from the same irreducible representation.* Thus, the representations given in tables 3 and 4 have direct physical meaning. They are classes of magnetic structures likely to appear together, as their basis vectors can be combined to form quadratic spin Hamiltonians that are invariant under the symmetry operations of the crystallographic system.

2.2.3 Symmetry and the Dzyaloshinsky-Moriya interaction

When analyzing the possibility of a Dzyaloshinsky-Moriya (DM) term in the spin Hamiltonian it is imperative to know what happens to the magnetic ions and their spin components when subjected to the symmetry operations of the space group. In most cases the magnetic ion in question is moved to another position in another unit cell - for instance $2'_x \mathrm{r}_1 2'^{\dagger}_x \rightarrow \mathrm{r}_2 + 00\overline{1}$. These transformations and the transformation of spin coordinates have been calculated in [15] and are given in table 5. The unit cell translation is omitted.

G	1	$2'_x$	$2'_y$	$2'_z$	I	m'_{xy}	m_{xz}	m'_{yz}
r_1	r_1	r_2	r_3	r_4	r_3	r_2	r_1	r_4
r_2	r_2	r_1	r_4	r_3	r_4	r_1	r_2	r_3
r_3	r_3	r_4	r_1	r_2	r_1	r_4	r_3	r_2
r_4	r_4	r_3	r_2	r_1	r_2	r_3	r_4	r_1
S_x	S_x	S_x	$-S_x$	$-S_x$	S_x	$-S_x$	$-S_x$	S_x
S_y	S_y	$-S_y$	S_y	$-S_y$	S_y	$-S_y$	S_y	$-S_y$
S_z	S_z	$-S_z$	$-S_z$	S_z	S_z	S_z	$-S_z$	$-S_z$

Table 5: Transformation properties of the magnetic ions in the lithium orthophosphates and their spin under the symmetry operations of the *Pnma* space group.

The microscopic origin of the DM interaction as treated in 2.1.6 was first thought of by Toru Moriya in [11]. In that paper he estimated the order of several higher order (in the spin-orbit coupling) interactions, and treated the crystallographic aspects of the DM interaction. Since the DM interaction is anti-symmetric, a crystallographic space group of high symmetry will not leave much room for DM interactions. Magnetic ions with considerable orbital contribution situated in crystallographic environments with low symmetry, however, leave plenty of room for DM interactions - the lower the crystal symmetry the better. Moriya derived the following rather simple rules governing the nature of the DM coupling pseudo-vector $\mathbf{D}_{AB}$ between ions at A and B:

- If there is an inversion center in the point C bisecting the line AB, the $\mathbf{D}_{AB} = 0$.
- If a mirror plane perpendicular to AB passes through C, then $\mathbf{D} \perp AB$.
- When there is a mirror plane including A and B, then $\mathbf{D} \perp$ mirror plane.
- When a two-fold rotation axis perpendicular to AB passes through C, then $\mathbf{D} \perp$ two-fold axis.

In addition to these rules, Thomas B. S. Jensen derived a much more quantitative criterion in the case of the lithium orthophosphates in his thesis [15]. If one performs any of the symmetry operations $R \in G$ in $\mathrm{Li}M\mathrm{PO}_4$ on a DM term $\mathbf{D}_{AB}$, the following identity holds:

$$R\left[\mathbf{D}_{AB} \cdot (\mathbf{S}_A \times \mathbf{S}_B)\right] R^{\dagger} = R\mathbf{D}_{AB}R^{\dagger} \cdot (\mathbf{S}_{RAR^{\dagger}} \times \mathbf{S}_{RBR^{\dagger}}) \,. \tag{2.76}$$

Thus, at least in the lithium orthophosphates, performing a symmetry operation on a DM term is equivalent to transforming the constant $\mathbf{D}_{AM}$ pseudo-vector, and transforming only the ionic positions *while keeping the spin components unaltered.* Crudely speaking, the pseudo-vector transformation applied to the spin pseudo-vectors can be transferred to the DM coupling pseudo-vector (which is not an operator). Generally the overall Hamiltonian needs to be invariant under the symmetry operations; so a Hamiltonian containing a DM term - $\mathcal{H}_{DM}$ must also contain $R\mathcal{H}_{DM}R^{\dagger}$. This is possible if and only if the transformed DM-term between the untransformed positions A

and B is identical to the untransformed DM-term between the transformed ionic positions $RAR^\dagger$ and $RBR^\dagger$:

$$R\left[\mathbf{D}_{AB}\cdot(\mathbf{S}_A\times\mathbf{S}_B)\right]R^\dagger=\mathbf{D}_{RAR^\dagger RBR^\dagger}\cdot(\mathbf{S}_{RAR^\dagger}\times\mathbf{S}_{RBR^\dagger})\,. \tag{2.77}$$

Collecting equations 2.76 and 2.77 results in a straightforward condition for a non-zero DM coupling:

$$R\mathbf{D}_{AB}R^\dagger=\mathbf{D}_{RAR^\dagger RBR^\dagger} \tag{2.78}$$

Using these rules, it is possible to get a binary answer to whether or not there can be a DM coupling between two magnetic ions - and if there are - which spin components are coupled. For instance - the magnetic ions situated at $\mathbf{r}_1=(0.25+\varepsilon,0.25,1-\delta)$ and $\mathbf{r}_2=(0.75+\varepsilon,0.25,0.5+\delta)$ both lie in the $y=0.25$ plane - which is a mirror plane in the lithium orthophosphates. Thus, if these ions are coupled, then the DM pseudo vector points along y and a DM term can have the form $(0,D_{12}^y,0)\cdot[\mathbf{S}_1\times\mathbf{S}_2]$. Therefore it is seen that *if* a DM term between these two ions exists, then *only* the a and c directions can be coupled. In $LiNiPO_4$ the main AFM spin symmetry is polarized along the c direction, and is precisely such a DM that causes the spin canting observed in [4, 15]. The strength of the coupling is very difficult to calculate, and these rules only give information about the possible existence of DM terms.

3 Neutron Scattering

Neutron scattering is a direct, global and non-destructive probe used to study a wide range of phenomena in solid state physics. Its unique strengths compared to other experimental techniques justify billion euro facility construction costs several places around the world, and it is by far the most important tool used to study magnetic order and dynamics. Neutron scattering is a highly specialized technique, requiring both knowledge and practical experience in order to make use of its full potential. In this chapter, the foundational concepts of neutron scattering and instrumentation will be described. Results from basic non-relativistic quantum mechanics will be used without reference in this chapter, they can be found in textbooks such as [6].

3.1 Properties of the neutron

In this section the basic properties of the neutron will be described as well as the scattering of neutrons by means of the strong and electromagnetic forces.

3.1.1 Basic properties

The neutron is the neutral subatomic particle responsible for holding together the nucleus by virtue of the strong nuclear force, against the repulsive coulomb interactions between the positively charged protons. The neutron is only stable in its nuclear bound state; as a free particle it decays to a proton, an electron and an anti-neutrino with a half life of roughly 15 minutes (the mass of the neutron is comparable to, but slightly larger than that of the proton, namely 939.57 MeV/c^2). In itself the neutron is a composite particle, it consists of one up-quark and two down-quarks, which gives the neutron a fermionic ground state. Thus, ignoring gravitational effects, the neutron interacts with its surroundings due to two fundamental forces:

- **The strong nuclear force:** The neutron interacts strongly with every nuclei, but the magnitude of the cross section and sign of the phase shift varies from element to element, and even from isotope to isotope.
- **The electromagnetic force:** The spin of the neutron gives it a dipolar magnetic moment, which interacts mainly with the unpaired electrons of the surrounding atoms due to the magnetic dipole-dipole interaction. There is no coulomb interaction, which makes the neutron an ideal probe of atomic magnetism as it ignores the charge of the electrons.

Because of the large neutron mass, a Maxwell-Bolzmann distribution of neutrons at 300 Kelvin will mainly consist of neutrons with a de-Broglie wavelength of around 1 Å and a kinetic energy of around 100 meV. These are the order of magnitudes of the inter atomic distances and vibrational excitation energies in solid state compounds respectively, making the neutron such a unique tool. The magnetic moment μ_n of the neutron is given by the neutron magnetogyric ratio (γ) and the nuclear magneton:

$$\mu_n = \gamma\mu_N = -1.913\frac{e\hbar}{m_p}, \tag{3.1}$$

where e is the elementary charge and m_p is the proton mass. Because it is a neutral particle, the neutron interacts weakly with its surroundings compared to x-rays and electrons for instance. Therefore, thermal neutron radiation penetrates several centimeters into all materials except a few containing special isotopes, which allows for a direct measurement of collective properties of a bulk sample, but at the expense of the demand for large samples. In the next two sections the relevant interactions of the neutron with its surroundings will be described.

Note on cross sections

When describing neutron interactions, a formalism suitable for scattering experiments is used. One takes the neutron to be incident on the scattering particle and thus, one would like to describe the initial and final states of the neutron in terms of the scattering potential. In a neutron experiment, one irradiates a sample with beam of neutrons with a well defined momentum vector and incoming flux and measures the scattered neutrons in some angle using a detector covering a finite spatial angle. When relating the measured neutron intensities to theory, one is interested in the probability for a neutron to be scattered into the spatial angle covered by the detector. The probability for a neutron to be scattered in any direction is given by the neutron scattering cross section:

$$\sigma = \frac{1}{\Phi}\frac{dN}{dt}, \tag{3.2}$$

where Φ is the incoming neutron flux in units of $(\text{area} \cdot \text{time})^{-1}$, and $\frac{dN}{dt}$ is the number of scattered neutrons per unit of time. Thus suitably, the unit of cross sections is an area and is measured in units of *barns*, 1 barn $= 10^{-24}$ cm^2. When measuring a small spatial angle with a detector, the relevant quantity is the differential cross section $\frac{d\sigma}{d\Omega}$. When measuring dynamics using neutrons, one is interested in the energy loss of the neutron and thus a given channel only measures a narrow energy interval. In this case, one is interested in the partial differential cross section: $\frac{d^2\sigma}{d\Omega dE_f}$, where E_f is the final neutron energy. The relations between these quantities are simple:

$$\sigma = \frac{1}{\Phi}\frac{dN}{dt} = \int \frac{d\sigma}{d\Omega} d\Omega' = \int\int \frac{d^2\sigma}{d\Omega dE_f} d\Omega' dE_f'. \tag{3.3}$$

3.1.2 Nuclear interactions

In the following, all neutrons will be assumed to have a wavelength relevant for neutron scattering, which is between 1-20 Å. To be able to derive the scattering cross section, two basic assumptions need to be made:

- The neutron and the scattering nucleus - or system of nuclei - is described as being in a very large box of volume Y. This makes the energy levels of the neutron discrete and allows for a calculation of the density of states. This is a well known assumption called *box normalization*, and it works as long as the resulting equations are independent of the box volume.
- The nuclear potential can be described as spherically symmetric point scatterer, mathematically described by a Dirac delta function. This is justified by the large wavelength of the neutrons compared to the size of any nucleus. This assumption results in the nuclear form factor being independent of neutron momentum transfer, which is also what is observed.

There is only one neutron in the box, so the neutron density is $1/Y$. Ignoring the spin of the neutron, the neutron wave function is a solution to the free particle Schrödinger equation ($\hat{H} = \frac{\hat{p}^2}{2m}$) and can be described as a plane wave with a wave vector $\mathbf{k}$:

$$\Psi_{\mathbf{k}}(\mathbf{r}) = \frac{1}{\sqrt{Y}} \exp(i\mathbf{k} \cdot \mathbf{r}), \tag{3.4}$$

where $\frac{1}{\sqrt{V}}$ is the normalization factor, $\mathbf{k}$ is the wave vector of the neutron and $\mathbf{r}$ is a position vector. When calculating the transition rate from the initial neutron state to the continuum of final states, denoted $W_{i\to f}$, Fermi's Golden Rule is used:

$$W_{i\to f} = \frac{2\pi}{\hbar}\rho_{\mathbf{k_f}}(E_f)|\langle\Psi_f|\hat{V}|\Psi_i\rangle|^2, \tag{3.5}$$

where $\rho_n(E)$ is the density of states, Ψ_i and Ψ_f are the initial and final states of both the neutron and the scattering system, E_f is the final energy comparable to the initial energy and $\hat{V}$ is the scattering potential. When we evaluate the density of states, a restriction to an infinitesimal solid angle $d\Omega$ is convenient. For a free particle in a box, we have the well known energy-wave vector relation:

$$E = \frac{\hbar^2 k^2}{2m_n} \Rightarrow \frac{dE}{dk} = \frac{\hbar^2 k}{m_n}, \tag{3.6}$$

where m_n is the neutron mass and k is the length of the wave vector. In case of a free particle in a box, the de Broglie wavelength of the particle needs to be periodic in the box. Otherwise the wave function would be nonzero at the box edges, and the wave function would be discontinuous. This requirement of periodicity results in a discrete set of allowed wave vectors; a lattice in k-space. The unit cell (smallest box with corners on lattice points) volume of this lattice is:

$$v_k = \frac{(2\pi)^3}{Y} \tag{3.7}$$

Consider a volume in k-space, consisting of the interval of wave vectors with energies in the interval $[E : E + dE]$ and pointing in the direction of the solid angle $d\Omega$. The number of states in this infinitesimal volume (given in states pr. unit volume) is exactly the density of states, which is by definition $\rho_{\mathbf{k_f}}(E)dE$:

$$\rho_{\mathbf{k_f}}(E)dE = \frac{1}{v_k} k_f^2 dk d\Omega \tag{3.8}$$

Combining this with equation 3.7 and 3.6, gives an expression for the density of states as a function of the length of the wave vector:

$$\rho_{\mathbf{k_f}} = \frac{Y}{(2\pi)^3} k_f \frac{m_n}{\hbar^2} d\Omega \tag{3.9}$$

This is dependent of Y and has no physical meaning, but it provides a useful framework for calculating the desired transition rate induced by the nuclear potential. This is clear when evaluating the differential cross section. The incoming neutron flux is the product of the density of neutrons and the velocity:

$$\Phi = \frac{\hbar}{Y m_n} k_i \tag{3.10}$$

Using this relation, equation 3.4 and the definition of the cross section (equation 3.2), the differential cross section can be derived, assuming that the state of the nucleus is not changed by the scattering process; then the initial and final states to consider are just the states of the neutron:

$$\begin{aligned} d\sigma &= \frac{Y m_n}{\hbar k_i} d\Omega \frac{dN}{dt} \Rightarrow \\ \left(\frac{d\sigma}{d\Omega}\right)_{k_i \to k_f} &= \frac{k_f}{k_i} \left(\frac{m_n}{2\pi\hbar^2}\right)^2 |\langle e^{-i\mathbf{k}_f \cdot \mathbf{r}} | \hat{V} | e^{i\mathbf{k}_i \cdot \mathbf{r}} \rangle|^2, \end{aligned} \tag{3.11}$$

where $\frac{dN}{dt}$ is exactly the transition rate described by Fermis Golden Rule. The scattering potential is assumed to be symmetric and point like and is thus described by the Fermi pseudo potential, which is a real number (imaginary numbers represent absorption) multiplied by the 3-dimensional Dirac delta function. Assuming that the nucleus is placed at position vector $\mathbf{r_i}$, the potential has the following form:

$$\hat{V}_i(\mathbf{r}) = \frac{2\pi\hbar^2}{m_n} b_i \delta(\mathbf{r} - \mathbf{r_i}). \tag{3.12}$$

The form of the prefactor has been chosen for convenience. The evaluation of the matrix element is straightforward:

$$\begin{aligned} \langle e^{-i\mathbf{k}_f \cdot \mathbf{r}} | \hat{V} | e^{i\mathbf{k}_i \cdot \mathbf{r}} \rangle &= \frac{2\pi\hbar^2}{m_n} b_i \int \exp(-i\mathbf{k_f} \cdot \mathbf{r}) \delta(\mathbf{r} - \mathbf{r_i}) \exp(i\mathbf{k_i} \cdot \mathbf{r}) d^3\mathbf{r} \\ &= \frac{2\pi\hbar^2}{m_n} b_i \exp(i\boldsymbol{\tau} \cdot \mathbf{r}), \end{aligned} \tag{3.13}$$

where $\boldsymbol{\tau} = \mathbf{k}_i - \mathbf{k}_f$. This leads to a simple differential cross section for nuclear scattering. It is assumed that the nucleus scatters the neutron elastically, meaning that the lengths of the incoming and outgoing wave vector are the same. In this case the differential cross section for scattering by a single nucleus is:

$$\left(\frac{d\sigma}{d\Omega}\right) = b^2, \tag{3.14}$$

which is independent of the arbitrary chosen volume Y.

Incoherent nuclear scattering

In a system of nuclear scatterers, different isotopes of the same element can have different scattering lengths. This can be due to nuclear spin or the presence of different isotopes of the given element. The average value for b and b^2 are:

$$\overline{b} = \sum_i f_i b_i \quad \overline{b^2} = \sum_i f_i b_i^2 \tag{3.15}$$

Where f_i in the relative frequency of occurrence for the scattering length value b_i. These variations are assumed to be completely uncorrelated. Therefore, when calculating the scattering cross section for a system consisting of a large number of nuclei (done in [17]), a term appears which only depends on the temporal correlation between the position of a single nuclei leaving out interference effects. This term scales with the *incoherent* cross section:

$$\sigma_{inc} = 4\pi\left(\overline{b^2} - (\overline{b})^2\right) \tag{3.16}$$

This is the variance squared of the distribution of cross sections.

3.1.3 Magnetic interactions

As mentioned in section 3.1.1 both the neutron and the electron have a magnetic dipole moment, giving rise to a magnetic interaction between the two particles. If the electron has angular momentum there is a magnetic moment associated with this as well. A similar approach as in the nuclear case is adopted - describing the incoming and outgoing neutron plane waves as they scatter off a potential. The value of the intrinsic magnetic dipole moment of the electron is

$$\boldsymbol{\mu}_e = -2\mu_B \mathbf{S}_e, \quad \text{where} \quad \mu_B = \frac{e\hbar}{2m_e} \tag{3.17}$$

is the Bohr magneton, m_e is the electron mass, e is the electron charge and $\mathbf{S}$ is the spin operator. The vector potential and magnetic field from the magnetic dipole at a point $\mathbf{R}$ from the electron is

$$\mathbf{A}_S = \frac{\mu_0}{4\pi}\frac{\boldsymbol{\mu}_e \times \hat{\mathbf{R}}}{R^2} \quad \mathbf{B}_S = \frac{\mu_0}{4\pi}\nabla \times \frac{\boldsymbol{\mu}_e \times \hat{\mathbf{R}}}{R^2}, \tag{3.18}$$

where $\hat{\mathbf{R}}$ is a unit vector in the direction of $\mathbf{R}$. However, in addition to the intrinsic magnetic moment, electrons can cause magnetic fields by simply moving (a dipole moment in case of circular or elliptical motion). If the electron carries momentum $\mathbf{p}$ there is a current giving rise to a magnetic field. The infinitesimal current element $Id\mathbf{l}$ for the electron is:

$$Id\mathbf{l} = -\frac{e}{m_e}\mathbf{p} = -\frac{2\mu_B}{\hbar}\mathbf{p}, \tag{3.19}$$

where I is the current, dl is an infinitesimal path in space and $\mathbf{p}$ is the electron momentum. The magnetic field at a point $\mathbf{R}$ from the infinitesimal current element follows from the Biot-Savart law:

$$\mathbf{B}_L = \frac{\mu_0}{4\pi} I \frac{d\mathbf{l} \times \hat{\mathbf{R}}}{R^2} = \frac{\mu_0}{4\pi} \frac{2\mu_B}{\hbar} \frac{\mathbf{p} \times \hat{\mathbf{R}}}{R^2} \tag{3.20}$$

In principle, using the Biot-Savart law - which holds only for steady currents - on a point charge is problematic since a point charge does not constitute a steady current. Integrating over the electron path is also problematic in a quantum mechanical system. However, for non-relativistic electrons, the Biot-Savart law is accurate, and the orbital angular momentum $\mathbf{L} = \mathbf{p} \times \hat{\mathbf{R}}$ is well described in atomic systems. As evident from equation 3.20, $\mathbf{B}_L$ is the magnetic field resulting from the orbital momentum of the un-paired electrons of the magnetic atom in question. Thus the magnetic field from the localized electrons of atoms has two origins - spin and orbital momentum. The magnetic potential of a neutron in such a field is

$$V_m(\mathbf{R}) = -\mu_n \cdot (\mathbf{B}_S(\mathbf{R}) + \mathbf{B}_L(\mathbf{R})) = -\frac{\mu_0}{2\pi} \gamma \mu_N \mu_B \mathbf{S}_n \cdot \left(\nabla \times \left(\frac{\mathbf{S}_e \times \hat{\mathbf{R}}}{R^2} \right) + \frac{1}{\hbar} \frac{\mathbf{p} \times \hat{\mathbf{R}}}{R^2} \right), \tag{3.21}$$

where $\mathbf{S}_n$ is the spin of the neutron and $\mathbf{S}_e$ is the spin of the electron. The partial differential cross section is a natural combination of equation 3.11 and 3.21:

$$\left(\frac{d^2\sigma}{d\Omega dE_f} \right)_{\mathbf{k}\sigma\lambda \to \mathbf{k}'\sigma'\lambda'} = \frac{k_f}{k_i} \left(\frac{m_n}{2\pi\hbar^2} \right)^2 |\langle \mathbf{k}'\boldsymbol{\sigma}'\lambda' | V_m | \mathbf{k}\boldsymbol{\sigma}\lambda \rangle|^2 \delta(E_\lambda - E_{\lambda'} + \hbar\omega), \tag{3.22}$$

where $\boldsymbol{\sigma}$ is the spin of the neutron which is orthogonal to the spatial part of the wave function, and the delta function represents the physical constraint of energy conservation of the neutron scatterers system as a whole; energy absorbed in the scattering system comes from the neutron and vice versa. Using mathematical results proven in [17][2] and temporarily focusing only on the wave vector part of the wave function, $\langle \mathbf{k}' | V_S | \mathbf{k} \rangle$ is evaluated, where V_S is the spin potential of an electron situated at $\mathbf{r_i}$:

$$\begin{aligned} \langle \mathbf{k}' | V_S | \mathbf{k} \rangle &= \int e^{-i\mathbf{k}'\cdot\mathbf{r}} \left[\nabla \times \frac{\mathbf{S}_e \times \hat{\mathbf{R}}}{R^2} \right] e^{i\mathbf{k}\cdot\mathbf{r}} d\mathbf{r} \\ &= \frac{1}{2\pi^2} \int \int e^{i\boldsymbol{\tau}\cdot\mathbf{r}} \hat{\mathbf{q}} \times (\mathbf{S}_e \times \hat{\mathbf{q}}) e^{i\mathbf{q}\cdot\mathbf{R}} d\mathbf{q} d\mathbf{r} \\ &= 4\pi e^{i\boldsymbol{\tau}\cdot\mathbf{r}} \left[\hat{\boldsymbol{\tau}} \times (\mathbf{S}_e \times \hat{\boldsymbol{\tau}}) \right], \end{aligned} \tag{3.23}$$

where $\mathbf{r} = \mathbf{r_i} + \mathbf{R}$, and $\mathbf{R}$ is the distance between the neutron and the scattering electron (making integration over $\mathbf{R}$ or $\mathbf{r}$ equivalent), and $\boldsymbol{\tau} = \mathbf{k}_f - \mathbf{k}_i$ is the momentum transfer vector of the neutron. The same can be done with respect to the orbital potential V_L situated at $\mathbf{r_i}$, using another result from [17][3]:

$$\begin{aligned} \langle \mathbf{k}' | V_L | \mathbf{k} \rangle &= \int e^{i\boldsymbol{\tau}\cdot\mathbf{r}} \frac{\mathbf{p} \times \hat{\mathbf{R}}}{R^2} d\mathbf{r} \\ &= \frac{1}{\hbar} e^{i\boldsymbol{\tau}\cdot\mathbf{r_i}} \int e^{i\boldsymbol{\tau}\cdot\mathbf{R}} \frac{\mathbf{p} \times \hat{\mathbf{R}}}{R^2} d\mathbf{R} \\ &= \frac{4\pi i}{\hbar\tau} e^{i\boldsymbol{\tau}\cdot\mathbf{r_i}} (\mathbf{p} \times \hat{\boldsymbol{\tau}}) \end{aligned} \tag{3.24}$$

In case of more than one scatterer, one just adds the potential from each of the scatterers; hence for a general system of scatterers the following definition comes naturally from equations 3.24 and

[2] $\nabla \times \frac{\mathbf{S} \times \hat{\mathbf{R}}}{R^2} = \frac{1}{2\pi^2} \int \hat{\mathbf{q}} \times (\mathbf{S} \times \hat{\mathbf{q}}) e^{i\mathbf{q}\cdot\mathbf{R}} d\mathbf{q}$

[3] $\int \frac{\hat{\mathbf{R}}}{R^2} e^{i\boldsymbol{\tau}\cdot\mathbf{R}} d\mathbf{R} = 4\pi i \frac{\hat{\boldsymbol{\tau}}}{\tau}$

3.23:

$$\mathbf{Q}_\perp \equiv \frac{1}{4\pi}\sum_i \langle \mathbf{k}'|V_S + V_L|\mathbf{k}\rangle = \sum_i e^{i\boldsymbol{\tau}\cdot\mathbf{r_i}}\left[\hat{\boldsymbol{\tau}}\times(\mathbf{S_i}\times\hat{\boldsymbol{\tau}}) + \frac{i}{\hbar\tau}(\mathbf{p_i}\times\hat{\boldsymbol{\tau}})\right] \tag{3.25}$$

Collecting the constant factors in 3.21 and 3.22 the partial differential cross section can be written in terms only of the initial and final spin states of the neutron and the initial and final states of the scattering system:

$$\left(\frac{d^2\sigma}{d\Omega dE_f}\right)_{\sigma\lambda\to\sigma'\lambda'} = (\gamma r_0)^2\frac{k_f}{k_i}|\langle\sigma'\lambda'|\boldsymbol{\sigma}\cdot\mathbf{Q}_\perp|\sigma\lambda\rangle|^2\delta(E_\lambda - E_{\lambda'} + \hbar\omega), \tag{3.26}$$

where r_0 is the classical electron radius ($r_0 = 2.818\times10^{-15}m$). The operator $\mathbf{Q}_\perp$ deserves some attention. The spin part of $\mathbf{Q}_\perp$ can be written as

$$\begin{aligned}\mathbf{Q}_{\perp\mathbf{S}} &= \sum_i e^{i\boldsymbol{\tau}\cdot\mathbf{r_i}}[\hat{\boldsymbol{\tau}}\times(\mathbf{S_i}\times\hat{\boldsymbol{\tau}})] = \hat{\boldsymbol{\tau}}\times(\mathbf{Q_S}\times\hat{\boldsymbol{\tau}}), \quad \text{where} \\ \mathbf{Q_S} &= \sum_i e^{i\boldsymbol{\tau}\cdot\mathbf{r_i}}\mathbf{S_i}.\end{aligned} \tag{3.27}$$

$\mathbf{Q_S}$ has a direct physical meaning. Is is the Fourier transform of the electron spin density:

$$\begin{aligned}\mathbf{Q_S} &= \int \rho_\mathbf{S}(\mathbf{r})e^{i\boldsymbol{\tau}\cdot\mathbf{r}}d\mathbf{r}, \quad \text{where} \\ \rho_\mathbf{S}(\mathbf{r}) &= \sum_i \delta(\mathbf{r}-\mathbf{r_i})\mathbf{S_i}.\end{aligned} \tag{3.28}$$

As the relationship between spin and magnetization is simple $\mathbf{M_S}(\mathbf{r}) = -2\mu_B\rho_\mathbf{S}(\mathbf{r})$, $\mathbf{Q}_{\perp\mathbf{S}}$ can be defined in terms of the Fourier transform of the spin magnetization:

$$\mathbf{Q}_{\perp\mathbf{S}} = -\frac{1}{2\mu_B}\hat{\boldsymbol{\tau}}\times(\mathbf{M_S}(\boldsymbol{\tau})\times\hat{\boldsymbol{\tau}}) \tag{3.29}$$

Conveniently, a similar result holds in for the orbital momentum part, by treating the current density in a similar way. The derivation found in [17] will not be given here. The orbital part of $\mathbf{Q}_\perp$ can be written as:

$$\begin{aligned}\mathbf{Q}_{\perp\mathbf{L}} &= -\frac{1}{2\mu_B}\hat{\boldsymbol{\tau}}\times(\mathbf{M_L}(\boldsymbol{\tau})\times\hat{\boldsymbol{\tau}}), \quad \text{where} \\ \mathbf{M_L}(\boldsymbol{\tau}) &= -2\mu_B\mathbf{Q_L} = \int \mathbf{M_L}(\mathbf{r})e^{i\boldsymbol{\tau}\cdot\mathbf{r}}d\mathbf{r}\end{aligned} \tag{3.30}$$

This enables a definition of total magnetization for a general system of electrons - both spin and orbital:

$$\begin{aligned}\mathbf{M}(\boldsymbol{\tau}) &= \int \mathbf{M}(\mathbf{r})e^{i\boldsymbol{\tau}\cdot\mathbf{r}}d\mathbf{r}, \quad \text{where} \\ \mathbf{M}(\mathbf{r}) &= \mathbf{M_S}(\mathbf{r}) + \mathbf{M_L}(\mathbf{r})\end{aligned} \tag{3.31}$$

The operator $\mathbf{Q}_\perp$ can now be written in terms of the Fourier transform of the total magnetization of the system:

$$\mathbf{Q}_\perp(\boldsymbol{\tau}) = -\frac{1}{2\mu_B}\hat{\boldsymbol{\tau}}\times(\mathbf{M}(\boldsymbol{\tau})\times\hat{\boldsymbol{\tau}}). \tag{3.32}$$

The fact that both the spin and orbital part of $\mathbf{Q}_\perp$ can be collected in the form presented in equation 3.32 and that it represents the total magnetization of the system of electrons, spawns two facts directly used in the interpretation of neutron scattering experiments:

- As $\mathbf{Q}_\perp$ reflects net magnetization only *unpaired electrons* - giving rise to net magnetization - can interact magnetically with neutrons.
- $\mathbf{Q}_\perp$ only reflects the projection of the magnetization vector onto the plane *perpendicular* to $\boldsymbol{\tau} = \mathbf{k}_f - \mathbf{k}_i$.

In the calculation of the matrix element, the next step is to take the neutron spin into consideration. First, the following definition is convenient

$$\mathbf{Q} \equiv \mathbf{Q_S} + \mathbf{Q_L} = -\frac{1}{2\mu_B}\mathbf{M}(\tau). \tag{3.33}$$

$\mathbf{Q}_\perp^\dagger \cdot \mathbf{Q}_\perp$ can be expressed conveniently in terms of $\mathbf{Q}$:

$$\mathbf{Q}_\perp{}^\dagger \cdot \mathbf{Q}_\perp = \sum_{\alpha\beta} (\delta_{\alpha\beta} - \hat{\tau_\alpha}\hat{\tau_\beta}) Q_\alpha^\dagger Q_\beta, \tag{3.34}$$

where $\alpha, \beta = x, y, z$ and $\delta_{\alpha\beta}$ is the Kronecker delta (1 if $\alpha = \beta$ and 0 otherwise). It is clear that $\mathbf{Q}_\perp$ is the projection of $\mathbf{Q}$ onto the plan perpendicular to $\boldsymbol{\tau}$. The partial differential cross section describes the probability of scattering a beam of neutrons consisting of a set of initial states into a spatial angle. All final states which scatter into that spatial angle are counted. Thus, we need to sum over the final states and average over the initial states of the neutron. Essentially, this is the following sum:

$$\sum_{\sigma\sigma'} p_\sigma |\langle \sigma'\lambda' | \boldsymbol{\sigma} \cdot \mathbf{Q}_\perp | \sigma\lambda \rangle|^2 \tag{3.35}$$

The vector operator dot product $\boldsymbol{\sigma} \cdot \mathbf{Q}_\perp = \sigma_x Q_{\perp x} + \sigma_y Q_{\perp y} + \sigma_z Q_{\perp z}$ allows for a separation of variables, since $\boldsymbol{\sigma}$ only depends on the spin of the neutron, and $\mathbf{Q}_\perp$ only depends on the spins and positions of the unpaired electrons. The two sets of coordinates are independent, so:

$$\langle \sigma'\lambda' | \sigma_x Q_{\perp x} | \sigma\lambda \rangle = \langle \sigma' | \sigma_x | \sigma \rangle \langle \lambda' | Q_{\perp x} | \lambda \rangle \tag{3.36}$$

When multiplying $\boldsymbol{\sigma} \cdot \mathbf{Q}_\perp$ with its complex conjugate, all terms have the following form since σ is hermitian:

$$\langle \sigma | \sigma_\alpha | \sigma' \rangle \langle \sigma' | \sigma_\beta | \sigma \rangle \langle \lambda | Q_{\perp\alpha}^\dagger | \lambda' \rangle \langle \lambda' | Q_{\perp\beta} | \lambda \rangle \tag{3.37}$$

As we sum over all the final spin states in equation 3.35, the following is true (the closure relation):

$$\begin{aligned} \text{for } \alpha = \beta: \quad & \sum_{\sigma'} \langle \sigma | \sigma_\alpha | \sigma' \rangle \langle \sigma' | \sigma_\beta | \sigma \rangle = \langle \sigma | \sigma_\alpha^2 | \sigma \rangle \\ \text{for } \alpha \neq \beta: \quad & \sum_{\sigma'} \langle \sigma | \sigma_\alpha | \sigma' \rangle \langle \sigma' | \sigma_\beta | \sigma \rangle = \langle \sigma | \sigma_\alpha \sigma_\beta | \sigma \rangle \end{aligned} \tag{3.38}$$

Along any given direction the neutron can only have spins $\pm\frac{1}{2}$ in units of $\hbar$. Using the standard basis, let $|\uparrow\rangle$ and $|\downarrow\rangle$ denote spin up and spin down states along the z-direction. Expressing the Pauli spin operators using standard raising and lowering operators ($\sigma_x = S^+ + S^-$ and $\sigma_y = -i(S^+ - S^-)$), the inner products in equation 3.38 can be evaluated:

$$\begin{aligned} \forall \alpha \in \{x, y, z\}: \quad & \langle \uparrow | \sigma_\alpha^2 | \uparrow \rangle = \langle \downarrow | \sigma_\alpha^2 | \downarrow \rangle = 1 \\ \forall \alpha, \beta \in \{x, y, z\} \mid \alpha \neq \beta: \quad & \langle \uparrow | \sigma_\alpha \sigma_\beta | \uparrow \rangle = -\langle \downarrow | \sigma_\alpha \sigma_\beta | \downarrow \rangle = i \end{aligned} \tag{3.39}$$

In this work, only unpolarized neutrons are used, which makes the evaluation of the summation in equation 3.35 particularly simple because of the sign change when mixing different Pauli-matrices

seen in equation 3.39. For unpolarized neutron the probability of being in a spin up or spin down state is $p_\uparrow = p_\downarrow = \frac{1}{2}$, therefore:

$$\begin{aligned} \forall \alpha \in \{x,y,z\}: \quad \sum_\sigma p_\sigma \langle \sigma | \sigma_\alpha^2 | \sigma \rangle &= 1 \quad \text{and} \\ \forall \alpha,\beta \in \{x,y,z\} \mid \alpha \neq \beta: \quad \sum_\sigma p_\sigma \langle \sigma | \sigma_\alpha \sigma_\beta | \sigma \rangle &= 0 \quad \Rightarrow \\ \sum_{\sigma\sigma'} p_\sigma |\langle \sigma' \lambda' | \boldsymbol{\sigma} \cdot \mathbf{Q}_\perp | \sigma \lambda \rangle|^2 = \sum_\alpha \langle \lambda | Q_{\perp\alpha}^\dagger | \lambda' \rangle \langle \lambda' | Q_{\perp\alpha} | \lambda \rangle & \end{aligned} \tag{3.40}$$

when combining equations 3.40 and 3.26, an expression is obtained for the partial differential cross section for scattering of unpolarized neutrons by a general system of unpaired electrons:

$$\left(\frac{d^2\sigma}{d\Omega dE_f}\right) = (\gamma R_0)^2 \frac{k_f}{k_i} \sum_{\lambda\lambda'} p_\lambda \sum_\alpha \langle \lambda | Q_{\perp\alpha}^\dagger | \lambda' \rangle \langle \lambda' | Q_{\perp\alpha} | \lambda \rangle \delta(E_\lambda - E_{\lambda'} + \hbar\omega) \tag{3.41}$$

As it is more directly physically interpretable to use $\mathbf{Q}$ instead of $\mathbf{Q}_\perp$ because $\mathbf{Q}$ directly expresses the electron magnetization, equation 3.41 can be reformulated using equation 3.34:

$$\begin{aligned} \left(\frac{d^2\sigma}{d\Omega dE_f}\right) &= (\gamma R_0)^2 \frac{k_f}{k_i} \sum_{\alpha\beta} (\delta_{\alpha\beta} - \hat{\tau}_\alpha \hat{\tau}_\beta) \\ &\times \sum_{\lambda\lambda'} p_\lambda \langle \lambda | Q_\alpha^\dagger | \lambda' \rangle \langle \lambda' | Q_\beta | \lambda \rangle \delta(E_\lambda - E_{\lambda'} + \hbar\omega) \end{aligned} \tag{3.42}$$

3.2 Scattering from ordered systems

The general description of the magnetic interaction between neutrons and systems of unpaired electrons can be restricted to large ordered systems of atoms. In section 2.2 a description is given of the concepts convenient to describe such systems. As previously mentioned, a perfect crystal can be described by infinitely many identical unit cells closely packed in all three crystallographic directions, consisting of a so-called basis of one or more formula units. As previously described, elements in the iron group have quenched orbital momenta, resulting from the electric field of the crystal environment. There are effective alterations of the spin moments due to the spin orbit coupling (only the ground state has $L = 0$), but this is a minor correction assumed to be of dipolar nature. Therefore, a case with scattering from spin only is assumed. Let $\mathbf{R}_{ld}$ be the position of the atom in the lth unit cell at atomic position d, and r_ν be the position of the νth unpaired electron of that particular atom relative to the nucleus. These electrons are assumed to be localized close to the ions only perturbed by thermal fluctuations. The goal is to develop a description of the neutron scattering off the crystal as a whole, where the symmetries of the system and the constituent atoms are conceptually separated from the internal arrangement of scatterers in the individual ion. To meet this end, it is necessary to assume that the spins of each unpaired electron ($\mathbf{S}_\nu$) within the ion combine to form a single resultant spin for the ion ($\mathbf{S}_{ld}$). This allows for a separation of the τ-dependency of the scattering within the individual types of magnetic ions from the sum over states in equation 3.42. Inserting $\mathbf{r}_i = \mathbf{R}_{ld} + \mathbf{r}_\nu$ into the expression of $\mathbf{Q_S}$ in equation 3.28 gives

$$\mathbf{Q} = \mathbf{Q_S} = \sum_{ld} e^{i\boldsymbol{\tau}\cdot\mathbf{R_{ld}}} \sum_{\nu(d)} e^{i\boldsymbol{\tau}\cdot\mathbf{r}_\nu} \mathbf{S_i}, \tag{3.43}$$

which can be inserted directly into the matrix element from equation 3.42, giving

$$\begin{aligned} \langle \lambda' | \mathbf{Q} | \lambda \rangle_{ld} &= \langle \lambda' | e^{i\boldsymbol{\tau}\cdot\mathbf{R_{ld}}} \sum_{\nu(d)} e^{i\boldsymbol{\tau}\cdot\mathbf{r}_\nu} \mathbf{S}_\nu | \lambda \rangle \\ &= \langle \lambda' | g_{ld} \sum_\nu f_\nu \mathbf{S}_\nu | \lambda \rangle, \quad \text{where} \\ f_\nu = e^{i\boldsymbol{\tau}\cdot\mathbf{r}_\nu} \quad &\text{and} \quad g_{ld} = e^{i\boldsymbol{\tau}\cdot\mathbf{R_{ld}}}. \end{aligned} \tag{3.44}$$

The closure relation ($\langle i|AB|f\rangle = \sum_j \langle i|A|j\rangle\langle j|B|f\rangle$) can be used to rewrite equation 3.44:

$$\begin{aligned}\langle\lambda'|g_{ld}\sum_\nu f_\nu \mathbf{S}_\nu|\lambda\rangle &= \sum_{\lambda''}\sum_\nu \langle\lambda'|f_\nu|\lambda''\rangle\langle\lambda''|g_{ld}\mathbf{S}_\nu|\lambda\rangle \\ &= \sum_{\lambda''}\langle\lambda'|f_\nu|\lambda''\rangle\langle\lambda''|g_{ld}\sum_\nu \mathbf{S}_\nu|\lambda\rangle \end{aligned} \tag{3.45}$$

The last step in equation 3.45 is due to the Pauli principle stating that any multi-fermion quantum state needs to be anti-symmetric with respect to electron exchange. Therefore the spatial part of the electron states are either symmetric or antisymmetric (since the spin part is also either symmetric or anti-symmetric). Therefore, the matrix element $\langle\lambda'|f_\nu|\lambda''\rangle$ is independent of the electron index (this can be shown for for any operator depending on position and for any multi-electron spatial function [17]). The energy of the neutron is of the order meV which is usually not enough to change neither the spin quantum number nor the spatial part of the electronic state of the ion. Thus, the states relevant for the summation in equation 3.42 only differ in spin orientation and nuclear position. Since f_ν only depends on the position of the electrons, both the nuclear position and the electronic spin parts of the states $|\lambda'\rangle$ and $|\lambda''\rangle$ must be identical for $\langle\lambda'|f_\nu|\lambda''\rangle$ to be non-zero (they are orthogonal and not affected by the operator f_ν). Equation 3.45 then becomes

$$\langle\lambda'|g_{ld}\sum_\nu f_\nu \mathbf{S}_\nu|\lambda\rangle = \langle\lambda'|f_\nu|\lambda'\rangle\langle\lambda'|g_{ld}\sum_\nu \mathbf{S}_\nu|\lambda\rangle. \tag{3.46}$$

Since the spatial part of the electronic states is the same, $\langle\lambda'|f_\nu|\lambda'\rangle = \langle\lambda|f_\nu|\lambda\rangle$. The nuclear position and electronic spin parts of $\langle\lambda|$ are orthogonal, and since the matrix element is independent of ν, $\langle\lambda'|f_\nu|\lambda'\rangle$ is essentially the spatial Fourier transform of the unpaired electron density divided by the number of unpaired electrons. In mathematical terms:

$$\langle\lambda'|f_\nu|\lambda'\rangle = \int \zeta_d(\mathbf{r})e^{i\boldsymbol{\tau}\cdot\mathbf{r}_\nu}d\mathbf{r} \equiv F_d(\tau), \tag{3.47}$$

where $\zeta_d(\mathbf{r})$ is called the normalized unpaired electron density and $F_d(\mathbf{r})$ the *magnetic form factor* for the ion at unit cell position d. An important point is that unlike the nuclear case where the scattering length is independent of neutron momentum transfer, the magnetic form factor has a τ-dependency due to the finite extent of the electron wave functions compared to the wavelength of the neutron. It is very important to know the τ-dependency of this form factor since it directly determines how strong the magnetic scattering is as a function of the neutron momentum transfer. The actual form factors for four relevant ions are given in section 3.3.6 (simple isotropic case). Defining $\mathbf{S}_{ld} \equiv \sum_\nu \mathbf{S}_\nu$ equation 3.44 can now be written as follows:

$$\begin{aligned}\langle\lambda'|\mathbf{Q}|\lambda\rangle &= \sum_{ld}\langle\lambda'|e^{i\boldsymbol{\tau}\cdot\mathbf{R}_{ld}}\sum_{\nu(d)} e^{i\boldsymbol{\tau}\cdot\mathbf{r}_\nu}\mathbf{S}_\nu|\lambda\rangle \\ &= \sum_{ld} F_d(\tau)\langle\lambda'|e^{i\boldsymbol{\tau}\cdot\mathbf{R}_{ld}}\mathbf{S}_{ld}|\lambda\rangle. \end{aligned} \tag{3.48}$$

Putting this directly into equation 3.42 gives the cross section for the ordered system as a whole:

$$\begin{aligned}\left(\frac{d^2\sigma}{d\Omega dE_f}\right) &= (\gamma R_0)^2\frac{k_f}{k_i}\sum_{\alpha\beta}(\delta_{\alpha\beta}-\hat{\tau_\alpha}\hat{\tau_\beta})\sum_{l'd'}\sum_{ld}F_d^*(\tau)F_d(\tau) \\ &\times \sum_{\lambda\lambda'} p_\lambda\langle\lambda|e^{-i\boldsymbol{\tau}\cdot\mathbf{R}_{l'd'}}S^\alpha_{l'd'}|\lambda'\rangle\langle\lambda'|e^{i\boldsymbol{\tau}\cdot\mathbf{R}_{ld}}S^\beta_{ld}|\lambda\rangle\delta(E_\lambda - E_{\lambda'}+\hbar\omega) \end{aligned} \tag{3.49}$$

In further calculations $F_d(\tau)$ will be replaced with $\frac{1}{2}gF_d(\tau)$ to account for an eventual $\mathbf{L}\cdot\mathbf{S}$ coupling altering the effective spin quantum number. The Lande splitting factor g[4] has the value of 2 in

[4] $1+\frac{S(S+1)-L(L+1)}{J(J+1)}+\frac{1}{2}+\frac{L(L+1)-S(S+1)}{2J(J+1)}$

case of no $\mathbf{L}\cdot\mathbf{S}$ correction. The form factor in case of both spin and orbital angular momenta is treated in [18]. The probability p_λ is dependent on temperature T and is given by the Boltzmann distribution:

$$p_\lambda = \frac{1}{Z}e^{-\frac{E_\lambda}{k_BT}}, \quad \text{where} \quad Z = \sum_\lambda e^{-\frac{E_\lambda}{k_BT}}, \tag{3.50}$$

where k_B is the Boltzmann constant. Defining the thermal average and writing the time-dependency of an operator as

$$\langle A\rangle = \sum_\lambda p_\lambda\langle\lambda|A|\lambda\rangle \quad \text{and} \quad S^\beta_{ld}(t) = e^{\frac{iHt}{\hbar}}S^\beta_{ld}e^{\frac{-iHt}{\hbar}}, \tag{3.51}$$

one can rewrite the summation over λ' and average of λ in equation 3.49 using two results from [17][5] [6] in the following way:

$$\sum_{\lambda\lambda'} p_\lambda\langle\lambda|e^{-i\boldsymbol{\tau}\cdot\mathbf{R}_{l'd'}}S^\alpha_{l'd'}|\lambda'\rangle\langle\lambda'|e^{i\boldsymbol{\tau}\cdot\mathbf{R}_{ld}}S^\beta_{ld}|\lambda\rangle\delta(E_\lambda - E_{\lambda'} + \hbar\omega) \tag{3.52}$$

$$= \frac{1}{2\pi\hbar}\int_{-\infty}^{\infty}\langle e^{-i\boldsymbol{\tau}\cdot\mathbf{R}_{l'd'}(0)}S^\alpha_{l'd'}(0)e^{i\boldsymbol{\tau}\cdot\mathbf{R}_{ld}(t)}S^\beta_{ld}(t)\rangle e^{-i\omega t}dt. \tag{3.53}$$

The above integral is over time only, which makes it convenient to separate the static part of the atomic positions from the dynamic part. Therefore, let

$$\mathbf{R}_{ld} = \mathbf{l} + \mathbf{d} + \mathbf{u}_{ld}(t), \tag{3.54}$$

where $\mathbf{l}$ is the unit cell position vector of unit cell l, $\mathbf{d}$ is position vector of ion d within the unit cell and $\mathbf{u}_{ld}(t)$ is the time-dependent atomic displacement from the static equilibrium position. Assuming that the spin orientation interacts weakly with the atomic position, one can separate the phase factors from the spin operators and insert the result into equation 3.49 to obtain the magnetic partial differential cross section for a crystallographic system of magnetic ions:

$$\left(\frac{d^2\sigma}{d\Omega dE_f}\right)_{mag} = \frac{(\gamma R_0)^2}{2\pi\hbar}\frac{k_f}{k_i}\sum_{\alpha\beta}(\delta_{\alpha\beta} - \hat{\tau}_\alpha\hat{\tau}_\beta)\sum_{l'd'ld}\frac{1}{4}g_{d'}g_dF^*_d(\boldsymbol{\tau})F_d(\boldsymbol{\tau})e^{i\boldsymbol{\tau}\cdot(\mathbf{l}+\mathbf{d}-\mathbf{l}'-\mathbf{d}')}$$
$$\times \int_{-\infty}^{\infty}\langle e^{-i\boldsymbol{\tau}\cdot\mathbf{u}_{l'd'}(0)}e^{i\boldsymbol{\tau}\cdot\mathbf{u}_{ld}(t)}\rangle\langle S^\alpha_{l'd'}(0)S^\beta_{ld}(t)\rangle e^{-i\omega t}dt. \tag{3.55}$$

This cross section is of course model-dependent but within that given model, this cross section describes virtually any magnetic interaction between unpolarized neutrons, the lattice of magnetic ions and the orientation of the spins. In case of nuclear scattering, the same procedure of summing over λ', averaging over λ and using the integral representation of the δ-function for energy can be used to obtain the coherent nuclear partial differential cross section for a crystallographic system of nuclei:

$$\left(\frac{d^2\sigma}{d\Omega dE_f}\right)_{nuc} = \frac{1}{2\pi\hbar}\frac{k_f}{k_i}\sum_{l'd'ld}\bar{b}_{d'}\bar{b}_d e^{i\boldsymbol{\tau}\cdot(\mathbf{l}+\mathbf{d}-\mathbf{l}'-\mathbf{d}')}\int_{-\infty}^{\infty}\langle e^{-i\boldsymbol{\tau}\cdot\mathbf{u}_{l'd'}(0)}e^{i\boldsymbol{\tau}\cdot\mathbf{u}_{ld}(t)}\rangle e^{-i\omega t}dt, \tag{3.56}$$

where $\bar{b}$ is the average over isotopes and nuclear spin of the nuclear scattering lengths. In equations 3.55 and 3.56, t represents a time interval, since we take thermal averages of the product of two operators each at two different times. These averages are in fact *time dependent pair correlation functions*, and represents the correlation between the positions of two atoms separated in time (t) and space ($\mathbf{R}_{ld} - \mathbf{R}_{l'd'}$ (generally, but not always; the two points could be the same). The

[5] $\delta(E_\lambda - E_{\lambda'} + \hbar\omega) = \frac{1}{2\pi\hbar}\int_{-\infty}^{\infty}e^{i(E_{\lambda'}-E_\lambda)t/\hbar}e^{-i\omega t}dt$

[6] $e^{iHt/\hbar}|\lambda\rangle = e^{iE_\lambda t/\hbar}|\lambda\rangle$

term $\langle e^{-i\boldsymbol{\tau}\cdot\mathbf{u}_{l'd'}(0)}e^{i\boldsymbol{\tau}\cdot\mathbf{u}_{ld}(t)}\rangle$ evident in both the nuclear and magnetic cross section represents the correlation of the phase factor of the scattered neutron between the two points caused by the corresponding correlated displacement of the scatterers from the equilibrium position (nuclei or electrons). A correlation of this sort is a wave of atomic displacements (stationary or propagating) known as a *phonon*. They are the collective discrete modes of resonant atomic displacements for the whole crystal. Phonons exhibit particle like behavior since they can have both well defined momentum and well defined energy, and can be created and annihilated by neutrons. There are several kinds of such collective particle-like modes of different physical origin, and they are rightfully called *pseudo-particles*. Measuring the phonons by measuring the energy- and momentum-transfer of the neutrons creating and annihilating phonons provides information of the inter atomic couplings. However, the phonons also cause an effective reduction of the scattering cross section even at zero energy transfer, since each individual atom has an average displacement from its equilibrium position by its own right. This can be seen from the following. Let

$$\begin{aligned}\langle e^{-i\boldsymbol{\tau}\cdot\mathbf{u}_{l'd'}(0)}e^{i\boldsymbol{\tau}\cdot\mathbf{u}_{ld}(t)}\rangle &= \langle e^U e^V\rangle, \quad \text{where} \\ U = -i\boldsymbol{\tau}\cdot\mathbf{u}_{l'd'}(0) &\quad \text{and} \quad V = i\boldsymbol{\tau}\cdot\mathbf{u}_{ld}(t).\end{aligned} \tag{3.57}$$

Assuming that the displacement behaves like a harmonic oscillator the displacement probability function is a Gaussian. Using only this physical assumption, it can be proven ([17]) that

$$\langle e^U e^V\rangle = e^{\frac{\langle U^2\rangle}{2}} e^{\frac{\langle V^2\rangle}{2}} e^{\langle UV\rangle} \tag{3.58}$$

The zero point of time and therefore t is arbitrarily chosen; what matters in the pair correlation functions is the time *interval* t. Therefore, the terms $e^{\langle U^2\rangle/2}$ and $e^{\langle V^2\rangle/2}$ are time independent - they are two snap shots at times 0 and t of a time independent quantities originating from the thermal average of the absolute atomic displacement of the individual atoms, which is a function of temperature. The term $e^{\langle UV\rangle}$ however, describes the pair correlations in space and time and hence the propagating phonons. Measuring phonons is well without the scope of this thesis, so the working assumption is that the atomic displacements are uncorrelated meaning that $\langle UV\rangle = 0$ and $e^{\langle UV\rangle} = 1$. This removes the time dependency and hence energetic pair correlations left for the neutron to create or annihilate; there is no energy transfer between the system and the neutron and the lengths of the initial and final wave vectors are the same ($k = k'$). This is known as *elastic scattering*. Furthermore, the range of any interaction between two atoms is assumed to be negligible compared to the size of the crystal. Thus, the surroundings are exactly the same for every unit cell, meaning that for every value of l, the summation over l' is the same. The sum over ll' is therefore equivalent to N times the sum over l from some initial unit cell $l' = 0$. The cross section then becomes:

$$\left(\frac{d^2\sigma}{d\Omega dE_f}\right)_{nuc} = \frac{1}{2\pi\hbar}\frac{k_f}{k_i}N\sum_l e^{i\boldsymbol{\tau}\cdot\mathbf{l}}\sum_{dd'}\overline{b}_d\overline{b}_{d'}e^{i\boldsymbol{\tau}\cdot(\mathbf{d}-\mathbf{d}')}e^{-W_d}e^{-W_{d'}}\int_{-\infty}^{\infty}e^{-i\omega t}dt, \tag{3.59}$$

where $W_d = 1/2\cdot\langle(\boldsymbol{\tau}\cdot\mathbf{u}_{ld})^2\rangle$. The term e^{-W_d} is called the *Debye-Waller factor* and describes the loss in the elastically scattered intensity due to the thermal smearing of the individual atomic positions which are induced by phonons. Describing these vibrations can be very difficult in practice, since they are in principle different for each atom in the unit cell and can be anisotropic. In [17] it is shown that

$$\int_{-\infty}^{\infty}e^{-i\omega t}dt = 2\pi\hbar\delta(\hbar\omega), \tag{3.60}$$

which confirms that the cross section is elastic. The sum over dd' is a sum of complex numbers, which can be simplified to be the complex amplitude squared of a simple expression unique for the

unit cell:

$$\sum_{dd'} \bar{b}_d \bar{b}_{d'} e^{i\boldsymbol{\tau}\cdot(\mathbf{d}-\mathbf{d}')} e^{-W_d} e^{-W_{d'}} = \left| \sum_d \bar{b}_d e^{i\boldsymbol{\tau}\cdot\mathbf{d}} e^{-W_d} \right|^2 = |F_N(\boldsymbol{\tau})|^2, \tag{3.61}$$

where $|F_N(\boldsymbol{\tau})|^2$ is called the *unit cell structure factor.* Since the integral over all energies of this delta function in energy is 1 and $k = k'$, the nuclear elastic differential cross section becomes:

$$\left(\frac{d\sigma}{d\Omega}\right)_{nuc} = \int_0^\infty \left(\frac{d^2\sigma}{d\Omega dE_f}\right)_{nuc} dE' = N \sum_l e^{i\boldsymbol{\tau}\cdot\mathbf{l}} |F_N(\boldsymbol{\tau})|^2. \tag{3.62}$$

Turning to the magnetic partial differential cross section in equation 3.55, the same displacement pair correlation function describing the phonons is present along with the spin pair correlation function. It is actually possible to induce a phonon via the magnetic interaction with a neutron, but again this is beyond the scope of this thesis. As in the nuclear case, we extract the time-independent Debye-Waller factors and neglect the contributions to the scattering involving phonons. In the lithium-ortho-phosphates, there is only one magnetic ion (Fe^{2+}, Co^{2+}, Ni^{2+}, Mn^{2+}). When this is the case, the Debye-Waller factor is a mere constant prefactor which can be taken out of the summation. Using this restriction and the same unit cell summation trick as in the nuclear case, the magnetic partial differential cross section can be somewhat simplified:

$$\left(\frac{d^2\sigma}{d\Omega dE_f}\right)_{mag} = \frac{(\gamma R_0)^2}{2\pi\hbar} \frac{k_f}{k_i} N_m |\frac{1}{2} g F(\boldsymbol{\tau})|^2 e^{-W_d} \sum_{\alpha\beta} (\delta_{\alpha\beta} - \hat{\tau}_\alpha \hat{\tau}_\beta) \sum_l e^{i\boldsymbol{\tau}\cdot\mathbf{l}} \sum_{d'd} e^{i\boldsymbol{\tau}\cdot(\mathbf{d}-\mathbf{d}')} \times \int_{-\infty}^{\infty} \langle S^\alpha_{0d'}(0) S^\beta_{ld}(t) \rangle e^{-i\omega t} dt, \tag{3.63}$$

where N_m is the number of *magnetic* unit cells. The term $\langle S^\alpha_{0d'}(0) S^\beta_{ld}(t) \rangle$ is the time-dependent pair correlation function of the spin directions. It describes the correlations separated in time and space of the direction of the spin dipole moment of two magnetic atoms. As in the case of phonons, a small change in the spin direction is a collective excitation of the whole magnetic system. Like phonons, these excitations are propagating waves with energy and momentum and they too can be created and annihilated with neutrons. They are called *magnons* or *spin waves.* If the correlation time interval is increased to infinity ($t \to \infty$), the value of the spin correlation function describes static and hence time-independent correlations:

$$\lim_{t\to\infty} \langle S^\alpha_{0d'}(0) S^\beta_{ld}(t) \rangle = \langle S^\alpha_{0d'} \rangle \langle S^\beta_{ld} \rangle. \tag{3.64}$$

Moving from unit cell 0 to unit cell l is equivalent to performing a lattice translation symmetry operation shifting from one ion in unit cell 0 to the equivalent ion in unit cell l with the exact same crystallographic surroundings. Therefore, the spin direction of the two ions must be the same and hence $\langle S^\alpha_{0d} \rangle = \langle S^\alpha_{ld} \rangle$. Putting the static unit cell spin components outside of the integral in equation 3.63, results in the same delta function in energy as in the nuclear case. Thus, the elastic magnetic differential cross section can be calculated:

$$\left(\frac{d\sigma}{d\Omega}\right)_{mag} = \int_0^\infty \left(\frac{d^2\sigma}{d\Omega dE_f}\right)_{mag} dE' = (\gamma R_0)^2 N_m |\frac{1}{2} g F(\boldsymbol{\tau})|^2 e^{-W_d} \sum_{\alpha\beta} (\delta_{\alpha\beta} - \hat{\tau}_\alpha \hat{\tau}_\beta) \sum_l e^{i\boldsymbol{\tau}\cdot\mathbf{l}} \sum_{d'd} e^{i\boldsymbol{\tau}\cdot(\mathbf{d}-\mathbf{d}')} \times \langle S^\alpha_{d'} \rangle \langle S^\beta_d \rangle \tag{3.65}$$

This can be slightly reformulated using equations 3.32 and 3.34, and defining a structure factor for the magnetic unit cell:

$$\begin{aligned}\left(\frac{d\sigma}{d\Omega}\right)_{mag} &= (\gamma R_0)^2 N_m |\frac{1}{2} g F(\boldsymbol{\tau})|^2 e^{-W_d} \sum_l e^{i\boldsymbol{\tau}\cdot\mathbf{l}} |\hat{\boldsymbol{\tau}} \times (F_M(\boldsymbol{\tau}) \times \hat{\boldsymbol{\tau}})|^2, \quad \text{where} \\ F_M(\boldsymbol{\tau}) &= \sum_d e^{i\boldsymbol{\tau}\cdot\mathbf{d}} \langle \mathbf{S}_d \rangle \end{aligned} \tag{3.66}$$

$F_M(\boldsymbol{\tau})$ is the *magnetic unit cell structure factor.*

3.2.1 Bragg's law and reciprocal space

In both the elastic nuclear and magnetic cross section (equations 3.62 and 3.66), there is a sum of neutron phase factors for all the unit cells which is called the *lattice sum.* The number of unit cells is huge, so for any arbitrary momentum transfer vector $\boldsymbol{\tau}$ the complex phase factors will cancel out in the sum, unless

$$\boldsymbol{\tau} \cdot \mathbf{l} = n2\pi$$

for all l and integer n. This coherence condition is only satisfied for specific momentum transfer vectors. In fact, is is possible to define a 3-dimensional space of lattice points where any vector between two lattice points satisfies the coherence condition using the crystal lattice vectors as a starting point. Let $\mathbf{a}$, $\mathbf{b}$ and $\mathbf{c}$ be the translational symmetry vectors chosen to describe a unit cell. The *reciprocal lattice* is defined using the following basis:

$$\mathbf{a}^* = \frac{2\pi}{V_0}(\mathbf{b} \times \mathbf{c}) \quad \mathbf{b}^* = \frac{2\pi}{V_0}(\mathbf{c} \times \mathbf{a}) \quad \mathbf{c}^* = \frac{2\pi}{V_0}(\mathbf{a} \times \mathbf{b}), \quad \text{where} \tag{3.67}$$

$$V_0 = \mathbf{a} \cdot (\mathbf{b} \times \mathbf{c}) \tag{3.68}$$

is the volume of the unit cell. As $\mathbf{l} = n_a\mathbf{a} + n_b\mathbf{b} + n_c\mathbf{c}$ is any crystallographic lattice vector, it follows from equations 3.67 and 3.68 that if $\boldsymbol{\tau} = \mathbf{G}$, where $\mathbf{G}$ is any reciprocal lattice vector $\mathbf{G} = h\mathbf{a}^* + k\mathbf{b}^* + l\mathbf{c}^*$, then

$$\boldsymbol{\tau} \cdot \mathbf{l} = hn_a 2\pi + kn_b 2\pi + ln_c 2\pi = n2\pi. \tag{3.69}$$

It is shown in [17] that

$$\sum_l e^{i\boldsymbol{\tau}\cdot\mathbf{l}} = \frac{(2\pi)^3}{V_0} \sum_{\mathbf{G}} \delta(\boldsymbol{\tau} - \mathbf{G}) \tag{3.70}$$

This formulates the condition $\boldsymbol{\tau} = \mathbf{G}$ which is known as the *Laue condition* and is an elegant formulation of the scattering condition. The scattering is indeed off crystal planes in real space, which can be seen by the following([19]). Define a crystal plane by the plane with intercepts $\frac{\mathbf{a}}{h}$, $\frac{\mathbf{b}}{k}$ and $\frac{\mathbf{c}}{l}$ seen from the unit cell origin. The indices h, k and l are called *Miller indices.* Knowing these intercept vectors, one can easily define two linearly independent vectors in the crystal plane

$$\mathbf{u}_1 = \frac{\mathbf{c}}{l} - \frac{\mathbf{a}}{h} \quad \text{and} \quad \mathbf{u}_1 = \frac{\mathbf{a}}{h} - \frac{\mathbf{b}}{k}. \tag{3.71}$$

The crystal plane can be spanned by these basis vectors $\mathbf{v} = n_1\mathbf{u}_1 + n_2\mathbf{u}_2$. The dot product of $\mathbf{G}$ and $\mathbf{v}$ is

$$\begin{aligned}\mathbf{G} \cdot \mathbf{v} &= (h\mathbf{a}^* + k\mathbf{b}^* + l\mathbf{c}^*) \cdot \left((n_2 - n_1)\frac{\mathbf{a}}{h} - n_2\frac{\mathbf{b}}{k} + n_1\frac{\mathbf{c}}{l}\right) \\ &= 2\pi\,(n_2 - n_1 - n_2 + b_1) = 0, \end{aligned} \tag{3.72}$$

and hence G and v are perpendicular. This is exactly what a reciprocal lattice vector $\mathbf{G} = (h, k, l)$ describes: A crystal plane in real space *perpendicular* to G that intercepts $\frac{\mathbf{a}}{h}$, $\frac{\mathbf{b}}{k}$ and $\frac{\mathbf{c}}{l}$ from the unit cell origin. The distance from the plane to the origin d is the projection of any vector connecting two planes (origin to plane) projected onto any unit vector perpendicular to the plane ($\hat{\mathbf{G}}$ for instance):

$$d = \frac{\mathbf{G}}{|\mathbf{G}|} \cdot \frac{\mathbf{a}}{h} = \frac{2\pi}{|\mathbf{G}|} \Rightarrow |\mathbf{G}| = \frac{2\pi}{d}. \tag{3.73}$$

Using that $\boldsymbol{\tau} = \mathbf{k}_i - \mathbf{k}_f$ and for elastic scattering $|\mathbf{k}_i| = |\mathbf{k}_f|$, the Laue condition can be reformulated

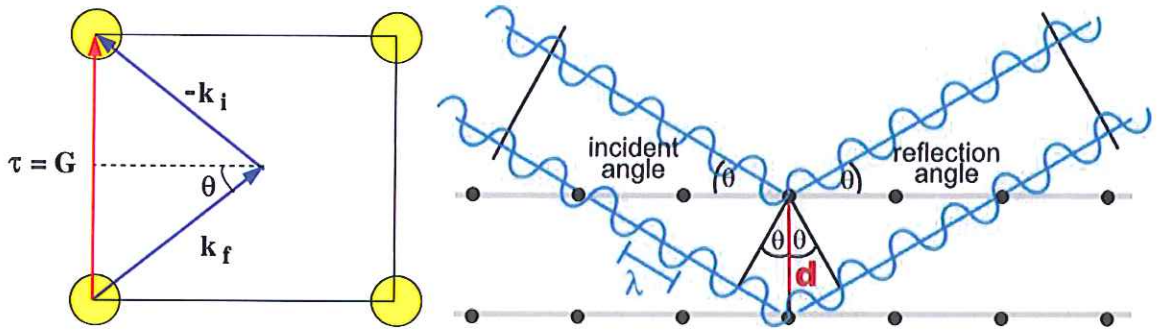

(a) The scattering triangle (b) Bragg's law

Figure 8: (a) The scattering triangle in reciprocal space fulfilling the scattering condition. The yellow circles are reciprocal space lattice points and 2θ is the neutron scattering angle. (b) Braggs law visually expressed in terms of in-going and out-going waves and the interference between them caused by diffraction from the crystal planes.

as

$$G^2 = 2\mathbf{G} \cdot \mathbf{k}_i.$$

As $\mathbf{G} \cdot \mathbf{k}_i = 2k\sin(\theta)$, where θ is half the angle between the incoming and outgoing wave vector, the Laue condition can be reformulated in terms of plane distance, neutron wavelength and scattering angle:

$$n\lambda = 2d\sin(\theta) \tag{3.74}$$

where n is any integer. This is the famous *Bragg's law*, describing the scattering condition for a stack of infinitely many crystal planes. This law can be derived in a much simpler way using a real space wave picture (see figure 8b). For wave interference to occur between the scattered waves from each crystal plane, the increase in wave travel distance from one plane to another ($2d\sin(\theta)$) must be equal to a multiple of the wavelength. The Laue condition is illustrated in 2 dimensions in figure 8a. When fulfilling the Laue condition, the length of the momentum transfer vector is $|\boldsymbol{\tau}| = 2k\sin(\theta)$, which is the reciprocal space version of Bragg's law. It should be noted that the Laue condition and Bragg's law are simple consequences of the lattice sum over unit cells without taking the crystal basis into consideration; they are binary statements referring only to where there can be elastic scattering and where there cannot. The intensities and additional extinction rules stemming from crystal symmetries are determined by the unit cell structure factor, which is exactly what needs to be measured and properly interpreted in elastic scattering experiments.

This concludes the description of the interactions of the neutrons with the ordered nuclear and magnetic potentials in crystals. When performing experiments, there are some important points worth summarizing:

- Microscopically, a single neutron sees the spatial Fourier transform of the scattering potential. The transformed magnetic potential depends on momentum transfer, while the transformed nuclear potential does not.

- Macroscopically, a beam of neutrons probes *collective* properties of a large single crystal; the cross section depends on a sum of thermal averaged pair correlation functions between atoms, which are Fourier transformed in both time and space.

- Magnetically, the neutrons interact with the *unpaired electrons* giving rise to net magnetization and only the projection of the magnetic moment vector onto a plane perpendicular to the momentum transfer vector $\boldsymbol{\tau}$.

3.3 Neutron instrumentation

Neutron instrumentation is a vast subject; there is a variety of techniques and tricks resulting from theoretical considerations, simulation but mostly plain practical experience. The experimental work presented in this thesis is the result of numerous different neutron experiments. The purpose of this section is to establish the concepts necessary to discuss and interpret the data presented in the thesis. A more detailed and broad description of neutron diffraction and spectroscopy can be found in textbooks such as [20] and [21].

3.3.1 Neutron sources

A high flux of neutrons can presently be produced in two ways: 1) It is possible to utilize the high neutron flux present in the core of fission reactors. There is a steady equilibrium in these reactors, resulting in a constant neutron flux which is quite stable. One experiment presented in this thesis was performed at a reactor source at the HMI in Berlin. 2) By generating an intense beam of high energy protons (roughly 1 GeV) and directing it towards a target consisting of some neutron abundant heavy elements, it is possible to peel off several neutrons from the heavy nuclei in a process called *spallation*. Accelerators generate pulsed high energy beams, which means that the neutron flux is also pulsed. This can be utilized in time-of-flight measurements. Most experiments presented in this thesis were performed at the spallation source at the PSI in Villigen, Switzerland. Since the free neutrons are generated by nuclear processes, the energy of the neutrons are several MeV's and are called *fast neutrons*. In order for neutrons to have the proper wavelength of $1 - 5$ Å, the neutrons need to be slowed down. This is done by using a so-called *moderator*, where the neutrons are brought into thermal equilibrium with a substance consisting of light atoms - such as light water. The flux distribution as a function of neutron velocity (v) and of moderator temperature T_m is a Maxwellian distribution (or a combination of Maxwellians):

$$\Phi(v) \propto v^2 e^{-\frac{m_n v^2}{2k_B T_m}}. \tag{3.75}$$

Since fast neutrons are able to penetrate shielding and reach the neutron detectors of the instruments, it is preferable to place the neutron spectrometer as far away from the source as possible. In order to avoid the $1/r^2$ flux drop-off with distance from the source of the thermal neutrons, considerable efforts have been made to invent guides for the neutrons optimized for transmitting low energy neutrons. These guides can reflect neutrons for sufficiently low scattering angles, thus keeping the neutrons with low incident angles in the guide. There is a *critical scattering vector* Q_c, above which the reflectivity drops below 1 ([22]). There is typically an interval above Q_c where the reflectivity is above 0.5 after which it drops rapidly to some infinitesimal value. The consequences of the critical scattering vector is that high velocity neutrons get absorbed by the guide unless they have a very low incident angle (Nickel is a typical guide material $Q_{c,Ni} = 0.0219$ Å^{-1}). In effect, after traveling through a long guide, most of the high velocity neutrons have been absorbed.

3.3.2 General concepts and components

In this section, the most widely used concepts and components used in designing spectrometers will be described, as they will be used frequently in the sections describing the data analysis.

- **Mosaicity:** A macroscopic single crystal is very rarely perfect in terms of perfect alignment of the crystal planes. Each crystal plane is perfectly aligned with its neighbor, but throughout the crystal the normal vectors of the crystal planes do not coincide perfectly, they are distributed around some mean vector. Conceptually, this distribution is assumed to be Gaussian in any given direction, and the width of this Gaussian is called the *mosaicity*.

- **Monochromator/Analyzer:** The white beam exiting a guide consists of a wide distribution of wavelengths (possibly with a low wavelength cutoff due to the guide), but in most instruments a monochromatic beam of neutrons is needed. This is achieved by placing a crystal - a *monochromator* - just after the guide and adjusting the rotation of that crystal and the placement of the sample table so that the setup fulfills the scattering condition for the wavelength desired. The same principle is used when one wants to single out a specific reflected energy from the sample. Allowing the reflected neutron to hit a rotatable crystal - an *analyzer* - and adjust the detector position to measure the chosen energy. Usually, crystals with a finite mosaicity are used, which allows for a wavelength distribution satisfying the scattering condition, thus increasing the flux at the sample and decreasing the resolution.

- **Divergence:** The geometry of any instrument accepts an finite angular distribution of neutrons. The extent of this angular distribution (FWHM) is called the beam divergence.

- **Collimator:** In many cases it is desirable to be able to control the beam divergence in order to be able to control the resolution function and minimize the background. To this end *collimators* are used, of which there are two mainly used types: 1) A series of apertures made from neutron absorbing material separated by some distance collimates the beam traveling in them as they set a natural limit of the divergence. Circular apertures give an isotropic divergence. 2) A series of neutron absorbing plates placed parallel to the beam and separated by some distance, collimates the beam only in the direction perpendicular to the plates. This is desirable in cases where an open geometry is accepted in some direction due to the need for high neutron flux.

- **Resolution function:** The geometry of a spectrometer is always more or less open in the sense that the spectrometer accepts distributions of wave vectors to reach both the sample and the detector. The monochromator is designed to reflect a narrow but finite distribution of neutron wavelengths onto the sample, and the aperture/collimator systems before and after the sample are designed to allow for a finite beam divergence. So even when scattering off a perfect crystal, moving the instrument just a little away from the scattering condition will still result in scattering reaching the detector because of the finite resolution. The function describing this resolution is called the *resolution function*, and is three-dimensional for elastic scattering and four-dimensional for inelastic scattering. The three parameters for elastic scattering are the width of the distribution of wave vector lengths and the two divergences. The three distributions are generally assumed to be Gaussian. In reciprocal space the resolution function is an ellipsoid through which one moves the reciprocal lattice vector to reach the scattering condition. In most cases the calculation of the resolution ellipsoid is quite complex and requires detailed knowledge of the geometry of the spectrometer.

- **Filters:** When using a monochromator, the Bragg's law for any given wavelength may also be fulfilled for neutrons with half that wavelength if present in the white beam. These second order neutrons will pass through to the detector causing erroneous measurements as two

different scattering conditions can be fulfilled at the same time. To avoid this, one can put in energy filters to choose one of these well separated narrow bands of energy to be used in the spectrometer. For instance, polycrystalline *Be* only transmits neutrons with a wavelength above 3.9 Å with a very sharp transmission curve. When working with 4 Å neutrons, one can remove 2 Å neutrons by using a *Be* filter.

- **Monitor:** When measuring and comparing data, it is necessary to know how many neutrons are actually hitting the sample for any given setup of the instrument so that one can normalize the final detector count. As the source output can and will vary from time to time it is necessary to have a detector that transmits almost all neutrons but detects a small fraction of them. This is called a *monitor*, and putting one before the sample allows one to electronically start and stop collecting neutrons when a certain amount of neutrons has been detected by the monitor.

3.3.3 Two-axis diffractometers - TriCS

In a single crystal there is an almost infinite number of different stacks of scattering planes to scatter from; one for each reciprocal lattice vector. From a few peaks one can gain a lot of information about a system, the lattice parameters, some information about the symmetries of the system as well as the rough orientation of the spins. However, when one wants to create and test a model of the system as a whole - exact atomic positions, Debye-Waller factors, exact spin configuration and moment size, one needs as much information on the system as possible. This is gained by collecting the diffracted intensity from as many crystal planes as possible. Any model can then be tested and refined using hundreds of reflections, until the model fits the data. The reflections can be collected using a single crystal neutron diffractometer such as TriCS at the PSI, see figure 9.

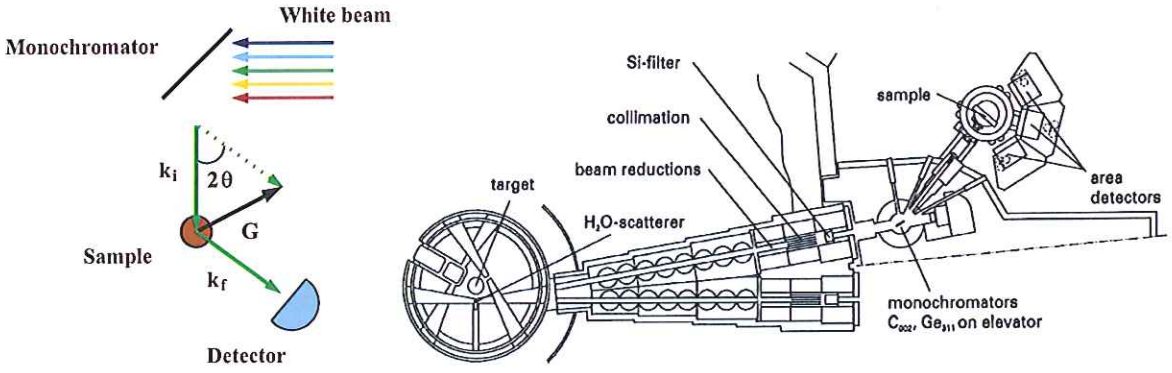

(a) The principle of a neutron diffractometer.

(b) TriCS @ PSI

Figure 9: (a) Layout of the principle of neutron diffractometry. (b) The TriCS spectrometer at the PSI. There are two different monochromators and possibility of using a 2D detector array.

Knowing the unit cell parameters, a few representative peaks are used to create a rough computer model that connects the reciprocal lattice points to the geometry of the instrument. This called a *UB-matrix*, and it allows for an automatic collection of all the reflections reachable by the instrument. TriCS uses thermal neutrons (coming from a source with $T = 300K$ with a wavelength of 1 Å, and has a quite wide geometry. This causes the instrument to have a broad resolution function, which is desirable since one will still get a credible reflection intensity measurement if the UB-matrix is a little off (which it always is). Since the sample has a finite mosaicity, in principle one should scan a whole volume around the reciprocal lattice vector to obtain a correct measure of the intensity. However, in practical experiments one has an open geometry vertically usually

catching the full τ-distribution in that direction. TriCS has a relaxed resolution in 2θ for small τ where one performs only a scan of the sample rotation θ through the reflection to collect all the intensity. For large τ one performs a $\theta - 2\theta$-scan. TriCS also has the possibility of using a 2D-detector and of tilting the position of the 1D-detector. Without an analyzer, TriCS accepts all energies reaching the detector from the sample and sample-holder. Furthermore, since TriCS is designed to measure the integrated intensity of many elastic reflections, the detector shielding does not have top-priority as usually one can model the background and still get a good measure of the integrated intensity. Therefore, the background of diffractometers is rather high.

3.3.4 Cold triple-axis spectrometers - FLEX and RITA-II

A triple axis spectrometer is a bit more complicated; it uses an analyzer after the sample (see figure 10 a)) so that the path between the sample and analyzer and the path between the analyzer and detector satisfies Bragg's law for a given wavelength. In doing this, one can measure a length difference between the neutron wave vector incident on the sample and the wave vector leaving the sample - inelastic scattering. One can actually measure the wave vector (q_m) and energy (ΔE_m) of the propagating spin waves as the neutron creates and annihilates collective excited states within the sample.

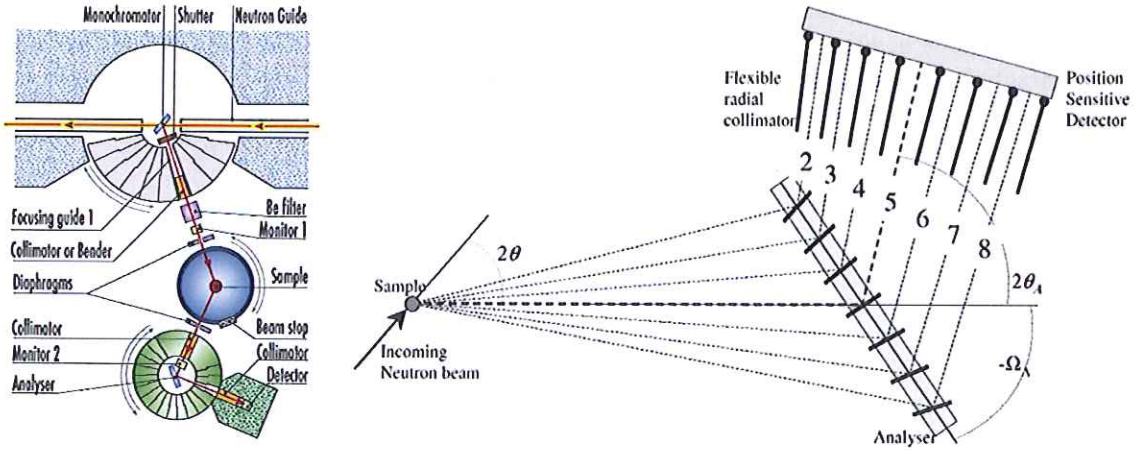

(a) IN14 @ ILL

(b) Analyzer of RITA-II

Figure 10: (a) Layout of a conventional neutron triple-axis spectrometer (IN14 at ILL). (b) The unique analyzer setup of the RITA-II spectrometer at the PSI. A 2D-detector is also called a position sensitive detector. Ω_A denotes the collective rotation of all 7 analyzer blades and $2\theta_A$ denotes the scattering angle of the middle blade.

There is a possibility of the sample having several different branches (in $(\tau_m, \Delta E_m)$-space) of spin excitations close to each other. Furthermore, it is desirable to be able to measure low energy excitations, which means that the elastic signal should not stretch too far into the energy transfer regime due to the resolution function. Therefore, *cold neutrons* are used. The neutrons come from a cold moderator $T = 35\ K$, which means that the Maxwellian flux distribution as a function of neutron wavelengths is narrower and higher. This makes it possible to have a narrow distribution of wavelengths coming from the monochromator while maintaining a reasonable flux. Therefore, the resolution of cold spectrometers is better than for thermal diffractometers. The FLEX spectrometer, which in this thesis is used for diffraction at 17.3 T, is a conventional triple-axis spectrometer principally built as outlined in figure 10 a).

The RITA-II spectrometer is unconventional; hence the name: Re-Invented Triple Axis spectrometer. The neutrons scattering off spin waves scatter in all directions with different energy transfers. Therefore, the RITA-II uses seven rectangular tall analyzers, individually and collectively rotatable, and a 2D-detector array, to be able to scan the energy transfers of seven different wave vector transfers at the same time with a high resolution (see figure 10). The inelastic scattering cross sections are several orders of magnitude smaller than the elastic cross sections, causing the signal to be very weak. In order to be able to measure anything, a low background always has top-priority when building triple-axis spectrometers. The RITA-II spectrometer is excellent in this respect; the whole analyzer-detector setup is placed in a large shielded box. The background from the target station reaching the detector is as low as 0.2 counts pr. minute.

Most of the elastic scattering experiments presented in this thesis were performed at the RITA-II triple axis spectrometer. This is for two reasons: 1) The RITA-II spectrometer has a 15 T cryomagnet option, allowing one to probe the phase diagram at such fields. Furthermore, as magnetic cross sections scales with the square of the moment, an eventual field induced magnetic signal is much easier to discover at 15 T than at 5 T for instance. 2) Small details of the magnetic structure are difficult to discover if the background is high, since the small magnetic signal simply drowns in the noise. Using the analysis presented in 2.2, one can gain a lot of information by looking at a few key reflections, and the setup provided by RITA-II allows for detection of quite small signals originating from quite large physical effects.

3.3.5 Small angle neutron scattering - SANS-II

Diffractometers and triple-axis spectrometers are designed to probe structural and magnetic ordering on the scale of inter atomic distances. Ordering in a much larger scale of course occurs in nature, and in order to probe correlations between points 600-2000 *nm* apart, *small angle neutron scattering (SANS)* can be used. In order to measure correlations on such a long length scale, the momentum-transfer vector $\boldsymbol{\tau}$ must be very short, compared to that of aforementioned spectrometers. This can be ensured by designing the instrument to measure very small scattering angles, hence the term small angle neutron scattering. To do this with a decent precision, the neutron needs to be very well collimated ensuring a low divergence. Therefore, SANS instruments have very long collimation sections between the beam port and the sample (see figure 11 a). To maximize the $|\boldsymbol{\tau}|$-range of the instrument, a 2D-detector detects the signal at a specified distance from the sample (typically between 1 m and the collimation distance). Thus, SANS-instruments are very long (10-60 m) and very simple. Since the requirement for collimated neutrons is so crucial, it is preferable to widen the incoming wave vector distribution. Furthermore, it is an advantage to have more control of the average wavelength for flexibility reasons. This is done elegantly by the *velocity selector*, which is a rotating cylinder with separated neutron absorbing blades being tilted vertically (see figure 11 b). In order for a neutron to pass through the cylinder, the time-interval for the neutrons to travel the path length s needs to match the time it takes for one channel between two blades to pass the point of entry. The equations determining the mean wavelength and the relative FWHM of the wavelength distribution are the following:

$$\begin{aligned} \lambda_0 &= \frac{h}{m_n R\omega}\tan(\alpha) \\ \frac{\Delta\lambda}{\lambda_0} &= \frac{d}{s\tan(\alpha)}. \end{aligned} \tag{3.76}$$

It is easily seen that tuning the tilt and angular velocity of the cylinder, one can adjust the mean and relative width of the wavelength distribution. All of the SANS experiments analyzed in this thesis are from the SANS-II instrument developed at Risø and positioned at the PSI. It has a 6 m long collimation section, with a possible aperture inset for every 1 m. The detector-tank is 6 m long, and the 2D-detector has 128 × 128 pixels of size 4.345 mm.

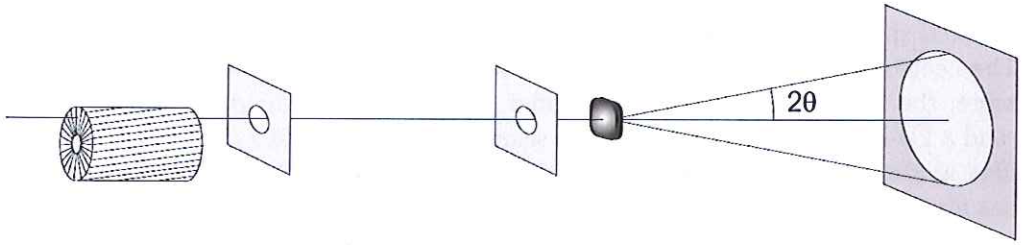

(a) Layout of a SANS-machine

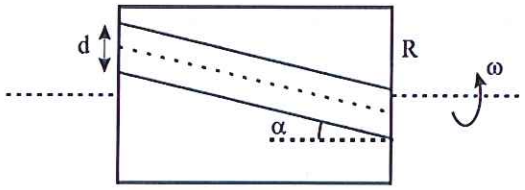

(b) Principle behind a velocity-selector

Figure 11: (a) The general layout of a small angle neutron scattering instrument. (b) A velocity selector cylinder with dimension $d \times R$ rotating with angular velocity ω. The blades are separated by a distance d, and tilted an angle α away from horizontal. Pictures from [23].

3.3.6 Magnetic form factor

In order to use magnetic intensity measurements they need to be corrected for effect due to the magnetic form factor. For the ions in the iron group, these are monotonic curves with a maximum at $\tau = 0$. The shape of the curve can be calculated from the radial distribution of the unpaired electrons in a given shell. An approximate description is given by the following function (taken from [24]):

$$f(s) = Ae^{-as^2} + Be^{-bs^2} + Ce^{-cs^2} + D, \tag{3.77}$$

where a, b and c are parameters to be looked up in [24], and $s = \sin(\theta)/\lambda$. The possible values of the form factors in a typical TriCS experiment ($\lambda = 1.18$ Å) for the four iron group ions relevant in this thesis are given in figure 12 as a function of θ.

3.3.7 Lorentz factor

As previously mentioned, when measuring the integrated intensity, it is necessary to rotate the crystal through the scattering condition. This scan is called a *rocking curve*. This will measure the mocaicity of the crystal; if the mosaicity is smaller than the width of the resolution function (as is often the case in neutron scattering), one will obtain a nice Gaussian representing a convolution of the resolution function with the angular distribution of reciprocal lattice vectors in the crystal in the direction of rotation. However, there is a systematic effect that needs to be accounted for when measuring rocking curves. Inserting the sum of reciprocal lattice delta functions (equation 3.70) in the elastic nuclear scattering cross section gives

$$\left(\frac{d\sigma}{d\Omega}\right)_{nuc} = N\frac{(2\pi)^3}{V_0}\sum_{\mathbf{G}}\delta(\boldsymbol{\tau} - \mathbf{G})|F_N(\boldsymbol{\tau})|^2. \tag{3.78}$$

In doing elastic scattering on the spectrometers described above, one has a fixed incident wave vector with a well defined wavelength hitting the sample fixed in space. Let ω be the angle between

4 Field- and temperature-induced magnetic phase transitions in $LiNiPO_4$

Due to competing antiferromagnetic exchange interactions combined with an XY-type single ion anisotropy, $LiNiPO_4$ exhibits a very rich phase diagram with both spontaneous and field induced incommensurate (IC) order. The phase diagram for $\mu_0 H < 14.7\ T$ was mapped out using neutron scattering by T. B. S. Jensen *et. al.* [4], where both the zero field IC and the high field IC structures were suggested to be the same linearly polarized structure due to lack of evidence to the contrary. Using the exchange interactions derived from inelastic neutron scattering experiments [25], Jens Jensen from the University of Copenhagen predicted that the IC structure at high fields and low temperature cannot be linearly polarized but should rather be a spiral. This part of the thesis describes the experimental confirmation of this prediction and it is shown that the phase diagram consists of three different IC phases for fields below 17.3 tesla - a high temperature linearly polarized phase, a low-temperature and high field spiral phase as well as a pseudo-commensurate phase at low temperatures and magnetic fields larger than 16 tesla.

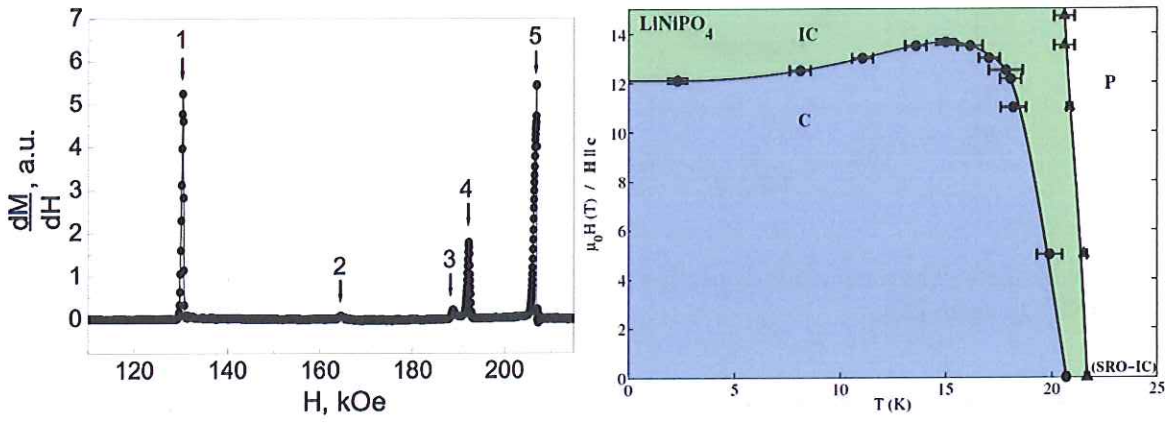

Figure 13: *Left:* Phase transitions in $LiNiPO_4$ measured by pulsed magnetization. The large peak at 120 kOe shows the increase in magnetization due to the C-IC transition. A minor peak is evident at 160 kOe. *Right:* The phase diagram of $LiNiPO_4$ up to 14.7 T as determined by T. B. S. Jensen *et. al.* [4]

$LiNiPO_4$ exhibits spontaneous long range IC magnetic order [26] with general ordering vector $\tau_{ic} = (0, q_{IC}, 0)$ at $T_{NC} < T < T_N = 21.7$ K - where T_{NC} and T_N is the commensurate and incommensurate ordering temperature, respectively - and short range correlations in the temperature range $T_N < T < 40$ K. The low temperature commensurate (C) canted AFM order undergoes a field induced first order C-IC transition at magnetic fields 12 T $< \mu_0 H <$ 13 T depending on temperature [4]. Figure 13 (left) shows pulsed magnetization measurements performed by V. M. Khrustalyov *et. al.* [27] at low temperatures. The aforementioned field induced phase transition is clearly visible as a large peak in the differential magnetic susceptibility ($\frac{dM}{dH}$). The next transition at 2 K occurs at $\mu_0 H \approx 16$ T and has a much smaller peak than the C-IC transition.

J_b	J_c	J_{ab}	J_{ac}	J_{bc}	D_a	D_b
0.670(9)	-0.05(6)	0.30(6)	-0.11(3)	1.04(6)	0.339(2)	1.82(3)

Table 6: The exchange interactions and single ion anisotropies as given in [25]. All units are in meV

Figure 14 (left) shows the anomalous dispersion measured in [25]. Two shallow minima are evident at non-integer K, suggesting competing interactions. A model for the exchange interactions was established by T. B. S. Jensen in [25], based on and successfully describing the spin wave excitations of $LiNiPO_4$. Figure 14 (right) depicts the relevant interactions shown in the magnetic pseudo face centered orthorhombic unit cell (which is just the crystallographic unit cell shifted by $(-0.25, -0.25, 0)$). The strength of the interactions as well as the single ion anisotropies are given in table 6. As evident in figure 14, the two strongest exchange-interactions J_{bc} and J_b are antiferromagnetic, of comparable strength and cannot both be satisfied. This is the reason for the spontaneous IC order in this system.

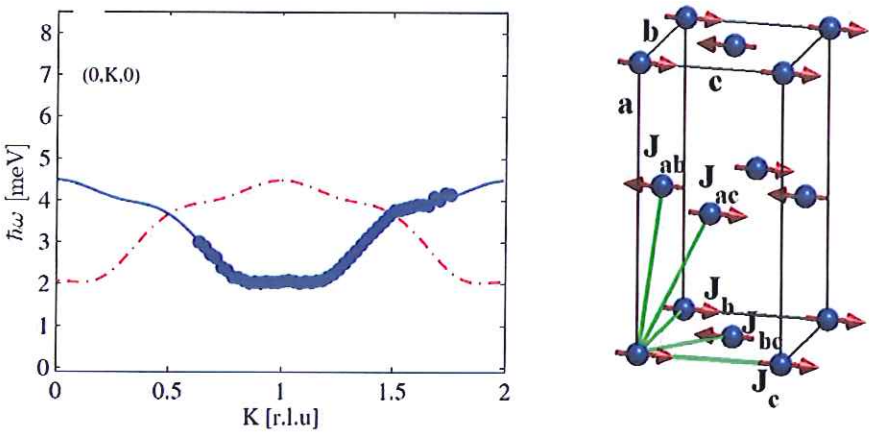

Figure 14: *Left:* The anomalous dispersion as measured in [25] *Right:* The five exchange interactions in $LiNiPO_4$, from [25].

The main reason that the low temperature IC structure should be a spiral in $LiNiPO_4$ is the relatively weak anisotropy along the a direction compared to the anisotropy along b. The thermal mean values of the spins $\langle \mathbf{S} \rangle$ are large at low temperatures. Shortening the spin lengths costs an exchange energy that exceeds the cost of slightly changing the spin angle in the easy ac-plane, as long as this angular change is small (meaning a spiral with large modulation along k). This is not the case at higher temperatures where the spin lengths are much smaller. Close to T_N it is energetically favorable to modulate the spin length (with a small length change between unit cells as the lengths are already small), instead of the angle resulting in the linearly polarized spin structure depicted in figure 15 (right)

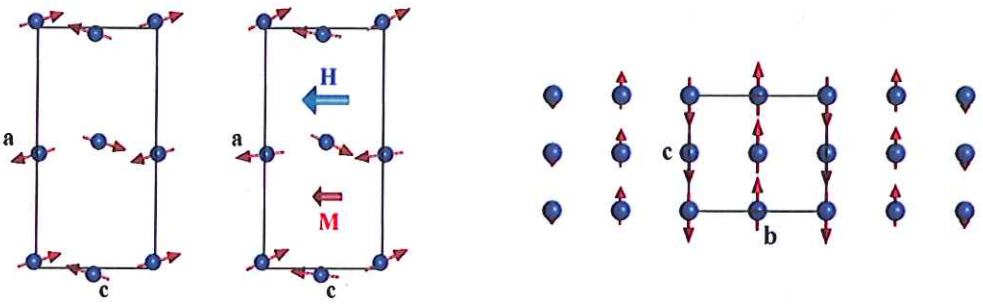

Figure 15: *Left:* Spin canting in zero field and in applied field along c [4]. *Right:* The linearly polarized IC spin structure proposed in [4]. Pictures from [15].

$LiNiPO_4$ also exhibits a zero field spin canting. Using the analysis presented in section 2.2, Jensen suggested that this canting is caused by the Dzyalyshinsky-Moriya (DM) mechanism, and developed a model for the ME effect using the established Hamiltonian [4]:

$$\mathcal{H} = \frac{1}{2}\sum_{ij} J(ij)\mathbf{S}_i \cdot \mathbf{S}_j + \mathcal{H}_{\mathrm{DM}} + \sum_{\alpha,i} D_\alpha S_{\alpha i}^2, \tag{4.1}$$

where the DM Hamiltonian is given by

$$\mathcal{H}_{\mathrm{DM}} = D_{14} \sum_{ij\in \mathrm{n.n.}} \left[S_z(1i)S_x(4j) - S_x(1i)S_z(4j) + S_z(3i)S_x(2j) - S_x(3i)S_z(2j)\right], \tag{4.2}$$

where the ion numbering is given in equation 2.65. The sum over i and j are over nearest neighbors only. In principle the same spin canting can be caused by a similar coupling between ions $1-2$ and $3-4$; the two cannot be distinguished by the present experiments. The strength of the proposed DM interaction *cannot* be determined from the spin wave analysis, but from the canting angle. It has a strength as large as $0.3meV$ which is very large for a second order interaction (it is actually comparable to the exchange energies).

The irreducible basis vectors in case of a propagation vectors $\mathbf{k}_{\mathrm{ic}} = (0, k_{\mathrm{ic}}, 0)$, are different from in the commensurate case. There is an additional phase factor of $\beta = e^{i\pi k_{\mathrm{ic}}}$ due to the modulation of the moments and the basis vectors are as follows: $A_\alpha = (+,-,-\beta,+\beta)$, $G_\alpha = (+,-,+\beta,-\beta)$, $C_\alpha = (+,+,-\beta,-\beta)$ and $F_\alpha = (+,+,+\beta,+\beta)$. There are only four irreducible representations in the incommensurate case [15]

$$\begin{array}{ll} \Gamma_1: \{A_x, G_y, C_z\} & \Gamma_2: \{G_x, A_y, F_z\} \\ \Gamma_3: \{C_x, F_y, A_z\} & \Gamma_4: \{F_x, C_y, G_z\}. \end{array} \tag{4.3}$$

Evidence for a C_z and an A_x component was found [15, 4], both in the zero field high temperature IC structure and in the high field low temperature IC structure. The proposed linearly polarized structure is a canted IC structure modulated along b. The modulation itself was found to vary heavily on both field and temperature. This indicates that the modulation is a central adjustable parameter for the system to lower its energy upon changing both temperature and field.

4.1 Experimental setup - RITAII

In the RITA-II experiment a $5 \times 5 \times 9$ mm single crystal was used. Both elastic and inelastic neutron scattering experiments were performed on the RITA-II triple-axis spectrometer at the Paul Scherrer Institute (SINQ, PSI) with the crystal oriented on an aluminum sample holder with the c axis vertical in a 14.9 T Oxford cryomagnet. No collimation was used. The diffraction studies were performed with 4.04 Å (5 meV) neutrons using only the central blade of the analyzer.

4.2 Evidence of a low temperature spiral and a second order transition to a linearly polarized structure

The previously determined high-field IC structure with ordering wave vector $(0, k_{\mathrm{ic}}, 0)$ had basically C_z symmetry with a small A_x canting plus small commensurate F_z and G_x components induced by the field.[4, 15] In order to check for spiral components, the temperature dependence of three magnetic IC peaks $(0, 1+k_{\mathrm{ic}}, 0)$, $(1, k_{\mathrm{ic}}, 0)$ and $(1, 2+k_{\mathrm{ic}}, 0)$ at 14.7 T was measured.

As shown in Fig. 16 a), the extension of the neutron diffraction experiments has now shown that there is intensity in the $(1, k_{\mathrm{ic}}, 0)$ reflection. This reflection derives mainly from an A_y or an A_z component according to table 7. The intensity disappears below and not at $T_N \approx 20.8$ K indicating the presence of a second magnetic phase transition at 17.7 K. Referring to Eq. (4.3) it is seen that the

	F_C^2	F_A^2	F_G^2	F_F^2	P_x^2	P_y^2	P_z^2
$(0, 1+k_{\rm ic}, 0)$	16	0	0	0	1	0	1
$(1, k_{\rm ic}, 0)$	0	15.6	0.4	0	0.09	0.91	1
$(1, 2+k_{\rm ic}, 0)$	0	15.6	0.4	0	0.93	0.07	1

Table 7: Squared structure (F) and polarization (P) factors for the three IC peaks used to establish the spiral structure in terms of the irreducible representations. The structure factors are normalized to unit spin lengths of the spin components. $k_{\rm ic} = 0.18$ rlu have been used, but note that small changes of $k_{\rm ic}$ have no effect on our conclusions.

order parameter between 17.7 K and T_N belongs to the irreducible Γ_1 representation, whereas the new order parameter appearing below 17.7 K has the symmetry of the Γ_2 or the Γ_3 representation depending on whether the $(1, k_{\rm ic}, 0)$ peak is due to an A_y or an A_z component, repectively. In order to check this, the temperature dependence of the strong peak intensity at $(0, 1+k_{\rm ic}, 0)$ is depicted in Fig. 16 c). Table 7 shows that the two components C_z and C_x are weighted equally and are the only ones appearing in this scan. The abrupt increase shown by the $(0, 1+k_{\rm ic}, 0)$ peak intensity at 17.7 K for decreasing temperatures allows a clear choice between the two possibilities for the new order parameter. A Γ_3 order parameter, which contains a C_x component, contributes directly to the $(0, 1+k_{\rm ic}, 0)$ peak, whereas the possibility of a Γ_2 order parameter can be dismissed since it has no effect on this scan. The behavior of the $(1, 2+k_{\rm ic}, 0)$ intensity as a function of temperature shown in Fig. 16 b) and c) is consistent with this result. This peak intensity reflects the A_x and A_z components, and for increasing temperatures it shows a rapid drop at 17.7 K indicating a vanishing A_z component. The intensity, which remains above 17.7 K, is due to the A_x component being non-zero up to T_N. Table 7 shows that both the $(1, k_{\rm ic}, 0)$ and the $(1, 2+k_{\rm ic}, 0)$ peak may contain contributions from the possible G components. However, since none of the peaks which are dominated by the G components have been seen, they may safely be neglected here, where their contributions are weighted with an intensity factor of 1/40 compared with the A components.

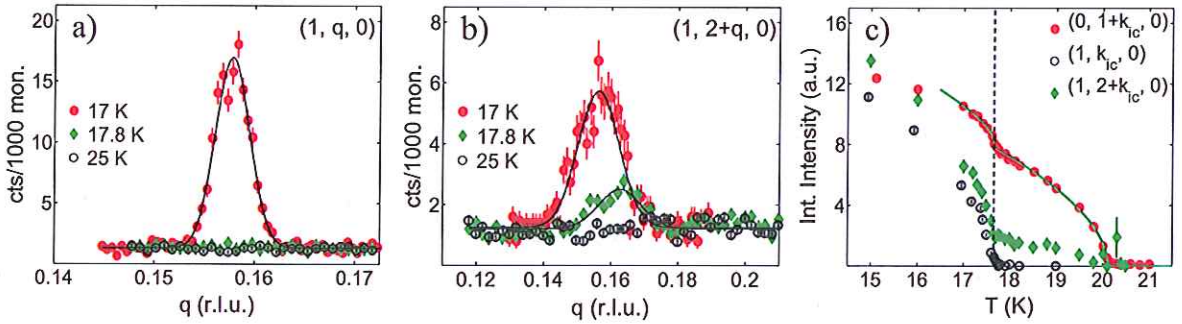

Figure 16: a)-b) Neutron-diffraction scans through the $(1, k_{\rm ic}, 0)$ and the $(1, 2+k_{\rm ic}, 0)$ peaks at 14.7 T applied along the c axis at temperatures close to the transition temperature at 17.7 K. The two peaks reflect, respectively, the A_z (neglecting A_y as discussed in the text) and the weighted sum of the A_z and A_x components of the spiral structure. The A_z component disappears above 17.7 K while the A_x component persists. c) Integrated intensities of $(0, 1+k_{\rm ic}, 0)$, $(1, k_{\rm ic}, 0)$ and $(1, 2+k_{\rm ic}, 0)$ as functions of temperature at 14.7 T applied along the c axis. The integrated intensity from the $(1, k_{\rm ic}, 0)$ and the $(1, 2+k_{\rm ic}, 0)$ peaks have been multiplied by a factor of 140 and 170, respectively. The onset of an additional order parameter below 17.7 K is evident.

In the present case the system may approach a circular polarization of the moments by either combining the C_z component with a C_x or with a C_y component. The unique identification above, that the new order parameter below 17.7 K belongs to the Γ_3 representation, shows that the

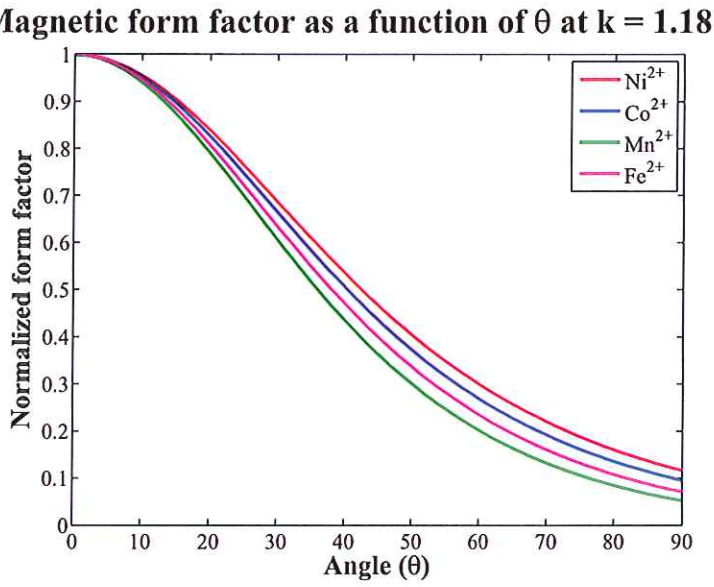

Figure 12: Calculated magnetic form factors for the four magnetic ions Ni^{2+}, Co^{2+}, Mn^{2+} and Fe^{2+}, using equation 3.77.

some reciprocal lattice vector (moving with the sample) and the incident wave vector. Then, defining the vector $\boldsymbol{\rho} = \mathbf{k} - \mathbf{G}$, $|\boldsymbol{\rho}| = \rho$, equation 3.78 can be integrated as ([17])

$$\sigma_{nuc} = N\frac{(2\pi)^3}{V_0}\frac{2}{\rho}|F_N(\mathbf{G})|^2\delta(G^2 - 2kG\cos\omega). \tag{3.79}$$

Assume that the reciprocal lattice vector is oriented horizontally and can be rotated about a vertical axis. This is actually a requirement for $\mathbf{G}$ to lie in the plane spanned by $\mathbf{k}_i$ and $\mathbf{k}_f$, which is called the *scattering plane*. Set the scattering angle 2θ to satisfy Bragg's law, thus only rotating the sample through the scattering condition without moving the detector. The counting rate for the reflection $\mathbf{G}$ as a function of omega can be expressed as follows:

$$\begin{aligned} R &= \Phi\int_0^{\pi}\sigma_{nuc}d\omega \\ &= \Phi N\frac{(2\pi)^3}{V_0}|F_N(\mathbf{G})|^2\int_0^{\pi}\frac{2}{\rho}\delta(G^2 - 2kG\cos\omega). \end{aligned} \tag{3.80}$$

The integration is done by substitution, putting $x = 2k\tau\cos\omega$, and due to the delta function putting $\rho = k$ and $\tau = 2k\cos\omega$ (the equivalent of the Laue condition)

$$R = \frac{V}{v_0^2}\Phi\frac{\lambda^3}{\sin\theta}|F_N(\mathbf{G})|^2, \tag{3.81}$$

where $V = Nv_0$ is the volume of the crystal (which is easy to obtain). Note the peculiar λ^3-dependency - the wavelength of the neutrons matters. Usually one compares two peaks, and in order to do this, the difference in scattering angle needs to be accounted for:

$$\frac{R_1}{R_2} = \frac{F_N(\mathbf{G}_1)|^2/\sin\theta_1}{F_N(\mathbf{G}_2)|^2/\sin\theta_2}. \tag{3.82}$$

The factor of $\sin\theta$ is usually called the *Lorentz factor*.

system chooses the first one of the two possibilities. This choice is consistent with the fact that the anisotropy parameters derived from the spin-wave analysis ([25]) identifies the ac plane to be the easy one. Experimentally, it is difficult to measure the C_y component directly but the analysis above, where the irreducible representations, or symmetry arguments, are utilized in the interpretation of the experiments indicates that Γ_4, and thereby the C_y component, is probably zero. Even though a non-zero C_y component cannot be directly disproved, it is not necessary to explain the data, and it makes little sense to have an additional cycloidal component given the single ion anisotropies.

In conclusion, $LiNiPO_4$ shows two continuous phase transitions at decreasing temperatures in the presence of a c-axis field larger than 13.5 T. The ordered state just below T_N is described by an IC order parameter belonging to the irreducible representation Γ_1, with the dominating component C_z being slightly mixed with A_x. At about 17.7 K there is a new second-order phase transition, where the additional order parameter belongs to the Γ_3 representation and may be described as being the C_x component slightly mixed with the A_z component. The diffraction experiments do not allow a determination of the phase difference between the two order parameters, but the only relevant possibility is that the phases of the two components differ by 90°, since an elliptical polarization minimizes the variation of the lengths of the ordered moments. Had the two C-type components been in phase, the structure would just be a rotation of the linear IC structure towards a harder direction, which must be energetically unfavorable. The phase boundary between the linearly and elliptically polarized IC phases has been determined up to a field of 17.3 T. The two IC structures are illustrated in Fig. 21 a) and c), and the observed phase boundaries are shown in the phase diagram in Fig. 26.

4.3 Experimental setup - FLEX

4.04 Å neutrons were used on the V2/FLEX spectrometer, with a PG monochromator and analyzer. A $2 \times 2 \times 3$mm single crystal was used. In order to conduct the experiment the sample had to be aligned within 0.5° in a small open aluminum cylinder with height of 4 mm and a diameter of 6 mm clamped between two dysprosium magnets.

4.3.1 Alignment problems

The relatively complicated setup of having a sample holder in which two dysprosium pieces are clamped around the sample using mechanical springs, and fitted into a rod of only 20 mm in diameter filling the entire sample space caused some problems. Although there was control over the A3 motor for the sample rotation (or ω), the position sometimes slipped in an unreproducible manner, producing usable but irregular peaks as shown in figure 17. What caused these errors in sample rotation remains unresolved. It could have been casual jamming of the sample stick causing the A3 motor being off. On FLEX, the A3 angle is not absolute and there is no encoder, so a failure to rotate would cause the UB matrix to be off. The best solution to this problem was to discard the UB matrix entirely, and align on each measured peak using an iterative 4-step scan/centering procedure. Starting with an omega scan centered on the peak position according to the UB-matrix and performing an A3-A4 scan, another A3 scan ending with an A3-A4 scan, driving to the peak center after each scan, one should be able to iteratively end up on the peak position, irrespective of any offset in A3. To obtain the incommensurate modulation, both symmetry connected peaks $\boldsymbol{\tau}_+ = (0, 1+q, 0)$ and $\boldsymbol{\tau}_- = (0, 1-q, 0)$ were used employing the formula

$$|\mathbf{k}_{\mathrm{ic}}| = \frac{|\boldsymbol{\tau}_+| - |\boldsymbol{\tau}_-|}{|\boldsymbol{\tau}_{020}|}. \tag{4.4}$$

This procedure improved the determination of the modulation, but the peak shapes were still irregular yielding non-negligible systematic errors. Some improvement was achieved by simply

fitting the last A3-A4 scan to a Gaussian, and removing any point more than 4 standard deviations away from the fitted curve, refitting the reduced data points and using the obtained peak center as a slightly better measure of the true 2θ value of the IC peak. The relatively modest but still desirable effect of doing this is shown in figure 17.

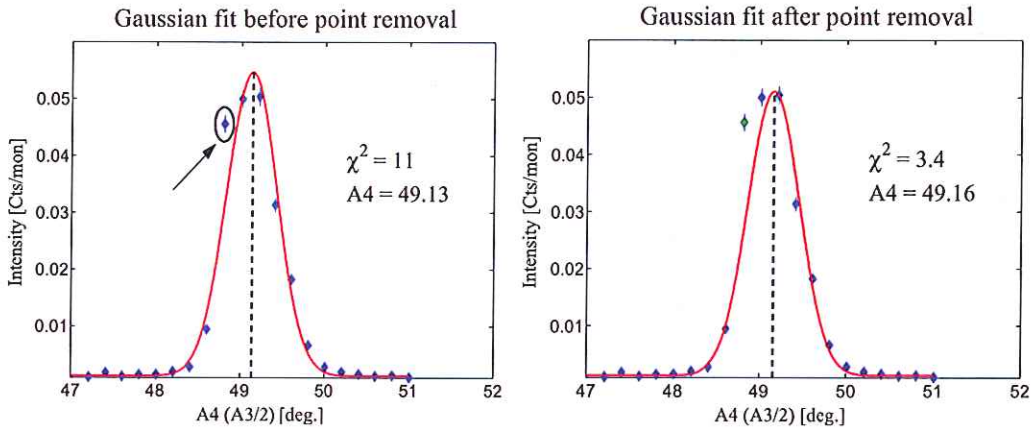

Figure 17: $\theta - 2\theta$ scan before and after removal of points lying more than 4σ way from initial fit. On this scan only the encircled point is affected, and green points are not used for fitting. There is a small shift in the determined peak center. It is important to emphasize that even though the uncertainty of the physical A4 position is probably larger than the shift presented above, assuming a statistical error in A4, the error in peak position of en entire scan will still be well below this shift.

These procedures really decrease the amount of data obtainable on a 7 day beam time, but it was still a small price to pay for doing neutron diffraction at 17.3 tesla, and determine the structure of the second field induced incommensurate phase.

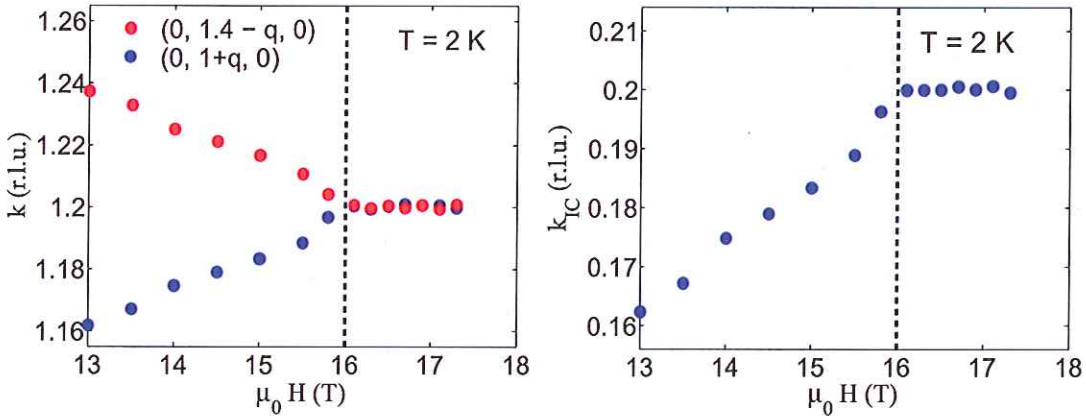

Figure 18: *Left:* $(0\ 1+q\ 0)$ and $(0\ 1-q\ 0)+(0\ 0.4\ 0)$ plotted together so a comparison between the symmetry connected peaks is possible. Similar behavior of the two peaks is clearly evident, which is as it should be. *Right:* k_{ic} as obtained from formula 4.4 as a function of applied field along c at 2 K. It is clear that the modulation stabilizes at $k_{ic} = 0.2$ for fields larger than 16 T.

4.4 Evidence of high field commensuration of the magnetic structure

Using the previously described method of obtaining the incommensurate modulation k_{ic}, the modulation was measured as a function of field at the base temperature 2 K. The results are shown in figure 18. The modulation increases linearly as a function of field up to $\mu_0 H = 16T$, where $|k_{ic}|$ stabilizes at 0.2 - corresponding to a quintupling of the crystallographic unit cell. Thus, increasing the field in the low temperature IC phase at base temperature tends to squeeze the spiral in real space up until attenuation at 16 tesla, where the spiral is a quasi-commensurate quintupling of the unit cell. To examine how stable this phase is upon increasing temperature, $|k_{ic}|$ was measured as a function of temperature at 17.3 tesla, which is shown in figure 19.

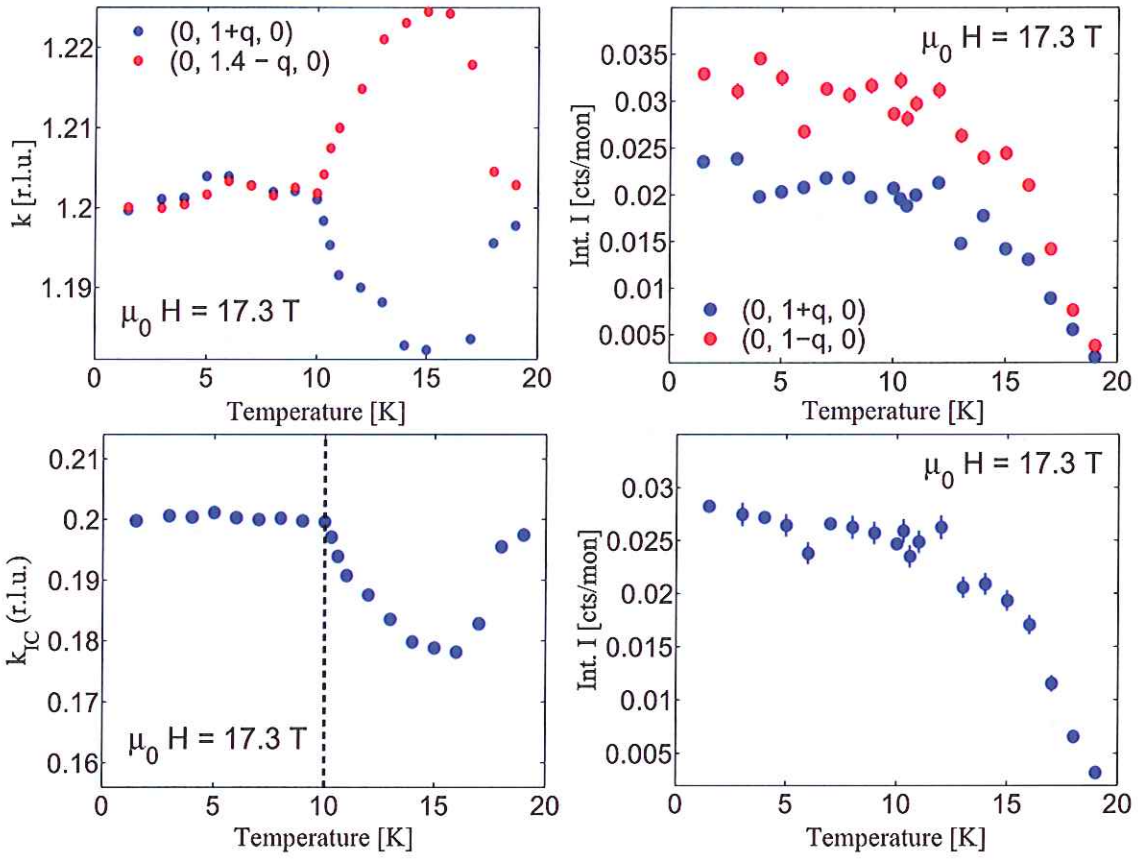

Figure 19: *Top left:* $(0\ 1+q\ 0)$ and $(0\ 1-q\ 0) + (0\ 0.4\ 0)$ plotted as a function of temperature at $\mu_0 H = 17.3T$. The position of the two symmetry connected peaks has substantial systematic variations but the sign and size of the shift from $Q = 0.2$ are comparable below 10 K. Thus the difference between τ_+ and τ_- has a stable value of 0.4 below 10 K. *Top right:* The integrated intensities of $(0\ 1-q\ 0)$ and $(0\ 1+q\ 0)$ as a function of temperature. They are both very irregular but still display the expected power law. *Bottom left:* $|k_{ic}|$ as a function of temperature at 17.3 T. The commensurate quintupling of the unit cell persists until incommensurability sets in at $T = 10\ K$. *Bottom right:* The average integrated intensity of the symmetry connected $(0\ 1+q\ 0)$ and $(0\ 1-q\ 0)$ peaks. A power law is evident within errors.

As evident in figure 19 (top left) the peak position has some systematic displacements from 0.2 as a function of temperature. However, the sign and size of the shifts are comparable for the two symmetry connected peaks, so the average modulation is 0.2 up to 10 K where k_{ic} starts to drop rapidly. At temperatures close to T_N, k_{ic} rises rapidly up to almost 0.2 before the system enters

the paramagnetic phase. Two more points on the phase boundary were measured at 5 and 8 K respectively, giving evidence of a phase boundary almost parallel to the $C \rightarrow IC$ boundary at lower fields (see figure 26). Both in figure 18 and 19 the error bars are smaller than the markers. Using the calculated error of the determined peak center position of the Gaussian fits made, the modulation values deviate more than their respective errors from 0.2. However, even without the systematic errors present in the presented data, any instrument will have some systematic errors when compared to the very small error of determined peak positions. Especially due to the systematic errors in this data set, it makes little sense to regard a determined modulation of 0.201 as significantly above 0.2. In spite of the insufficiency of the statistical errors, the author would anyway like to point out that the average of all the measured values of the modulation in the 1/5 phase shown in figure 19 (bottom left) and 18 (right) is $k_{ic-avg} = 0.19994 \pm 0.00009$, and that an actual quintupling of the unit cell is a solid interpretation.

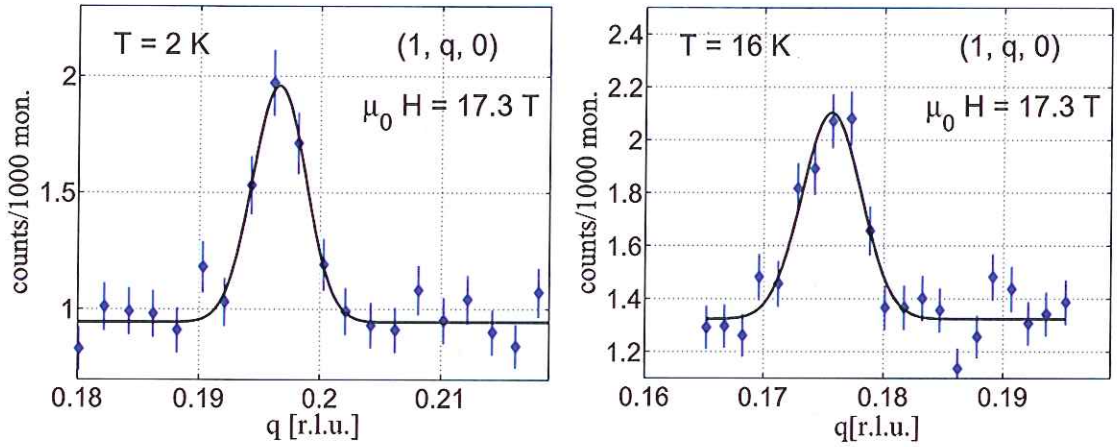

Figure 20: k-scans of the (1, k_{ic}, 0)-peak at $T = 2K$ (left) and $T = 16K$ (right). These scans were made before the alignment issue was resolved, so the intensities are not correct. The binary results that the peaks are there, of course, holds.

To firmly establish that the high field commensurate phase is indeed a spiral, the (1, k_{ic}, 0)-peak was measured at 2 K as well as above 10 K at $\mu_0 H = 17.3T$. Since the crystal used was 20 times smaller than the one used for the RITA-II experiment and with a considerable increase in background due to the amount of glue, the counting times were rather long. It was confirmed that the peak was observed at 2, 10 and 16 K. This was done before the alignment issue was resolved, so the intensities from the k-scans are faulty. It is confirmed however, that the high field commensurate structure is indeed a spiral.

In conclusion, the two high field neutron diffraction experiments at RITA-II and FLEX show that there are three distinct incommensurate magnetic phases below 17.3 tesla applied along c. At low temperatures the structure is a canted spiral rotating in the easy ac-plane and propagating along the b-direction. Upon increasing field one twists the spiral in real space. For magnetic fields above 16 tesla and for temperatures below 10 K, the canted spiral reaches a quasi-commensurate quintupling of the unit cell along b. At temperatures between $17.3-17.8$ K the canted spiral undergoes a second order transition to a linearly polarized canted IC structure. The phase boundary for this transition seems to follow the T_N phase boundary. The full phase diagram can be seen in figure 26.

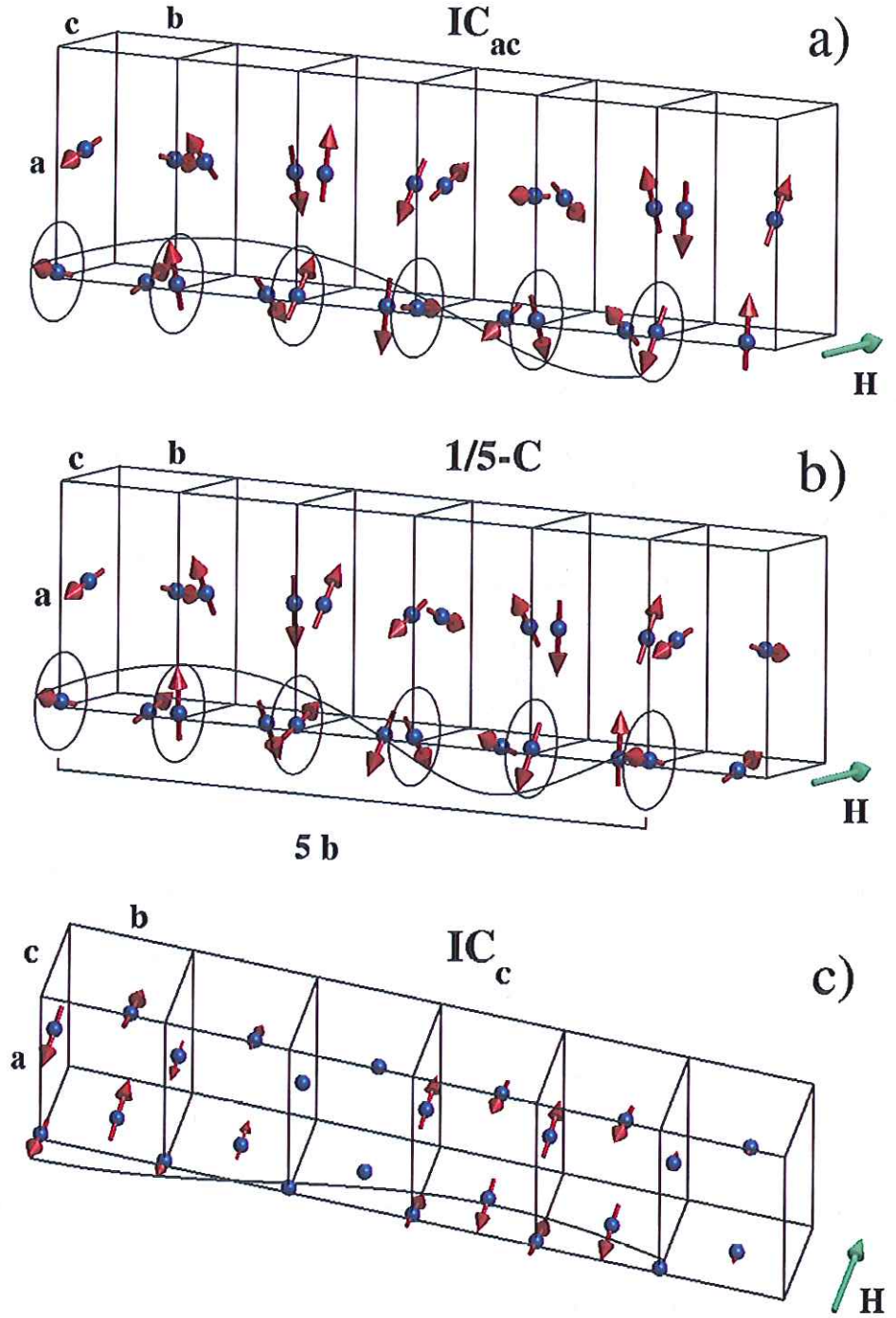

Figure 21: The three magnetic IC structures shown by stacking six unit cells along b. Only the four magnetic Ni^{2+} ions are shown in each unit cell. a) Magnetic IC spiral at 2 K and $\mu_0 H = 13$ T applied along c. The circles around the lower left ion marks the rotation plane of the spins and the black line marks the spiral itself. b) Lock-in commensurable spiral $\mu_0 H > 16$ T and $T < 10$ K. The 1/5 modulation is evident by comparing the 1st and the 6th unit cell. c) Linearly polarized IC structure; the line marks the sinusoidal modulation. In the phase diagram for fields along c, shown in Fig. 26, the three structures are denoted as IC_{ac}, 1/5-C and IC_c, respectively.

4.5 Magnetization measurements

Magnetization measurements were performed for fields applied along all three crystallographic directions. Jens Jensen from the University of Copenhagen has developed a mean field theory for $LiNiPO_4$ using the model established in [15, 25]. This enabled a straightforward comparison between theoretically and experimentally determined susceptibilities. Confirming the magnetic structural phase transition at 17.7 K from bulk magnetization data would also firmly establish the existence of the two IC phases. Unfortunately, the CFMS system at Risø is not able to go above 16 tesla, so the high field commensuration of the spiral could not be confirmed by magnetization measurements.

A CRYOGENIC cryogen free measurement system (CFMS) at Risø DTU was used to perform vibrating sample magnetization (VSM) measurements. The way the magnetization is measured is simply placing the sample in an external DC field and performing small vibrations parallel to the field. This vibration of magnetized material induces a current in two pickup coils which is proportional to the magnetization. Magnetic fields $0 \leq \mu_0 H \leq 16$ T were applied along all three principal axes for temperatures $2 < T < 300$ K. Susceptibilities are measured at $\mu_0 H = 1$ T, which lies within the linear regime of magnetization vs. field as evident in figure 23. There is evidence of a small amount of magnetic impurities when looking at the temperature-scans with an applied field of 1 and 16 tesla applied along b (see figure 22). At low temperatures, there seems to be a rather drastic increase of magnetization at 1 tesla which is not there at 16 tesla. This could be caused by the divergent susceptibility of impurities (most probably from unreacted nickel) at low temperatures, which is not there at 16 tesla. This is due to the fact that the impurity magnetization will have saturated at 16 tesla, and therefore, the fractional contribution is less (the magnetization in figure 22 is normalized to applied field).

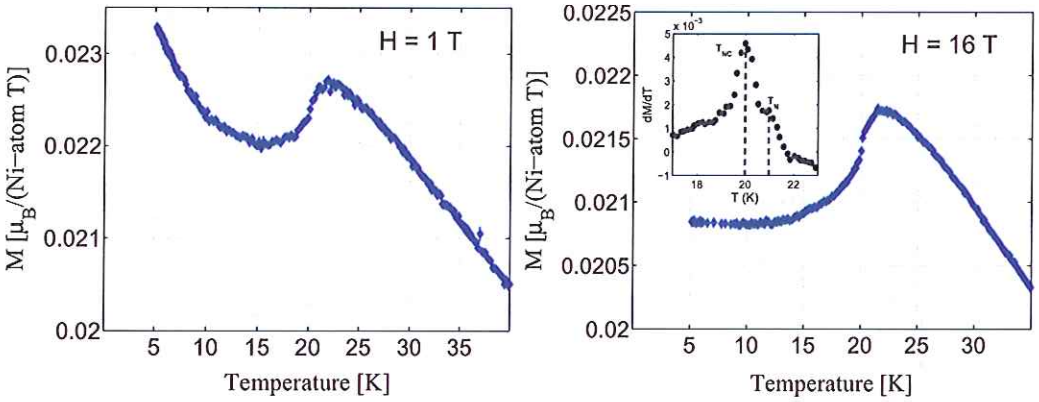

Figure 22: The magnetization in $\frac{\mu_B}{\text{Ni-atom}\cdot T}$ at 1 and 16 tesla applied along b. The Curie tail is evident at 1 tesla but not at 16 tesla.

Trying to level out the low field curves and comparing the susceptibilities with the results from [28], an impurity concentration of $c = 0.0035$ free nickel atoms pr. bound nickel atom was found to be a suitable value. Thus, from all the magnetization data a paramagnetic impurity magnetization from $S = 1$ and $g = 2.2$ free nickel ions had to be subtracted using the formula [8]:

$$\begin{aligned} M_{imp} &= cgS\left(\frac{2S+1}{2S}\coth\left(\alpha\frac{2S+1}{2S}\right) - \frac{1}{2S}\coth\left(\frac{1}{2S}\alpha\right)\right), \\ \text{where } \alpha &= \frac{g\mu_B S\mu_0 H}{k_B T}. \end{aligned} \tag{4.5}$$

This formula is directly applicable when using the unit μ_B/Ni-atom. Figure 23 (left) shows the

magnetization as a function of field at 5 K applied along all three crystallographic axes. A linear behavior at low fields is evident for all three axis, whereas in the full field range the magnetization increases a little more slowly. The critical field for the $C \rightarrow IC$ transition has been determined by performing field scans at constant temperature. A typical field scan at 13 K can bee seen in figure 23 (right). The differential magnetic susceptibility dM/dH is shown in the inset, and it is clear that a very precise peak determination can be done by eye. As the peak is not symmetric a Gaussian fit would not give a correct peak value, and it is the author's opinion that peak determination by eye is as free of systematic errors as any other reasonable method. The hysteresis loop at 5 K is shown in figure 23, and it is evident that a hysteresis of around 0.15 tesla is present at low temperatures. In this work, the $C \rightarrow IC$ phase boundary obtained from field scans is defined as the field of maximum differential magnetization upon increasing the field (as in [15] and [4]).

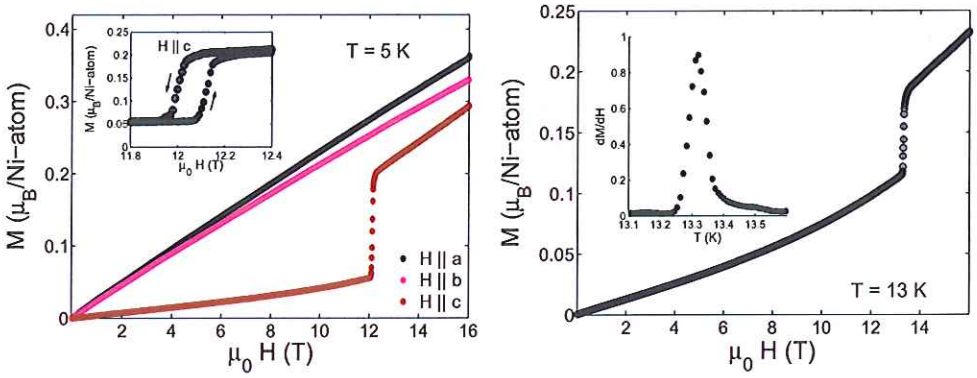

Figure 23: *Left:* Field scans at $T = 5\ K$ for all three crystallographic directions. The magnetization curves for fields applied along a and b are almost linear with a slightly decreasing susceptibility. For field along c the susceptibility is much lower than along the other two directions, and there is a clear jump at the $C \rightarrow IC$ transition. The inset shows the hysteresis loop. *Right:* A field scan at 13 K. The inset shows the differential magnetization allowing for a precise determination of the critical field.

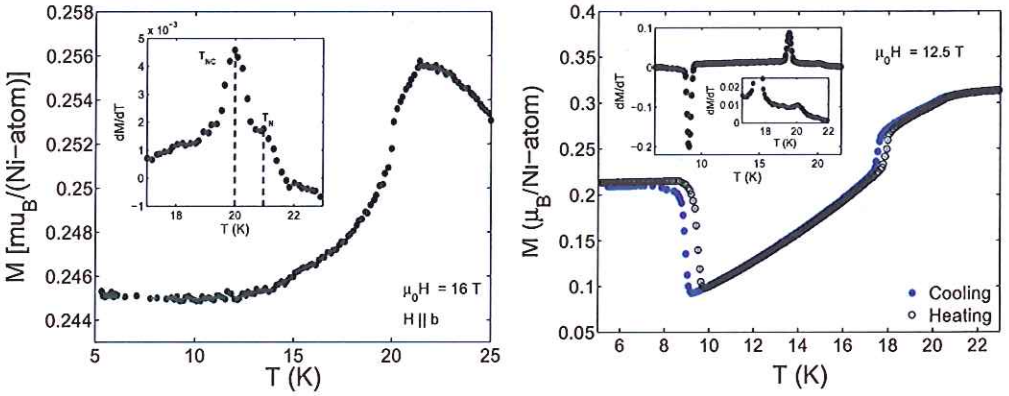

Figure 24: *Left:* Temperature scan at $\mu_0 H = 16\ T$ applied along b. T_N can be determined with low precision from the small peak in differential susceptibility preceding the larger peak that reflects T_{NC} *Right:* The temperature dependence of the magnetization at 12.5 T applied along the c axis. Two clear jumps in magnetization indicates the commensurate ordering temperature and the re-entrance into the IC phase upon cooling. The insets show the differential magnetization upon cooling with an additional focus on the kink at T_N.

For the sake of completeness, the phase diagram along b and c has been determined from magnetization measurements. Figure 24 (left) shows a typical temperature scan used to determine the two transition temperatures T_N and T_{NC}. The phase diagram is rather featureless and shown in figure 27. That the IC phase is much easier to magnetize along c is clearly evident in figure 24 (right), where the magnetization drops while cooling into the C phase after which is rises rapidly upon entering the IC phase again. This scan also directly confirms the dome-shaped $C \rightarrow IC$ phase boundary exhibited near $T = 10 - 15\ K$. The second order transition from a linearly polarized IC structure to a spiral rotating in the ac plane can also be seen in magnetization temperature scans if one knows where to look (as one does from neutron data). Figure 25 shows the magnetization as a function of temperature at 16 (left) and 14 tesla (right). At 16 tesla a kink is directly evident at 17.3 K, giving rise to a clear peak in the differential magnetization. Since the neutron data provide exact knowledge of the nature of the phase transition and the phase boundary, this kink is readily interpreted as a result of the decrease in magnetization along c due to the spins starting to be polarized along both a and c. At 14 tesla no kink is directly evident in the magnetization data. The differential magnetization, however, displays the same behavior as at 16 tesla, so the small peak at 17.5 K is interpreted as the phase boundary. This interpretation of the 14 T is doubtful though, and only reasonable in light of the neutron data and the 16 tesla kink.

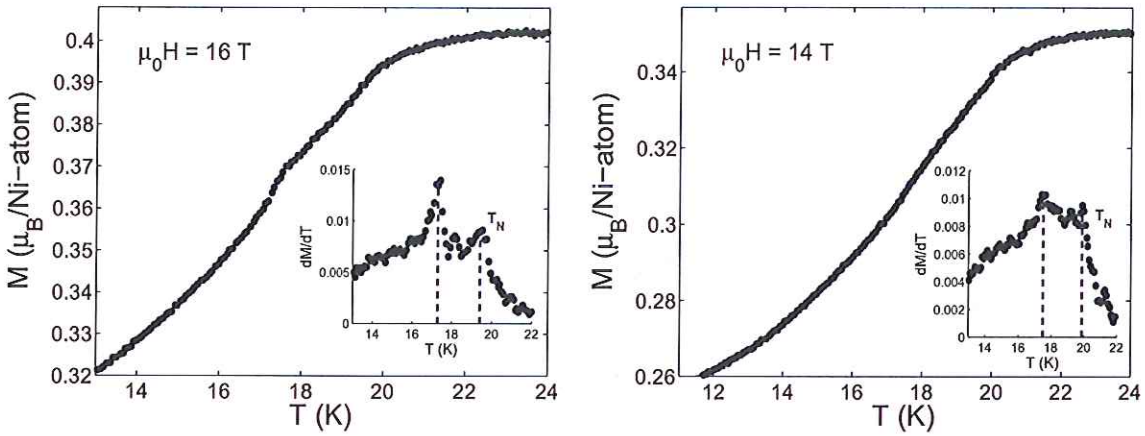

Figure 25: *Left:* Magnetization as a function of temperature at 16 tesla. A kink is clearly evident at 17.3 K. The inset shows the differential magnetization where a peak is very clear at 17.3 K *Right:* A temperature scan at 14 T. No kink is directly evident but the differential magnetization (inset) facilitates a determination of the phase boundary.

These magnetization data enable a very precise determination of the $C \rightarrow IC$ phase boundary, and in conjunction with the neutron data a very thorough phase diagram can be presented for the magnetic phase of $LiNiPO_4$ for up to 17.3 tesla applied along c.

4.6 $(\mu_0 H, T)$ phase diagrams of $LiNiPO_4$

The phase diagram for fields along c is shown in figure 26. The main features of the phase diagram were already determined in [4]. The dome-shaped $C \rightarrow IC$ phase boundary is clearly confirmed by magnetization measurements. The phase boundary between the spiral phase and the linearly polarized phase seems to be parallel to the incommensurate ordering phase boundary, which is clearly evident at higher fields. Furthermore, the phase boundary between the spiral and the 1/5 phase seems to be parallel to the $C \rightarrow IC$ phase boundary. As also indicated in the pulsed magnetization measurements performed in [27] the dome-shape should also hold for the 1/5 phase. The triple point between the two IC phases and the C phase shown in figure 26 has not been

confirmed by direct measurements. It is just a consequence of keeping the linear-spiral phase boundary parallel to the ordering phase boundary. Should the triple point be there, it could be interesting since the two phase transitions are of 1st ($C \rightarrow IC$) and 2nd order (linear-spiral). Figure 27 shows the featureless phase diagram as measured by applying field along b. The incommensurate and commensurate ordering temperatures are only slightly less at 16 T than at zero field. The phase diagram for fields applied along a is almost identical.

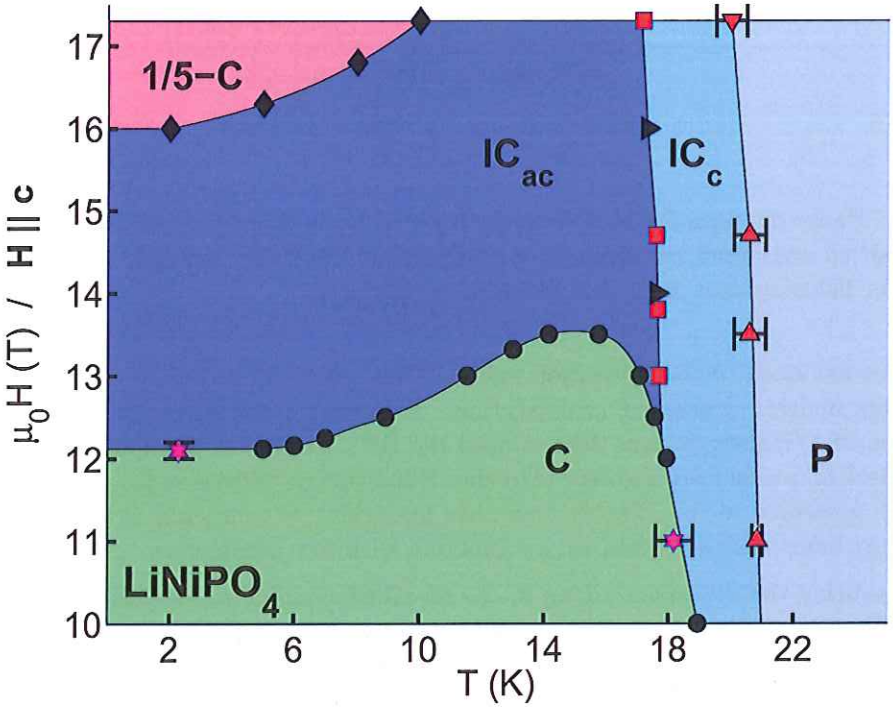

Figure 26: $(\mu_0 H, T)$ phase diagram of $LiNiPO_4$ for $\mu_0 H > 10$ T applied along the c axis. The black circles mark the C–IC phase boundary as found using magnetization data, supported by neutron diffraction data taken from [4] (stars). The diamonds mark the lock-in phase boundaries found using V2/FLEX data. The squares mark the boundary of the IC spiral phase found at RITA-II (below 15 T) and V2/FLEX (above 15 T), while the two right-pointing triangles indicate the phase boundary detected by VSM measurements. The linearly polarized IC ordering temperatures are taken from [4] (up-pointing triangles) supported by a measurement from V2/FLEX (down-pointing triangle). The errors on the VSM measurements are much smaller than the markers, while the error bars on the neutron-diffraction measurements are comparable to the marker size if not explicitly given. IC_c denotes the IC structure linearly polarized mainly along c, while IC_{ac} denotes the IC spiral in the ac-plane.

4.7 Spin excitations in the high field spiral phase

It should be emphasized that spin excitations have not been a major focus of this work. In $LiNiPO_4$, the zero field spin waves were thoroughly measured by Thomas B. S. Jensen. He proposed a model for the exchange interactions based on said spin waves, which is well described in [15] and published in [25]. That model is the basis for the Random Phase Approximation (RPA) calculations performed by Jens Jensen. Since no spin wave calculations have been done by the author, no theoretical emphasis has been given to this interesting subject. The RPA - described in [29] - aims to directly calculate the two point spin correlation functions in 3.55, assuming that the thermal mean value

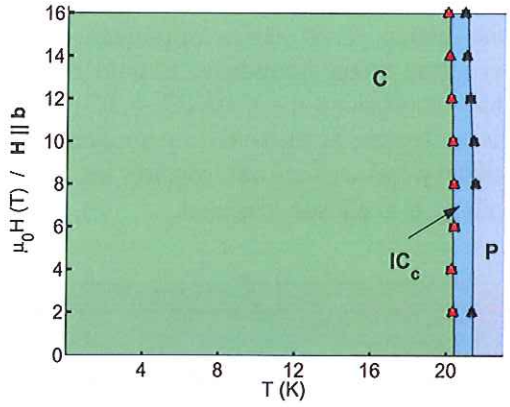

Figure 27: Phase diagram for $\mu_0 H||b$ as determined from magnetization measurements. The zero field transition temperatures seem to extent almost vertically upwards up to 16 T. The phase diagram for fields applied along a is identical within error.

of the spins are close to the saturation value. These correlation functions are directly coupled to the inelastic neutron scattering cross section. Assuming a spiral structure at 13.5 Tesla with a modulation of 1/7 along b, Jens Jensen used the RPA to predict the spin excitation spectrum in the high field IC phase from the zero field spin Hamiltonian derived in [15, 25]. The measured spin excitations presented in this chapter have thus been directly compared to those calculated by Jens Jensen; they have not been fitted to any function with free parameters.

When measuring the dispersion along k, the so-called *imaging* mode was used; the angle of each blade is adjusted to the blade position with respect to the sample in a way so as each blade is set to reflect the same neutron energy. The reflected neutrons from each blade hit a designated area on a 2D neutron detector. Cross-talk between the seven channels is eliminated by a set of separate collimators. The dispersions measured in this work were done by performing energy scans; the incoming neutron energy was varied while the neutron momentum transfer Q and the final neutron energy was fixed (measuring the magnon creation cross section). A Be-filter was placed before the analyzer to remove higher order neutrons (absorbing all neutrons with a higher energy than the fixed outgoing energy of 5 meV). In imaging mode, one can only control the position of the central blade. So when measuring the dispersion along $(0, q, 0)$, the blades are positioned to measure seven points in reciprocal space forming a line parallel to the K axis. Along K an energy scan is thus effectively seven energy scans at seven different constant values of K. However, when measuring along H the blades still span a line along K, so when measuring the dispersions along $(q, 1, 0)$ and $(q, 1 + k_{\mathrm{ic}}, 0)$, the intensity from only the three central blades was collected.

Figure 28 shows a typical scan along $(0, 1+q, 0)$, the K values given as Q are indicated. Two peaks are evident in all scans, confirming that there are two separate branches along K. Four different energy scans were performed along K, giving the dispersion shown on the upper part of figure 29.

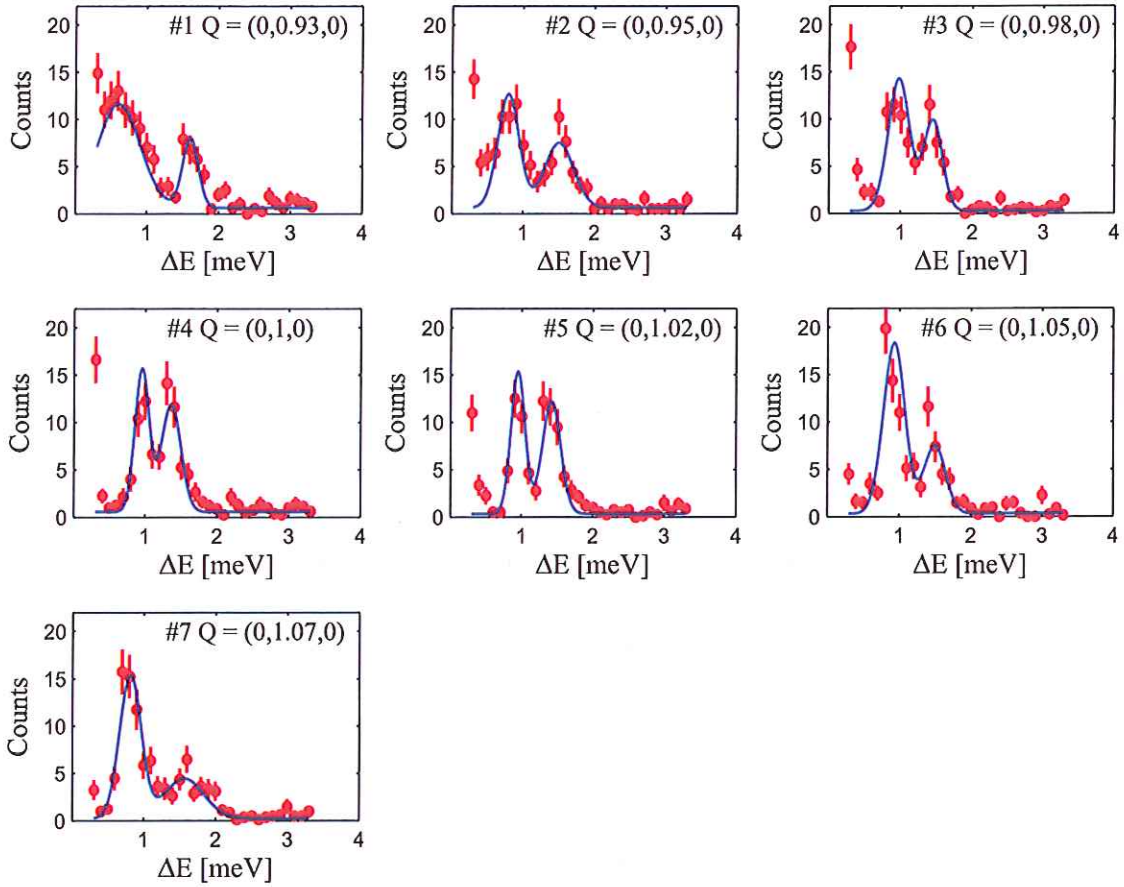

Figure 28: A single energy scan as measured by all 7 analyzer blades along $(0, 1+q, o)$. The resolution in q is very good along k, which allows for thorough measurements of the dispersion along k.

If $LiNiPO_4$ were completely isotropic in the ac-plane instead of having a weak preference along c, the ground state would have been a spiral also at zero field. In this hypothetical isotropic case; before settling on any magnetic structure, the ac-plane would have exhibited a continuous symmetry, namely any rotation around the b axis. When cooling into the spiral phase, the structure settles into a spiral (in principle two types of spirals with different chirality) and this continuous symmetry is spontaneously broken. A pseudo-particle spectrum follows from this symmetry breaking with modes with arbitrarily low energy. These modes are called *Goldstone modes*. In this case we have no continuous symmetry to begin with as there *is* anisotropy in the ac plane, but as evident in figure 29 the spin wave energies approach zero energy at the IC peak position within the resolution of the spectrometer. The physical reason for these low-energy excitations is as follows. Any translation along b merely results in a phase shift of the spiral. A local phase shift away from the IC modulation costs energy and can propagate like a spin wave, but an arbitrarily small phase shift is possible with a resulting arbitrarily low excitation energy. These modes are called *phasons* and this is what is observed.

The dispersions in the high field IC spiral phase at 2 K along $(H, 1+k_{ic}, 0)$ and $(H, 1, 0)$ were also measured. Again, there are two branches. Along $(H, 1, 0)$, these branches merge or become indistinguishable at high H values. Again, there is excellent agreement with the RPA calculations.

In conclusion, all measured spin wave dispersions are as predicted in the RPA calculations performed by Jens Jensen. This confirms that $LiNiPO_4$ is very well understood.

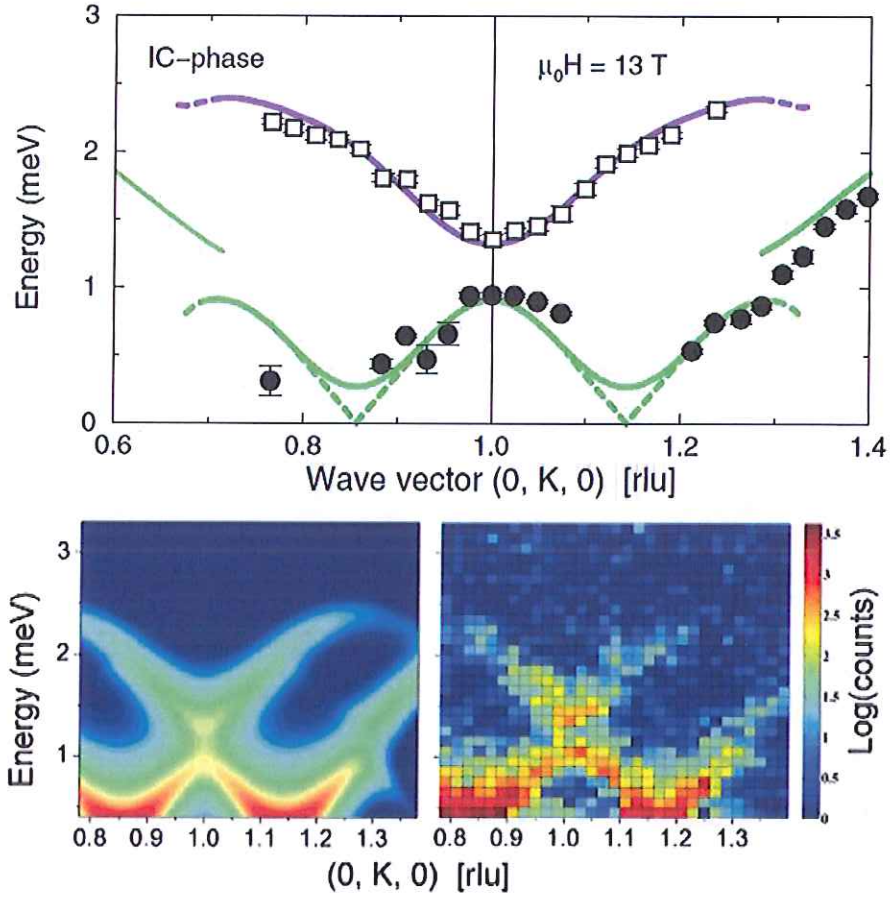

Figure 29: Dispersion measured along $(0, 1+K, 0)$ for 13.5 tesla applied along c. *Top:* The peak values from Gaussian fits such as those depicted in figure 28. The purple line represents the RPA calculation. *Bottom left:* Calculated spin wave intensities along K. *Bottom right:* Color plot representing the measured spin wave intensities. An excellent agreement is clearly evident.

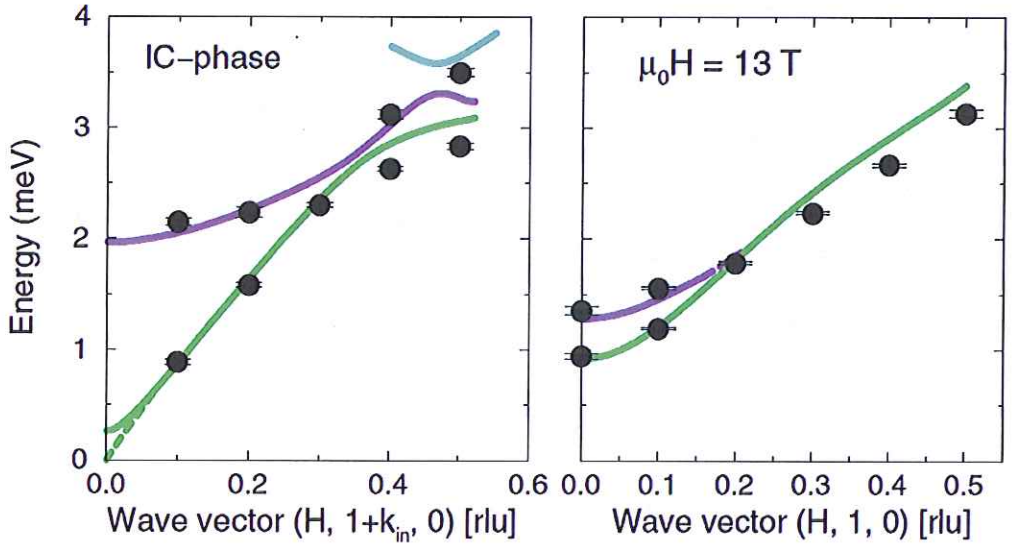

Figure 30: Spin-wave dispersions in the IC-phase at 2 K and 13 T along $(H, 1+k_{\mathrm{ic}}, 0)$ and $(H, 1, 0)$.

4.8 Magnetoelectricity in the high field spiral phase

No magnetoelectric effect has been observed in the linearly polarized IC phase of $LiNiPO_4$ [26, 30]. In the spiral phase two irreducible representations - or order parameters - co-exist. It has been shown for cycloid structures in $Ni_3V_2O_8$ [31] and $TbMnO_3$ [32] that a so-called trilinear term can be responsible for magnetoelectricity. Let σ_i and σ_j be the magnetic order parameters belonging to irreducible representations Γ_i and Γ_j, respectively. Terms in the free energy expansion could have the following form:

$$V = \sum_{ij\mu} \epsilon_{ij\mu} \sigma_i(k) \sigma_j(-k) P_\mu, \tag{4.6}$$

where P_μ is a polarization vector along $\mu = x, y, z$. Without elaborating further on the Landau theory of the free energy expansion, such terms need to be invariant under the symmetry operations in the little group $G_{\mathbf{k}_{ic}}$. It is clear that this is only possible if the product of the two irreducible representations transforms identically with at least one polarization vector under all the symmetry operations. If this is the case, the term in equation 4.6 is invariant under the symmetry operations of $G_{\mathbf{k}_{ic}}$, and a non-zero $\epsilon_{ij\mu}$ is possible. The character tables for the four irreducible representations $\Gamma_1 - \Gamma_4$, the product $\Gamma_1\Gamma_3$ and the three polarization vectors P_μ, $\mu = x, y, z$ are given in table 8.

(a) Character table of the four irreducible representations

	1	$2'_y$	m'_{xy}	m'_{yz}
Γ_1	1	β	1	β
Γ_2	1	$-\beta$	1	$-\beta$
Γ_3	1	β	-1	$-\beta$
Γ_4	1	$-\beta$	-1	β
$\Gamma_1\Gamma_3$	1	β^2	-1	$-\beta^2$

(b) Character table of the three polarization vectors

	1	$2'_y$	m'_{xy}	m'_{yz}
P_x	1	-1	1	-1
P_y	1	1	1	1
P_z	1	-1	-1	1

Table 8: How the four irreducible representations and the three polarization vectors transform under the symmetry operations of $G_{\mathbf{k}_{ic}}$.

From tables 8a and 8b it is evident that no term of the form in 4.6 is possible when the order parameters are represented by Γ_1 and Γ_3. This concludes the description of the work done on $LiNiPO_4$. Three IC magnetic phases have been identified and the phase boundaries mapped out. The spin excitations in the spiral phase have been measured and found in almost perfect accordance with the spin wave calculations of Jens Jensen.

5 Continuous spin flop and bicritical fluctuations in isotropic $LiMnPO_4$

5.1 Introduction

$LiMnPO_4$ differs fundamentally from the other lithium orthophosphates in two ways. The magnetoelectric tensor describing the coupling is diagonal; $\alpha_{ii} \neq 0$ and $\alpha_{ij} = 0$ for $i \neq j$. In addition, the Mn^{2+} ion has an $L = 0$ ground state which means that to leading order there is no possibility of DM-interactions and no single ion anisotropy term. In spite of this, however, there will still be some anisotropy. This is due to the fact that even though the orbital momentum quantum number is said to be zero in Mn^{2+}, this is only an approximation - a very good one - since l is not a good quantum number. There is no continuous rotational symmetry due to the crystal field, and there will be some mixing of different LS multiplets, even though this mixing should be very weak. The spin waves in $LiMnPO_4$ have been measured in [33], where a Hamiltonian with a single ion anisotropy term has been used. Due to the spin-only nature of the ground state of Mn^{2+}, this is a bit misleading. However, since a small anisotropy is expected, the anisotropies extracted from the spin waves will have some merit, even though the cause of anisotropy is not necessarily straightforward. These anisotropies and the exchange parameters are listed in table 9.

J_b	J_c	J_{ab}	J_{ac}	J_{bc}	D_c	D_b
0.20(4)	0.076(4)	0.036(2)	0.062(3)	0.48(5)	0.007(1)	0.009(1)

Table 9: The exchange interactions and anisotropies in $LiMnPO_4$ as given in [33]. All units are in meV

Note that all the exchange constants are antiferromagnetic in nature, and that the anisotropies are two orders of magnitude smaller than those of $LiNiPO_4$. $LiMnPO4_4$ has an antiferromagnetic ordering temperature of $T_N = 33.8\ K$, and the magnetic structure has been determined to be a C-type structure polarized along the a-axis [16]. At zero temperature, the thermal mean value of the spins is $S = 5/2$ which is seen by maximizing the spin of the 5 electrons in the $3d$ obeying Hund's first rule.

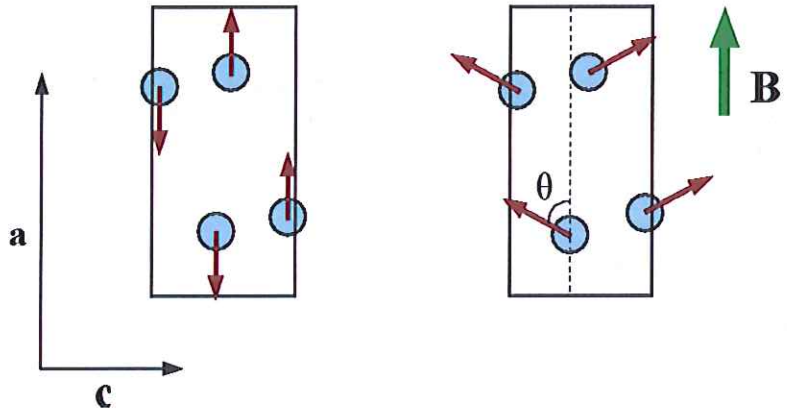

Figure 31: Spin flopping in $LiMnPO_4$. *Right:* The low field spin structure of $LiMnPO_4$. The spins are colinear and pointing along a. *Right:* The flopped spin state. The AFM spin configuration is probably a C-type polarized along c as expected from the anisotropy constants. This state is easy to magnetize by simply canting the spins along the field; which gains Zeeman energy on all four spins. This canting is resisted by the exchange interaction.

Applying a field along the a-axis at zero temperature leaves little room for magnetizing the material, as this can only be done by changing the thermal mean value of spins anti-parallel to the field. However, by flopping the spins perpendicular to the field (see figure 31), magnetizing the material is much easier as the system can gain Zeeman energy by canting the spins an angle θ (see figure 31). This canting has an exchange energy cost of the order $J \cdot cos(\theta)$, and the flopping itself costs anisotropy energy. At some critical field, when these costs are balanced out by the gain in Zeeman energy, the system chooses to flop along the easiest of the two axes perpendicular to the field, and the canting angle (as defined in figure 31) gradually decreases with field until saturation. A spin flop in $LiMnPO_4$ is nothing new, it was discovered by J. H. Ranicar and P. R. Elliston in 1967 using magnetization measurements [34], where the critical field as a function of temperature was also measured with an uncertainty of 0.1 tesla. They found the critical flop field to be 4 tesla at 4 K. In this work, the flopped structure is thoroughly determined using neutron diffraction. The nature of the $(\mu_0 H, T)$ phase diagram is determined with high precision near the bi-critical point, where the two antiferromagnetic phases join with the paramagnetic phase. Lastly, increased static fluctuations near the bicritical point are observed and reported.

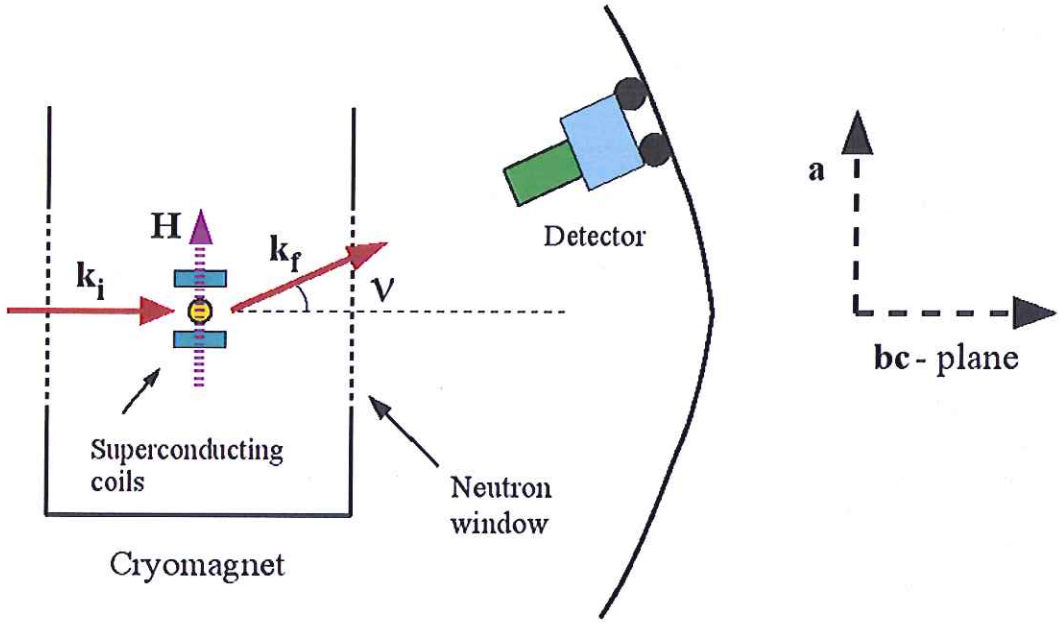

Figure 32: The instrumental setup in the TriCS experiment on $LiMnPO_4$. The magnetic field is vertical and parallel to the a axis. The detector can be tilted out of the scattering plane to reach reflections out of said plane.

5.2 The TriCS experiment - continuous spin flop and structure determination

In this section, the first diffraction experiment on $LiMnPO_4$ is described and interpreted. The magnetic structure in the spin flop phase is thoroughly determined both by analysis of a few key peaks and by a full structural refinement.

5.2.1 Experimental details

To examine the structure of the spin flop transition, a neutron diffraction experiment using the TriCS diffractometer at the PSI was performed. A single crystal of very irregular shape - best described by a wedge - and a weight of 220.14 mg was used. The crystal was aligned within 0.5° on

a x-ray Laue camera and glued to an aluminum sample holder, mounted with the crystallographic a axis vertical. A 6 T Oxford cryomagnet was used with a vertically enlarged neutron window to allow outgoing wave vectors significantly out of the horizontal plane. The experimental setup is shown in figure 32.

The vertically enlarged window allows for TriCS to measure reflections out of the scattering plane since the 1D detector at TriCS can be tilted by an angle $-10° < \nu < 40°$, see figure 32. In this setting, since the long crystallographic axis is vertical (and hence the short axis in reciprocal space), three non-equivalent scattering planes can be measured in relatively strong magnetic fields. Sadly, there was a problem with the magnet, which had a tendency to quench when going above 4.5 tesla. This prevented the author to examine the whole phase diagram in this experiment. 40′ both vertical and horizontal collimation was used between the sample and the monochromator. The incoming beam propagates in a nose which ended in a 10 mm circular slit in this case. 80' collimation was used between the sample and the detector.

5.2.2 Flopped structure determined using key peaks

One of the magnetic peaks reflecting the C_x symmetry is (010). The structure factor is zero for all other spin structures than C_x and C_z. This peak and another peak reflecting C type components along all three crystallographic directions is an obvious place to start. To get a good idea of the flopped structure, the integrated intensity of three different C-type peaks as a function of field - (010), (012) and (230) - was measured. The structure factors for the nuclear cross section and for the magnetic basis vectors are given in table 10.

	F_C^2	F_A^2	F_G^2	F_F^2	P_x^2	P_y^2	P_z^2	F_N^2
$(0,1,0)$	16	0	0	0	1	0	1	0
$(0,1,2)$	14	2	0	0	1	0.86	0.14	0
$(2,3,0)$	13.6	0	0	2.4	0.87	0.13	1	20

Table 10: Squared structure (F) and polarization (P) factors for the three peaks used to establish the flopped structure in terms of the irreducible representations. The structure factors are normalized to unit spin lengths of the components. The structure factor of the strongest nuclear peaks is 4000 for comparison.

Figure 33 shows the integrated intensity of the (010) peak as a function of field and A3 scans of (012) at 0 and 4.5 tesla, respectively, measured at 2 K.

The intensity of the (012) reflection decreases drastically when ramping through the spin flop transition, far beyond what can be explained by a spin flop along b. In addition, the integrated intensity of the (010) peak is constant over the measured field range. So the structure is C type in both AFM phases and polarized in the ac plane in the flopped transition. The only reasonable explanation is that the spins flop in the ac-plane from being polarized along a to being polarized along c. To firmly establish this, the integrated intensity of the (230) peak was measured as well, as the intensity should increase about 15 percent upon entering the flopped phase, which is indeed evident in figure 34. It is important, however, not to over interpret the intensities of a few peaks, as we have a fairly large crystal with a large moment. Therefore, it is probable that there is extinction in the strong magnetic peaks. Furthermore, $LiMnPO_4$ contains lithium which has a large absorption cross section. So when dealing with an irregular shaped crystal - as in this case - absorption effects could be significant as well, due to a difference in neutron paths when measuring different peaks. In spite of this, the general picture is quite clear though. Note that the critical field increases with temperature; an increase of up to 0.5 T in the measured temperature range of 2-20 K.

Figure 34 shows the integrated intensities of the three peaks as a function of field, consistent with a spin flop $C_x \rightarrow C_z$. The heavily decreasing peak (012) has been used for determination of the critical field; all the used scans are shown in figure 34. The critical field has been defined as the maximum value of dI/dH as determined by eye, with manually estimated uncertainties. Figure 34 also shows

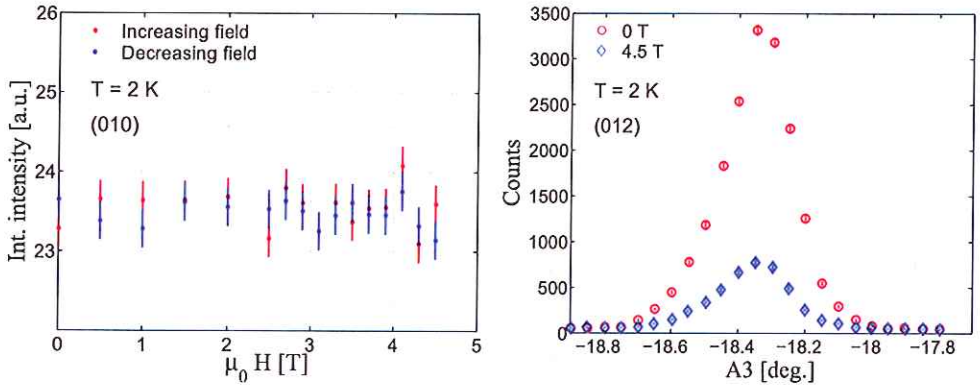

Figure 33: *Left:* Integrated intensity of (010) as a function of field. The intensity is constant over the entire field range within errors.*Right:* A3 scans of (012) at 0 and 4.5 tesla. A drastic drop in intensity is evident.

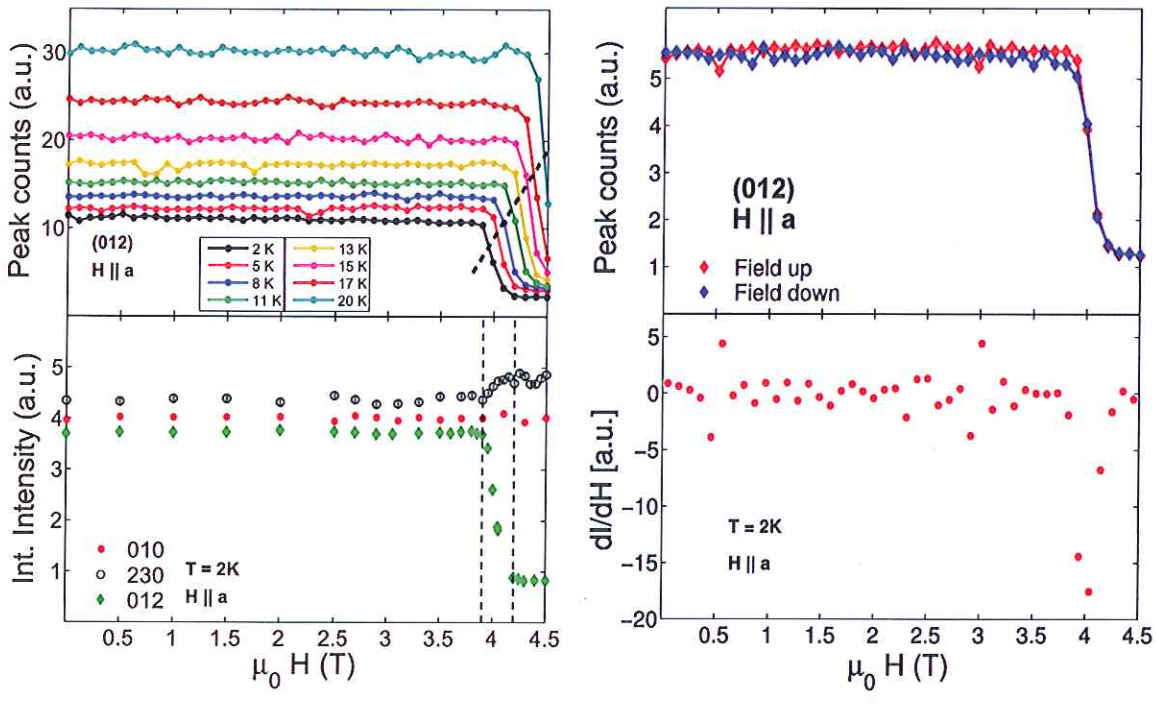

Figure 34: *Top left:* Peak intensity of (012) as a function of field at various temperatures; these are the scans used for phase boundary determination. *Bottom left:* Integrated intensities of the (010), (012) and (230) peaks as a function of field. The data are consistent with a C-type flop of polarization from a to c, using table 10. *Top right:* Peak intensity of (012) as a function of both increasing an decreasing field - no hysteresis is evident *Bottom right:* Slope of the intensity vs. field curve for increasing field as given above, used for determination of critical field.

the peak intensity of (012) as a function of both increasing and decreasing field. Interestingly, no hysteresis is evident at all. This lack of hysteresis warrants an important comment.

Angular range of the spin flop as a first order transition

The importance of field alignment when inducing a spin flop has been investigated in [35, 36, 37]. In the very simple case of one antiferromagnetic interaction between two sub-lattices of strength J_{ex} and an anisotropy energy of E_{an}, the critical angle Ψ_c below which the transition is first order, and above which the transition is a second order spin flop like transition can be estimated as

$$\Psi_c(T=0) \approx 28.6^\circ \frac{E_{an}}{J_{ex}} \text{ [deg.]} \tag{5.1}$$

The dominating exchange parameter determining the C-type structure in $LiMnPO_4$ is $J_{bc} \approx 0.48$ meV. The very weak anisotropy is $D_c = 0.007$ meV. Substituting these values into equation 5.1 yields

$$\Psi_c^{\text{LiMnPO}_4}(T=0) \approx 0.42^\circ \tag{5.2}$$

This critical angle *decreases* as a function of temperature going to zero at the so-called *bi-critical point* at H_b and T_b (note that $T_b \neq T_N$), where the spin flop (SF) and antiferromagnetic (AF) phases join with the disordered paramagnetic phase at higher temperatures. The temperature dependency of the critical angle is

$$\Psi_c(T) \approx \Psi_c(0)\frac{(T_b - T)}{T_b}. \tag{5.3}$$

It is worth mentioning that these results were obtained from mean field approximations, which are not valid at the critical temperature. Nevertheless the necessary degree of alignment is easily obtainable.

5.2.3 Structural refinement of the TriCS data

The structure of the spin flopped phase of $LiMnPO_4$ has been determined by Rietveld refinement of the single crystal diffraction data using the FullProf open source package, available on the Internet. To obtain the integrated magnetic intensity of all reachable peaks, omega scans of these reflections were performed at 4.5 T/2 K and 0 T/60 K respectively. These omega scans were fitted to single Gaussians with constant background, and the integrated intensity taken to be the area of said Gaussian. The magnetic intensity is thus the difference between the areas of the fitted curves in the SF and paramagnetic phases respectively, corrected for the Lorentz factor. Some of the measured peaks, however, need to be discarded for various reasons.

Figure 35 shows two typical discarded peaks (left and middle scans) compared to an accepted peak (the right scan). The leftmost figure shows a very irregular peak shape which was found in some of the reflections. The alignment-scans performed on a two-axis alignment instrument (Morpheus at the PSI) showed no such irregularities, so since they cannot be ascribed to the mocaicity of the crystal, they can be discarded. When doing magnetic neutron scattering of a relatively large single crystal (roughly 300 mg) of a $S = 5/2$ compound, the problem of *extinction* can occur. Extinction can have several causes; the one considered here is merely the possibility that a large fraction of the incoming beam is diffracted, so that the incoming neutron flux is not constant throughout the crystal. With the current collimation setup before the monochromator, the incoming neutron flux on the sample position is $9 \cdot 10^5 n/cm^2/s$ (the relevant data is on the TriCS web site). The crystal cross section is never more than 0.25 cm^2, so roughly $2 \cdot 10^5$ neutrons hit the sample pr. second. This is without taking the bulky magnet into consideration which stops a large fraction of both

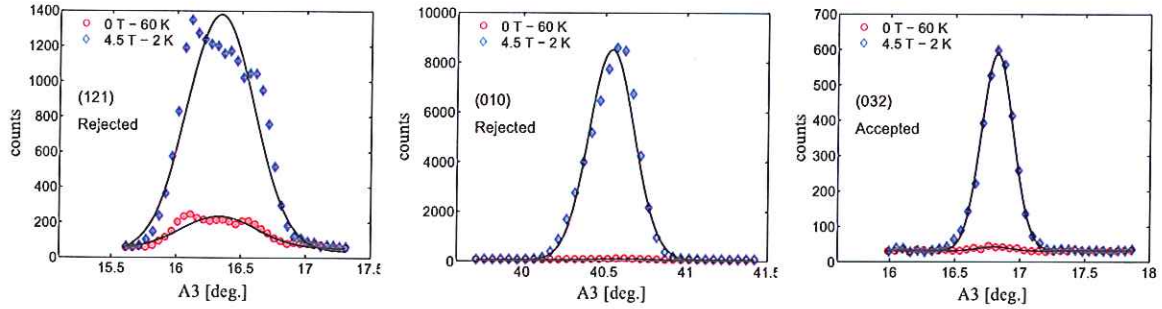

Figure 35: *Left:* Erroneous peak shape with a very irregular shape *Middle:* The strong (010) reflection. *Right:* The (032) reflection. All plots have been normalized to 50000 monitor which corresponds roughly to 2 seconds of measurement time at maximum source flux.

the incoming and outgoing neutrons. In addition, the collimation between the sample and the detector also absorbs a large fraction of the diffracted neutrons; reducing the signal but reducing the background even more. Due to the vertically focusing mode - providing a very broad vertical resolution function so that the diffracted intensity is less dependent on the angle ν in figure 32 - not all the diffracted intensity is measured in an omega scan. So one can assume that these effects can be absorbed in a reduced incoming neutron intensity of say $5 \cdot 10^4$ neutrons pr. second. The middle plot in figure 35 shows an omega scan of the very strong (010) reflection normalized to 50000 monitor which roughly corresponds to 2 seconds. The peak intensity is thus roughly 5000 neutrons which is 10 percent of the incoming flux - a large fraction, especially due to the fact that the strongest magnetic peaks will have the smallest relative uncertainties and hence the largest weight in a refinement procedure. Therefore, peaks with a peak intensity of more than 1000 neutrons pr. second have been discarded.

The refinement has been done using the 49 peaks left after implementing this selection procedure, using the single crystal option in FullProf. Due to the fact that the (010) reflection has a constant intensity throughout the spin flop transition, the only reasonable trial vector to refine in the flopped phase is $c_1 \cdot C_z + c_2 \cdot F_x$, where $c_2 \ll c_1$. FullProf varies the parameters c_1 and c_2 and calculates the structure factor as well the parameter

$$M = \sum_n \frac{\left(F^2_{obs,n} - F^2_{calc,n}\right)^2}{\sigma_n^2}, \tag{5.4}$$

where n is the observation index (a total of N reflections) and $F_{obs,n}$ and $F_{calc,n}$ are the square of the observed and calculated structure factors respectively. σ_n is the statistical error of observation n. The observed structure factors are deduced from the integrated intensities by correcting for the Lorentz factor (done by the author) and the magnetic form factor (done by FullProf). Thus, M is a measure of the χ^2 which is exactly what FullProf minimizes. FullProf returns the following parameters:

$$R_{F^2} = 100 \cdot \frac{\sum_n \left[\left|F^2_{obs,n} - F^2_{calc,n}\right|\right]}{\sum_n F^2_{obs,n}} \quad R_{wF^2} = 100 \cdot \sqrt{\frac{M}{\sum_n \frac{F^2_{obs,n}}{\sigma_n^2}}},$$

$$R_F = 100 \cdot \frac{\sum_n \left[\left|F_{obs,n} - \sqrt{F^2_{calc,n}}\right|\right]}{\sum_n F_{obs,n}} \quad \text{and} \quad \chi^2 = \frac{M}{N-p}, \tag{5.5}$$

where p is the number of parameters to refine. χ^2 is thus actually the *reduced* χ^2 which is the most widely used indicator of the goodness of the fit. Figure 36 shows the observed structure

factors of the 49 peaks as a function of $\sin(\theta)/\lambda$ (essentially τ in a diffraction experiment) plotted along with the calculated structure factors after refining the two parameters c_1 and c_2 in the vector $c_1 \cdot C_z + c_2 \cdot F_x$. The absolute difference $|F_{obs} - F_{calc}|$ is plotted below so that the goodness of fit for each individual peak can be evaluated. There seem to be substantial deviations of the observed structure factors from the calculated ones, but the error bars on the observed structure factors are merely statistical. Absorption effects, minor extinction effects, effects stemming from the sample not being centered on the axis of rotation and the bulky magnet have not been accounted for in these error bars. Therefore, reduced χ^2 values of any refinement are*expected* to be significantly above 1.

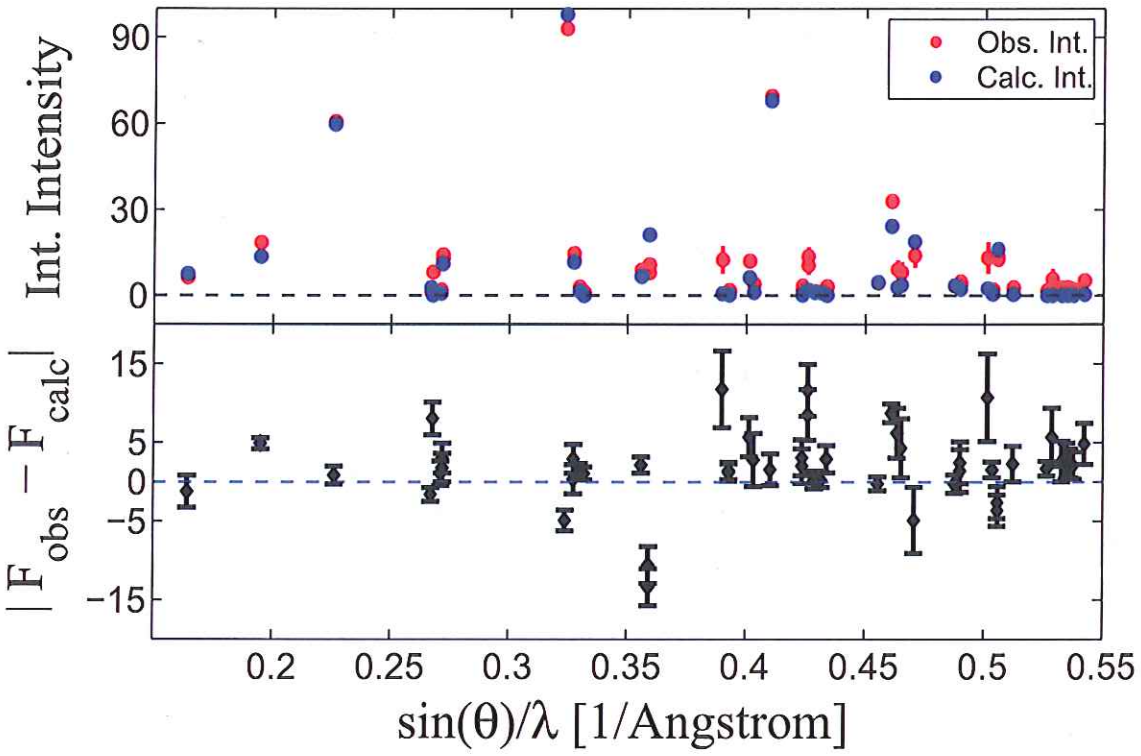

Figure 36: *Top:* Integrated intensity of all peaks accepted by the author and FullProf as valid magnetic peaks plotted along with the calculated values. *Bottom:* Difference between observed and calculated intensities. There are significant deviations but not enough to doubt the $C_z + F_x$ structure in the author's opinion.

Thus, the fit seems reasonable by looking at figure 36. The refined parameters and goodness-of-fit values are given in table 11.

	c_1	c_2	R_{F^2}	R_{wF^2}	R_F	χ^2
$c_1C_z + c_2F_x$	3.93(3)	0.37(6)	32.8	15.8	32.4	5.93
$c_1C_z + c_2F_y$	3.93(3)	0.45(12)	34.6	16.3	34.6	6.31
c_1C_z	3.93(3)	-	35.5	16.8	37.8	6.42

Table 11: Refinement parameters and goodness-of-fit parameters for three different spin structure vectors. As evident, the most physical refinement is the one with the low reduced χ^2.

Table 11 also shows the results from refinements with the vectors c_1C_z and $c_1C_z + c_2F_y$. The C-type structure polarized along z is maintained but the credibility of the refined field induced canting can

be estimated by performing these two refinements. It is clear that the finite F_x component reduces the chi square significantly compared to the refinements with y-polarization and with no canting at all. The refinement with $C_z + F_y$ components shows a finite F_y component within uncertainty. However, the structure factors are the same for F_y as for F_x with the polarization factor as the only difference. This is therefore as expected - the relative uncertainty of the F_x component is much smaller than that of the F_y component and the overall reduced χ^2 of the refinement is smaller. Actually, introducing a F_y component does not make much of a difference at all compared to the case where only the C_z structure is refined. The prefactors c_1 and c_2 are actually the magnetic moments, but the value of c_1 is significantly smaller than the expected value of $5\mu_B$. The relative magnitude of these constants are determined by the relative intensities of the magnetic peaks, the absolute magnitude is determined by the scale factor of a refinement of the nuclear structure. This has been done, and the scale factor has been introduced in the refinements presented above. However, with such a large crystal containing neutron absorbing lithium, this scale factor cannot be completely trusted without a refinement of absorption corrections. This is difficult however, since the crystal shape is very irregular. In this work, therefore, the absolute moment as determined by the FullProf refinement is discarded and only the relative values of c_1 and c_2 are trusted. This has little consequence as L = 0 and hence the magnetic moment is not expected to differ from 5 μ_B. The refinement of the $c_1 C_z + c_2 F_x$ vector thus gives a field induced canting angle in the flop phase of $5.4° \pm 0.9°$ at 4.5 T. Again, this uncertainty is merely statistical.

5.3 Magnetization measurements

Magnetization measurements have been performed on the same crystal as used in the TriCS experiment. The crystal was glued onto a plastic tip, which was mounted in a plastic straw attached to the sample stick. VSM measurements were performed as a function of both temperature (at constant field) and field (at constant temperature) and the phase diagram determined.

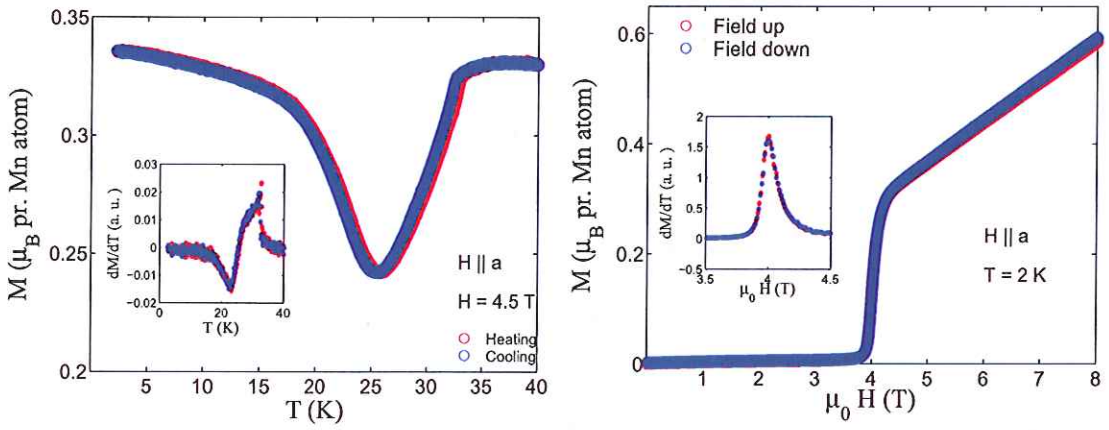

Figure 37: *Left:* Magnetization as a function of temperature at 4.5 T applied along a. At roughly 33 K the magnetization decreases sharply with almost a discontinuous jump in differential magnetization (inset). Upon further cooling $LiMnPO_4$ enters the flopped phase and the magnetization rises. *Right:* Magnetization as a function of field applied along a at 2 K. At low fields, $LiMnPO_4$ is difficult to magnetize. At 4 T however, the spin flop occurs followed by a heavily increased susceptibility.

Figure 37 (left) shows a temperature scan at 4.5 tesla applied along a, which is just above the critical field at low temperatures and just below the critical field at the ordering temperature. The slope of the phase boundary as found by neutron diffraction is easily confirmed as the magnetization

shows a drastic increase upon cooling into the flopped phase. A field scan at 2 K is shown in figure 37 (right). The critical field is defined as the point of maximum slope found by eye on a differential magnetization plot. The huge difference in susceptibility of the two phases is directly evident. In both figures a low temperature magnetization at 4.5 tesla of roughly 0.33 μ_B pr. Mn atom is extractable (again by eye). Since $L = 0$ one can relatively safely assume $\Delta g = 0$ and $S = 5/2$. Assuming this moment, the canting angle due to the Zeeman term is roughly 7.5°, which is higher than the refinement value within error but not alarmingly so, since any systematic uncertainties have not been accounted for in the error of the refinement canting angle. If one allows for paramagnetic impurities in the crystal and assumes that the sample holder (bulk plastic) and glue contribute to the magnetization to some degree, the two canting angles are consistent.

Suitable field- and temperature scans have been made to determine the phase diagram and the susceptibility was measured in a field of 0.1 tesla. Figure 38 (left) shows the inverse susceptibility as a function of temperature which is linear in the interval between 50 and 300 K. Thus, the susceptibility has a $1/T$-dependency in this regime before it starts to drop rapidly to zero at $T_N \approx 33.4\ K$. The $1/\chi$ curve deviates a little bit from linearity at roughly 45 K - somewhat above T_N - which is expected especially since dynamical magnetic fluctuations has been observed up to 50 K [33].

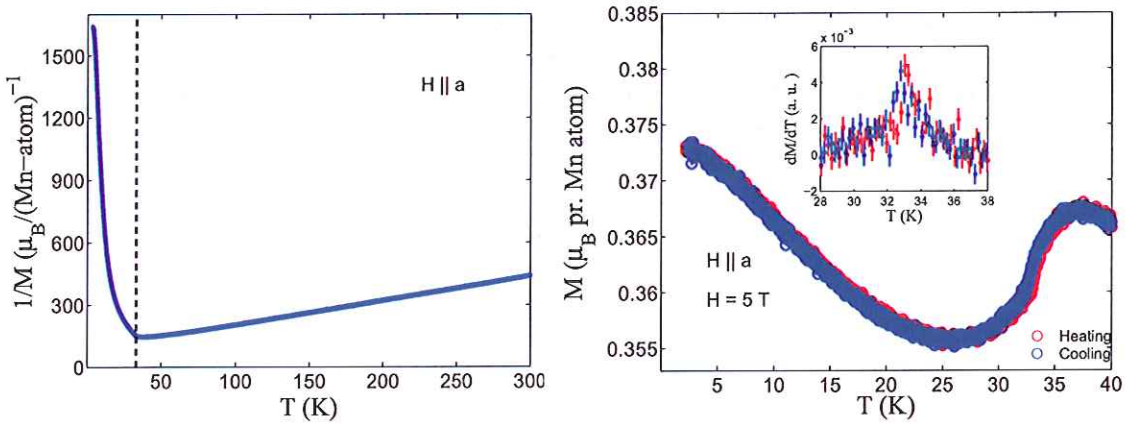

Figure 38: *Left:* The susceptibility for $T = 2 - 300\ K$ as measured by VSM in a DC field of 0.1 T *Right:* Magnetization as a function of temperature at $\mu_0 H = 5\ T$ which is above the spin flop field at all temperatures.

Figure 38 (right) shows the magnetization as a function of temperature at 5 T. This scans shows how all temperature scans for fields above the high temperature flop field look like; they display an almost constant magnetization as a function of temperature when cooling below T_N. The shape of the curve makes it very difficult to define an ordering temperature and to prove that the experimental criteria for long range order is the same above and below the flop field. This makes it very difficult to examine details of the phase boundary near the ordering temperature, using only magnetization measurements.

5.4 Magnetic phase diagram and bicriticality in $LiMnPO_4$

In this section the phase boundaries as measured on the RITA-II spectrometer will be presented along with the effects seen near the bicritical point.

5.4.1 Experimental details

To examine the phase boundaries near the point in the phase diagram where the two ordered and the disordered paramagnetic phase meet - the so-called bicritical point at (T_b, H_b) - neutron diffraction has been used for reasons clarified above. The same sample as used on TriCS and magnetization measurements was used. The triple axis spectrometer RITA-II at the PSI was used with the Oxford 15 T cryomagnet. The incoming and outgoing neutron energy was 5 meV, and there was a 40' collimator between the monochromator and the sample and a 80' collimator between the sample and the analyzer (mounted within the Be-filter). The same plastic sample holder as used in the magnetization measurement was used in the RITA-II experiment. This could result in poor thermal contact between the sample and the heater situated near the end of the sample stick (not the sample holder). Therefore, the heater itself was switched off and only the exchange gas was used to stabilize the temperature. This took several minutes of waiting time until equilibrium was reached.

5.4.2 The ordering phase boundary

In order to examine the ordering phase boundary, the integrated intensity of the (010) reflection can be used when cooling into both the zero field and the flopped phase. Since the neutron scattering cross section is proportional to the square of the thermal average of the magnetic moments, one can deduce the sub-lattice magnetization $M^\dagger$ as simply the square root of the integrated intensity - $M^\dagger \propto \sqrt{I_{010}}$. Figure 39 shows the sub-lattice magnetization as a function of temperature for temperature intervals near the ordering temperature at zero field, the high temperature critical field - 4.7 tesla - and 12 tesla. These curves have been fitted to the following function:

$$M^\dagger = \begin{cases} A|T - T_N|^\beta & \text{if } T < T_N, \\ 0 & \text{if } T > T_N \end{cases} \tag{5.6}$$

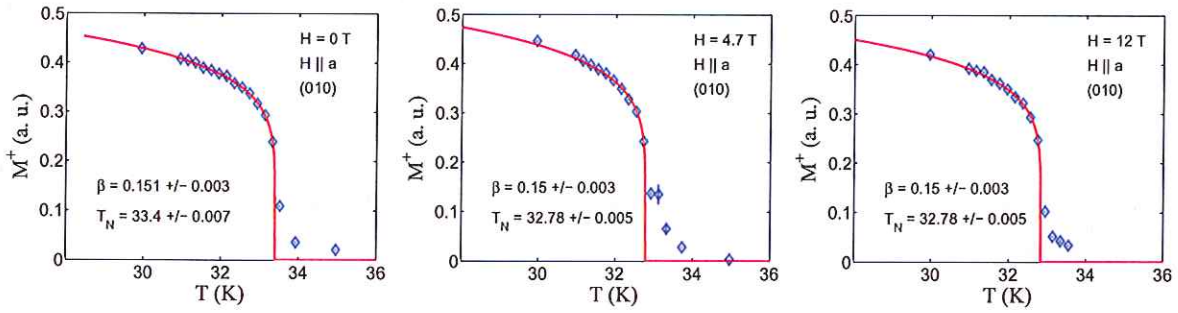

Figure 39: Sub-lattice magnetization as a function of temperature near T_N at 0 T (*left*), 4.7 T (*middle*) and 12 T (*right*). The data have been fitted to the function in equation 5.6 with a fixed background of 0. As evident, the critical temperature at the flop field is significantly lower than that in zero field, but the critical exponent is the same.

It is clear that the critical temperature is significantly lower at the spin flop field of 4.7 T than at zero field - this is not only due to the errors on the fit parameters but can be seen by eye. Hints of this shape of the phase boundary were seen by magnetization measurements as well, which was the main reason for doing the RITA-II experiment. The critical exponents are the same within error. Above the ordering temperature there is a finite intensity when measuring a rocking curve at zero energy transfer. This is due to critical fluctuations representing small statically ordered domains embedded in the otherwise disordered paramagnetic phase above T_N of size - or more correctly

- *correlation length* ξ. A system with infinite correlation length has structure factors which are sharp delta functions at reciprocal lattice points giving rise to the resolution limited Gaussian peak shapes. Above T_N however, there are no long range order and the peaks assume a broad Lorentzian shape centered at reciprocal lattice points (still to be convoluted with the experimental resolution) with a peak width inversely proportional to the correlation length. There is a hint that the intensity of these broad peaks is a little bit higher at the flop field than at 0 and 12 tesla. This will be elaborated on in section 5.4.4.

5.4.3 The phase diagram

The phase diagram as determined by TriCS measurements, VSM magnetization measurements and RITA-II measurements is shown in figure 40.

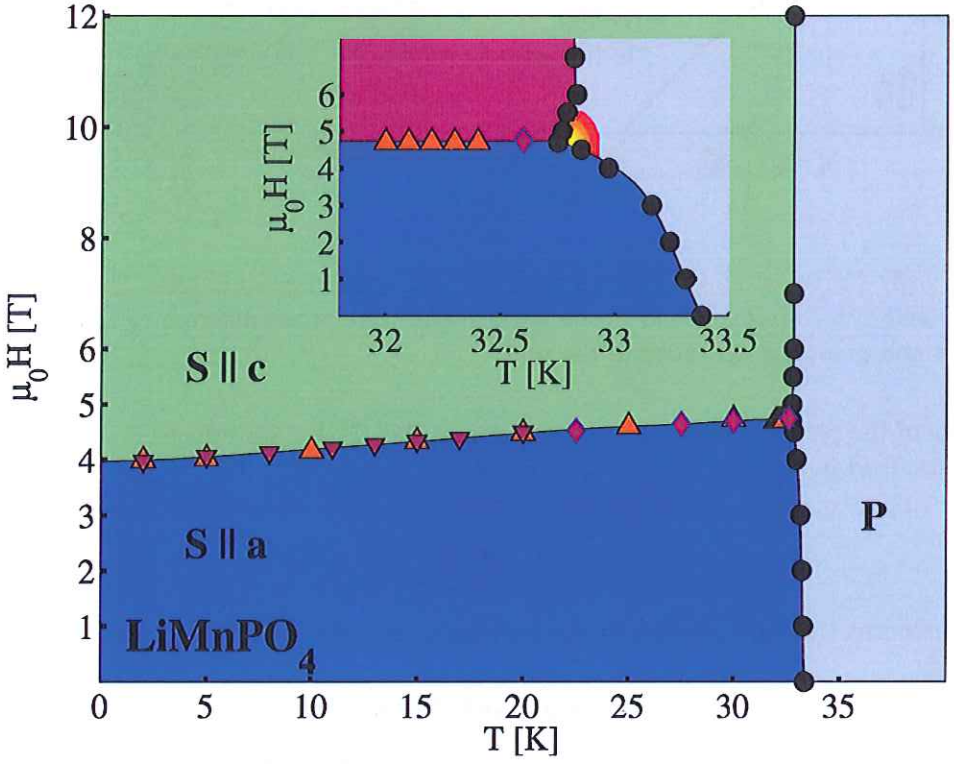

Figure 40: Phase diagram of $LiMnPO_4$ for fields applied along a. The up-pointing orange triangles represent the critical fields as measured by VSM magnetization measurements. The down-pointing purple triangles are the critical fields as determined by the TriCS measurements of the (012) reflection, and the purple diamonds represent the critical fields as determined by the RITA-II measurement of the (001) reflection as a function of field. The black circles represent the ordering temperature as found from power-law fits to the integrated intensity of the (010) reflection as measured on RITA-II. The spin flop boundary has a modest slope with the critical field increasing with temperature. The inset shows that phase boundary close to the bi-critical point. The low-field AFM phase boundaries merge with the spin flop phase boundary *tangentially* and the ordering temperature seems slightly suppressed at the critical field.

The spin flop phase boundary has a slope; the critical field increases with temperature. The ordering phase boundary seems to be a vertical line - with a Neel temperature independent of field and spin orientation. This is not the case when zooming in on the bicritical point however.

The ordering phase boundaries form a wedge of paramagnetic phase and they seem to approach the bicritical point *tangentially* to the spin flop phase boundary. This phase diagram near the critical temperature has actually been predicted by Michael E. Fisher, David R. Nelson and J. M. Kosterlitz [38, 39, 40]. The predicted phase diagram is shown in figure 41 along with the experimentally determined phase diagram - the similarity is close. So one can say that the phase diagram near the bicritical point shows no surprises. Similar phase diagrams - with more or less subtle differences - have been found in [41, 42, 37, 36].

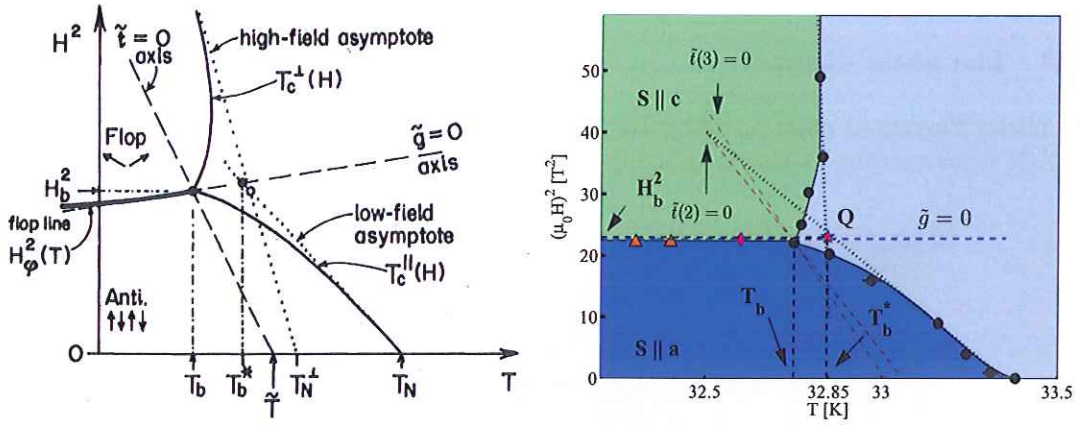

Figure 41: *Left:* Universal phase diagram for a spin flop system given in [38]. The two scaling field axes $\tilde{g} = 0$ and $\tilde{t} = 0$ are explained in the text. *Right:* The phase diagram of $LiMnPO_4$ with the asymptotes and points as described in the text.

An analysis of the phase boundaries can be found in [38]. Fisher introduced a *scaled* temperature and magnetic field in terms of the bicritical point (T_b, H_b)

$$t = \frac{T - T_b}{T_b} \quad \text{and} \quad g = H_{||}^2 - H_b^2, \tag{5.7}$$

where $H_{||}$ denotes the field parallel to the easy axis. He then introduces the so-called optimum scaling fields

$$\tilde{t} = t + qg \quad \text{and} \quad \tilde{g} = g - pt, \tag{5.8}$$

The axes of this scaled $((\mu_0 H)^2, T)$ coordinate system - $\tilde{g} = 0$ and $\tilde{t} = 0$ - are calculated and drawn on the phase diagram of $LiMnPO_4$ in figure 41. The axis $\tilde{t} = 0$ can be calculated from the zero field asymptote of the ordering phase boundary and from the dimensionality of the fluctuating spin components n [38]. In the case of $LiMnPO_4$ there is not much difference between the calculated axes for $n = 2$ and $n = 3$. The $\tilde{t} = 0$ axis is predicted to intersect the $H^2 = 0$ field axis in the middle third of the interval $[T_b : T_N]$ and both axes do. So the two possible dimensionalities cannot be distinguished using this axis. One could fit the ordering phase boundary to get a fully consistent theoretical description (in principle), but in this case, there are not enough points on the phase boundary. Furthermore, the alignment was not under complete control neither in the RITA-II experiment nor in the VSM magnetization experiment. It is the author's opinion, that one cannot just use the plug-and-play sample inserts of neither RITA-II nor the Risø CFMS system if one wants to be aligned better than 0.1° for instance. Therefore, an unambiguous determination of the dimensionality of the fluctuations from a fit to the ordering phase boundaries - as proposed in [38] - is not justified by the data. The phase diagram still displays a remarkable resemblance with the one predicted. In the next section, the neutron diffraction results from examining the wedge in the phase diagram are presented.

5.4.4 Criticality at the flop field H_b

On figure 39 there was a hint of increased intensity of the critical scattering near the spin flop field $H_b = 4.7\ T$. This was examined in more detail at the RITA-II experiment. Figure 42 shows some of the (0 1 L) scans of the (010) peak at temperatures above T_N that were made during the RITA-II experiment. The critical temperatures at the two fields - 0 T and 4.7 T - differ of roughly 0.65 K. Note the logarithmic intensity scale. The scans have been fitted to a *Voigt* function - which is a convolution between a Lorentzian reflecting the finite size of the domains and a Gaussian reflecting the resolution. The width of the Gaussian has been fixed to the width of a low temperature Bragg peak - which is Gaussian within errors. On figure 42 it is evident that relative to the ordering temperature, there is a substantial increase of intensity at the critical field realtive to zero field.

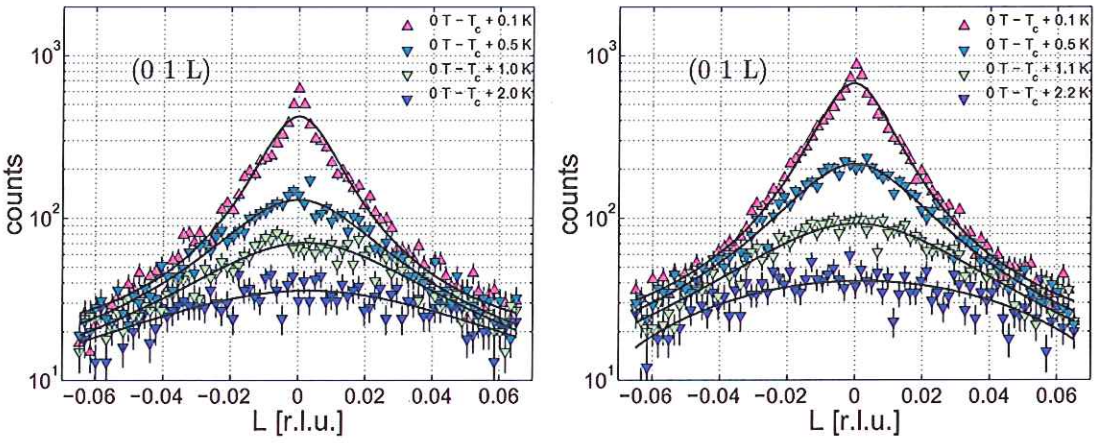

Figure 42: *Left:* Long L-scans at 4 different temperatures above $T_N = 33.4$ at zero field *Right:* Long L-scans at 4 different temperatures above $T_b = 32.75\ K$ at $H_b = 4.5\ T$. The logarithmic intensity scale tones it down a little bit, but there is a substantial increase in critical scattering at the bicritical field.

The fit is not very good close to the peak center on both plots at temperatures very close to T_N (0.1 K). This is probably caused by the onset of long range order causing a narrow Gaussian superimposed on the Voigt function. The Lorentzian peak shape can be described as $I \propto 1/(q^2+\Gamma^2)$. The correlation length along the direction in which one is scanning can be extracted as $\xi = 2\pi/\Gamma$, where Γ is readily extracted from the voigt fit parameters.

Figure 43 (left) shows the integrated intensity of the critical scattering as a function of $T - T_N$. On that plot it is very clear that intensity at the flop field shows a significant increase both when comparing to the zero field and the 10 T case. So there is simply more order at the critical field than there is a both higher and lower fields at temperatures close to T_N. Figure 43 (right) shows the extracted correlation lengths along the c-axis for all three fields as a function of temperature. The correlation length does not show a significant change at the critical field. The correlation lengths have been fitted to the same temperature-dependency as in [33] (for comparison):

$$\xi(T) = Ae^{\frac{B}{(T-T_c)^\nu}} \tag{5.9}$$

In [33], they used the 2D-XY model found in [43]. The fits are reasonably good, but the data are not good enough to unambiguously determine the critical exponent or unambiguously distinguish between models. For example, reasonable fits can be obtained to the data presented in figure 43 with a fixed ν anywhere between 0.1 and 0.5. Therefore, little energy has been put into the interpretation of the temperature dependence of the correlation lengths. A much more dedicated experiment is necessary to determine the dimensionality of the fluctuations.

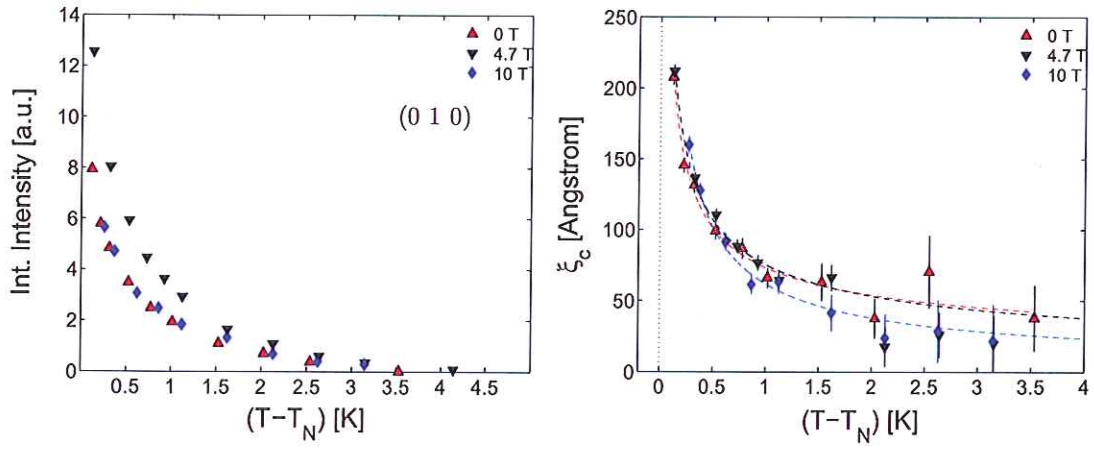

Figure 43: *Left:* Integrated intensity of the long (010) L-scans as those presented in figure 42 as a function of $T - T_N$ at 0 T, 4.7 T and 10 T respectively *Right:* The domain correlation length along the crystallographic c-axis as a function of temperature at 0 T, 4.7 T and 10 T respectively. There is a clear increase of critical scattering intensity at the flop field which is not there at neither 0 T nor 10 T. The correlation length along c as a function of temperature, however, remains the same at all three fields within errors.

However, it is peculiar that the increase in neutron scattering intensity is not accompanied by an increase in average correlation length or domain size. Just for the sake of argument - one could assume that the correlation length is unchanged at the flop field along the two other crystallographic directions (which is admittedly completely without empirical cause). The only way to have an increased integrated intensity at the flop field, is that the *density* of ordered domains is increased. One could imagine the scenario sketched in figure 44. At zero field and above the critical temperature, there are small volumes with short range order - domains of only C_y symmetry - embedded in a disordered bulk sample. At the critical field the critical temperature is reduced because the system cannot decide whether to order in a $C_x + F_x$ or $C_z + F_x$ type structure. Furthermore, at the critical field, domains from both $C_x + F_x$ and $C_z + F_x$ may appear increasing the density of ordered domains which in turn gives rise to an increase in the critical scattering.

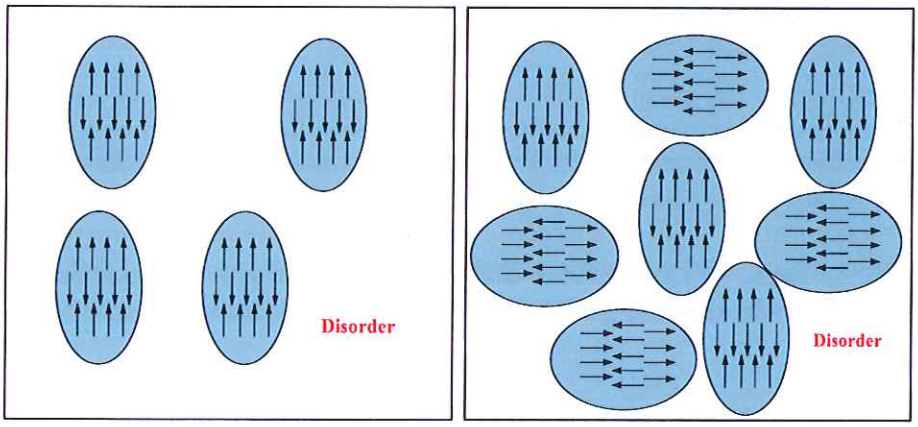

Figure 44: *Left:* The proposed zero field case - small volumes of order is embedded in a disordered bulk material. *Right:* The density of such domains is allowed to increase a lot more at the critical field before long range order is established.

In conclusion, the spin flop phase diagram of $LiMnPO_4$ has been determined, and the structure in the flopped phase has been determined to be a $C_z + F_x$ type structure. Details of the phase diagram has been determined near the bicritical point, and the phase boundaries have been found to be as predicted by theory. An increase in critical scattering intensity without a corresponding increase in correlation length (at least along c) has been observed.

6 Zero field spin structure and field induced spin canting in anisotropic $LiCoPO_4$

6.1 Introduction

$LiCoPO_4$ is the lithium orthophosphate with the strongest magnetoelectric (ME) effect - 20 times larger than that of $LiNiPO_4$ and 40 times larger than in $LiMnPO_4$ - coupling the crystallographic a- and b-axis [3, 44]. It is interesting to note that $LiMnPO_4$ is the lithium orthophosphate with the weakest ME effect while $LiCoPO_4$ has the strongest. Applying Hund's rules, a first approximation of the Co^{2+} moment is $S = 3/2$. However, $LiCoPO_4$ has a strong spin-orbit coupling and hence a high effective g-factor ($\Delta g/g \approx 0.3$) - much higher than in $LiNiPO_4$ - as elaborated on in section 6.1.1. Since all the lithium ortho-phosphates are isostructural with only minor differences in the location of the ions within the unit cell, the DM-interaction observed in $LiNiPO_4$ is likely to exist in $LiCoPO_4$ and it is possibly stronger than in $LiNiPO_4$. The spin arrangement forms a C_y-type structure below $T_N = 20.8K$ [1].

The spin waves of $LiCoPO_4$ have been measured by Wei Tian *et. al.* in [45]. The inelastic peaks observed were much wider than the experimental resolution, and no double peak profile was seen. Some of the data from [45] can be seen in figure 45

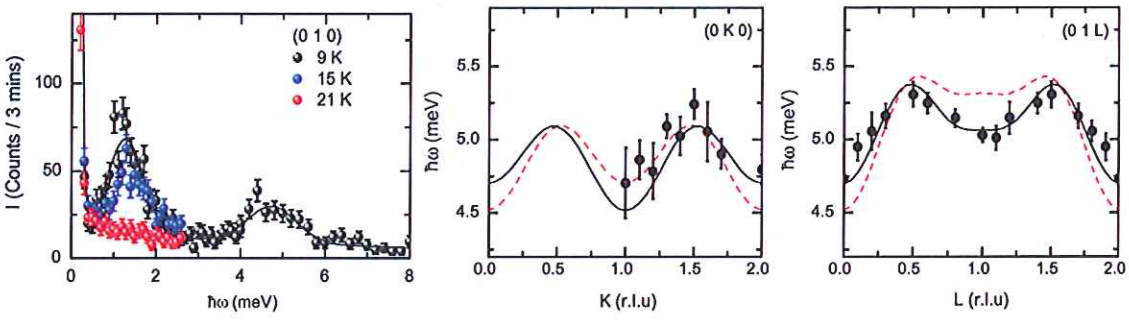

Figure 45: *Left:* Energy scan at (010). There are two dispersions of which the authors have only used the high energy branch to fit the exchange parameters. The data are from SPINS at NIST with a resolution of 0.28 meV. *Middle and right:* Dispersions of the high energy branches as measured by the BT7 thermal spectrometer at NIST with a resolution of 1 meV. The solid lines mark the fit and the dashed lines the calculated second dispersion.

As evident in figure 45 (left) Tian *et. al.* observed two distinct branches; both of them have little dispersion. They used the high energy branch for fitting the exchange parameters - using the same model as given in [15, 25]. The branch at lower energies was not explained by the authors. The width of the peaks in the energy scans is much larger than the experimental resolution on SPINS (roughly 0.28 meV). This can be due to the fact that the two predicted high energy branches have a weak dispersion and it can be difficult to distinguish the two. It can also be caused by the sample consisting of two large crystallites which are misaligned with respect to one another and therefore effectively causes four branches in the same energy regime (spin waves disperse in all directions). The exchange and single ion anisotropy parameters as given in [45] are listed in table 12 .

Table 12 shows that the dominating exchange interaction J_{bc} is much stronger than any other exchange interaction. This has to be stated cautiously though, since the errors of the determined exchange parameters are quite large. It is also noteworthy that the anisotropies are both of the order J_{bc} and almost equal. Thus, the system is Ising-like and has essentially no preferred direction in the hard plane as in the case of $LiNiPO_4$ which is XY-like.

Two unexpected effects have been seen in $LiCoPO_4$. First of all, non-zero magnetic intensity in

J_b	J_c	J_{ab}	J_{ac}	J_{bc}	D_a	D_c
0.11(16)	0.19(13)	-0.18(13)	-0.16(8)	0.74(19)	0.72(19)	0.8(2)

Table 12: The exchange interactions and anisotropies in $LiCoPO_4$ as given in [45]. All units are in meV. The very large uncertainties on most of the parameters should be noted.

the reflection (010) has been found [46], reflecting a non-zero C_x or C_z component. Second of all, weak ferromagnetism along the crystallographic b axis has been discovered. These two effects are rather surprising, since there is a mirror plane perpendicular to the b axis in $LiCoPO_4$ [47]. Furthermore, the original paper by Toru Moriya - the paper presenting a microscopic origin of the Dzyaloshinsky-Moriya interaction - proposed DM interactions as the origin of weak ferromagnetism in certain *trigonal* systems such as $MnCO_3$, $CoCO_3$. However, this is not likely in $LiCoPO_4$ under the assumption of a *Pnma* space group. The three *experimentally* proven structures C_y, C_x/C_z and F_y belong to three different irreducible representations of *Pnma*, which is not like in $LiNiPO_4$ where the small canting component A_x belongs to the same representation as the main spin component C_z.

Magnetization measurements have been performed on $LiCoPO_4$ as well. H. Wiegelmann discovered a field induced magnetic phase transition occurring at roughly 12 T [48]. In 2010, N. F Kharchenko performed pulsed magnetization measurements for fields up to 30 T and discovered three phase transitions [49].

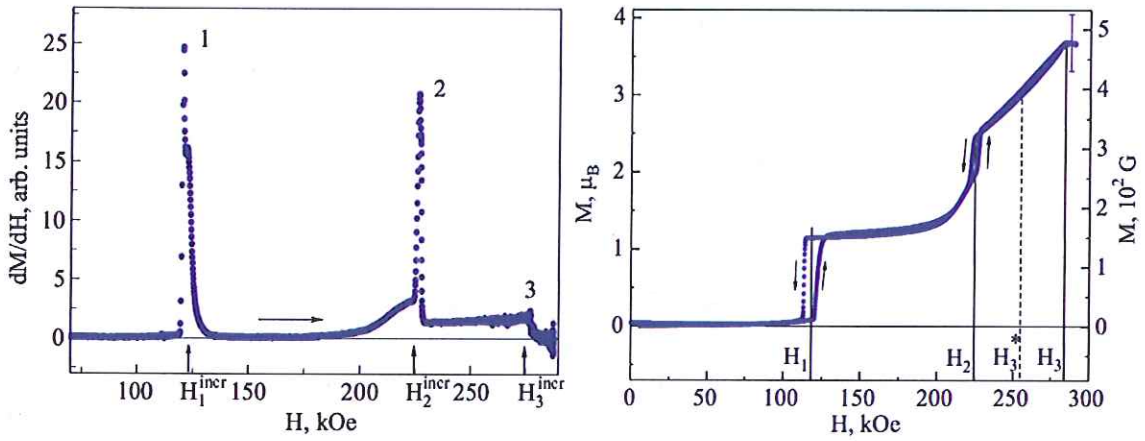

Figure 46: *Left:* Field induced phase transitions in $LiCoPO_4$ measured by pulsed magnetization. Two distinct peaks are evident followed by a constant plateau with a relatively high susceptibility. *Right:* Magnetization as a function of field. These magnetization measurements should be estimated with caution since thermal equilibrium is not reached and the field is strongly time-dependent. Results from [49].

Figure 46 (left) shows the differential magnetization as a function of field at 4.7 K. Two distinct peaks suggest two field induced magnetic phase transitions, the third phase transition being a second order gradual increase in magnetization until saturation is reached. In [49], it is suggested that saturation magnetization is reached through three different magnetic phases. Thus the first phase transition should be a field induced transition from the commensurate phase to a so-called *metamagnetic* phase with $M = 1/3M_S$ (M_S is the magnetization at saturation), where some of the spins are flipped to lower the Zeeman energy (1/6 of the spins of $M = M_S$). These magnetization measurements should be taken with a grain of salt, since in a pulsed field, the field is by definition strongly time dependent and thermal equilibrium is not reached.

6.1.1 Calculations done by Jens Jensen

In order to evaluate how close the branches are in the spin wave dispersion, Jens Jensen performed RPA calculations as the ones presented in 4.7. The results are shown in figure 47.

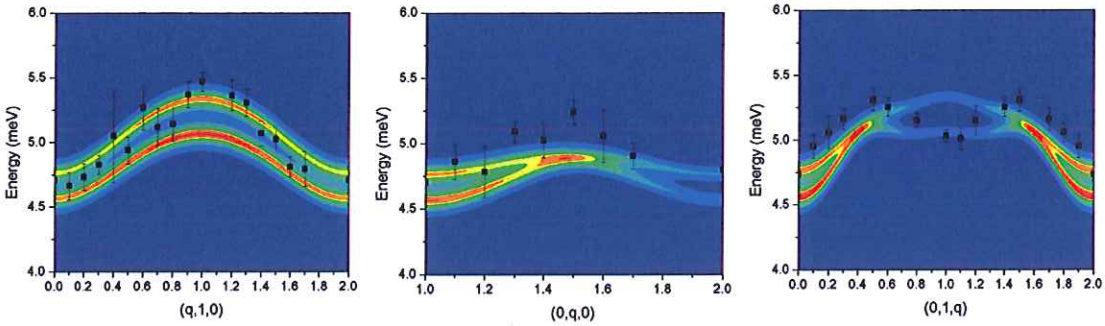

Figure 47: Spin wave calculations done by Jens Jensen assuming the exchange an anisotropy parameters reported in [45].

As evident the two branches lie within 0.3 meV, a little too close for a cold triple axis spectrometer, and way too close for a thermal one. A way to improve the rather important determination of the exchange parameters is to measure these dispersions on a spectrometer with better resolution, and on a crystal which has been certified as being monodomain. Jens Jensen also used a realistic model for the Co^{2+} ion, and calculated the spin and orbital contributions to the ordered moment J_z - he determined $S = 1.15$ and $L = 0.87$, and thus an ordered moment of $3.17\mu_B$ which is smaller than the moment reported in [46]. This calculation also implies $\Delta g/g \approx 0.3$, which is three times the value for $LiNiPO_4$. Thus, both Dzyaloshinsky-Moriya and anisotropic exchange interactions are expected to be much stronger in $LiCoPO_4$ than in $LiNiPO_4$. It should be noted, however, that such a large orbital contribution can not be considered as a simple perturbation of the quenched ground state. The effective g-value is in reality an effective *g-tensor*, which can be expected to result in a highly anisotropic moment.

6.2 Zero field spin structure - the TriCS experiment

6.2.1 Experimental setup

In order to determine the zero field spin structure, the TriCS single crystal diffractometer at the PSI was used. In many diffraction experiments a high background is accepted since a good background determination would still allow peak intensities to be well measured. When enough peaks are gathered, a good refinement of the magnetic structure can be obtained. In this experiment however, the aim was to prove or disprove very small spin components as small as $0.2\mu_B$ (as in $LiNiPO_4$). Therefore, a high background is unacceptable. A main cause of background in neutron scattering experiments is incoherent scattering from the glue used to mount the sample, that almost inevitably contains a lot of hydrogen which has a very large incoherent scattering cross section. In order to achieve a low background a very small crystal of $LiCoPO_4$ (50 mg) was wrapped in aluminum foil, twisting the foil until the crystal was fixed and the foil itself made up a rigid rod. This rod was mounted onto an aluminum sample holder with a small brass bolt.

In the TriCS experiment 1.18 Å neutrons were used. Between the source and the monochromator 80' collimation was used both vertically and horizontally, and there was no collimation between the sample and the detector. The nose between the monochromator and the sample ended in a 7 mm circular aperture. Since only the zero field structure should be determined, a so-called 4-circle

setup was used. The 4-circle setup (or Euler cradle) allows the user to virtually reach a spherical shell of reciprocal space the thickness of which is only limited by the 2θ-range of the diffractometer - which is thousands of reflections in practice. The 4-circle works by mounting the sample on a sample stick which is able to rotate round the axis of symmetry - the angle ϕ - with the sample centered on that axis. This sample stick is mounted onto the cradle, which is able to rotate the sample stick in the plane of the cradle with the sample centered on the axis of rotation - called the angle χ. The cradle-sample stick ensemble as a whole is able to rotate in the scattering plane of the detector - which is the conventionally define ω or A3 angle of diffractometers. The 2θ angle is defined as usual and is independent of the 4-circle setup. The angles are illustrated in figure 48.

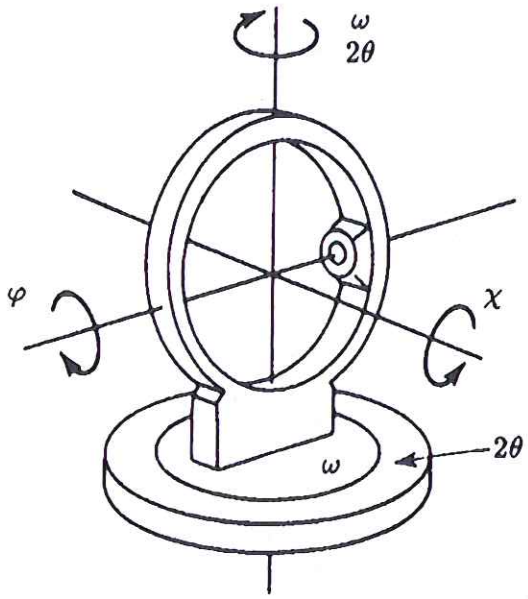

Figure 48: The definitions of angles in the 4-circle setup, which are explained in the text.

In the 4-circle setup there are three angles determining the orientation of the crystal, where in principle only two angles are needed. Often one sets up the software of the diffractometer to have the cradle plane in the plane bisecting the incoming and outgoing wave vector - containing the reciprocal lattice vector τ. If this is the case, a χ rotation is simply a rotation of the scattering vector τ in the plane containing vertical and τ itself. This is convenient since it simplifies the intuitive understanding of the angles as well as keeps the poor vertical resolution coupled to only one angle. In this setup approximately 500 reflections were collected at zero field with very low background.

6.2.2 Simplification of the possible structure using key peaks

To heavily reduce the set of irreducible basis vectors to be considered in the final refinement of the zero field magnetic structure of $LiCoPO_4$, the reflections forbidden by the selection rules of the *Pnma* space group were measured with very high statistics. The forbidden peaks with low values of $|\tau|$ were chosen to maximize the magnetic form factor. The monitor preset was a factor of ten higher compared to what is normally used for low $|\tau|$ reflections - counting 20 seconds pr. point. Figure 49 shows 4 such peaks, normalized to 50000 monitor - which is a counting time of roughly 2 seconds.

As evident from figure 49, all four peaks have zero magnetic intensity within errors. The (300) peak rules out A_z and A_y components while the (120) reflection shows a vanishing A_x component

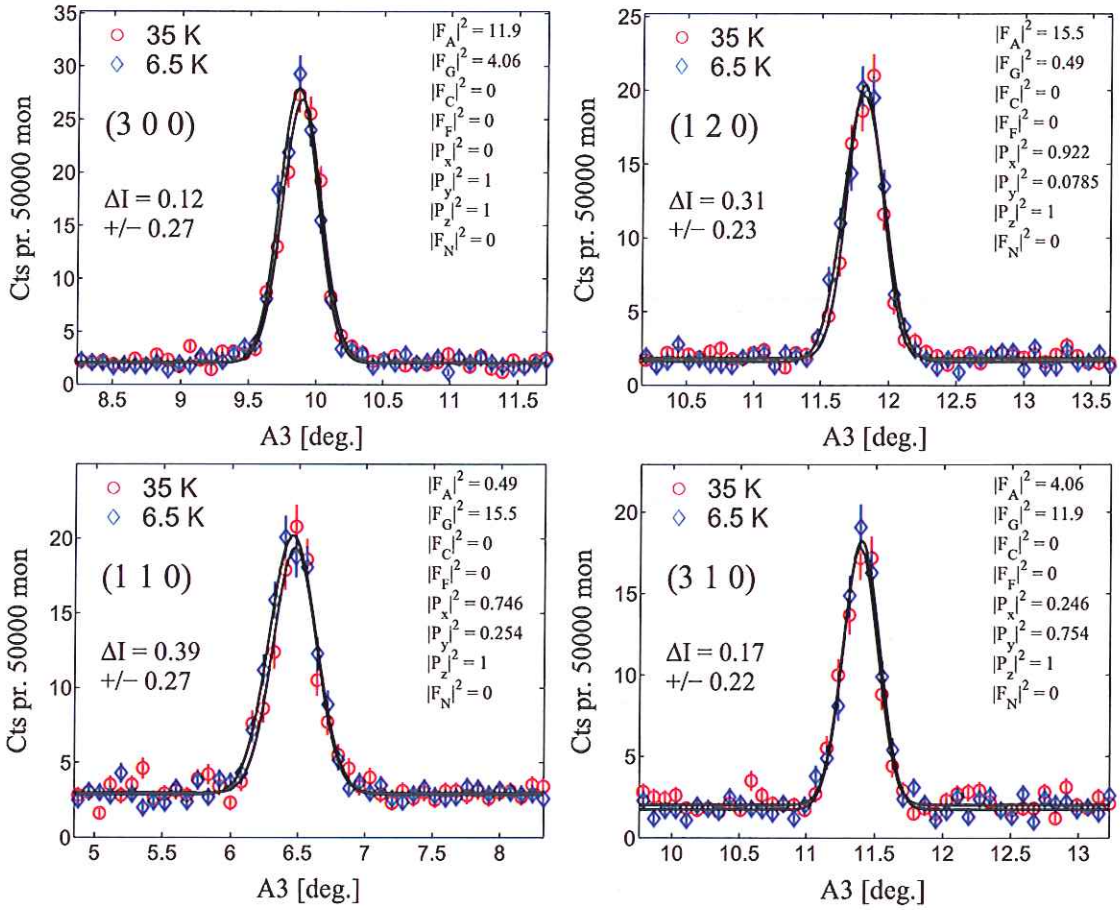

Figure 49: The reflections (300), (120), (110) and (310) - central for ruling out the A and G type components - as measured at 6.5 K and 35 K respectively. The plots show the difference between the two integrated intensities - ΔI - and the calculated structure and polarization factors in terms of the irreducible representations. Notice the low background of 2 counts pr. 50000 monitor, compared to 30 counts in the $LiMnPO_4$ experiment.

in zero field. All G type components are ruled out by the (110) and (310) reflections in zero field, as evident on the two bottom peaks in figure 49. The F-type components are very difficult to rule out by neutron scattering since the forbidden peaks have a zero structure factor of zero for ferromagnetic components. They have been ruled out, however, by magnetization measurements, to the extent relevant for neutron scattering experiments [47]. The weak ferromagnetism found in [47] is far below what can be expected to be seen in a neutron diffraction experiment. The extent to which the A and G type components have been ruled out can be estimated by considering the two reflections (001) and (003) plotted in figure 50.

Figure 50 shows the (001) and (003) reflection as measured by TriCS. Assuming a zero G component, the intensity observed in these peaks can be ascribed to the non-zero C-type structure factor. Assuming that the form factor squared is roughly the same when comparing the (300) and (001) reflection (even though $|\tau|$ is roughly the same, the form factor could be anisotropic), there would be an intensity of roughly $|F_A^{300}|/|F_C^{001}| \cdot I_{001}^{mag} \approx 252[(\text{cts} \cdot \text{deg.})/\text{mon}]$ in the (300) reflection if the structure consisted solely of an A_y or an A_z component. The zero in the (300) reflection is therefore determined within an error 0.1 % of the expected intensity in case of an A_z or A_y structure. The

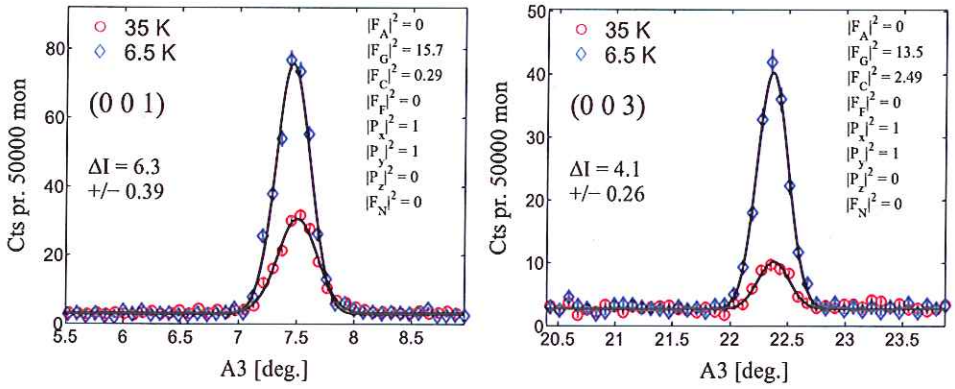

Figure 50: The reflections (001) and (003) central for estimating the experimental precision. The plots show the omega scan measuring the integrated intensity, the difference between the two integrated intensities - ΔI - and the calculated structure and polarization factors in terms of the irreducible representations.

staggered AFM moment of A type structure is therefore determined to be less than

$$\delta M^{\dagger}_{A,G} \approx \sqrt{0.001} \cdot 3.5\mu_B \approx 0.1\mu_B \tag{6.1}$$

This precision is quite respectable for a neutron diffraction experiment and can be entirely attributed to the low background.

6.2.3 Refinement of the zero field magnetic structure of $LiCoPO_4$

In this TriCS experiment there were no irregular peaks as in the $LiMnPO_4$ experiment with the cryomagnet. Like in the $LiMnPO_4$ the peaks with very high intensity were discarded. The peaks with a high nuclear cross section were discarded as well. In total 51 magnetic Bragg peaks were used in the refinement. In the $LiCoPO_4$ the crystal was much smaller than in the $LiMnPO_4$ (as mentioned in the experimental details). Furthermore, the crystal was more regularly shaped than the $LiMnPO_4$ crystal; the dimensions are comparable in all directions (although the shape can hardly be classified as spherical). Furthermore, the 4-circle setup is designed for diffraction experiments, while the magnet used in the $LiMnPO_4$ experiment caused some irregular peaks. All in all, it can be said that a refinement of the magnetic moment and the magnetic structure is somewhat more trustworthy in this experiment, due to the aforementioned factors and the low background. The scale factor to be used in the magnetic refinement (crucial for a correct determination of the size of the ordered magnetic moments) was obtained from a rough refinement of the nuclear structure using peaks measured at 35 K. This refinement only has the atomic positions and the scale factor as refinement parameters; absorption corrections, extinction corrections, Debye-Waller factors have been left out. The observed and calculated structure factors for such a rough nuclear refinement are shown in figure 51

As evident in figure 51 the scale factor refinement is not a good structural refinement - with $R_{F^2} = 23.3$ and $\chi^2 = 111$ - but the scale factor seems to be reasonably well determined in the entire range. Both increase and decrease of the slope of only 10 % worsen the fit considerably. The peaks used in both the nuclear and magnetic refinements are all from the same quadrant which ensures that the crystal orientation in the beam is roughly constant - so any absorption effects is expected to be constant to some extent and therefore absorbed in the scale factor.

As mentioned previously, any A, G or F components have been thoroughly ruled out by TriCS data and magnetization data. The relevant components to refine are therefore merely C_x, C_y and C_z.

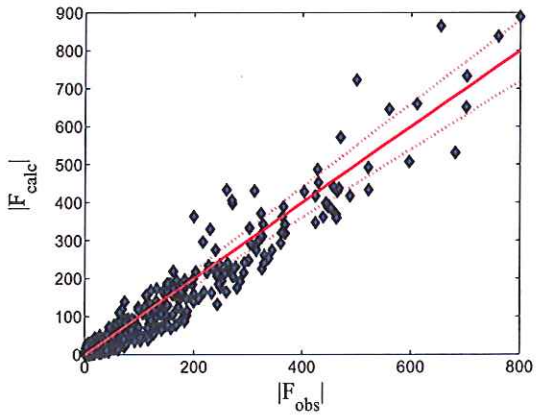

Figure 51: Observed and calculated structure factors for the refinement of the nuclear structure. The solid red line shows the $F_{obs} = F_{calc}$ line and the two stapled lines denote a 10 percent increase and decrease in structure factor, respectively

Therefore, three different magnetic vectors have been refined for comparison: c_1C_y, $c_1C_y + c_2C_x$ and $c_1C_y + c_2C_z$. The results and goodness of fits are listed in table 13

	c_1	c_2	R_{F^2}	R_{wF^2}	R_F	χ^2
$c_1C_y + c_2C_x$	3.32(4)	0.57(10)	29.5	20.4	24.5	2.06
$c_1C_y + c_2C_z$	3.16(4)	0.007(130)	29.3	22.4	23.7	2.49
c_1C_y	3.16(4)	-	29.3	22.4	23.7	2.44

Table 13: Refinement parameters and goodness-of-fit parameters for three different spin structure vectors. As evident, the $C_y + C_x$ structure gives the lowest reduced χ^2.

As evident in table 13, the best fit to the data is the $c_1C_y + c_2C_x$ structure. This spin structure has the lowest weighted R value and the lowest χ^2. Even though the R_{F^2} and R_F values are actually smaller when refining with the c_1C_y and $c_1C_y + c_2C_z$ structures, these values do not take the error of the peak intensities into consideration. The fact that the $c_1C_y + c_2C_z$ does not produce a C_z component within errors makes this structure even more rejectable. From the ruling out of F-, G- and A-type components, it is therefore straightforward to conclude from the refinement of the $c_1C_y + c_2C_x$ vector, that the zero field spin structure is a $3.3\mu_B \cdot C_y + 0.6\mu_B \cdot C_x$. This gives a spin rotation of $\theta_x = 9.5° \pm 1.7°$, which is quite a lot. The observed and calculated structure factors and the difference between the two is shown in figure 52, along with an illustration of the zero field magnetic structure in $LiCoPO_4$ as determined by TriCS.

The angle of rotation is almost a factor of 2 higher than that determined in [46]. In [46], the authors use elastic peaks (not specified in the text) obtained at a thermal triple axis spectrometer using $\lambda = 2.36$ Å. So the wavelength used in [46] is twice that used on TriCS. Since $R \propto \lambda^3$, the reflectivity will be 8 times that of TriCS. The crystal size is not specified in [46], but if they had used a crystal larger than 50 mg as that used on TriCS there could have been substantial extinction and absorption effects. A full refinement of the magnetic structure has not been done in [46], so there is a probability that these effects could have caused errors in the estimation of canting angle and total moment. The moment determined in [46] is 4.2 μ_B which is 30 % larger than the TriCS result. Overestimating the total moment could result in an underestimation of the angle of rotation, if the (010) reflection is the only reflection used to determine the angle. The uncertainty of the angle of rotation as determined by TriCS is quite high: 1.7°. So the TriCS result could be overestimated. No error of the canting angle is given in [46], but the error could hardly have been

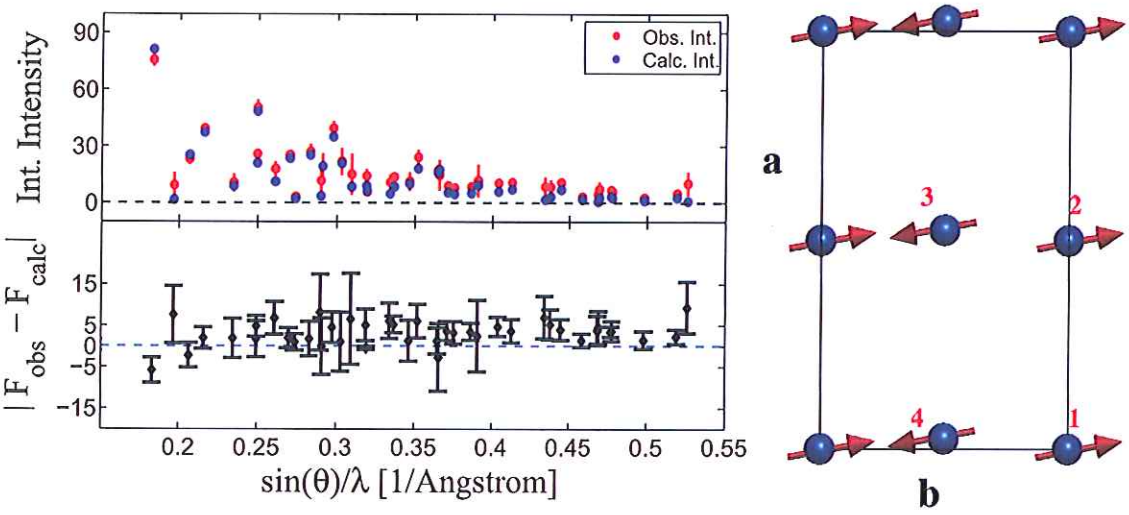

Figure 52: *Top left:* Integrated intensity of all peaks accepted by the author and FullProf as valid magnetic peaks plotted along with the calculated values for a $C_y + C_x$ refinement. *Bottom left:* Difference between observed and calculated intensities. *Right:* The zero field magnetic structure of $LiCoPO_4$. The angle of collinear spin rotation towards the a-axis has been exaggerated for the sake of illustration.

less than $1° \approx 0.05\mu_B$ which must be considered as a reasonable lower limit of what can be seen in neutron diffraction experiments. So the democratically determined angle of rotation would be:

$$\theta_x = 7.1° \pm 2°, \tag{6.2}$$

which is still quite a lot.

It is interesting that the refined ordered moment is $\sqrt{C_y^2 + C_x^2} \approx 3.35\mu_B$ when comparing to the prediction of Jens Jensen of $3.17\mu_B$, which were virtually independent of the strength of the exchange interactions and therefore robust with respect to the poor quality of the spin wave data. Therefore, this structural refinement provides experimental support to the theoretical calculation of $\Delta g/g \approx 0.3$ showing significant orbital contributions - and therefore to the probability of strong DM and anisotropic exchange interactions. If these two effects are much stronger than in $LiNiPO_4$, the question remains if this collinear rotation of the spins could have been caused by any one of these interactions. In case of the DM interaction the answer is simply no, since no canting is seen. However, the strength of the anisotropic exchange Hamiltonian $\mathcal{H}_{ax} = \mathbf{S}_i \cdot \mathcal{T}_{ij}^{(2)} \cdot \mathbf{S}_j$ should be much stronger than in $LiNiPO_4$ and the term itself could cause such a coupling. That may be so, but under the assumption of a *Pnma* space group, *no Hamiltonian quadratic in spins* can cause such a spin rotation. This is due to the mirror plane perpendicular to the b-axis (m_{zx}, see table 5). This symmetry element transforms $\mathbf{r}_i \to \mathbf{r}_i$ for $i = 1, 2, 3, 4$ and takes the spin components $(S_x, S_y, S_z) \to (-S_x, S_y, -S_z)$. It therefore holds for any Hamiltonian quadratic in spins that

$$\text{For any } \mathcal{H}_{rot,x} = \sum_{kij} \varepsilon_{kij} S_i^x S_j^y : \quad m_{xz} \mathcal{H}_{rot,x} m_{xz}^\dagger = -\mathcal{H}_{rot,x}, \tag{6.3}$$

and similarly for a Hamiltonian $\mathcal{H}_{rot,z}$ rotating the spins towards the c-axis. The general Hamiltonian is simply not invariant under the mirror plane symmetry. Therefore, assuming a quadratic Hamiltonian, at least the mirror plane must be broken below T_N in $LiCoPO_4$. This is also supported by the fact that all the forbidden nuclear reflections seem to have finite - but very small - intensity.

6.3 Magnetic structure of $LiCoPO_4$ in field applied along a

To examine the magnetic structure of $LiCoPO_4$ in applied field, the RITA-II triple axis spectrometer was used with the 15 T cryomagnet. The low background on a cold triple axis spectrometer, the longer neutron wavelength and the high field available makes this setup ideal to detect small changes in the magnetic structure. To reach high $|\tau|$ reflections, second order neutrons were used; the analyzer was set to reflect 20 meV neutrons and the Be-filter removed. 40' collimation was used between the monochromator and the sample, and no collimation was used between the sample and the detector. Only the intensity from the central blade was used. The crystal was mounted with the a-axis vertical and the bc plane coinciding with the scattering plane of the spectrometer. All the peaks reachable in a single quadrant of reciprocal space were measured in zero field and at 13 tesla applied along a.

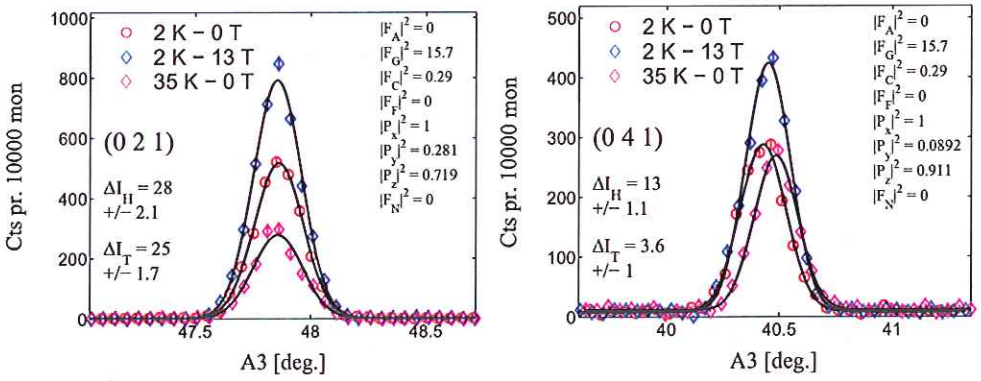

Figure 53: The integrated intensity of the (021) and (041) reflections at zero field and 13 tesla respectively. The finite nuclear background recorded at 35 K in zero field is plotted for comparison. These two reflections reflect the same magnetic symmetries and they both show a significant increase in intensity - ΔI_H - upon applying field along a. The zero field magnetic intensity ΔI_T is shown as well.

Figure 53 shows a significant increase of integrated intensity in both the (021) and the (041) reflections, both reflecting G type and a little C type components normalized to 10000 monitor which is roughly 10 s of counting time on RITA-II. This is by itself quite peculiar since both C and G type components are antiferromagnetic; applying a field along a induces staggered magnetism. This induced intensity *could* be nuclear, and using unpolarized neutrons the author possesses no evidence to the contrary, which is important to underline. After all, magnetoelectricity is exactly the effect of moving atoms with an applied magnetic field. However, the atomic shifts necessary for generating the observed polarization are very small. In a field of 13 T, the *maximum* polarization density of $LiCoPO_4$ is $1 \cdot 10^{-2}$ $\mu C/cm^2$. Multiplied with the volume of the unit cell in cm - $3 \cdot 10^{-22} cm^3$ - and converting from cm to Å and from C to e gives a separation of two ions in the neighborhood of 10^{-3} Å! This is simply not enough to cause an intensity effect in a neutron scattering experiment - at least not in a simple triple axis setup. Furthermore, if the increase in intensity is directly understandable in terms of the irreducible representations of the magnetic structure, chances are that this will be the physical explanation. This is, however - as previously mentioned - not empirically shown in this work. The intensity increase in figure 53 points towards an induced G_x or a G_z component. In principle it can also be a C type component, but if that was the case, it should be of the same order of magnitude as the size of the ordered, which is unthinkable.

To conclusively determine the symmetry of the field induced staggered magnetization, the reflections (001), (032) and (050) were measured at 13 tesla both in applied and zero field. The omega scans

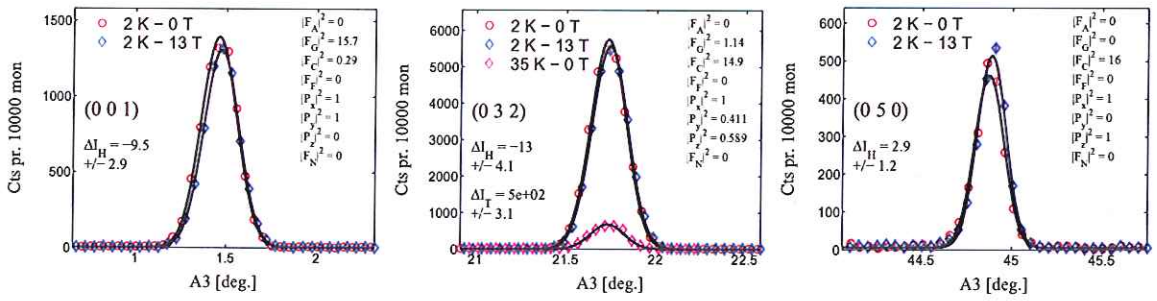

Figure 54: The integrated intensity of the (001), (032) and (050) reflections at zero field and 13 tesla applied along a respectively. The nuclear background has only been measured on the (032) peak. As evident the (001) reflection rules out G_x and G_y components, while the (032) and (050) rule out any C-type components. There is a small increase of intensity in the (050) peak, but nowhere near enough to be comparable to the field induced signal in the (041) reflection which has a comparable magnetic form factor.

are shown in figure 54. As evident, there is no field induced intensity in the (001) peak reflecting G_x and G_y components. Furthermore, neither the (032) reflection not the (050) reflection has noticeable field induced intensity. Hence, the C-type components can be ruled out definitively. The only remaining possibility is that the field induced antiferromagneic order has a G_z structure. Hence, there is a coupling between F_x and G_z components. This is indeed very possible when considering the $Pnma$ symmetries; F_x and G_z belong to the same irreducible representation - as evident in table 3 - and therefore terms coupling these two spin structures are allowed in a quadratic spin Hamiltonian.

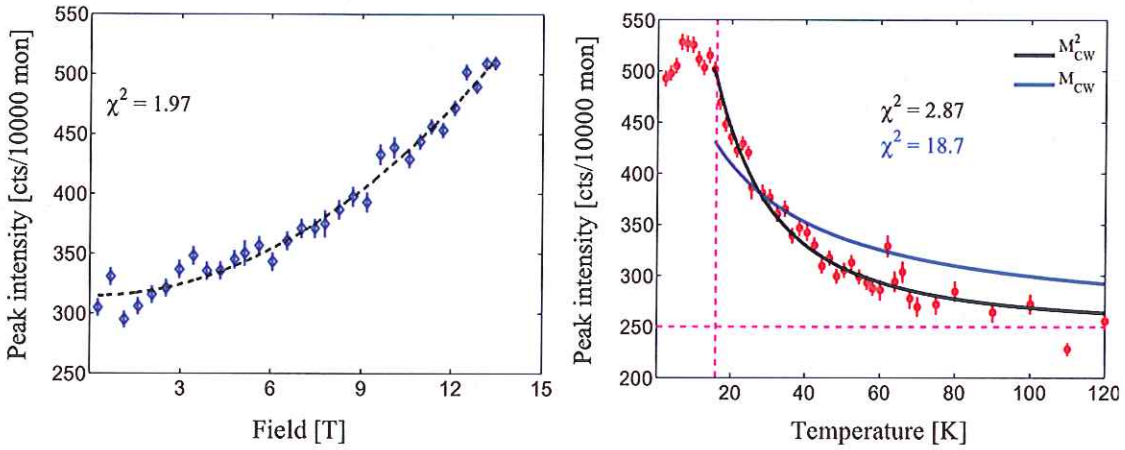

Figure 55: *Left:* Peak intensity of the (021) reflection as function of field at T = 2 K. The curve has been fitted to the polynomial $I = H^2 + I_0$ - the fit is quite acceptable *Right:* Peak intensity of the 021 reflection as a function of temperature at $\mu_0 H = 13.5T$. The curve has been fitted to an AFM Curie-Weiss (CW) law *squared* $M^2_{CW} = I_0 + \left(\frac{A}{(T_N+T)}\right)^2$ as well as a CW law for comparison. In both cases, the background and Neel temperature was fixed to observed values, $I_0 = 250$ and $T_N = 16$ K. As evident, the squared CW law gives the best fit, in agreement to the fact that the neutron scattering cross section is proportional to the square of the moment.

Figure 55 (left) shows the peak intensity of the (021) reflection as a function of field. If the G_z staggered component is directly proportional to the field induced ferromagnetic moment F_x, then

the cross section - and hence the peak intensity - should grow as the square of the applied field. As evident, this is indeed the case, the fit to the function $I_{021} = H^2 + I_0$ is as good as can be expected. Figure 6.3 (right) shows the peak intensity of (021) as a function of temperature. As there is a finite ordered F_x component in an applied field even above T_N the peak intensity should drop off as $I_{021} \sim 1/T$ above T_N. Again, this is the case; even above T_N there is a field induced G_z component that drops off as a Curie-Weiss law above T_N. This strongly supports the assumption that this field induced intensity is magnetic in origin.

Normally, the mixing of two different irreducible basis vectors in the structure factor of one reflection is a bit inconvenient, but in trying to estimate the size of the staggered G-type moment along z the mixing is immensely convenient as no assumptions about the magnetic form factor is needed (the two contributions reveal themselves in the same scattering vector). Even better, the Lorentz factor and the absorption correction cancel out. Since the peak intensity at maximum is below 100 counts pr. second - extinction effects are expected to be negligible. The relationship between the two magnetic intensities extractable from the (021) data is

$$\frac{I_H}{I_T} = \frac{M_{G_z}^{\dagger 2}|F_G|^2|P_z|^2}{M_{C_y}^{\dagger 2}|F_C|^2|P_y|^2} \Rightarrow M_{G_z}^{\dagger} = \sqrt{\frac{I_H M_{C_y}^{\dagger 2}|F_C|^2|P_y|^2}{I_T|F_G|^2|P_z|^2}} = 0.30 \pm 0.02\mu_B, \tag{6.4}$$

where I_H and I_T is as shown on figure 53. This corresponds to a canting angle of $5.2° \pm 0.35$ with respect to the main C_y component! The uncertainties given here are the statistical ones calculated by propagation of uncertainties and should be regarded as an absolute minimum. This is a quite high moment; the zero field canting moment in $LiNiPO_4$ is also 0.3 μ_B but this is a result of DM coupling proportional to the *main* spin component with moment 2.2 μ_B. In $LiCoPO_4$ the staggered moment of 0.3 μ_B is a result of a coupling which is only proportional to the *field induced moment*, which must be much smaller than 2.2 μ_B. The spin structure for strong field applied along a is illustrated in figure 56.

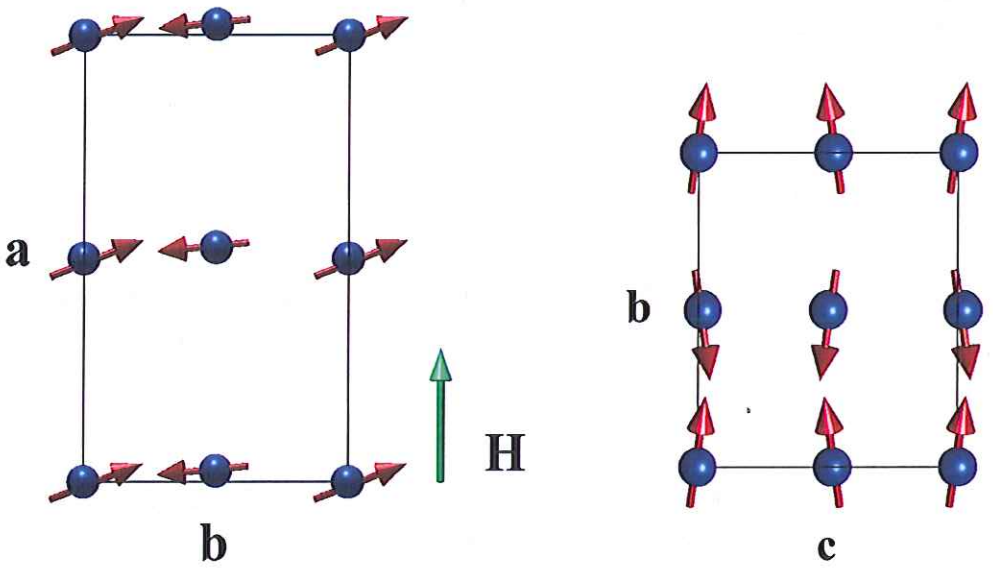

Figure 56: *Left:* Spin structure projected onto the ab-plane showing the C_y, C_x and F_x components. *Right:* Projection of the spin structure onto the bc-plane showing the C_y and the G_z components.

6.3.1 Dzyaloshinsky-Moriya interaction in $LiCoPO_4$

Thomas B.S. Jensen proposed in [15], that the zero field canting in $LiNiPO_4$ is caused by a DM mechanism coupling either ions $1 \leftrightarrow 4$, $2 \leftrightarrow 3$ or $1 \leftrightarrow 2$ and $3 \leftrightarrow 4$. He applied the symmetry arguments mentioned in 2.2.3, to exclude all other forms of $\mathbf{D}$ than $\mathbf{D}_{14} = (0, D^y_{14}, 0) = -\mathbf{D}_{23} \equiv \mathbf{D}$ and $\mathbf{D}_{12} = (0, D^y_{12}, 0) = \mathbf{D}_{34} \equiv \mathbf{D}$. This would cause DM Hamiltonians on the form (written only for a single unit cell):

$$\begin{aligned} \mathcal{H}^1_{DM} &= \mathbf{D}_{14} \cdot [\mathbf{S}_1 \times \mathbf{S}_4] - \mathbf{D}_{14} \cdot [\mathbf{S}_2 \times \mathbf{S}_3] \\ &= D^y_{14}(S^z_1 S^x_4 - S^x_1 S^z_4 - (S^z_2 S^x_3 - S^x_2 S^z_3)), \quad \text{and} \qquad (6.5) \\ \mathcal{H}^2_{DM} &= \mathbf{D}_{12} \cdot [\mathbf{S}_1 \times \mathbf{S}_2] + \mathbf{D}_{12} \cdot [\mathbf{S}_3 \times \mathbf{S}_4] \\ &= D^y_{12}(S^z_1 S^x_2 - S^x_1 S^z_2 + (S^z_3 S^x_4 - S^x_3 S^z_4)). \qquad (6.6) \end{aligned}$$

In the case of $LiNiPO_4$, this DM interaction favors an A_x component since the main spin structure is C_z. In the case of $LiCoPO_4$ in an applied field along x, there is a field induced ferromagnetic component along x - F_x - and the spin components along x are the same for all magnetic ions - S^x. Thus, the DM terms become:

$$\begin{aligned} \mathcal{H}^1_{DM} &= D^y_{14} S^x (S^z_1 - S^z_4 - (S^z_2 - S^z_3)) \quad \text{and} \qquad (6.7) \\ \mathcal{H}^2_{DM} &= D^y_{12} S^x (S^z_1 - S^z_2 + (S^z_3 - S^z_4)). \qquad (6.8) \end{aligned}$$

Thus, both these terms favors a $(+,-,+,-)$ symmetry along z in case of a finite F_x component, which is exactly the observed G_z component. It can therefore be said that the DM interaction that was shown in [15] to exist in $LiNiPO_4$ also exists in $LiCoPO_4$. In principle, this DM term also couples the observed minor C_x component in $LICoPO_4$ to an A_z component, but since the C_x component is so small the canting moment would be too small to observe in the TriCS experiment. In principle, it could be observable in a dedicated experiment with high flux and low background.

This existence of a strong DM term in $LiCoPO_4$ becomes even more interesting in light of the empirical evidence that some of the symmetry elements of $Pnma$ are broken in $LiCoPO_4$ - at least the mirror plane m_{xz}. There is a possibility that the breaking of certain symmetry elements makes new DM possible, and if so, that the strength of these interactions could be significant since a very strong DM mechanism is now on firm empirical ground. The possible consequences of a strong DM interaction and even a strong anisotropic exchange term will be examined in the next section.

6.4 Possible additional DM mechanisms in $LiCoPO_4$

Now that the existence of a strong DM interaction has been proposed as a probable cause for the substantial field induced staggered moment, it is interesting to evaluate the DM interaction in light of the accumulated evidence that some of the symmetry elements are simply not there in $LiCoPO_4$. In this section, the consequences of a hypothetically broken symmetry in terms of allowed DM interactions is examined using the same tools as developed in [15]. Scrutinizing these possible DM interactions may also lead to some insight into which symmetries are broken. It is important to underline that these considerations are merely speculative and only the DM term proposed in the previous section has been shown experimentally. For convenience the transformed magnetic ions and the transformed spin components are re-stated in table 14 (identical to table 5).

The method used to determine possible DM-terms is the same as in [15]. The first and foremost requirement is that any DM-coupling between two ions needs to be antisymmetric with respect to ion exchange:

$$\mathbf{D}_{ij} = -\mathbf{D}_{ji} \qquad (6.9)$$

G	1	$2'_x$	$2'_y$	$2'_z$	I	m'_{xy}	m_{xz}	m'_{yz}
$\mathbf{r}_1$	$\mathbf{r}_1$	$\mathbf{r}_2$	$\mathbf{r}_3$	$\mathbf{r}_4$	$\mathbf{r}_3$	$\mathbf{r}_2$	$\mathbf{r}_1$	$\mathbf{r}_4$
$\mathbf{r}_2$	$\mathbf{r}_2$	$\mathbf{r}_1$	$\mathbf{r}_4$	$\mathbf{r}_3$	$\mathbf{r}_4$	$\mathbf{r}_1$	$\mathbf{r}_2$	$\mathbf{r}_3$
$\mathbf{r}_3$	$\mathbf{r}_3$	$\mathbf{r}_4$	$\mathbf{r}_1$	$\mathbf{r}_2$	$\mathbf{r}_1$	$\mathbf{r}_4$	$\mathbf{r}_3$	$\mathbf{r}_2$
$\mathbf{r}_4$	$\mathbf{r}_4$	$\mathbf{r}_3$	$\mathbf{r}_2$	$\mathbf{r}_1$	$\mathbf{r}_2$	$\mathbf{r}_3$	$\mathbf{r}_4$	$\mathbf{r}_1$
S_x	S_x	S_x	$-S_x$	$-S_x$	S_x	$-S_x$	$-S_x$	S_x
S_y	S_y	$-S_y$	S_y	$-S_y$	S_y	$-S_y$	S_y	$-S_y$
S_z	S_z	$-S_z$	$-S_z$	S_z	S_z	S_z	$-S_z$	$-S_z$

Table 14: Transformation properties of the magnetic ions in the lithium orthophosphates and their spin under the symmetry operations of the *Pnma* space group.

The second requirement is the elegant trick derived in [15]: The *transformed* pseudo vector components D^i_{14} of the *untransformed* ionic sites 1 and 4 - $RD^i_{14}R^\dagger$ - has to be equal to the *untransformed* pseudo vector components of the *transformed* sites $D^i_{R(1)R^\dagger R(4)R^\dagger}$, where $R \in G$

$$RD^i_{14}R^\dagger = D^i_{R(1)R^\dagger R(4)R^\dagger} \tag{6.10}$$

The last consideration only used once in this section is that if two ions i and i' have identical surroundings and two other ions j and j' have identical surroundings then $\mathbf{D}_{ij} = \mathbf{D}_{i'j'}$ if the exchange path between i and j and between i' and j' are equivalent. This is perhaps not surprising. The considerations in the next sections are summed up in the following:

- **In section 6.4.1** it is assumed that only the mirror plane - m_{xz} - is broken as suggested using equation 6.3. This will be shown to have little consequence for the possible DM interactions in zero field. The transformation tables comparing the left and right hand sides of equation 6.10 for all symmetry elements are given in this section, and used throughout the following sections.
- **In section 6.4.2** the possibility of the DM interaction and the anisotropic exchange interaction causing weak ferromagnetism is examined. Since DM terms causes spin canting and can therefore not explain the ferromagnetic component parallel to the spins, a possible anisotropic exchange-Hamiltonian will be suggested as a candidate for causing weak FM. This requires that several of the *Pnma* symmetry elements are note there in zero field.
- **In section 6.4.3** a possible anisotropic exchange-Hamiltonian will be suggested as a candidate for the collinear rotation of the spins towards the x-axis. The symmetry elements that need to be broken in order for this to be possible are given as well.
- **Lastly, in section 6.4.4** The DM interaction is suggested as a mechanism for causing a magneto-electric effect. It is shown that in an applied field, the system could be able to use the field induced ferromagnetic component in conjunction with the zero-field magnetic structure components to lower the DM magnetic energy by facilitating a polarization. In the case of fields applied along the y axis, this would require the mirror plane m_{xz} to be broken in order to explain a ME effect. The possible DM-terms is not claimed to be the primary cause of the ME-effect, but merely suggested as a possible magnetic mechanism for causing polarization.

6.4.1 Removal of mirror plane - possible DM interactions

In section 6.2.3 and especially in equation 6.3, it was shown that *any* Hamiltonian quadratic in spins that couple x and y spin components is forbidden in zero field by the mirror plane perpendicular

to b, m_{xz}. An instructive first step is simply removing this symmetry from the group - G - of $Pnma$ symmetry elements. Applying the condition in equation 2.78 that $R\mathrm{D}_{AB}R^{\dagger} = \mathrm{D}_{RAR^{\dagger}RBR^{\dagger}}$ needs to be satisfied in order for a DM term to be invariant, results in a straightforward method to evaluate possible terms.

DM coupling between ions $1 \leftrightarrow 4$ and $2 \leftrightarrow 3$

In the case of a coupling between ions $1 \leftrightarrow 4$ and $2 \leftrightarrow 3$, the transformation table for DM pseudo vector components $(D^x_{14}, D^z_{14}, D^z_{14})$ and the ions themselves is given below

-	1	$2'_x$	$2'_y$	$2'_z$	I	m'_{xy}	m_{xz}	m'_{yz}
$RD^x_{14}R^{\dagger}$	D^x_{14}	D^x_{14}	$-D^x_{14}$	$-D^x_{14}$	D^x_{14}	$-D^x_{14}$	$-D^x_{14}$	D^x_{14}
$D^x_{R(1)R^{\dagger}R(4)R^{\dagger}}$	D^x_{14}	D^x_{23}	D^x_{32}	D^x_{41}	D^x_{32}	D^x_{23}	D^x_{14}	D^x_{41}
$RD^y_{14}R^{\dagger}$	D^y_{14}	$-D^y_{14}$	D^y_{14}	$-D^y_{14}$	D^y_{14}	$-D^y_{14}$	D^y_{14}	$-D^y_{14}$
$D^y_{R(1)R^{\dagger}R(4)R^{\dagger}}$	D^y_{14}	D^y_{23}	D^y_{32}	D^y_{41}	D^y_{32}	D^y_{23}	D^y_{14}	D^y_{41}
$RD^z_{14}R^{\dagger}$	D^z_{14}	$-D^z_{14}$	$-D^z_{14}$	D^z_{14}	D^z_{14}	D^z_{14}	$-D^z_{14}$	$-D^z_{14}$
$D^z_{R(1)R^{\dagger}R(4)R^{\dagger}}$	D^z_{14}	D^z_{23}	D^z_{32}	D^z_{41}	D^z_{32}	D^z_{23}	D^z_{14}	D^z_{41}

Table 15: Transformation table for the *transformed* pseudo vector components (D^i_{14}) of the *untransformed* ionic sites 1 and 4 - $RD^i_{14}R^{\dagger}$ - and the *untransformed* eigenvector components on the *transformed* sites $D^i_{R(1)R^{\dagger}R(4)R^{\dagger}}$. For a DM term to be invariant the two quantities have to be equal.

As evident in table 15, the mirror plane m_{xz} excludes all but a D^y_{14} component. And if such a component exists, the glide plane m'_{xy} requires that there must be a D^y_{23} component as well with the opposite sign. This is exactly the DM interaction proposed in the previous section to explain the field induced signal on the (021) and (041) reflections. However, removing the mirror plane m_{xz} does not change this situation. The glide plane m'_{yz} requires that $D^x_{14} = D^x_{41}$ which is prevented by the antisymmetric nature of the DM interaction: $D^x_{14} = D^x_{41} = -D^x_{14} = 0$. When this is established, several other symmetry elements require the x component of the DM pseudo vector between ions 2 and 3 to be zero as well. This can be seen in table 15. Furthermore, the two-fold screw axis $2'_z$ requires the z component of the DM pseudo vector to be 0, envoking the exact same arguments as in the case of the x component

-	1	$2'_x$	$2'_y$	$2'_z$	I	m'_{xy}	m_{xz}	m'_{yz}
$RD^x_{12}R^{\dagger}$	D^x_{12}	D^x_{12}	$-D^x_{12}$	$-D^x_{12}$	D^x_{12}	$-D^x_{12}$	$-D^x_{12}$	D^x_{12}
$D^x_{R(1)R^{\dagger}R(2)R^{\dagger}}$	D^x_{12}	D^x_{21}	D^x_{34}	D^x_{43}	D^x_{34}	D^x_{21}	D^x_{12}	D^x_{43}
$RD^y_{12}R^{\dagger}$	D^y_{12}	$-D^y_{12}$	D^y_{12}	$-D^y_{12}$	D^y_{12}	$-D^y_{12}$	D^y_{12}	$-D^y_{12}$
$D^y_{R(1)R^{\dagger}R(2)R^{\dagger}}$	D^y_{12}	D^y_{21}	D^y_{34}	D^y_{43}	D^y_{34}	D^y_{21}	D^y_{12}	D^y_{43}
$RD^z_{12}R^{\dagger}$	D^z_{12}	$-D^z_{12}$	$-D^z_{12}$	D^z_{12}	D^z_{12}	D^z_{12}	$-D^z_{12}$	$-D^z_{12}$
$D^z_{R(1)R^{\dagger}R(2)R^{\dagger}}$	D^z_{12}	D^z_{21}	D^z_{34}	D^z_{43}	D^z_{34}	D^z_{21}	D^z_{12}	D^z_{43}

Table 16: Transformation table for the *transformed* pseudo vector components (D^i_{14}) of the *untransformed* ionic sites 1 and 2 - $RD^i_{12}R^{\dagger}$ - and the *untransformed* pseudo vector components on the *transformed* sites $D^i_{R(1)R^{\dagger}R(2)R^{\dagger}}$. For a DM term to be invariant the two quantities have to be equal.

DM coupling between ions $1 \leftrightarrow 2$ and $3 \leftrightarrow 4$

The same procedure is used in the case of a coupling between ions $1 \leftrightarrow 2$ and $3 \leftrightarrow 4$. The transformation table for this type of DM term is given in table 16. Again it is evident that the removal of the mirror plane m_{xz} from the symmetry group makes no difference. The two screw axes $2'_y$ and $2'_z$ require that the x component fulfills $D^x_{12} = -D^x_{34} = -D^x_{43}$ which is impossible unless the x components of the DM pseudo vector are 0. The same holds for possible z-components of **D** which is clear when considering the symmetry elements $2'_z$ and m'_{yz}. The only possible component is $D^y_{12} = D^y_{34}$ components, which can also explain the observed field induced G_z component, by the way.

DM coupling between ions $1 \leftrightarrow 3$ and $2 \leftrightarrow 4$

The case of a coupling between ions $1 \leftrightarrow 3$ and $2 \leftrightarrow 4$ is especially easy. The transformation table is shown below:

-	1	$2'_x$	$2'_y$	$2'_z$	I	m'_{xy}	m_{xz}	m'_{yz}
$RD^x_{13}R^\dagger$	D^x_{13}	D^x_{13}	$-D^x_{13}$	$-D^x_{13}$	D^x_{13}	$-D^x_{13}$	$-D^x_{13}$	D^x_{13}
$D^x_{R(1)R^\dagger R(3)R^\dagger}$	D^x_{13}	D^x_{24}	D^x_{31}	D^x_{42}	D^x_{31}	D^x_{24}	D^x_{13}	D^x_{42}
$RD^y_{13}R^\dagger$	D^y_{13}	$-D^y_{13}$	D^y_{13}	$-D^y_{13}$	D^y_{13}	$-D^y_{13}$	D^y_{13}	$-D^y_{13}$
$D^y_{R(1)R^\dagger R(3)R^\dagger}$	D^y_{13}	D^y_{24}	D^y_{31}	D^y_{42}	D^y_{31}	D^y_{24}	D^y_{13}	D^y_{42}
$RD^z_{13}R^\dagger$	D^z_{13}	$-D^z_{13}$	$-D^z_{13}$	D^z_{13}	D^z_{13}	D^z_{13}	$-D^z_{13}$	$-D^z_{13}$
$D^z_{R(1)R^\dagger R(3)R^\dagger}$	D^z_{13}	D^z_{24}	D^z_{31}	D^z_{42}	D^z_{31}	D^z_{24}	D^z_{13}	D^z_{42}

Table 17: Transformation table for the *transformed* pseudo vector components (D^i_{14}) of the *untransformed* ionic sites 1 and 3 - $RD^i_{13}R^\dagger$ - and the *untransformed* pseudo vector components on the *transformed* sites $D^i_{R(1)R^\dagger R(3)R^\dagger}$. For a DM term to be invariant the two quantities have to be equal.

Like in the other two cases, interactions between these two pairs of ions are not affected by removing the mirror plane. The inversion symmetry element I requires $D^i_{13} = D^i_{31} \quad i =, x, y, z$ which is forbidden by the asymmetry of the DM interaction. That this causes any D^i_{24} term to be zero can be seen in the table above.

DM terms coupling ions $1 \leftrightarrow 1'$, $2 \leftrightarrow 2$, $3 \leftrightarrow 3'$ and $4 \leftrightarrow 4'$, where the prime denotes the same ionic position but in an adjacent unit cell are all forbidden. This is because the two interacting ions have the same surroundings, and the exchange path between the two ions does not change when interchanging the ions. Therefore, the interactions between ions on the same position can not possibly be antisymmetric, and hence DM interactions of this kind are forbidden by symmetry.

In conclusion, the straightforward assumption that the mirror plane m_{xz} is broken does not change much. No additional DM terms are allowed when removing this symmetry elements. However, there are other relevant considerations. The collinear spin rotation away from the crystallographic b axis can not be explained by a DM term. However, the direction of rotation might point to other broken symmetry elements than just m_{xz}. The same goes in the case of the observed weak ferromagnetism; establishing a term (not necessarily a DM term) explaining the F_y component might point to broken symmetry elements. Lastly, the polarization of the crystal in an applied field implies that the symmetry elements forbidding polarization is broken. These considerations will be given in the following sections.

6.4.2 Possible causes of weak ferromagnetism

In $LiCoPO_4$ weak ferromagnetism along the b direction has been observed [47]. The moment is far too small to be observed in neutron scattering experiments. Actually, the first paper presenting a microscopic origin of the DM interaction proposes the DM interaction as the cause of weak ferromagnetism in some trigonal systems [11]. However, since the DM interaction is proportional to the *cross product* of the spin pseudo vectors of the two ions interacting, no DM interaction coupling the main C_y spin component to a F_y component is possible. As the largest ferromagnetic component is *parallel* to the main spin component it can not be caused by a DM term as the ferromagnetic component does not constitute a canting. A DM term could couple the observed minor C_x component to a F_y component, but not without inducing an even larger F_x component via the main C_y type structure. This has not been observed. However, since the very large $\Delta g/g \approx 0.3$ makes anisotropic exchange a viable option, there is still some room for constructing a Hamiltonian causing (very) weak ferromagnetism. Consider a simple form

$$\mathcal{H}^F_{A-EX} = -\Lambda_F \left(S^y_1 S^y_2 + S^y_2 S^y_1 - S^y_3 S^y_4 - S^y_4 S^y_3\right), \tag{6.11}$$

which is possible only via anisotropic exchange. This term is zero if the structure can be described solely by either a F_y component or a C_y component. However, inserting a linear combination of the two: $aC_y + bF_y = S(a+b, a+b, -a+b, -a+b)$, the picture changes. Inserting this into 6.11 gives

$$\mathcal{H}^F_{A-EX} = -\Lambda_F S^2 \left(2(a+b)^2 - 2(b-a)^2)\right) = -8\Lambda_F S^2 ab \tag{6.12}$$

Such a term is only invariant under symmetry elements leaving the ions unchanged or interchanging $1 \leftrightarrow 2$ and $2 \leftrightarrow 3$. The transformation properties can be evaluated from table 14, and the symmetry elements satisfying this property are the following

$$G_{C_y \to F_y} = \left\{1,\ 2'_x,\ m'_{xy},\ m_{xz}\right\}. \tag{6.13}$$

The author admits that constructing such a term is rather circumstantial. Other anisotropic exchange terms can be constructed to give a F_y component, but the term above *only* gives an F_y in the presence of an C_y component. In $LiNiPO_4$ for instance, weak ferromagnetism has been observed along the z direction which is also parallel to the main spin component along z. The presence of the term in equation 6.11 in $LiNiPO_4$ does not create an unobserved F_y component. In the next section, other anisotropic exchange terms are constructed to try to explain the observed C_x component which has been observed in $LiCoPO_4$.

6.4.3 Hamiltonians that cause spin rotations

In this section, potential Hamiltonians that could cause a $C_y \to C_x$ coupling will be setup to examine their transformation properties under the *Pnma* symmetry elements. These are not necessarily DM terms; in fact, they cannot be, since in order for a C_x component to lower the magnetic energy of the system via a coupling to the main C_y component, all terms must have the same sign. However, since $\Delta g/g \approx 0.3$, a possible anisotropic exchange interaction could have a strength of roughly one third of the DM interaction; so even this weak interaction - second order in the $\hat{L} \cdot \hat{S}$-coupling - might still be significant.

By a first glance - four possible simple quadratic spin Hamiltonians come to mind when trying to make a designer-Hamiltonian with a $C_y \to C_x$ coupling. They are the following:

$$\mathcal{H}^{11}_{A-EX} = \Lambda_{11} \left(S^x_1 S^y_1 + S^x_2 S^y_2 + S^x_3 S^y_3 + S^x_3 S^y_3\right) \tag{6.14}$$
$$\mathcal{H}^{12}_{A-EX} = \Lambda_{12} \left(S^x_1 S^y_2 + S^x_2 S^y_1 + S^x_3 S^y_4 + S^x_4 S^y_3\right) \tag{6.15}$$
$$\mathcal{H}^{13}_{A-EX} = \Lambda_{13} \left(S^x_1 S^y_3 + S^x_3 S^y_1 + S^x_2 S^y_4 + S^x_4 S^y_2\right) \tag{6.16}$$
$$\mathcal{H}^{14}_{A-EX} = \Lambda_{14} \left(S^x_1 S^y_4 + S^x_4 S^y_1 + S^x_2 S^y_3 + S^x_3 S^y_2\right) \tag{6.17}$$

The coupling strength Λ_{ij} has been assumed to be a constant for all the terms. Using table 14 it can be seen that these four Hamiltonians are invariant with respect to arbitrary true permutations of the ionic positions. For instance, the permutation $\mathbf{r}_1 \rightarrow \mathbf{r}_2$, $\mathbf{r}_4 \rightarrow \mathbf{r}_3$,$\mathbf{r}_2 \rightarrow \mathbf{r}_1$, $\mathbf{r}_3 \rightarrow \mathbf{r}_4$ does not change any of the Hamiltonians above. The same holds for the other permutations of ionic positions in table 14. Hence, it is the change of sign of the spin components under a given transformation that determines whether or not the four Hamiltonians are invariant. In fact, in that respect, the four Hamiltonians are exactly the same; they all require $(S_x, S_y) \rightarrow (S_x, S_y)$ or $(S_x, S_y) \rightarrow (-S_x, -S_y)$ in order to be invariant. The symmetry elements fulfilling these conditions are the following:

$$G_{C_y \rightarrow C_x} = \left\{1,\ 2'_z,\ m'_{xy},\ I\right\}. \tag{6.18}$$

These are the only symmetry elements which allow the Hamiltonians 6.14. There could be other terms of course, but these are by far the simplest, and they are quadratic in spins as all the magnetic interactions treated in section 2.1.

6.4.4 Possible DM interactions in applied fields along magnetoelectrically active axes

Lastly, it would be instructive to check which DM interactions are in play when a magnetic field is applied along a magnetoelectrically active crystallographic direction. Applying a magnetic field along an axis $i = x, y, z$ introduces a Zeeman term:

$$\mathcal{H}_Z^i = -g\mu_B \sum_j H^i S_j^i, \tag{6.19}$$

where $j = 1, 2, 3, 4$ denotes the ion numbering. Thus, simply by introducing this term in the Hamiltonian, the symmetry elements taking $S^i \rightarrow -S^i$ are removing since the Zeeman term is not invariant under such symmetry operations. Thus, in fields applied along x and y the symmetry elements left resulting only from the applying a field are:

$$G_{H||x} = \{1, 2'_x, I, m'_{yz}\} \tag{6.20}$$
$$G_{H||y} = \{1, 2'_y, I, m'_{xz}\} \tag{6.21}$$

In addition to the Zeeman term, the magnetoelectric property of $LiCoPO_4$ has consequences in terms of symmetry breaking for fields applied along x and y. The field induces a polarization perpendicular to the field, which is only possible in the absence of certain symmetry elements. The polarization is a physical vector $\mathbf{P} = (P_x, P_y, P_z)$, describing a macroscopic property. If there exists a polarization P_i for $i = x, y, z$ any symmetry element taking $i \rightarrow -i$ will take $P_i \rightarrow -P_i$. Such a symmetry element *must therefore be broken* if such a polarization is observed.

In this section, the consequences of applying a field along a magnetoelectrically active axis is examined in terms of the Dzyaloshinsky-Moriya interaction. It is shown that by breaking the symmetry elements that allows a polarization, the system is able to lower its magnetic energy by coupling the field induced F_i component to either the main C_y component of the smaller C_x component via the DM interaction. Thus, the DM terms is shown to be a possible mechanism for a magnetoelectric effect.

DM interactions in case of a polarization P_y

Assume in the following that there is a polarization vector component P_y - as in the case of an applied field along a. In this case, all symmetries taking $y \rightarrow -y$ must be broken, which leaves the following symmetries:

$$G_{P_y} = \left\{1,\ 2'_y,\ m'_{xy},\ m'_{yz}\right\}. \tag{6.22}$$

In addition to this, the field itself causes symmetries to be broken leaving only two symmetry elements in a field along x:

$$G_{P_y}^{H||x} = \{1,\ m'_{yz}\}\,. \tag{6.23}$$

In case of a DM coupling between ions $1 \leftrightarrow 4$ and $2 \leftrightarrow 3$, table 15 shows that the glide plane m'_{yz} forbids any D_{14}^x and D_{23}^x component. However, z components are allowed, and even a different coupling strength between the two sets of ions - D_{14}^z and D_{23}^z. The requirement on the y component loosened $D_{14}^y \neq D_{23}^y$. So when assuming that only the symmetry elements in $G_{P_y}^{H||x}$ hold, an additional D^z component is allowed.

The DM coupling between ions $1 \leftrightarrow 2$ and $3 \leftrightarrow 4$ is changed as well. Table 16 shows that all three components are allowed with $\mathbf{D}_{12} = (D_{12}^x, D_{12}^y, D_{12}^z) = (-D_{34}^x, D_{34}^y, D_{34}^z)$

The otherwise forbidden DM coupling between ions $1 \leftrightarrow 3$ and $2 \leftrightarrow 4$ opens up when switching to $G_{P_y}^{H||x}$. All three components are allowed with $\mathbf{D}_{13} = (D_{13}^x, D_{13}^y, D_{13}^z) = (-D_{24}^x, D_{24}^y, D_{24}^z)$

The transformed pseudo vector components concerning D_{23}^i, D_{34}^i and D_{24}^i are not given explicitly in tables 15, 16 and 17, but similar arguments as in the cases D_{14}^i, D_{12}^i and D_{13}^i hold.

As evident there is quite a difference between assuming G and assuming $G_{P_y}^{H||x}$. The question remains if this has any physical consequence. Since the ME coupling in $LiCoPO_4$ exists between the a and b axes, it makes sense to focus on the D^z components, which couple exactly x and y components of the spins. The two allowed DM Hamiltonians in case of a G_{P_y} symmetry groups are

$$\mathcal{H}_{DM-z}^{14} = D_{14}^z\left(S_1^x S_4^y - S_4^x S_1^y\right) + D_{23}^z\left(S_2^x S_3^y - S_3^x S_2^y\right) \tag{6.24}$$

$$\mathcal{H}_{DM-z}^{13} = D_{13}^z\left(S_1^x S_3^y - S_3^x S_1^y + S_2^x S_4^y - S_4^x S_2^y\right). \tag{6.25}$$

$$\mathcal{H}_{DM-z}^{12} = D_{12}^z\left(S_1^x S_2^y - S_2^x S_1^y + S_3^x S_4^y - S_4^x S_3^y\right). \tag{6.26}$$

Applying a magnetic field along x induces an F_x component; all x components have the same sign. Inserting this F_x component into the two first of the above Hamiltonians gives a C_y symmetry. The third Hamiltonian gives a G_y component. Thus the DM terms 6.24 and 6.25 can couple the field induced F_x type structure to the main zero field structure C_y and lower the magnetic energy. Thus, in principle, when applying a field along a the system could be able to lower its energy by breaking the symmetry elements taking $y \to -y$ (causing polarization), which opens up two DM channels coupling F_x and C_y type structures. The parts of the DM Hamiltonians causing this could be written on the form - collecting $D_{14}^z + D_{13}^z = D^z$

$$\mathcal{H}_{DM}^{ME} = D_{H||x}^z\left[F_x \cdot C_y\right]. \tag{6.27}$$

The Hamiltonians 6.24 and 6.25 couple more basis vectors than just the two written above, but these are the ones relevant for the coupling conjectured above. So if the system - by displacing the atoms in a way that polarizes the material along y, can cause the DM pseudo vector component D^z to increase in absolute value - the DM energy of system can be lowered. The displacements - in the case of an applied field along a - need to break the same symmetries that need to be broken in order to allow a finite polarization along y.

DM interactions in case of a polarization P_x

If there is a polarization vector component P_x - as in the case of an applied field along b - all symmetries taking $x \to -x$ must be broken. The symmetries left are the following:

$$G_{P_x} = \{1,\ 2'_x,\ m'_{xy},\ m_{xz}\}\,. \tag{6.28}$$

The field itself causes symmetries to be broken leaving only two symmetry elements in a field along y:

$$G_{P_y}^{H||y} = \{1,\ m_{xz}\}\,. \tag{6.29}$$

In this case, the mirror plane m_{zx} is very important, as it forbids x and z components of $\mathbf{D}_{14}$, $\mathbf{D}_{12}$ and $\mathbf{D}_{13}$. There are only two differences between assuming the full symmetry group $Pnma$ and G_{P_x}. The first is that it loosens the requirement D_{12}^y and D_{34}^y such that $0 \neq D_{12}^y \neq D_{34}^y \neq 0$. The second is that the absence of inversion symmetry allows for a $D_{13}^y = -D_{24}^y$ component. This is not terribly exciting since in an applied field along b, there is the F_y, C_y and the C_x component, and none of these can couple by virtue of the DM terms allowed under $G_{P_x}^{H||y}$. However, the accumulated evidence that some of the $Pnma$ symmetries are probably broken in zero field, might change this fact.

DM interactions in case of a polarization P_x in the absence of m_{zx}

In sections 6.4.2 and 6.4.3 it was examined which symmetries allowed a term causing the observed weak ferromagnetism ($G_{C_y \to C_x}$) and an anisotropic exchange term causing a C_x component (G_{A-EX}). In the two cases, the symmetries that needed to be broken in zero field were the following

$$G/G_{C_y \to F_y} = \{2'_y,\ 2'_z,\ I,\ m_{yz'}\} \quad \text{and} \quad G/G_{C_y \to C_x} = \{2'_x,\ 2'_y,\ m'_{yz},\ m_{xz}\} \tag{6.30}$$

As evident from the previous section, the mirror plane perpendicular to b, m_{xz} forbids any DM pseudo vector components along both x and z. In order for any D^z term - which is able to couple F_y and C_x components - to be allowed by symmetry for fields along y, this mirror plane needs to be broken *in zero field*. Luckily, due to the observed C_x component, this is indeed very probable as stated in section 6.2.3. It was shown that *any* Hamiltonian coupling y and y spin components - the general term written in equation 6.3 - cannot be invariant with respect to this exact mirror plane. No assumptions about the origin or nature of the spin coupling - other that it be quadratic in spins - is necessary to show this. Furthermore, since the observed C_x component is rather large, the absence of this mirror plane is directly observed to have significant consequences for the magnetic interactions. Thus, in an applied field along y, the only symmetry element that holds is the identity - 1.

This leaves no requirements on the DM terms allowed in a field along y, and thus, terms of the form D_{ij}^z terms are allowed. As in the case of fields along x, the three relevant Hamiltonians coupling x and y components are of the form

$$\mathcal{H}_{DM-z}^{14} = D_{14}^z\,(S_1^x S_4^y - S_4^x S_1^y) + D_{23}^z\,(S_2^x S_3^y - S_3^x S_2^y) \tag{6.31}$$
$$\mathcal{H}_{DM-z}^{13} = D_{13}^z\,(S_1^x S_3^y - S_3^x S_1^y) + D_{24}^z\,(S_2^x S_4^y - S_4^x S_2^y)\,. \tag{6.32}$$
$$\mathcal{H}_{DM-z}^{12} = D_{12}^z\,(S_1^x S_2^y - S_2^x S_1^y) + D_{34}^z\,(S_3^x S_4^y - S_4^x S_3^y)\,. \tag{6.33}$$

As evident, the terms above are slightly different from the terms 6.24, 6.25 and 6.26. This is because the requirements $D_{13}^z = D_{24}^z$ and $D_{12}^z = D_{34}^z$ are lifted. However, this makes little difference. Inserting an $F_y = (S, S, S, S)$ structure reveals that Hamiltonians 6.31 and 6.32, couples this F_y spin structure to a C_x structure. Thus, it has been shown that assuming the absence of the mirror plane m_{xz} in zero field allows for the following Hamiltonian expressed in terms of irreducible basis vectors:

$$\mathcal{H}_{DM}^{ME} = D_{H||x}^z\,[F_x \cdot C_y] + D_{H||y}^z\,[F_y \cdot C_x] \tag{6.34}$$

Thus, the system could lower its magnetic energy in fields applied along y by creating a polarization along x. In the following two notes, a summary of this possible DM facilitated ME-effect is given followed by an evaluation of the experimental evidence for zero field symmetry breaking.

D^z-terms as the cause of the ME effect - summary

In the previous section it has been shown that in an applied field along a, the system can lower its DM energy by breaking the symmetries that allows for a polarization along y, P_y. This energy gain is facilitated by DM-components along z: $D^z_{13} = D^z_{24}$ and $D^z_{14} = D^z_{23}$, which causes a coupling between $F_x \rightarrow C_y$ and $F_y \rightarrow C_x$ spin structure components. It is more tricky for fields applied along the b axis, where D^z_{ij} components are forbidden even when breaking the symmetries that are impossible in the presence of a polarization P_x and a field H_y. However, if one assumes that the symmetry element m_{xz} are broken *in zero field*, such a DM-facilitated energy gain by electric polarization becomes possible. That this exact symmetry is indeed broken in zero field is made plausible by the observed C_x component in zero field. It is important to underline that applying a field along b induces a smaller F_y component than the F_x component induced by applying a similar field along a. This is experimentally confirmed in [46], where the susceptibility for fields along y is roughly 4/10 of the susceptibility along x. Furthermore, as the TriCS experiment determined $C_x/C_y \approx 1/7$, the C_x component necessary for a DM-facilitated ME-effect for fields along b is much smaller (1/7) than the C_y component necessary for fields along a. Therefore, the ME-effect for fields along y should be *much* smaller for fields applied along b. This is not the case, the ME-tensor along y is half the value for fields along x at maximum [44]; which is smaller but not much smaller. It is the author's opinion that the DM-interaction is not necessarily entirely responsible for the ME-effect in $LiCoPO_4$, but it is certainly relevant. It may be one of the reasons why the ME-effect is so strong in $LiCoPO_4$; perhaps the allowed DM-terms enhance an effect already there. It should be emphasized that the considerations given in this section merely speculates whether or nor a coupling is possible; no information about the strength of the couplings is obtained.

Zero field crystal structure in $LiCoPO_4$

All the considerations concerning the DM interaction and its possible consequences, all rest on the assumption that the *Pnma* space group is the symmetry group to start out with and that the true unit cell is the one proposed by Newnham and Redman in [13] in the 60's. This is not necessarily the case at all. As evident in figures 53 and 54 some of the zero field nuclear peaks are there. In fact, as the author performed more and more experiments on this compound, it was evident that *all* of the *Pnma*-forbidden peaks were there. Checks have been made for second order contamination and multiple scattering, and these two effects can be ruled out. The peaks were observed both using $\lambda/2$ neutrons at RITA-II - where $\lambda/4$ neutrons are absorbed by the neutron guide - and at TriCS which has no second order contamination. At TriCS, Ψ-scans were made - rotating the sample around the axis defined by the reciprocal lattice vector in the scattering condition - and the peaks were still there. Thus, multiple scattering is highly unlikely. The peaks where measured in a furnace on a 4-circle setup - and they were there at temperatures up to 600 K. So it is not simply a case of a structural phase transition occurring below 300 K to a structure with a symmetry group that is some subgroup of *Pnma*; if these peaks are to be taken seriously (which they are in the author's opinion) the assumption of *Pnma* symmetry is simply wrong at all temperatures. Therefore, the most important next step in order to progress in the understanding of $LiCoPO_4$ is determining the right structure. This would be a necessary starting point if the role of DM interactions and anisotropic exchange is to be understood. The low energy branch in the spin wave spectrum is also not understood, and a proper determination of the structure is a crucial first step. The author has performed an initial structural refinement of the high temperature TriCS data, but without success. A dedicated effort to understand this is necessary and there was not time to do this in this work.

6.5 Field induced magnetic phase transition for fields applied along b

As mentioned in the introduction to this chapter, $LiCoPO_4$ has a field-induced magnetic phase transition at fields around 11 Tesla applied along the spin polarization direction b. This was first discovered by Martin Wiegelmann in [48] where he examined magnetoelectric effects in strong magnetic fields. Before the publication of [49] the author performed a neutron diffraction experiment examining this phase transition. The results will be described in the following.

6.5.1 The first RITA-II experiment for fields applied along b using a vertical 15 T cryomagnet

In October 2009, a RITA-II experiment using the same 50 mg crystal as in the TriCS experiments were used. The crystal was mounted on an aluminum sample holder placed in the Oxford 15 T cryomagnet with the b axis vertical, and the ac-plane coinciding with the scattering plane of the spectrometer. There was an 80' collimator between the monochromator and the sample, and no collimation between the sample and the detector. The Be-filter was removed and the analyzer set to 20 meV, in order to use second order neutrons from the monochromator.

Figure 57 (top left) shows the peak intensity of the (301) reflection as a function of field. The intensity drops rather slowly down to a lower value at roughly 10.3 tesla. This is a lower transition field than observed in [48], but an alignment better than 0.5° is required when using the 15 T cryomagnet, so 10.3 tesla can be said to be the true critical field. Well into the experiment, it was thought that the magnetic intensity dropped to zero. After searching thoroughly for incommensurate peaks along a and c, the integrated intensity of all reachable peaks were thoroughly measured at 13.5 tesla and base temperature - well above the critical field - and compared to the intensity at 60 K and 13.5 tesla. Surprisingly there was a *remnant* of magnetic intensity at the commensurate AFM C-type peaks at 13.5 tesla, with roughly 10 % of the zero field intensity (see figure 57 bottom left). The integrated intensity of this remnant drops as a power law as a function of temperature with a critical temperature of around 6 K (see figure 57 bottom right). An elegant explanation would be that the two spins opposite the field decrease to one third of their zero field length, composing a structure $1/3F_y + 2/3C_y = (S, S, -1/3S, -1/3S)$. This would give a magnetization of $1/3M_S$; as well as explain the unobserved intensity as the ferromagnetic components are mainly reflected in strong nuclear peaks. Another possible explanation is that the high field structure is incommensurate, and that the remnant intensity in the (301) reflection is just a field induced commensurate ferromagnetic component. If this is the case, the maximum ferromagnetic component would be $1/3F_y = (1/3S, 1/3S, 1/3S, 1/3S)$. The structure factor for these two scenarios and the zero field structure evaluated in the (301) peak is given in table 18

Structure	$\lvert F_{struc}\rvert^2$
C_y	11.72
$1/3F_y + 2/3C_y$	5.65
$1/3F_y$	0.44
F_{obs}	0.8

Table 18: Structure factors evaluated in the (301) reflection for the zero field structure C_y, the proposed ferrimagnetic structure $1/3F_y + 2/3C_y$ and a ferromagnetic commensurate magnetization $1/3F_y$.

As evident in the structure factor calculation, the elegant ferrimagnetic solution - $1/3F_y + 2/3C_y$ - is not consistent with the data. The $1/3F_y$ structure has roughly half of the observed structure factor, which is rather close. A linear polarized (along b) IC structure would give a finite commensurate

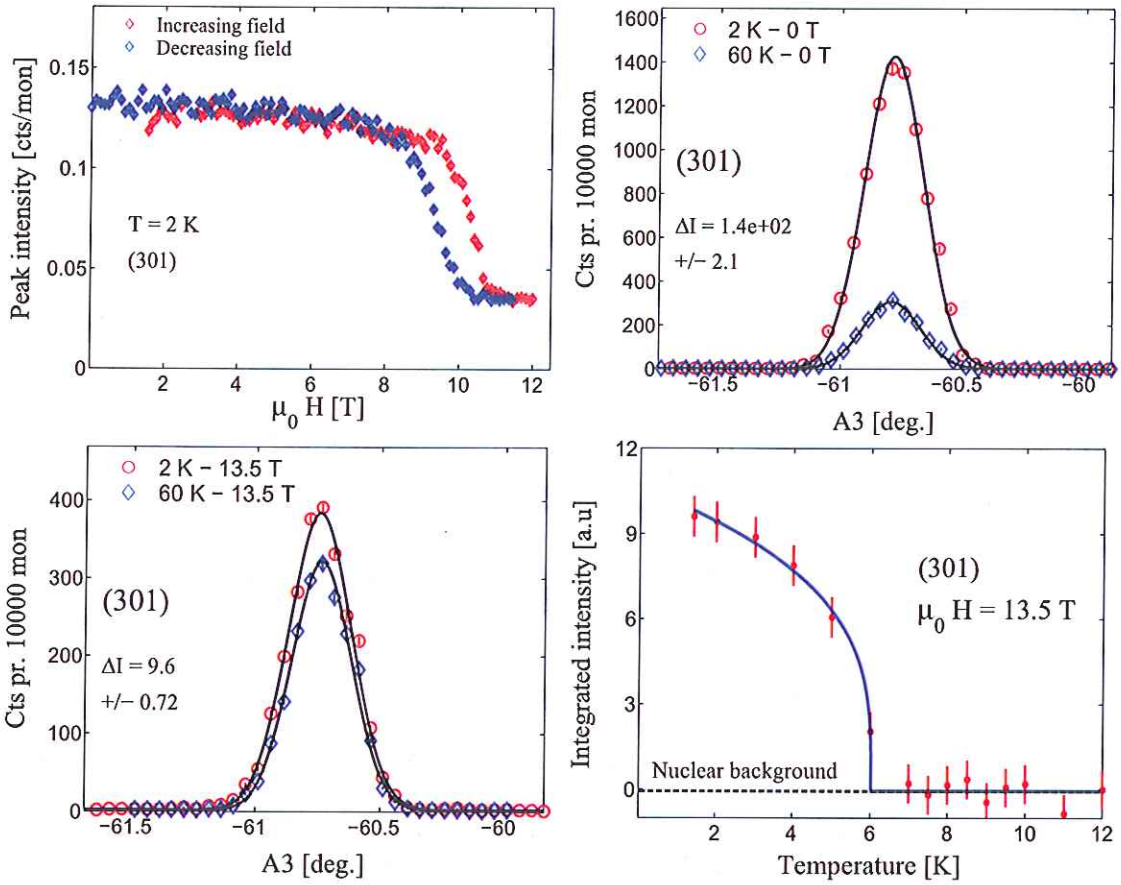

Figure 57: *Top Left:* Peak (not integrated) intensity of the (301) reflection as a function of field applied along b. As evident, the intensity drops over a substantial field range at roughly 10.3 tesla. There is a substantial hystersis of 1 tesla. *Top Right:* Omega scans of the (301) reflection in zero field at 2 and 60 K respectively. *Bottom Left:* The (301) peak at 13.5 tesla at 2 and 60 K respectively. There is a remnant of magnetic intensity of roughly 1/3 of the zero field intensity. *Bottom Right:* Integrated magnetic intensity of the (301) peak as a function of temperature at 13.5 tesla. The intensity drops off as a power law with a critical temperature of 6 K.

ferromagnetic component. There is a slight possibility of magnetostriction (the atomic positions *are* coupled to the applied field in this material) causing the nuclear structure factor to slightly increase in field. However, there is not enough experimental evidence to make any final conclusions about the magnetic structure in the this high field phase.

The phase diagram has been obtained by performing field scans and temperature scans of the (301) reflection. The field induced phase boundary has been defined as the point of maximum slope of an intensity vs. field curve. The critical temperature is found from fitting the integrated intensity as a function of temperature to a power law, in both the commensurate and the 'remnant' phase. The obtained phase diagram can be seen in figure 59.

Thorough attempts have been made to find the rest of the magnetic intensity of the high field phase at low temperatures in the *ac* scattering plane. No other intensity than the remnant was found. In principle an enlargement of the unit cell (commensurate and truly incommensurate) could occur along the b-axis. As mentioned previously, pulsed magnetization measurements reported in [49] found the magnetization to occur in steps of $1/3M_s$; where a unit cell of dimensions $2b \times 3c$ is proposed. In order to examine such a modulation at fields higher than 10 T, one needs a quite

powerful horizontal magnet. An attempt has been made to find this intensity using an 11 T SANS-magnet on a triple axis spectrometer, which will be elaborated in the next section.

6.5.2 The RITA-II experiment with an 11 T horizontal field cryomagnet

A very large $LiCoPO_4$ crystal of approx. 1 g was mounted on an aluminum sample stick and placed in the 10.8 tesla SANS cryomagnet mounted on RITA-II, with the crystallographic *bc* plane coinciding with the scattering plane of the spectrometer. The SANS 10.8 tesla cryomagnetic has a very limited geometry. There are narrow two conical openings, allowing the beam to pass, which are perpendicular to one another. They are $\pm 8°$ and $\pm 15°$ respectively. Thus only a very limited portion of reciprocal space can be reached as the range is highly limited by the fact that either the sample rotation or the 2θ angle only has a possible interval of 15^{circ}. However, the possibility of changing the incoming energy on a triple axis spectrometer, remedies this fact quite a bit, although one is still nowhere near the flexibility of a vertical magnet. 40' collimation was used between the monochromator and the sample, and no collimation between the sample and the analyzer. Both first and second order neutrons were used as the energy was varied. The incoming energies used were 20, 15, 10, 7 and 5 meV. The range of reciprocal space reachable using these energies and accounting for the limited geometry can be seen in figure 58 (left). It is clearly evident that even when using the entire energy range (20 meV is the maximum energy due to the fact that the guide absorbs higher energy neutrons), the range in reciprocal space is still very limited.

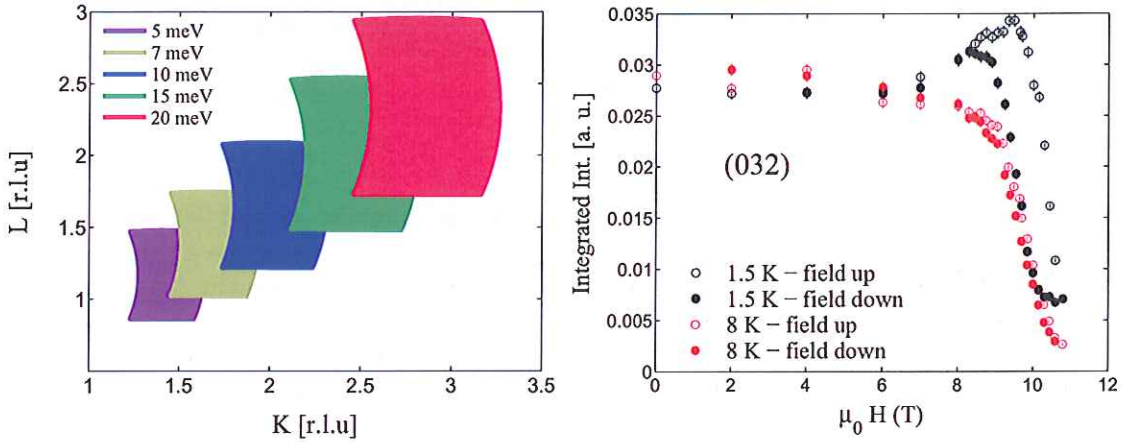

Figure 58: *Left:*The range in reciprocal space reachable using 5, 7, 10, 15 and 20 meV neutrons on RITA-II with the horizontal field SANS cryomagnet mounted. *Right:* Integrated intensity of the (032) peak as a function of both increasing and decreasing field at 1.5 and 8 K, respectively. It is evident that the hysteretic behavior only exists in the low temperature phase.

A thorough search for any IC peaks was made in the available portion of reciprocal space. Since a one-third magnetization suggests that 1/6 of the spins have flipped, emphasis was made on all reciprocal space points representing unit cells with a number of magnetic atoms divisible by 6. Still, no intensity was found. To determine with certainty that there are two distinct high field phases, the integrated intensity of the (032) peak was measured at 1.5 and 8 K respectively, see figure 58. Substantial hysteresis is again evident in the 1.5 K scan while there is almost no hysteresis at 8 K. This confirms that there are two magnetic phases at high fields. It is interesting that there is an increase in (032) intensity a 2 K just before the critical field. It is difficult to explain this without having measured more than one magnetic peak. Such an increase was not seen in the (301) reflection in the vertical field experiment. This will not be commented further.

The magnetic phase diagram of $LiCoPO_4$

The phase diagram as obtained from the measurements on RITA-II using the 15 T vertical field cryomagnetic is shown in figure 59.

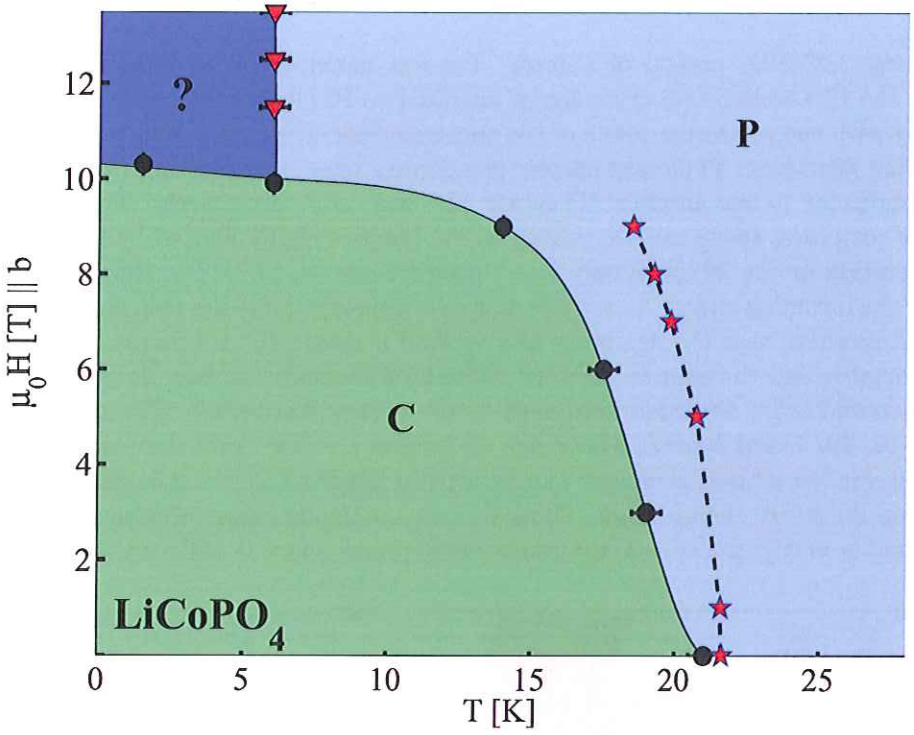

Figure 59: The phase diagram obtained after performing temperature- and field scans of the (301) reflection. The black circles denote the phase boundaries found using the commensurate (301), and the red triangles denote the phase boundaries found from the remnant (301) intensity. The commensurate phase boundary shows a flat plateau at low temperatures, and a gradual decrease in critical field at high temperatures. The critical temperature for the 'remnant' phase remains constant at fields between 10 and 13.5 tesla. The red pentagrams mark the ordering phase boundary as found by specific heat measurements in [50].

The limits of the high field phase are taken as the critical temperature for the remnant of the (301) reflection. Unfortunately, the structure at high fields has not been determined in this work. In addition, the author stumbled upon an article measuring the ordering phase boundary of $LiCoPO_4$ using specific heat measurements - a few weeks before handing in this thesis. These phase boundaries are several degrees above those measured by means of neutron scattering - as marked by the red pentagons in figure 59. These measurements could suggest that there is a high temperature incommensurate phase at most fields; perhaps even a spontaneous IC phase. Upon measuring the IC ordering temperature in $LiNiPO_4$, it was seen that the change in magnetization upon cooling into the IC phase was not big; perhaps it was missed in previous work. This whole phase diagram is certainly something to follow up on and understand in the time to come. A linearly polarized IC structure is certainly possible in this Ising-like system, and precisely due to the Ising like nature of the single ion anisotropies, the system cannot be expected to conform to a spiral at low temperatures. The cost in anisotropy energy is simply too large.

This concludes that description of the work done on $LiCoPO_4$. The zero field structure has been thoroughly determined to be a $3.35\mu_B C_y + 0.5\mu_B C_x$. Evidence of a very strong DM interaction

has been found, and possible consequences of this evaluated in terms of an empirically plausible loss of symmetry in zero-field. The DM mechanism has been proposed as being involved in causing the ME-effect. The phase diagram of $LiCoPO_4$ has been determined; the nature of the magnetic phase at low temperatures and high fields has not been established. Further work would be figuring out the nature of the high field phase, thorough investigations of field induced AFM structures for fields applied along b and a search for a possible high temperature IC phase.

7 The study of the Bragg glass phase of vortex matter - introduction

After he was able to liquify helium, H. K. Onnes discovered superconductivity in 1911. Upon measuring the electrical resistance of Mercury at the low temperatures reachable using liquid helium, he discovered a rapid drop of the electrical resistance at $T_c \approx 4.22K$ to an unmeasurably low value (see figure 60), instead of following the T^3 proportionality curve which was found to be valid at higher temperatures. In later experiments, the limits of conductivity in this superconducting state was sought by magnetically inducing a persistent current in a superconducting solenoid and measuring the decay of the trapped magnetic field over time. The decay time has been found to be more than 100000 years [51], so the resistivity is truly zero. Zero resistivity in zero field is a characteristic macroscopic property of the superconducting state in the so-called type-I superconductors which occurs in many metals, alloys and ceramics.

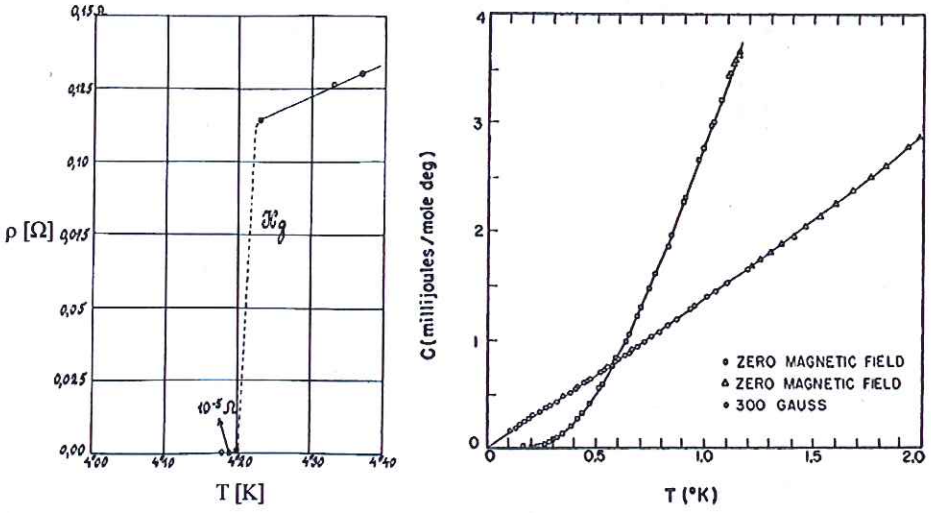

Figure 60: *Left:* The resistance of mercury near the superconducting transition temperature as measured by H. K. Onnes in 1911 [52] *Right:* The heat capacity of aluminum in the normal state and in the superconducting state - with $T_c = 1.1$ K [53].

This thermodynamical phase transition has other distinguishing macroscopic characteristics. The specific heat shows a sharp increase upon cooling into the superconducting state at the critical temperature T_c after which it drops exponentially ($e^{-\Delta/k_B T}$), drastically different from the linear temperature dependency of the normal state (see figure 60). The superconducting state also shows a drastical decrease in the thermal conductivity compared to the normal state (an indication of the fact that less conduction electrons are able to carry entropy [54]). The most central macroscopic characteristic relevant to this thesis is the superconductor's ability to completely expel a weak magnetic field, only allowing a finite field to penetrate a certain small depth - the *penetration depth* λ - into a bulk superconductor. This is the so-called *Meissner effect* [55], which is not an obvious consequence of perfect conductivity (magnetically induced eddy currents), since even a stationary field applied in the normal state gets expelled upon cooling below T_C. This implies that superconductivity resists magnetic order, and hence that by applying a high enough magnetic field - H_c - the superconducting state will be destroyed, since the energy density of the magnetic field will exceed the energy density of the superconducting condensation energy. The two remarkable electromagnetic effects exhibited by the superconducting state were first described by the so-called

London equations: (using cgs units)

$$\mathbf{E} = \frac{\partial}{\partial t}(\Lambda \mathbf{J_s}), \quad \text{and} \tag{7.1}$$

$$\mathbf{H} = -c\nabla \times (\Lambda \mathbf{J_s}) \;\Rightarrow\; \nabla^2 \mathbf{H} = \frac{\mathbf{H}}{\lambda^2}, \tag{7.2}$$

where Λ is an phenomenological parameter and $\mathbf{J}_s$ is the superconducting current density. The first London equation describes the uninhibited acceleration of charge upon applying an electrical field, and the second equation (after combining it with Maxwell's laws) describes the exponential screening of a magnetic field from a bulk sample, as depicted in figure 61.

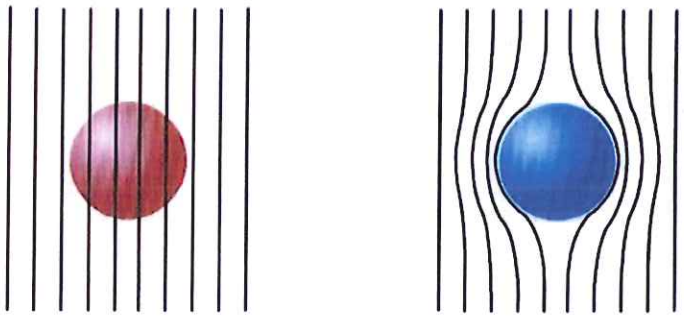

Figure 61: *Left:* The field penetrating the material in its normal state. *Right:* The Meissner effect: The superconductor expels all magnetic field from its interior when cooled through the superconducting transition. (Illustration from http://www.cm.ph.bham.ac.uk)

The second part of this thesis focuses on superconductors in an applied magnetic field. In some superconductors, upon applying a field strong enough, magnetic flux is able to penetrate the superconducting sample in the form of flux quanta or *flux lines*. These superconductors are called Type-II superconductors. As will be evident in later chapters, the properties of these flux line ensembles are strongly linked with the electron transport properties of most useful superconductors.

A basic understanding of these ensembles of quantized magnetic flux is interesting by itself though. They constitute a two-dimensional ordered array of one-dimensional objects embedded in a three-dimensional condensate. The ordered flux lines interact with one another and hence the ensemble can be described as elastic. In addition, the flux lines can interact with normal volumes in the superconducting condensate which are caused by crystallographic defects and impurity inclusions. Thus, as will be evident in subsequent chapters, the flux line ensembles are systems in which a lattice with finite elasticity is subject to random forces. Taking the pinning force as a perturbation of the vortex lattice, such systems can be shown to have no long range order - the displacements of the flux lines simply increase linearly with flux line separation. When including the possibility of several metastable states, the displacements increase much more slowly - but still there is no long range order. This changes when taking into account that the pinning potential is random, and that the Fourier components commensurable with the lattice perturb the ensemble differently than the other Fourier compoents. It can be shown that when taking the periodicity of the vortex lattice into account long range order is restored - in theory. This results in a glassy-like system with quasi-long-range order in which it is possible to change the lattice constant and the elasticity by simply changing the applied field - the so-called Bragg glass. This thesis aims to test the Bragg glass theory by performing Reverse Monte Carlo simulation on high resolution SANS data.

The following two chapters concern the work done on the vortex lattice of vanadium. The next chapter collects various theoretical concepts in some detail, while the last chapter describes the analysis of the obtained SANS and VSM data.

8 Conventional superconductivity and the Bragg glass phase of vortex matter

This chapter focuses on describing the theory necessary for understanding superconductors in general and flux line ensembles in particular. First a brief account will be given of some central features of the microscopic theory of conventional superconductivity developed by J. Bardeen, L. N. Cooper and J. R Schrieffer, the so-called BCS theory [56]. This has little importance for the interpretation of the results in this thesis, but the theory provides a framework for the understanding of the phenomenological origin of superconductivity and is treated for the sake of completeness. This is followed by a short description of the more practical Ginzburg-Landau theory of superconductivity, which is also derivable from the BCS theory. This leads to the possibility of type-II superconductors and the possibility of a lattice of vortex lines. Next, a short account of the relevant theories for the vortex lattice and the so-called *pinning* of vortex lines will be given. Lastly, a description of the Bragg glass theory amongst others will hopefully establish the concepts needed for an interpretation of the results shown here. Concepts from quantum field theory will be sporadically used in this chapter, an introduction can be found in [57].

8.1 BCS theory of superconductivity

In conducting materials electrical current is carried by the conduction electrons which are not bound by any single atom, but feel the periodic potential of the whole atomic lattice. This enables the electrons to delocalize and carry a macroscopic current [58] when subjected to an external electrical field. These conduction electrons will collide with and scatter from anything that can interact with the electron allowing them to transfer kinetic energy to the lattice (phonons or impurities), generating heat. The proportionality between the electrical equilibrium current and the applied electrical field can be shown to be

$$\mathbf{j} = \frac{ne^2\tau}{m_e}\mathbf{E}, \tag{8.1}$$

where τ is the average collision time, n is the density of free electrons and m_e is the electron mass. Equation 8.1 is the well known Ohm's law, where $ne^2\tau/m_e$ is the electrical conductivity inversely proportional to the resistivity. If one purifies the metal in question to an extreme degree and cools the sample to helium temperatures, the mean free path of the electrons can be in the centimeter range, resulting in a very low resistance or a very high conductivity. The superconducting phase transition however, completely changes the way the electrons interact with each other and the lattice, having a huge impact on the heat capacity, heat conductivity and the electrical conductivity. The reason for this is that the basic nature of the conduction electrons gets changed upon entering the superconducting phase. They are somehow able to attract each other and form pairs with one another, forming composite pseudo-particles called *Cooper pairs* which - due to their pseudo integer-spin nature - behave like bosons. In the next chapter a description of the simple electron gas will be given, in the absence of interactions between electrons. This is followed by an inclusion of possible interactions and the resulting *fermi-liquid* will be described, after which the origin of the attractive interaction will be discussed. Lastly, a brief account of the superconducting gap will be appropriate since this has a direct link to the more applicable Ginzburg-Landau theory. This description of BCS theory follows that given in [59].

8.1.1 Non-interacting electron gas

In a perfect crystal lattice of ions - without imperfections or phonons - free non-interacting conduction electrons moving in the periodic potential of the lattice can be described by plane waves. In

the second quantization picture, the electronic Hamiltonian is simply a counting of occupied states with a given energy:

$$H = \sum_{\mathbf{k},\sigma} \varepsilon_{\mathbf{k}} c^{\dagger}_{\mathbf{k},\sigma} c_{\mathbf{k},\sigma}, \tag{8.2}$$

where $\varepsilon_{\mathbf{k}}$ is the energy of the state assumed independent of the spin σ, while $c_{\mathbf{k},\sigma}$ and $c^{\dagger}_{\mathbf{k},\sigma}$ are annihilation and creation operators respectively. This simple system of electrons has a well-known collective ground state, namely the state where all the states with lowest energy/momentum are occupied in accordance with the Pauli principle up to an energy level defined by the number of electrons in the gas, namely the *Fermi energy* ε_F. The probability amplitude of an electron initially in the state $(\mathbf{k}, \sigma)$ at the time t of being in the state $(\mathbf{k}', \sigma)$ at time t' is described by the so-called non-interacting single particle propagator:

$$G_0(\mathbf{k}, \mathbf{k}', t - t') = G_0(\mathbf{k}, t - t')\delta_{\mathbf{k},\mathbf{k}'} \tag{8.3}$$

The equality follows simply from the lack of any interaction changing the initial wave-vector. G_0 denotes the propagator in the absence of interactions. The Fourier transform of the above is:

$$G_0(\mathbf{k}, \omega) = \int_{-\infty}^{\infty} dt e^{i\omega t} G_0(\mathbf{k}, t) = \frac{1}{\omega - \varepsilon_{\mathbf{k}} + i\delta_{\mathbf{k}}}, \tag{8.4}$$

where $t - t'$ has been conveniently replaced by t, $\delta_{\mathbf{k}}$ is an infinitesimal number with the same sign as $(\varepsilon_{\mathbf{k}} - \varepsilon_F)$ and $\varepsilon_{\mathbf{k}}$ is the dispersion relation. The pole is $\omega = \varepsilon_{\mathbf{k}} - i\delta_{\mathbf{k}}$. The imaginary part of the propagator can be interpreted as the lifetime of the single particle excitations, which in this case must be infinite due to the lack of interactions; hence the infinitesimal imaginary part. The momentum distribution is given by a Heaviside step function:

$$n(\mathbf{k}) = \Theta(\varepsilon_F - \varepsilon_{\mathbf{k}}), \tag{8.5}$$

which is 1 for $\varepsilon_F - \varepsilon_{\mathbf{k}} > 0$ and zero otherwise.

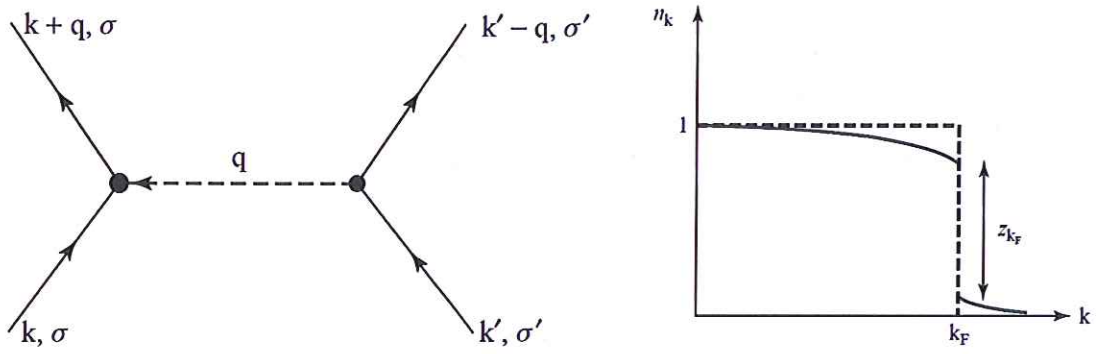

Figure 62: *Left:* Feynman diagram of an elastic electron-electron scattering event conserving spin. The timely axis is the vertical one while the spatial axis is horizontal. The propagator or matrix element is denoted by the dashed line. *Right:* The impact of the propagator residue on the momentum distribution is to lessen the discontinuity at the Fermi surface. Picture from [59].

8.1.2 Interaction between electrons and fermi-liquids

By allowing the electrons to interact in any way, the physics gets a little more interesting. Consider a simple elastic two-body electron-electron interaction of any kind, scattering two electrons in states

(k,σ) and (k',σ') into states $(\mathrm{k}+\mathrm{q},\sigma)$ and $(\mathrm{k}'-\mathrm{q},\sigma')$ conserving spin (see figure 62). In addition to the single electron energy, the interaction energy needs to be added, resulting in the Hamiltonian:

$$H = \sum_{\mathrm{k},\sigma} \varepsilon_{\mathrm{k}} c^{\dagger}_{\mathrm{k},\sigma} c_{\mathrm{k},\sigma} + \sum_{\mathrm{k},\mathrm{k}',\mathrm{q},\sigma,\sigma'} V_{\mathrm{k},\mathrm{k}',\mathrm{q}} c^{\dagger}_{\mathrm{k}+\mathrm{q},\sigma} c^{\dagger}_{\mathrm{k}'-\mathrm{q},\sigma'} c_{\mathrm{k},\sigma} c_{\mathrm{k}',\sigma'} \tag{8.6}$$

The propagator including this interaction is the following:

$$G^{-1}(\mathrm{k},\omega) = G_0^{-1}(\mathrm{k},\omega) - \Sigma(\mathrm{k},\omega), \tag{8.7}$$

where $\Sigma(\mathrm{k},\omega)$ is called the *self-energy* of the propagator, i.e. the energy of the propagator quasi particle due to the system it is part of. The real part can be interpreted as the excitation spectrum - or a *shift* of the spectrum of the non-interacting electron gas by an amount of Σ_R. The imaginary part represents the lifetime of the propagator - the time in which the propagator behaves as a quasi particle, or alternatively, the lifetime of the electronic state when subjected to the interaction. Assuming that the imaginary part of the self-energy is finite, but much smaller than the real part, the propagator of the interacting system of electrons can be written as:

$$G(\mathrm{k},\omega) = \frac{z_{\mathrm{k}}}{\omega - \tilde{\varepsilon}_{\mathrm{k}} + \frac{i}{\tau_{\mathrm{k}}}}, \quad \text{where} \tag{8.8}$$

$$z_{\mathrm{k}} = \left(1 - \frac{\partial \Sigma_R}{\partial \omega}\Big|_{\omega=\tilde{\varepsilon}_{\mathrm{k}}}\right)^{-1} \quad \text{and} \quad \frac{1}{\tau_{\mathrm{k}}} = -\frac{\Sigma(\mathrm{k},\tilde{\varepsilon}_{\mathrm{k}})}{1 - \frac{\partial \Sigma_R}{\partial \omega}\Big|_{\omega=\tilde{\varepsilon}_{\mathrm{k}}}}. \tag{8.9}$$

In the above equations, τ_{k} is the aforementioned lifetime of the electronic state and $\tilde{\varepsilon}_{\mathrm{k}} = \varepsilon_{\mathrm{k}} + \Sigma_R$, where ε_{k} represents the excitation spectrum of the free electron propagator. This looks a lot like the free energy propagator except for the shift in the energy spectrum and the finite interacting electronic state lifetime. The so-called *residue* z_{k} is an overall reduction of the free electron propagator. It is a reduction because $\frac{\partial \Sigma_R}{\partial \omega}$ is expected to be negative; the interaction energy shift of the excitation spectrum should decrease with increasing energy as fast electrons have less time to interact than slow ones. The residue evaluated near the Fermi wave vector gives information about to which degree the excitation spectrum of the interaction propagator resemble free particles with well defined energy and momentum. The effect that the interaction between electrons has on the momentum distribution of electrons is that the discontinuity at the Fermi surface lessens, and electrons occupying states with momentum near k_F leak out of the fermi-volume at zero temperature (see figure 62) occupying states with $k > k_F$. If z_{k} is large enough to reasonably describe the excitations near the fermi surface as quasi particles similar to the excitations in the non-interacting case, the electron system is called a *fermi liquid*. In such a system one can assume that there is a one-to-one correspondence between the quantum numbers of the non-interacting system and the system in which there is an interaction. Thus, one can use the non-interacting Fermi-gas as a starting point for perturbation theory. This is usually the case for repulsive interactions such as the Coulomb interaction; the effect of introducing the interaction is small and the free electron propagator is a good starting point for describing the excitations. This is, however, not always the case; an attractive interaction of a specific peculiar type is able to destabilize the fermi liquid as will be evident in the next section.

8.1.3 Attractive potential

Consider a Fermi-gas without any electron-electron interaction. Assume that two additional electrons in states at the fermi-surface interact with each other *attractively* through some effective interaction V_{eff}, but do not interact at all with the fermi-gas. Even more circumstantial, assume that only electrons on opposite sides of the fermi surface (with initial states $|\mathrm{k}\rangle$ and $|-\mathrm{k}\rangle$ and with

a total two electron energy of $2\varepsilon_{\mathbf{k}} > 2\varepsilon_F$) have a non-zero attraction and only in a thin shell around the fermi surface. The two particle wave function can thus be written as

$$|1,2\rangle = \sum_{\mathbf{k}} a_{\mathbf{k}} |\mathbf{k}, -\mathbf{k}\rangle, \tag{8.10}$$

resulting in the stationary Schrödinger equation

$$(H_0 + V_{eff}) \sum_{\mathbf{k}} a_{\mathbf{k}} |\mathbf{k}, -\mathbf{k}\rangle = E \sum_{\mathbf{k}} a_{\mathbf{k}} |\mathbf{k}, -\mathbf{k}\rangle, \tag{8.11}$$

where H_0 is the initial fermi gas Hamiltonian. The matrix element of the attractive potential in momentum space is assumed to be limited to a thin shell around the fermi surface, taking the simple form

$$\begin{aligned} \langle \mathbf{k}', -\mathbf{k}' | V_{eff} | \mathbf{k}, -\mathbf{k} \rangle &= -V \quad \text{if} \quad |\varepsilon_{\mathbf{k}} - \varepsilon_F| < \omega_0 & (8.12) \\ &= 0 \quad \text{if} \quad |\varepsilon_{\mathbf{k}} - \varepsilon_F| > \omega_0. & (8.13) \end{aligned}$$

Introducing the positive dimensionless quantity $\lambda \equiv VD(\varepsilon)$ where $D(\varepsilon)$ is the density of states and V is the attractive potential strength defined in equation 8.13, it can be shown ([59]) that the eigenvalue equation (8.11) leads to the identity

$$\frac{1}{\lambda} = \ln\left(1 + \frac{2\omega_0}{\Delta}\right) \Rightarrow \Delta = \frac{2\omega_0}{e^{1/\lambda} - 1}, \tag{8.14}$$

where $\Delta = 2\varepsilon_F - E$ and E is the eigenvalue. This leads to the requirement that the total eigen energy of the two electrons subjected to this circumstantial interaction is lower than that of two electrons with the exact fermi energy - $E < 2\varepsilon_F$. The basic assumption about the energy states below the fermi energy being filled thus breaks down; the fermi-gas assumption collapses in the shell near the fermi surface. In fact this bound state pairing energy below the fermi energy should be prohibited by the Pauli exclusion principle. The two electrons are able to pair up and *circumvent* the Pauli principle, gaining energy. This hints to the fact that the pairing fundamentally changes the fermionic nature of the electrons. This weird interaction causing the instability of the fermi surface was proposed by Leon Cooper, and the electronic pairs are called Cooper pairs. The interaction causing the pairs seems too artificial to have any justification in physics, but in fact it has, which will be evident in the following.

8.1.4 Phonon coupling

One of the very causes for electrical resistivity in materials is the ability of electrons to interact with the collective vibration modes of the crystal lattice - the *phonons*. Thus, in addition to the Coulomb repulsion between electrons there is a third party capable of mediating additional interactions between electrons. Physically, an electron can create a phonon - or induce a lattice distortion - which again can interact with a second electron. The phonons are quasi particles with well defined momentum, energy and lifetime. On the energy scale of the electron-phonon interactions, the lattice ions move much more slowly than the electrons due to their larger mass; hinting to the fact that the phonon lifetime is high compared to the speed of the electrons. Hence, such a third party interaction allows for the two interacting electrons to be well separated in space, minimizing the Coulomb interaction. Furthermore, it is natural to expect the Coulomb interaction to be minimized for electrons with opposite k for such an interaction - simply to minimize the time in which the coulomb interaction dominates over the phonon mediated interaction. This physically justifies some of the assumptions of the above mentioned interaction. Dealing with two interactions

one can write a second quantized Hamiltonian for the interacting electron gas:

$$H = \sum_{\mathrm{k},\sigma} \varepsilon_{\mathrm{k}} c^{\dagger}_{\mathrm{k},\sigma} c_{\mathrm{k},\sigma} + \sum_{\mathrm{k},\mathrm{k}',\mathrm{q},\sigma,\sigma'} \frac{e^2}{2\varepsilon_0 q^2} c^{\dagger}_{\mathrm{k}+\mathrm{q},\sigma} c^{\dagger}_{\mathrm{k}'-\mathrm{q},\sigma'} c_{\mathrm{k},\sigma} c_{\mathrm{k}',\sigma'} + \sum_{\mathrm{k},\mathrm{q},\sigma} M_{\mathrm{q}} \left(a^{\dagger}_{-\mathrm{q}} + a_{\mathrm{q}} \right) c^{\dagger}_{\mathrm{k}+\mathrm{q},\sigma} c_{\mathrm{k},\sigma}, \tag{8.15}$$

where $a^{\dagger}_{\mathrm{q}}$ and a_{q} are creation and annihilation operators of a phonon with momentum q, satisfying the boson commutation relation: $a^{\dagger}_{\mathrm{q}'} a_{\mathrm{q}} - a_{\mathrm{q}} a^{\dagger}_{\mathrm{q}'} = \delta_{\mathrm{q},\mathrm{q}'}$. M_{q} is the matrix element of the electron-phonon interaction describing the strength of the coupling while $c^{\dagger}_{\mathrm{k},\sigma}$ and $c_{\mathrm{k},\sigma}$ are the aforementioned fermionic electron creation and annihilation operators. The two simple first-order processes mediating the interaction are drawn in figure 63.

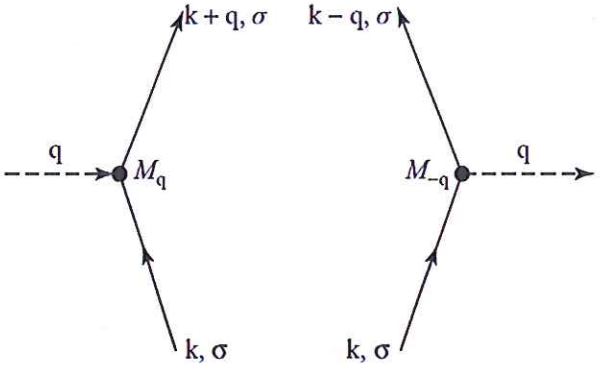

Figure 63: Feynman diagrams of phonon emission (*right*) and absorption (*left*) by electrons. The strength of the interaction is given by M_{q}. Picture from [59].

The matrix element is difficult to calculate within any usable precision but it can be shown that the following holds:

$$\lim_{\mathrm{q}\to 0} M_{\mathrm{q}} = 0 \quad \text{and} \quad M_{\mathrm{q}} \sim \mathrm{q}. \tag{8.16}$$

So the interaction is dipole-like - the induced and absorbed phonons can be described as local propagating electric dipole moments. Also, standing waves do not interact - at least to first order - with electrons. The two processes depicted in figure 63 can be combined to describe the combined process of one electron emitting a phonon and another electron absorbing the same phonon, causing the two electrons to effectively interact. The dashed line between the two electrons is the free phonon propagator which can be derived ([59]) to be

$$D(\mathrm{q},\omega) = \frac{2\omega_{\mathrm{q}}}{\omega^2 - \omega^2_{\mathrm{q}} + i\eta}, \tag{8.17}$$

where ω_{q} is the phonon frequency and η is infinitesimal. This gives an effective electron-electron interaction described by

$$V_{eff}(\mathrm{q},\omega) = \frac{2|M_{\mathrm{q}}|^2 \omega_{\mathrm{q}}}{\omega^2 - \omega^2_{\mathrm{q}}}, \tag{8.18}$$

where q is the momentum transfer between the two interacting electrons and ω is the energy transfer. Two important points are that for $\omega^2 < \omega^2_{\mathrm{q}}$, the interaction is attractive - with the aforementioned consequences near the fermi-surface - and that the interaction potential is diverging for $\omega \to \omega_{\mathrm{q}}$ and hence has the potential to dominate over the Coulomb potential for arbitrary small

values of $|M_q|^2$, in principle. The low-frequency requirement in equation 8.18 in order to achieve an attractive interaction reflects the fact that the electron supposed to absorb the previously emitted phonon needs to wait a little for the phonon initiating electron to pass before being able to be sucked in by the dipole moment of the local lattice distortion; hence there is an upper frequency cut-off. The sum of the two electron-electron interaction potentials is shown in figure 64.

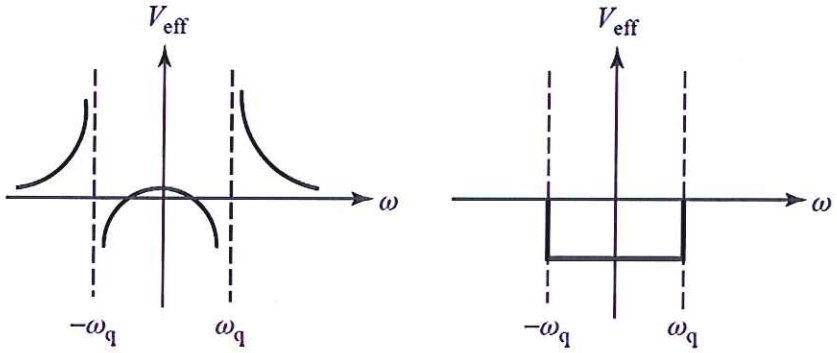

Figure 64: *Left:* The realistic sum of the phonon-mediated and the photon-mediated electron-electron interaction at fixed q. *Right:* The crude BCS simplification of the total electron-electron interaction for low energies. Picture from [59].

It is seen in figure 64 that for low energy transfers the interaction is repulsive; for long enough timescales the attractive nature of the phonon-mediated interaction disappears. Thus the conditions have to be just right in order to have an effective two electron attraction, but it can happen. A very crude simplification of this potential was made by Bardeen, Schrieffer and Cooper, justified by the following. In section 8.1.2 it was shown that a small repulsive interaction has a relatively little effect on the otherwise free electrons near the Fermi surface; the quasi particles induced by the interaction very much resemble the free electron propagators. It was shown in section 8.1.3 that an arbitrary weak attractive interaction causes a collapse of the Fermi surface. Therefore, the repulsive part of the total effective two-electron interaction is neglected and the attractive part is approximated by a square well, as evident in figure 64. If one assumes that the frequency range of the attractive interaction is much smaller than the corresponding Fermi energy, the energy of the two electrons in both their initial and final states needs to lie within a thin shell of the Fermi surface. For a thin shell this requirement simply amounts to the requirement that the two initial wave vectors need to have opposite direction - $\mathrm{k} = -\mathrm{k}'$, as illustrated in figure 65.

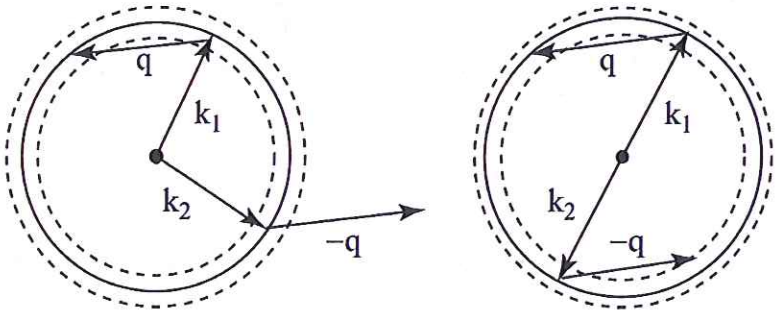

Figure 65: *Left:* The case of non anti parallel wave vectors under the assumption that the thin shell requirement is fulfilled for one of the electrons *Right:* The only case where all four considered electron states are within a thin shell of the Fermi surface. Picture from [59].

It can now be seen that a weak attractive electron-electron interaction exactly of the nature con-

sidered in 8.1.3 can be justified physically, and hence also justifying the existence of the composite bosonic Cooper pairs near the Fermi surface. The realistic effective two-electron interaction potential depicted in figure 64 hints that the attraction can only occur on a specific short time-scale and hence also in a specific short spatial range. It is then natural to enforce opposite spins on the two interacting electrons due to the Pauli principle. Enforcing anti parallel spins and momentum vectors and neglecting the repulsive part of the interaction gives the BCS electronic Hamiltonian:

$$H_{BCS} = \sum_{\mathrm{k},\sigma} \varepsilon_{\mathrm{k}} c^{\dagger}_{\mathrm{k},\sigma} c_{\mathrm{k},\sigma} + \sum_{\mathrm{k},\mathrm{k}',\sigma} V_{\mathrm{k},\mathrm{k}'} c^{\dagger}_{\mathrm{k},\sigma} c^{\dagger}_{-\mathrm{k},-\sigma} c_{-\mathrm{k}',-\sigma} c_{\mathrm{k}',\sigma}. \tag{8.19}$$

The ladder operators in the last term annihilate the two electron state $|-\mathrm{k}', -\sigma; \mathrm{k}', \sigma\rangle$ and create the state $|\mathrm{k}, \sigma; -\mathrm{k}, -\sigma\rangle$, only leaving matrix element of the form $\langle \mathrm{k}, \sigma; -\mathrm{k}, -\sigma | V_{eff} | -\mathrm{k}', -\sigma; \mathrm{k}', \sigma\rangle$ non-zero, satisfying the above requirements and implementing the simple constant interaction potential $V_{\mathrm{k},\mathrm{k}'}$ in the narrow frequency range as described previously. This is the BCS Hamiltonian; the foundation for the description of conventional superconductivity.

8.1.5 The BCS gap function

The above BCS Hamiltonian very much resembles the simple XY-Heisenberg model for magnetism with an applied field along the z-direction. This can be shown by replacing the spin operators σ^{+}, σ^{-} and σ^{z}

$$\tau^{+}_{\mathrm{k}} = 2c^{\dagger}_{\mathrm{k},\uparrow} c^{\dagger}_{-\mathrm{k},\downarrow}, \quad \tau^{-}_{\mathrm{k}} = 2c_{-\mathrm{k},\downarrow} c_{\mathrm{k},\uparrow} \quad \text{and} \quad \tau^{3}_{\mathrm{k}} = 2c^{\dagger}_{\mathrm{k},\uparrow} c^{\dagger}_{-\mathrm{k},\downarrow}. \tag{8.20}$$

Replacing this into the BCS Hamiltonian yields

$$H_{BCS-XY} = \sum_{\mathrm{k}} \varepsilon_{\mathrm{k}} \left(\tau^{3}_{\mathrm{k}} + 1\right) + \frac{1}{4} \sum_{\mathrm{k},\mathrm{k}'} V_{\mathrm{k},\mathrm{k}'} \left(\tau^{1}_{\mathrm{k}} \tau^{1}_{\mathrm{k}'} + \tau^{2}_{\mathrm{k}} \tau^{2}_{\mathrm{k}'}\right) \tag{8.21}$$

In this analogue, spin lattice sites are replaced by k-space lattice sites. Due to the fact that the phonon-mediated attractive interaction has short range, fluctuation effects can be assumed to have little significance and a mean field approach can be fruitful as it has been in the case of the magnetic counterpart. The electron is treated as being in the average field of its surroundings. In this case, an average Cooper pair density might be a good number to describe the superconducting state. Using this assumption, one can rewrite the Hamiltonian in terms of expectation values of Cooper pair creation and annihilation operators

$$b_{\mathrm{k}} = \langle c_{-\mathrm{k},\downarrow} c_{\mathrm{k},\uparrow} \rangle \quad \text{and} \quad b^{\dagger}_{\mathrm{k}} = \langle c^{\dagger}_{\mathrm{k},\uparrow} c^{\dagger}_{-\mathrm{k},\downarrow} \rangle \tag{8.22}$$

The operators themselves can then be written on the form $c_{-\mathrm{k},\downarrow} c_{\mathrm{k},\uparrow} = b_{\mathrm{k}} + \delta b_{\mathrm{k}}$, whereas the fluctuations can be written as $\delta b_{\mathrm{k}} = c_{-\mathrm{k},\downarrow} c_{\mathrm{k},\uparrow} - b_{\mathrm{k}}$. Inserting this into the BCS Hamiltonian, keeping only first order terms and introducing the so-called *gap-parameter*

$$\Delta^{\dagger}_{\mathrm{k}'} \equiv -\sum_{\mathrm{k}} V_{\mathrm{k},\mathrm{k}'} b^{\dagger}_{\mathrm{k}}, \quad \Delta^{\dagger}_{\mathrm{k}} \equiv -\sum_{\mathrm{k}'} V_{\mathrm{k},\mathrm{k}'} b_{\mathrm{k}'}, \tag{8.23}$$

yields the Hamiltonian

$$H_{BCS} = \sum_{\mathrm{k},\sigma} \varepsilon_{\mathrm{k}} c^{\dagger}_{\mathrm{k},\sigma} c_{\mathrm{k},\sigma} - \sum_{\mathrm{k}} \left(\Delta^{\dagger}_{\mathrm{k}} c_{-\mathrm{k},\downarrow} c_{\mathrm{k},\uparrow} + \Delta_{\mathrm{k}} c^{\dagger}_{\mathrm{k},\uparrow} c^{\dagger}_{-\mathrm{k},\downarrow} - b^{\dagger}_{\mathrm{k}} \Delta_{\mathrm{k}}\right). \tag{8.24}$$

This has now formally been reduced to a one body Hamiltonian with k-dependent cooper pair creation and and annihilation terms. Thus, this Hamiltonian is not in diagonal form. To do this,

one must define new pseudo particle creation and annihilation operators by making a clever unitary transformation (the so-called Bogoliubov transformation) of the old ones

$$c_{\mathrm{k}} = \cos(\theta)\eta_{\mathrm{k}} - \sin(\theta)\gamma_{\mathrm{k}} \quad \text{and} \quad c^{\dagger}_{-\mathrm{k}} = \sin(\theta)\eta_{\mathrm{k}} + \cos(\theta)\gamma_{\mathrm{k}}. \tag{8.25}$$

By ignoring the phase fluctuations of the complex gap parameter setting $\Delta^{\dagger}_{\mathrm{k}} = \Delta_{\mathrm{k}}$, one can choose θ as $\tan(2\theta) = \Delta_{\mathrm{k}}/\varepsilon_{\mathrm{k}}$, yielding the diagonalized BCS Hamiltonian

$$H_{BCS} = \sum_{\mathrm{k},\sigma}\left(\varepsilon_{\mathrm{k}} + \Delta_{\mathrm{k}} b^{\dagger}_{\mathrm{k}}\right) + \sum_{\mathrm{k}} E_{\mathrm{k}}\left(\eta^{\dagger}_{\mathrm{k}}\eta_{\mathrm{k}} - \gamma^{\dagger}_{\mathrm{k}}\gamma_{\mathrm{k}}\right) \quad \text{where} \quad E_{\mathrm{k}} = \sqrt{\varepsilon^2_{\mathrm{k}} + |\Delta_{\mathrm{k}}|^2}. \tag{8.26}$$

Due to the transformation which allowed for a diagonalization of the Hamiltonian, the two emerging fermionic pseudo particles can be interpreted as electron-hole singlets with $S = 0$ with identical excitation spectra. This spectra - E_{k} - has an *energy gap* - Δ_{k} - which is directly connected to the expectation value of the Cooper pair annihilation (creation) operators - *the order parameter of the superconducting state.* The magnetic analogue of this order parameter is the expectation value of the spin operator which is zero above the magnetic ordering temperature and non-zero below. The first term of the Hamiltonian is a constant term, while the second term involves excitations. The partition function for this system can then be written, yielding the free energy F of the system

$$Z = \exp\left[i\beta\sum_{\mathrm{k}}\left(\varepsilon_{\mathrm{k}} + \Delta_{\mathrm{k}} b^{\dagger}_{\mathrm{k}}\right)\right]\prod_{\mathrm{k}}\left(1 + e^{-\beta E_{\mathrm{k}}}\right)\left(1 + e^{\beta E_{\mathrm{k}}}\right) = \exp(-\beta F), \tag{8.27}$$

where $\beta = 1/k_B T$. The problem is to find the stationary point of the free energy F in the zero-temperature limit with respect to the gap parameter(s) Δ_{k} and $\Delta^{\dagger}_{\mathrm{k}}$. This results in the BCS gap self consistency equation

$$\Delta_{\mathrm{k}} = -\sum_{\mathrm{k}'} V_{\mathrm{k},\mathrm{k}'} \overbrace{\Delta_{\mathrm{k}'} \underbrace{\frac{\tanh\left(\beta E_{\mathrm{k}'}/2\right)}{2E_{\mathrm{k}'}}}_{\equiv\chi(\mathrm{k}')}}^{b^{\dagger}_{\mathrm{k}'}}. \tag{8.28}$$

The fraction involving $E_{\mathrm{k}'}$ describes the ability of the system to create Cooper pairs, and is known as the pair susceptibility. By assuming the simple potential depicted in figure 64 taking the Debye frequency (maximum phonon frequency) as the cutoff frequency, one obtains a k-independent gap function $\Delta_{\mathrm{k}} \to \Delta$. Introducing the parameter $\lambda \equiv V D_n(0)$, where V is the potential strength and $D_n(0)$ is the density of states at zero energy in the normal state, one obtains from the gap equation the following results for the transition temperature and gap magnitude at zero temperature

$$k_B T_c = 1.13\omega_D e^{-\frac{1}{\lambda}} \quad \text{and} \quad \Delta(T=0) = 2\omega_D e^{-\frac{1}{\lambda}}; \quad \text{hence} \quad 2\Delta(T=0) \approx 3.52 k_B T_c. \tag{8.29}$$

The coupling constant λ is difficult to calculate, but the ratio between the transition temperature and the superconducting gap at zero temperature is constant. Using the BCS partition function one can calculate the electronic heat capacity and show a discontinuity at T_c upon cooling followed by an exponential decrease due to the fact that there is now a minimum excitation energy (the gap) as opposed to a normal metal (see figure 60). It is important to underline that BCS superconductivity is a k-space phenomenon, the electrons forming a Cooper pair move in opposite directions and experience a short range coupling when in the vicinity of one another. It is then reasonable to imagine that a given electron changes Cooper partner continuously, only being correlated to any single electron for at certain time or length. A crude estimate of this length can be given by the Heisenberg uncertainty principle, assuming that the spread in Cooper pair kinetic energy is $\delta E = 2\Delta$. Reasonably assuming that $\delta p = \delta E / v_F$ one obtains for the *coherence length*:

$$\xi \sim \frac{\hbar v_F}{\Delta(0)}, \qquad \xi_{BCS} \equiv \frac{\hbar v_F}{\pi\Delta(0)}, \tag{8.30}$$

where the proper BCS definition has been given to the right for the sake of completeness. As previously mentioned, the finite phonon-assisted attractive coupling strength $V_{\mathrm{k,k'}}$ results in a gap in the pseudo particle excitation spectrum. This is the minimum energy required to break up the Cooper pair. For a low enough temperature, the Cooper-pairs are able to form without being destroyed by thermal fluctuations, yielding a non-zero expectation value of the pair creation/annihilation operators - the order parameter. Electrons near the fermi-surface *lower their energy* by forming composite bosons. Due to the *energy gap* in the *fermionic pseudo particle excitation spectrum* it is energetically favorable for all the Cooper-pairs to condense in the ground state, all having the same phase (reflecting the strong correlation of the electrons). This *coherent* phase results in an uncertainty of the ground state occupation number, so the BCS ground state is a superposition of states with different occupation number (the fractional uncertainty $\delta N/N$ is still small however). This coherence resembles laser light in the respect that one needs a large number of photons in the same state to create a propagating electrical field with well defined amplitude and phase. This is what superconductivity is: a pseudo bosonic condensate of phase-coherent Cooper-pairs reluctant to interact with their surroundings due to the energy gap in the pseudo particle spectrum near the Fermi surface. This *macroscopic wave function* enables one to successfully describe the macroscopic properties of a superconductor in a simple framework by expressing the free energy as a function of the spatially varying complex gap function $\Delta(\mathrm{r}) = |\Delta(\mathrm{r})|e^{i\phi}$. This concludes the description of the BCS theory.

8.2 Ginzburg-Landau theory of superconductivity

There is a long way from successfully calculating the excitation spectrum of a superconductor using the BCS theory, to being able to successfully treat cases where an applied field drastically changes the homogeneity of the condensate, as is the case in a vortex lattice. Some time before the publication of the BCS theory, V. L. Ginzburg and L. D. Landau (GL), published a macroscopic and phenomenological theory of superconductivity [60]. They expressed the free energy of the macroscopic system as an even function of a complex order parameter $\Psi(\mathbf{r})$, where $|\Psi(\mathbf{r})|^2$ would be proportional to the density of superconducting electrons (the free energy is expanded as an even function since the density is the square of the wave function). Their phenomenological theory was later derived from the BCS theory for temperatures near T_c [61], where $\Psi(\mathbf{r})$ was found to be proportional to the BCS gap $\Delta(\mathbf{r})$. From this viewpoint the free energy density should be an even function of the BCS gap since the free energy should be invariant with respect to a phase change of the complex gap function. In this section, a short description of the elements of GL theory leading to the theory of vortex lattices will be given, following the account given in [62]. In this section, Gaussian cgs units are used, as in [62] and many other books on superconductivity. The proposed Ginzburg-Landau form of the free energy is

$$F = F_0 + \alpha|\Psi|^2 + \frac{\beta}{2}|\Psi|^4 + \frac{1}{2m^*}\left|\left(\frac{\hbar}{i}\nabla - \frac{e^*}{c}\mathbf{A}\right)\Psi\right|^2 + \frac{H^2}{8\pi}, \tag{8.31}$$

where F_0 is the free energy in the normal state, m^* and e^* are the effective mass and charge of the superconducting electrons and $\mathbf{A}$ is the vector potential of an external electromagnetic field. The temperature dependence of the two expansion parameters can be found from BCS theory near T_c [63]:

$$\alpha(T) = N(0)\frac{T - T_c}{T_c} \quad \text{and} \quad \beta(T) = 0.3302\frac{N(0)}{\Delta_{BCS}(0)^2}, \tag{8.32}$$

where $N(0)$ is the density of states at the Fermi-energy and $\Delta_{BCS}(0)$ is the BCS gap at zero temperature. Note that at $T > T_c$, $\alpha > 0$ and the global minimum of free energy is at $|\Psi|^2 = 0$ - the normal state. The last term in equation 8.31 is the energy density of an applied field and the fourth term describes the effect of gradients and fields on the order parameter Ψ. In the absence of fields and gradients the last two terms vanish and the free energy of the superconducting electrons can be written as

$$F_s = F - F_0 = \alpha|\Psi|^2 + \frac{\beta}{2}|\Psi|^4. \tag{8.33}$$

These two terms are equivalent to a series expansion in Ψ retaining only the first two terms. In order to have a finite minimum in free energy, β must be positive, and therefore the minimum can only be non-zero if α is negative in the superconducting state. This gives a minimum at

$$|\Psi_\infty|^2 \equiv -\frac{\alpha}{\beta} \tag{8.34}$$

Inserting this in equation 8.33, the thermodynamical critical field can be estimated as

$$H_c^2 = \frac{4\pi\alpha^2}{\beta} \tag{8.35}$$

Above the critical temperature $\alpha(T)$ must be positive, resulting in a free energy minimum at $\Psi = 0$. It can be shown [62], that the three important parameters of this theory can be evaluated from

measurable quantities in the following way:

$$\begin{aligned} |\Psi_\infty|^2 &\equiv \frac{n_s}{2} = \frac{mc^2}{8\pi e^2 \lambda_{eff}^2} \\ \alpha(T) &= -\frac{2e^2}{mc^2} H_c^2(T) \lambda_{eff}^2(T) \\ \beta(T) &= \frac{16\pi e^4}{m^2 c^4} H_c^2(T) \lambda_{eff}^4(T). \end{aligned} \tag{8.36}$$

$H_c(T)$ and $\lambda_{eff}(T)$ can both be measured or calculated from the BCS theory, and are the only free parameters of the theory. The notation λ_{eff} has been used not to confuse it with the London penetration depth. The effective penetration depth depends on the amount of impurities and the dimensions of the sample. Using the empirically found forms of $H_c(T)$ and $\lambda_{eff}(T)$, the critical behavior of the three parameters near T_c are roughly:

$$\begin{aligned} |\Psi_\infty|^2 &\propto 1 - t^4 \approx 4(1-t) \\ \alpha(T) &\propto \frac{1-t^2}{1+t^2} \approx 1 - t \\ \beta(T) &\propto \frac{1}{(1-t^2)^2} \approx \text{const} \end{aligned} \tag{8.37}$$

These simple forms are valid under the assumption that only the leading order in the Taylor expansion has significance, which is true near T_c. The free energy expression in equation 8.31 and the relations 8.36 *extends* the BCS theory and provides a powerful tool to deal with gradients in $\Psi(\mathbf{r})$ and fields.

8.2.1 The Ginzburg-Landau differential equations

In the case described by equation 8.33 - the case without gradients or fields - the minimum energy is just the case with $\Psi = \Psi_\infty$ everywhere. It gets much more complicated, when one has to take the fourth term of equation 8.31 into account. The system adjusts the order parameter so as to minimize the overall free energy. This minimum can be found by using the variational principle, setting the variation of the overall free energy $\delta \int F_s dV$ to zero. This leads to two central equations describing the superconducting condensate:

$$\alpha\Psi + \beta|\Psi|^2\Psi + \frac{1}{2m^*}\left(\frac{\hbar}{i}\nabla - \frac{e^*}{c}\mathbf{A}\right)^2 \Psi = 0 \tag{8.38}$$

$$\mathbf{J} = \frac{e^*\hbar}{2m^*i}(\Psi^*\nabla\Psi - \Psi\nabla\Psi^*) - \frac{e^{*2}}{m^*c}\Psi^*\Psi\mathbf{A}, \tag{8.39}$$

where $\mathbf{J}$ describes the super current. An instructive first step in understanding these equations is to allow gradients in $\Psi(\mathbf{r})$ and set the field $\mathbf{A}(\mathbf{r})$ to zero. Evaluating equation 8.38, all imaginary terms thus vanish and one can take Ψ to be real. Focusing merely on the one dimensional case and normalizing the order parameter $f = \frac{\Psi}{\Psi_\infty}$ one obtains

$$\frac{\hbar^2}{2m^*|\alpha|}\frac{d^2f}{dx^2} + f - f^3 = 0. \tag{8.40}$$

This normalized zero-field GL equation defines a characteristic length scale for the variation of $\Psi(\mathbf{r})$ (equivalent to $\Delta(\mathbf{r})$ in the BCS theory), namely the so-called *coherence length*

$$\xi^2(T) = \frac{\hbar^2}{2m^*|\alpha(t)|} \propto \frac{1}{1 - T/T_c}. \tag{8.41}$$

The value of the coherence length in terms of the measurable and derivable $H_c(T)$ and $\lambda_{eff}(T)$ is

$$\xi(T) = \frac{\Phi_0}{2\sqrt{2}\pi H_c(T)\lambda_{eff}(T)}, \quad \text{where} \quad \Phi_0 = \frac{hc}{2e}. \tag{8.42}$$

As evident from the nature of the Cooper pairs themselves, magnetic field and superconductivity are to some extent mutually exclusive. The superconducting condensate expels magnetic fields, and strong enough magnetic fields destroy superconductivity - there is a competition between the two order parameters. Thus, in this macroscopic free energy treatment of superconductivity there are characteristic length scales for the two order parameters. The penetration depth describing the decay length of a magnetic field at the normal/superconducting interface and the coherence length describing the decay length of a perturbation in Ψ. This allows for a calculation of the surface energy associated with an interface between the superconducting and normal phases of matter.

8.2.2 Domain wall energy

A convenient parameter characterizing the interface between the superconducting and normal states is the relationship between the penetration depth and the coherence length

$$\kappa(T) \equiv \frac{\lambda_{eff}(T)}{\xi(T)}, \tag{8.43}$$

which is a dimensionless characteristic number for a given superconductor. This parameter can be readily interpreted using figure 66. A small κ implies that there is an interval where the magnetic field is fully suppressed at the cost of diamagnetic energy yet the superconducting order parameter is still below its optimal value Ψ_∞ at $x \to \infty$ - resulting in a positive surface energy. In case of a large κ, there is an interval where the superconducting order parameter is optimal, but still allowing a finite field density. This results in a negative condensation energy which has consequences at high enough fields.

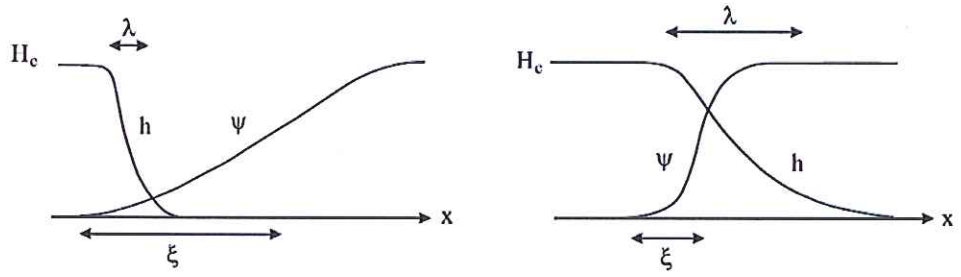

Figure 66: A one-dimensional illustration of the relevant region near an interface between the superconducting state and the normal state (a domain wall), in the two cases where $\lambda \gg \xi$ ($\kappa \gg 1$ - right) and $\lambda \ll \xi$ ($\kappa \ll 1$ - left)

Going back to the differential equations 8.38 and 8.39, figure 66 imposes two natural boundary conditions on the differential equations:

$$\Psi = 0 \quad \text{and} \quad h = H_c \quad \text{for} \quad x \to -\infty$$
$$\Psi = \Psi_\infty \quad \text{and} \quad h = 0 \quad \text{for} \quad x \to +\infty.$$

Using these boundary conditions it is possible [62] to get the following expression for the surface energy γ as a function of the magnetic field h, which is essentially the excess in Gibbs free energy G_{sH} over what it would be if there was no interface and $\Psi = \Psi_\infty \to G = f_s$ everywhere:

$$\gamma = \int_{-\infty}^{\infty} G_{sH} - f_s dx = \int_{-\infty}^{\infty} f_{sH} - \frac{hH_c}{4\pi} - f_s dx = \int_{-\infty}^{\infty} \left[-\frac{\beta}{2}|\Psi|^4 + \frac{h - H_c)^2}{8\pi} \right] dx. \tag{8.44}$$

Upon normalization to the magnetic energy density at critical field $H_c^2/8\pi$ one obtains:

$$\gamma\frac{8\pi}{H_c^2} = \int_{-\infty}^{\infty}\left[\left(1-\frac{h}{H_c}\right)^2 - \left(\frac{\Psi}{\Psi_\infty}\right)^4\right]dx. \tag{8.45}$$

In this last expression the competition between the energy required to facilitate the diamagnetic response and the condensation energy of the superconducting condensate is clearly revealed. It can be shown that the value of κ marking the crossover from negative to positive surface energy is exactly at $\kappa = 1/\sqrt{2}$. In case of a negative surface energy, it must be favorable to create many normal regions within the superconductor when applying strong enough fields, maximizing the domain wall surface. A finite field density should be allowed within these normal regions. So qualitatively one would expect that applying a strong enough field on a $\kappa > 1/\sqrt{2}$ superconductor, would result in a phase in which there are small normal tubes of width 2ξ parallel to the field carrying a magnetic flux. This would result in a non-zero magnetization of the superconducting sample, at least from a macroscopic point of view. Superconducting materials with $\kappa > 1/\sqrt{2}$ and hence negative surface energy are called *Type-II superconductors*, and are characterized by their ability to allow a strong enough magnetic field to penetrate the condensate in the form of quantized flux lines, which will be evident in the following section. Superconducting materials with $\kappa < 1/\sqrt{2}$ - Type-I superconductors - has positive domain wall surface energy and only allows a field to penetrate in the normal state above H_c.

Flux quantization

In order for the GL theory to make sense, the complex superconducting order parameter - $\Psi(\mathbf{r}) = |\Psi(\mathbf{r})|e^{i\phi(\mathbf{r})}$ - must be single valued for any $\mathbf{r}$. This is supported by the fact that the GL theory can be derived from the BCS theory with Ψ proportional to the gap $\Delta(\mathbf{r})$. This requires that the phase of Ψ is required to change by a multiple of 2π through any closed path:

$$\oint \nabla\phi \cdot d\mathbf{s} = 2\pi n = \oint \frac{1}{\hbar}\left(m^*\mathbf{v}_s + \frac{e^*\mathbf{A}}{c}\right)\cdot d\mathbf{s} \tag{8.46}$$

The last equality follows from the third term of the GL free energy expansion, which describes the kinetic energy of super current (see [62]). By choosing a path far away from the normal region allows for a neglection of the superconducting current, and by invoking Stokes theorem - $\Phi = \oint \mathbf{A}\cdot d\mathbf{s}$ - one obtains

$$2\pi n = \frac{e^*}{\hbar c}\oint \mathbf{A}\cdot d\mathbf{s} \Rightarrow \Phi = \frac{hc}{2e}n \tag{8.47}$$

This means that the normal regions of a type two superconductor can only carry discrete values of flux, integer multiples of the *fluxoid* - $\Phi_0 = hc/2e$. Since as many normal flux tubes are created as possible - to minimize the interface surface energy - it is reasonable to expect that the flux tubes will carry only one flux quantum.

8.2.3 The linearized Ginzburg-Landau equation and the Abrikosov vortex state

In order to be able to transparently investigate the bulk magnetic properties of a Type-II superconductor theoretically, it is instructive to assume a relatively small order parameter, $|\Psi|^2 \ll |\Psi_\infty|^2 = -\frac{\alpha}{\beta}$. This allows for a neglection of the β-term in equation 8.38, resulting in the linear differential equation

$$\left(\frac{\nabla}{i} - \frac{2\pi\mathbf{A}}{\Phi_0}\right)^2\Psi = \frac{2m^*\alpha}{\hbar^2}\Psi, \tag{8.48}$$

which is equivalent to the Schrödinger equation for a free particle in a magnetic field. Consider an infinite superconducting sample in a magnetic field $\mathbf{H} \parallel \hat{z}$, with a choice of gauge such that $A_y = Hx$ (Landau gauge). Substituting this into equation 8.48 and expressing it using the coherence length ξ gives

$$\left[-\nabla^2 + \frac{4\pi i}{\Phi_0} Hx \frac{\partial}{\partial y} + \left(\frac{2\pi H}{\Phi_0}\right)^2 x^2\right] \Psi = \frac{1}{\xi^2}\Psi, \tag{8.49}$$

As the vector potential only depends on the x-coordinate, a trial function could be on the following form

$$\Psi = e^{ik_y y} e^{ik_z z} f(x), \tag{8.50}$$

which after inserting the trial function into equation 8.49 results in

$$-\frac{\partial^2}{\partial x^2} f(x) + \left(\frac{2\pi H}{\Phi_0}\right)^2 (x - x_0)^2 f = \left(\frac{1}{\xi^2} - k_z^2\right) f, \quad \text{where} \quad x_0 = \frac{k_y \Phi_0}{2\pi H}. \tag{8.51}$$

This is the Schrödinger eigen energy equation of a harmonic oscillator - $\hat{H} = 1/2d^2/dx^2 + 1/2x^2$ - with the following eigen energy

$$E_n = \left(n + \frac{1}{2}\right) \hbar \left(\frac{2eH}{m^* c}\right), \tag{8.52}$$

which leads to the quantized field flux

$$H(n, k_z) = \frac{\Phi_0}{2\pi(2n+1)} \left(\frac{1}{\xi^2} - k_z^2\right) \Rightarrow H_{\max} = H(0,0) = \frac{\Phi_0}{2\pi\xi^2(T)} \equiv H_{c2}. \tag{8.53}$$

It is worth noticing that the assumptions leading to equation 8.49 are very valid at fields close to H_{c2} where the magnetic field has considerably reduced $|\Psi|^2$. So there is a maximum field above which superconductivity cannot exist and just below which the field density decreases in discrete steps. The eigenfunction f to equation 8.51 is

$$f(x) = \exp\left[-\frac{(x - x_0)^2}{2\xi^2}\right], \tag{8.54}$$

which is a Gaussian slice of superconductivity centered at $x = x_0$ with a width of ξ. Furthermore, it can be shown that [62]

$$H_{c2} = \sqrt{2}\kappa H_c, \tag{8.55}$$

confirming that the limiting value of κ separating Type-I from Type-II superconductors is indeed at $\kappa = 1/\sqrt{2}$. Despite that this solution is only valid at fields close to H_{c2}, equation 8.55 also hints that there are (at least) two magnetic phases in a Type-II superconductor. A phase below H_{c1} which excludes all magnetic field from its interior, and a phase for fields $H_{c1} < h < H_{c2}$, where a field is allowed to penetrate the sample in the form of quantized flux lines. In a bulk sample there are thus an infinite number of solutions at H_{c2} of the form:

$$\psi_k = e^{iky} f(x) = e^{iky} \exp\left[-\frac{(x - x_0)^2}{2\xi^2}\right], \quad \text{where} \quad x_k = \frac{k\Phi_0}{2\pi H} \tag{8.56}$$

Each of these solutions is local. A global space-filling solution to the linearized GL-equation can be achieved sensibly by enforcing periodicity on the solution as this is expected to be energetically

favorable compared to a random solution. Choosing k to be discrete with the period $q = 2\pi/\Delta y$ gives

$$k_n = nq, \quad x_n = \frac{nq\Phi_0}{2\pi H} \quad \text{and} \quad H\Delta X\Delta Y = \Phi_0. \tag{8.57}$$

This constructed solution has translational invariance along the x and y direction perpendicular to the field with primitive unit cells each containing one flux quantum. A general form of the solution is

$$\Psi_L = \sum_n C_n \exp(inqy) \exp\left[-\frac{(x - x_n)^2}{2\xi^2}\right], \tag{8.58}$$

where the coefficient C_n determines the structure of the lattice. This solution is constructed to be periodic in y, and should also be periodic in x in order to achieve two-dimensional periodicity. This is the case if C_n is periodic in n. A square lattice is described by the case $C_{n+1} = C_n$, while the case $C_{n+1} = iC_n$ describes a triangular lattice. Actually, these two solutions have almost the same

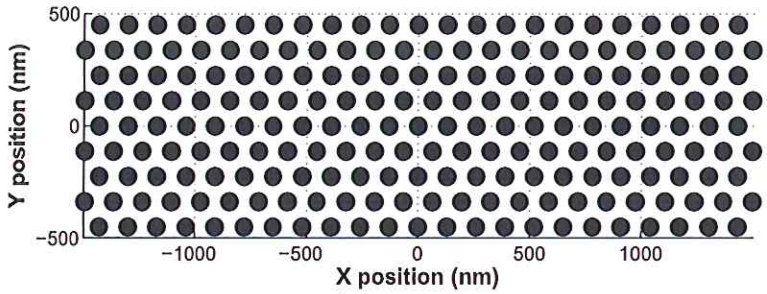

Figure 67: The hexagonal close-packed vortex lattice for an applied field of $130mT$

free energy, and in order to calculate which space-filling solution is expected to be observed the full GL-equations need to be considered, including the β-term. It has been shown that in the absence of effects due to the underlying crystal lattice, the triangular vortex lattice is the most favorable one [64]. This agrees with what one would expect intuitively - since the hexagonal close packed lattice is the densest way of packing circles in 2D - in this case the structure that maximizes the number of flux lines. An example of the triangular lattice is shown in figure 67. Assuming that each unit cell carries exactly one flux quantum, the area of the unit cell A_u and the applied field are inversely proportional $B = \Phi_0/A_u$, leading to the following relation between the applied field and the lattice constant a:

$$A_u = a^2 \sin(60) = \Phi_0/B \Rightarrow a = \sqrt{\frac{2\Phi_0}{\sqrt{3}B}} \tag{8.59}$$

This description of the vortex lattice is oversimplified. There are two important interactions that need to be accounted for, the interaction between flux lines and the interaction between vortex lines and parts of the superconductor which for some reason are in the normal state - called *pinning*.

8.3 Forces acting on and between flux lines

It is reasonable to expect that the field density within a flux tube in the normal state will decay outside the tube as the distance from the volume in the normal state increases - with the penetration depth as a characteristic length. When two flux lines are far away from each other they can be treated as two isolated flux lines, as the field far away from a flux line would vanish due to the

diamagnetic nature of the superconducting condensate. However, when the distance between the flux lines becomes comparable to the penetration depth, the field distribution of the two flux lines perpendicular to the field direction begins to overlap and thus one would qualitatively expect a repulsive interaction due to the increase magnetic energy of the overlap region. To quantify this it is necessary to determine this field distribution more accurately.

8.3.1 Structure of an isolated vortex

Assuming that the flux tube structure is independent of the z coordinate parallel to the field, the problem reduces to finding the field and order parameter distribution as a function of the radial distance from the flux tube, denoted $h(r)$ and $\Psi(r)$ respectively. When the applied field is exactly H_{c1}, the Gibbs free energy should be the same in the presence as in the absence of one flux line. Taking ϵ to be the flux line energy pr. unit length, this can be expressed as

$$G_s\Big|_{\text{no flux}} = G_s\Big|_{\text{one vortex}} \Rightarrow F_s = F_s + \epsilon L - \frac{H_{c1}\int h d\mathbf{r}}{4\pi}. \tag{8.60}$$

Equating $\int h d\mathbf{r}$ to $\Phi_0 L$, one can express the lower critical field H_{c1} as a function of the flux line energy

$$H_{c1} = \frac{4\pi\epsilon}{\Phi_0}. \tag{8.61}$$

Finding the radial field and order parameter distributions is in general difficult and requires numerical methods. It is instructive, however, to express the radial distribution of the vortex line order parameter in the form

$$\Psi = \Psi_\infty f(r) e^{i\theta}, \tag{8.62}$$

where θ is an angle describing the direction of r in the (x, y)-plane. The angle θ can be introduced due to the fact that the order parameter is single-valued and the phase of Ψ must change by a multiple of 2π when completing a closed circuit. This fixes the gauge choice to

$$\mathbf{A} = A(r)\hat{\theta}, \quad A(r) = \left(\frac{1}{r}\right)\int_0^r r' h(r') dr' \tag{8.63}$$

Using these definitions and the two GL differential equations (the non-linearized), it can be shown that a good approximation to f is [62]:

$$f(r) \approx \tanh\left(\frac{\nu r}{\xi}\right) \tag{8.64}$$

In evaluating $h(r)$ it is instructive to examine the high-κ limit. In this limit the coherence length is much smaller than the penetration depth, so it can be assumed that $f \to 1$ on a scale much smaller than the scale of variation of the field. So treating the case of a non-varying order parameter of magnitude $|\Psi|^2 = |\Psi_\infty|^2$ greatly simplifies equation 8.39 since the gradient term disappears. This results in a simple equation outside the core

$$\frac{4\pi\lambda^2}{c}\nabla \times \mathbf{J} + \mathbf{h} = 0 \tag{8.65}$$

The above equation gives zero flux for any path encircling the core, so the zero on the left hand side must be replaced with the expression $\hat{\mathbf{z}}\Phi_0\delta(r)$, to force the contained flux to be Φ_0 and hence compensate for the fact that this equation does not hold near the core containing the flux. In [62] it is shown that this gives an exact solution for the field distribution at high κ:

$$h(r) = \frac{\Phi_0}{2\pi\lambda^2} K_0\left(\frac{r}{\lambda}\right), \tag{8.66}$$

where K_0 is the so-called zeroth order Hankel function. The two relevant limiting cases are:

$$h(r) \to \frac{\Phi_0}{2\pi\lambda^2}\sqrt{\frac{\pi\lambda}{2r}}e^{-r/\lambda}, \quad \text{for} \quad r \to \infty \tag{8.67}$$

$$h(r) \approx \frac{\Phi_0}{2\pi\lambda^2}\left[\ln\left(\frac{\lambda}{r}\right) + 0.12\right] \quad \text{for} \quad \xi \ll r \ll \lambda \tag{8.68}$$

The case for $\kappa \approx 8$ is shown in figure 68

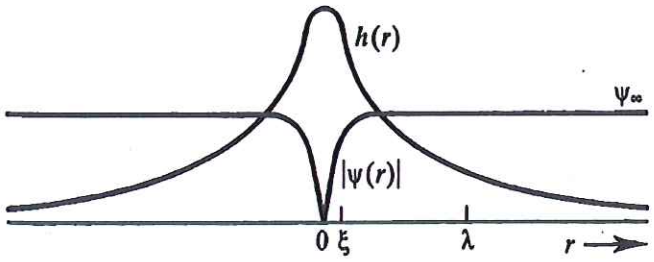

Figure 68: Radial dependency of both the superconducting order parameter ξ and the magnetic field h taken from the center of the flux line for $\kappa \approx 8$. Picture from [62].

Flux line energy

An instructive expression for the free energy pr. unit length of a flux line can be found by excluding the core. In that case only the free energy from the field energy and from the kinetic energy of the super currents contributes, yielding

$$\epsilon = \frac{1}{8\pi}\int \left(h^2 + \lambda^2|\nabla \times \mathbf{h}|^2\right) dS. \tag{8.69}$$

Using this and equation 8.68 it can be shown that

$$\epsilon \approx \left(\frac{\Phi_0}{2\pi\lambda^2}\right)^2 \ln(\kappa) \quad \text{or} \quad \epsilon \approx \frac{H_c^2}{8\pi} 4\pi\xi^2 \ln(\kappa), \tag{8.70}$$

under the assumption that $\kappa \gg 1$. Since H_c is the field density of energy equal to the energy density of the condensate, the line tension energy in this approximation is a factor of $4\ln(\kappa)$ larger than the condensation energy lost in the core of cross-sectional area $\pi\xi^2$. It is now possible to get the proper lower critical field H_{c1} for a Type-II superconductor, the field at which the flux starts to penetrate the sample

$$H_{c1} = \frac{4\pi}{\Phi_0}\epsilon \approx \frac{H_c}{\sqrt{2}\kappa}\ln(\kappa) \tag{8.71}$$

8.3.2 Interaction between flux lines

The total field from two flux lines located at $\mathbf{r}_1$ and $\mathbf{r}_2$ respectively for field applied along z can be expressed using the high-κ expression for $h(r)$ in equation 8.66:

$$h_z(\mathbf{r}) = h(|\mathbf{r} - \mathbf{r}_1|) + h(|\mathbf{r} - \mathbf{r}_2|) \tag{8.72}$$

The free energy of these two flux lines pr. unit length can be calculated in the same way as for a single flux line using equation 8.69, neglecting the core energy, to be

$$\epsilon_{1+2} = \frac{\Phi_0}{4\pi} h_1(\mathbf{r}_1) + \frac{\Phi_0}{4\pi} h_1(\mathbf{r}_2), \tag{8.73}$$

where the first term is the isolated line energies from the two flux lines, while the second term is the interaction energy. The two flux lines are identical and the hence energy is invariant with respect to flux line interchange. So one can express the free energy from the interaction between two flux lines as a function of the distance between them in the (x, y) plane

$$F_{12} = \frac{\Phi_0^2}{8\pi^2\lambda^2} K_0\left(\frac{r_{12}}{\lambda}\right), \tag{8.74}$$

where K_0 has the same limits as described in equations 8.67 and 8.68. The force between the flux lines is the derivative of F_{12} with respect to the distance between the flux lines. Doing this and combining with Maxwells 4. law - $\nabla \times \mathbf{h} = 4\pi\mathbf{J}/c$ - gives the following expression describing the force on flux line 2 due to the super current imposed by flux line 1:

$$\mathbf{f}_2 = \mathbf{J}_1(\mathbf{r}_2) \times \frac{\Phi_0 \hat{\mathbf{z}}}{c} \tag{8.75}$$

This can be generalized to the force felt by a vortex $\mathbf{f}$ due to the super current from all other vortices $\mathbf{J}_s$ including possible transport currents:

$$\mathbf{f} = \mathbf{J}_s \times \frac{\Phi_0 \hat{\mathbf{z}}}{c} \tag{8.76}$$

In a perfect triangular lattice, the super current at any flux line position due to the the surrounding flux lines would cancel due to the symmetry of the lattice. However, if there is a macroscopic transport current, the lattice as a whole would experience a net force. This is actually the cause for an effective non-zero electrical resistance in the vortex phase of a perfectly clean superconductor. The force perpendicular to the transport current causes the flux lines to move with a velocity $\mathbf{v}$, inducing an electrical field

$$\mathbf{E} = \mathbf{B} \times \frac{\mathbf{v}}{c} \tag{8.77}$$

which is perpendicular to the transport current. This causes a resistance at any finite transport current if no mechanism is present that opposes flux line movement. Dissipation of energy can also be caused by the normal cores being dragged through the condensate allowing the transport current to flow through the normal region (discussed in [62]). Since any transport current would create a magnetic field, restraining the vortices is an important aspect of creating usable superconductors so that a field below H_{c2} and not H_{c1} defines the critical current boundary. This restraint can be caused by flux line pinning, described in section 8.3.4.

8.3.3 Intermediate mixed state

In the previous sections, the geometry of a finite sample was not taken into consideration. When applying a small ($H < H_{c1}$) magnetic field on the sample, the total field is 0 inside the sample and H far away from the sample. This change occurs mainly near the sample edge, giving rise to a demagnetization factor. The free energy to minimize is thus not only the energy of the condensate in an applied field, but the free energy of the system as a whole including the demagnetization factor. For Type-I superconductivity, this can be shown ([62]) to result in an intermediate state near H_c where there are co-existing *macroscopic* domains in the Meissner phase and the normal phase respectively.

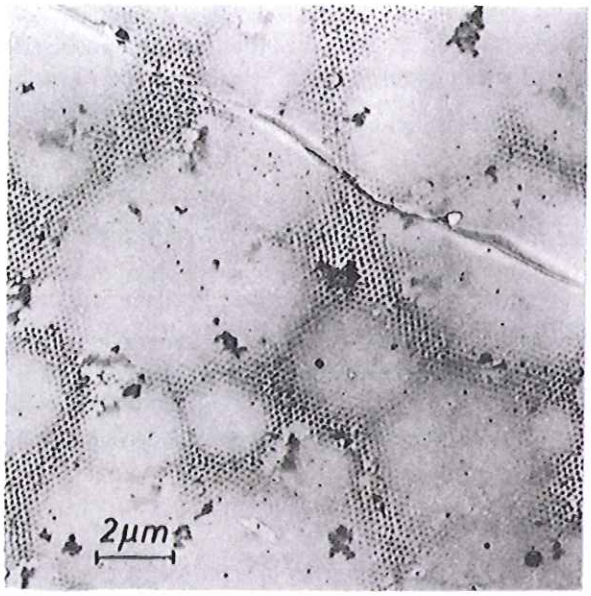

Figure 69: Intermediate mixed state in niobium as observed in [67].

This phase separation can also happen in Type-II superconductors - called the *intermediate mixed state*. Even though GL theory is actually a valid decription for a larger part of the phase diagram that one would naively expect, as derived in [65], BCS corrections are necessary for low fields and temperatures. A recent treatment of this intermediate mixed state is given in [66]. Such corrections are significant for $0.71 < \kappa < 1.5$ and they lead to an *attractive interaction* between fluc lines at large distances. Thus, the intermediate mixed state consists of large domains of Meissner phase and large domains of vortex lattice with an equilibrium lattice spacing a_{eq}. This intermediate mixed state has been observed in Bitter decoration experiments for a clean niobium disc [67] - as shown in figure 69. As the characteristics of the superconducting state in vanadium are very similar to those of niobium, such an intermediate mixed state could be possible near H_{c1} in the sample used in this work.

8.3.4 Flux line pinning

Assume that for some reason there is a microscopic volume in the superconducting condensate in which some irregularity enforces the normal state in the absence of any flux line. Crudely speaking, any normal region costs an energy of $VH_c^2/8\pi$, where V is the normal volume. Above H_{c1}, it is favorable to have tubes with normal centers of radius ξ carrying magnetic flux, even though there is a loss of condensation energy associated with creating such tubes. There is a free energy gain, however, by letting the normal tube center intersect any pre-existing normal region, simply due to the fact that one normal region is energetically favorable over two normal regions. This energy gain results in a force acting on the flux lines in the presence of such normal regions. It is reasonable to expect the range of such a force to be of the order ξ, since the order parameter of the flux line has been fully restored at distances $r \gg \xi$ from the normal center, resulting in a vanishing gradient in the potential.

There can be many causes of such normal regions, depending on the characteristics of the superconductor in question. If the normal region is much larger than ξ^3, the flux line would not gain much by intersecting such a volume since there would be an additional condensation energy loss from breaking up Cooper pairs in the regions with a finite order parameter. A normal region much

smaller than ξ^3 is not even possible due to the fact that the superconducting order parameter cannot change much on scales less than ξ. The possible nature and distribution of pinning potentials can therefore be entirely different when looking at different superconductors.

Pinning forces enable the actual application of superconductors, and they pose some of a challenge, theoretically. Assumptions have to be made about the nature of the pinning, and the validity of such assumptions can vary from superconductor to superconductor and even from sample to sample. When the center of a flux line is within $r \approx \xi$ of a pinning center, an attractive force will act between the pinning center and the flux line section nearest to it. This will be opposed by the lattice since the movement away from the equilibrium position will cost energy. Generally speaking, one is faced with the problem of an ensemble of tubes with a finite elasticity being perturbed by - more or less - random forces. It is even possible to change the lattice spacing in the flux line system and hence the elasticity constants, which makes the problem very interesting not only from the perspective of superconductor physics but from a perspective of random perturbations of elastic lattices in general. This difficult subject will be elaborated in the next section.

8.4 Collective properties of the vortex lattice: The Bragg glass theory and proposed phase diagrams

If the pinning forces are assumed to be randomly distributed throughout the sample, it is straightforward to argue that pinning cannot occur for a perfectly rigid lattice. The lattice as a whole would not be subject to any net force as every pinning force would be canceled out by another pinning force opposing it, due to the random nature of the distribution. If the lattice is elastic however, individual flux lines would be able to deviate from their ideal position, minimizing condensation energy at the cost of elastic energy. It is therefore appropriate to describe the lattice as elastic, allowing deformation at the cost of 'spring' energy. The assumptions made concerning pinning throughout this chapter are the following:

- The pinning forces acting on flux lines are point-like (as opposed to one-dimensional line segments or surfaces) - called pinning sites.
- The pinning sites are randomly distributed and *static* - often called *quenched.*
- The pinning strength is weak compared to the elasticity of the lattice.

These assumptions are by no means universal; in fact their validity can be dependent on the sample or the field and temperature condition. Whenever discussing generic vortex lattice phase diagrams, the pinning mechanism is always an obstacle, as there can be several reasons for pinning which in principle can co-exist and thus make a theoretical description difficult to generalize. These assumptions are assumed to be valid in the vanadium sample investigated in this work. Vanadium is an element, and therefore it is possible to make clean single crystals. The pinning sites are therefore expected to be a low density of impurity atoms causing small point-like normal volumes of size $4/3\pi\xi^3$.

The randomly distributed weak pinning forces influence the elastic vortex lattice. It is assumed that the elastic energy can be expressed in terms of the resistance of the lattice to three kinds of deformations, *compression*, *tilt* and *shear* (see figure 70). The free energy change associated with a deformation of the vortex lattice can be described as a sum of spring energy terms

$$\delta F = \frac{1}{2}C_{11}s_{11}^2 + \frac{1}{2}C_{44}s_{44}^2 + \frac{1}{2}C_{66}s_{66}^2, \tag{8.78}$$

where the stress coefficients s_{11}, s_{44} and s_{66} describe the level of deformation from the equilibrium configuration of compression, tilt and shear respectively. The configuration of the vortex ensemble

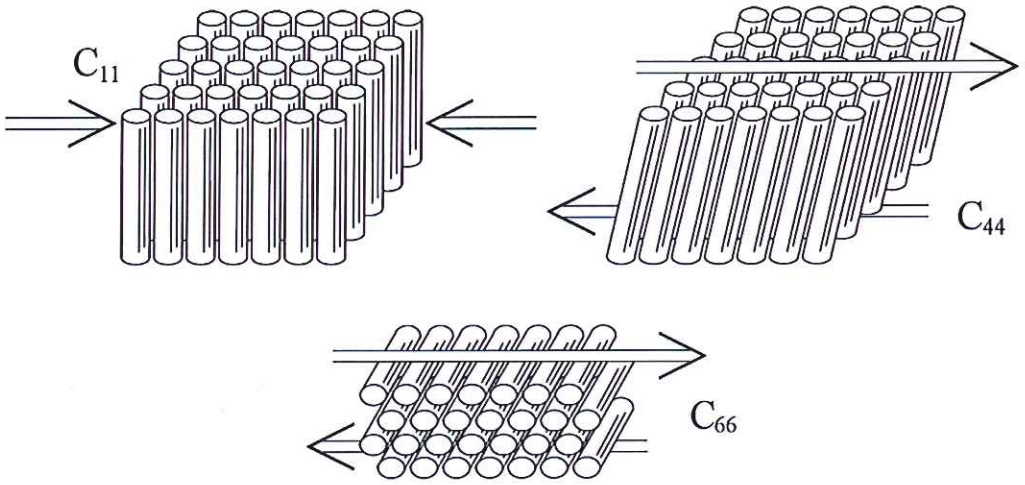

Figure 70: *Top left:* Compression - an applied force changes the lattice constant. *Top right:* Two forces of opposite direction acting on two different z-coordinates tilt the flux lines at the cost of flux line energy. *Bottom:* An illustration of shear - a displacement of one chain of flux lines from its neighboring chain. Picture from [59].

thus depends on the balance between accommodating the energy landscape produced by the pinning sites and minimizing the deformation energy. A good initial theory successfully describing critical current effects near H_{c2} was proposed by A. I. Larkin and Yu. N. Ovchinnikov in 1979 [68] and will be outlined in the next chapter. In the following let $\mathbf{u}(\mathbf{r})$ be the displacement vector $\mathbf{u}$ of the flux line situated at $\mathbf{r} = (r_\perp, z)$ for fields along z.

8.4.1 Phenomenological description of the elasticity

In equation 8.70 the flux line energy was shown to be proportional to the condensation energy lost in the core. It is reasonable to expect that the cost of extending a flux line would decrease as a function of temperature lessening the tilt and compression moduli. Another important point is that the flux line repulsion is proportional to the field overlap and hence the lattice constant. Thus, at very low fields, the flux lines are almost isolated and little interaction occurs resulting in a very soft lattice. Upon increasing the field the interaction grows leading to a harder lattice as the spring constant between the flux lines grows. However, when the field is increased further and the lattice constant is of the order of the coherence length $a \sim 3\xi$ the order parameter does not reach full height between the flux lines resulting in a decrease of flux line energy, and results in a softening of the lattice - extending and bending a flux line becomes less costly.

8.4.2 Larkin-Ovchinnikov theory

If every single flux line moved away from its equilibrium position throughout the entire flux line length - accommodating the pinning energy landscape in its vicinity - the cost in elastic energy would be high. Considering the assumed randomness of the pinning landscape it is reasonable to expect a collection of flux lines to keep their elastically optimal lattice configuration and collectively displace to a pinning energy minimum for the entire ensemble. This is the so-called *collective pinning* approach for correlated volumes.

The basis for this finite volume treatment of the pinning problem comes from the assumption that long range order is destroyed when the perfect elastic lattice is subjected to weak random forces. In

the general case of a continuous symmetry order parameter (as is the case with the superconducting order parameter), it can be shown that formation of domains or any type of disorder is energetically favorable in the presence of weak random forces when the dimensionality of the system is less than or equal to 4 (The so-called Imry-Ma argument [69]). The size of these domains depend on the magnitude of the random force but no matter how weak the force, in principle it will destroy order on a long enough scale. In the case of a vortex lattice in the presence of randomly distributed pinning sites, Larkin used perturbation theory to show that long range order cannot persist [70]. In fact, defining the *displacement correlator*

$$B(\mathbf{r}) = \overline{\langle [\mathbf{u}(\mathbf{r}) - \mathbf{u}(0)]^2 \rangle}, \tag{8.79}$$

where $\langle\rangle$ and $-$ define the thermal and disorder average respectively, he showed in [68] that $B(\mathbf{r})$ grows linearly with $r_\perp$, completely destroying the ordered lattice at large enough distances. An appropriate choice of volume is where the displacements are less than the range of the pinning force - r_f - described by two length scales $R_c||r_\perp$ and $L_c||z$. The relative displacements are then $s_{44} = r_f/L_c$ and $s_{66} = r_f/R_c$, and neglecting the effects of compression the increase in elastic free energy can be written:

$$\delta F_{el} = \frac{1}{2} C_{44} \left(r_f/L_c\right)^2 + \frac{1}{2} C_{66} \left(r_f/R_c\right)^2, \tag{8.80}$$

The pinning centers are randomly distributed, and thus any chosen pinning center close to a flux line will act on the ensemble as a whole in a random direction. There are nV_c such pinning centers in the correlation volume V_c, where n is the density of pinning sites. The resulting force acting on the correlation volume can then be described as a *random walk* with Gaussian distributed step size (Gaussian distributed force strength) - which scales as $\sqrt{nV_c}$. The Lorentz force density induced by the transport current scales with the current density J_t, so the total Lorenz force scales with $J_t V_c$. This actually means that in a perfect rigid lattice, any transport current can de-pin the vortices as the critical de-pinning current density (where the two forces are equal) scales with $V_c^{-1/2}$. So for a perfectly rigid lattice $J_c \to 0$ as $V_c \to \infty$. This is not the case in Larkin-Ovchinnikov theory, as one has finite correlated volumes. The resulting random force is proportional to $f\sqrt{nV_c}$, and with range r_f the resulting potential energy from the pinning forces is $\sim r_f f \sqrt{nV_c}$. The potential energy per unit volume can be directly inserted into equation 8.80 to yield the total free energy difference as a result of both elastic and pinning energy:

$$\delta F_{el} = \frac{1}{2} C_{44} \left(r_f/L_c\right)^2 + \frac{1}{2} C_{66} \left(r_f/R_c\right)^2 - f r_f \sqrt{\frac{n}{V_c}}. \tag{8.81}$$

This can be minimized to obtain the dimensions of the correlated volume,

$$L_c = \frac{2C_{44}C_{66}r_f^2}{nf^2}, \quad R_c = \frac{\sqrt{2C_{44}}C_{66}^{\frac{3}{2}}r_f^2}{nf^2} \quad \text{and} \quad V_c = \frac{4C_{44}^2 C_{66}^4 r_f^6}{n^3 f^6}. \tag{8.82}$$

In this model, the pinning force density is $f\sqrt{n/V_c}$. When the Lorentz force density resulting from transport currents exceeds this value, the individual correlated volumes begin to move, dissipating energy. This critical current density J_c is then described by the equation [71]

$$\frac{J_c B}{c} = \frac{n^2 f^2}{2C_{44}C_{66}^2 r_f^3} \tag{8.83}$$

So the softer the lattice, the larger the critical current, since the cost of conforming to the pinning energy landscape is smaller for the flux lines making the correlated volumes smaller. The exact calculation of the elastic moduli is tedious but necessary to predict the critical current. In [68] Larkin and Ovchinnikov were able to explain the so-called peak effect near H_{c2} where the critical

current suddenly rises before dropping to zero at the melting line in the (H,T) phase diagram. Close to H_{c2} the flux lines are close enough for the super current for any given flux line to be *screened* by the super currents from the neighboring lines, lessening the interaction and softening the lattice (or minimizing the correlation volume) - which leads to an increase in critical current. When $nV_c \sim 1$ each individual flux line is able to deform, conforming to the pinning landscape in its vicinity and resulting in a large critical current. Although the Larkin-Ovchinnikov theory deals with elasticity and pinning forces in an elegant and transparent manner yielding an easily interpretable expression for the critical current, it is far too simple to accurately describe the configurations of the vortex lattices. The reason for this is that at large scales, there is not necessarily a single ground state. The space of possible configurations explode at large scales, and several metastable configurations will be possible. Perturbation theory is unable to take several metastable states and the fluctuation between them into account, as it deals with one ground state [72]. So at transverse scales larger than the Larkin length R_c the linear increase of the displacement comes to a halt and beyond this scale order decays much more slowly. In fact, some degree of long range order persists in the presence of weak disorder, creating diffuse Bragg peaks, while the existence of many metastable states at long scales mostly resembles glassy states. Therefore, the proposed phase of vortex matter is called a *Bragg glass*, which will be the subject of the next chapter.

8.4.3 Bragg glass theory

The Bragg glass theory was developed by Thierry Giamarchi and Pierre Le Doussal (GD) [73, 74], who extended the work by Thomas Natterman [75], Jean-Phillipe Bouchaud, Marc Mezard and Jonathan S. Yedidia [76, 77] to describe the nature of the disorder of vortex lattice at large scales, making specific predictions about the correlations. Natterman predicted a logarithmic rise of the displacement correlator or *roughness* instead of the linear increase suggested by Larkin, while Bouchaud, Mezard and Yedidia applied the so-called *replica field theory* to the problem. This had previously been applied to the general problem of random manifolds by Marc Mezard and Giorgion Parisi[72][7]. The existence and importance of metastable states were recognized by Feigel'man et. al. [78], who predicted a powerlaw increase of the displacement correlator $B(\mathrm{r}) \sim r_f^{3/5} U_{LO}^{2/5}$, where U_{LO} is the displacement correlator suggested by Larkin and Ovchinnikov. So there were many suggestions that flux line correlations might not drop off as fast as suggested in LO-theory. In this chapter, two important quantities describe the flux line pair correlations as a function of length scale - the displacement correlator $B(\mathrm{r})$ given in equation 8.79 - and the so-called *translational correlation function*

$$C_g(r) = \overline{\langle e^{iK_0 \cdot [u(r) - u(0)]} \rangle}, \tag{8.84}$$

where K_0 is the reciprocal lattice vector of the perfect lattice. This function describes disorder average of the spatial coherence for the given length scale. $C_g(r)$ has a value of 1 for the perfect lattice at any length scale and 0 in the case of complete disorder. The linear increase of flux line displacement as a function of distance suggested in LO-theory results in an exponentially decaying translational correlation function [74].

The main reason for the existence of long range order - as mentioned previously - is the existence of many metastable states for large ensembles of flux lines. The proper way to deal with such

[7]The vortex lines themselves can in principle bend around in three dimensions, but on a small enough scale they can be said to be straight lines; an euclidean space of one dimension. Such an object which locally, but not necessarily globally, has the properties of euclidean space in a given dimension is called a *manifold*. The perfect Abrikosov lattice is thus a case of one-dimensional manifolds embedded in a 3-dimensional space (the condensate), which are ordered in two dimensions. The problem of weak quenched pinning is thus a subset of the problem of n-dimensional manifolds ordering in d-dimensional space with $m = d - n$-dimensional lattice vectors subject to a quenched weak disorder potential. This general class of problem has been studied extensively in different forms, but using almost the same language. For instance the displacement correlator defined in equation 8.79, is usually referred to as the *roughness*.

a diversity of states is by using the rather abstract replica field theory. Another crucial point recognized and implemented by Giamarci and Doussal was the importance of the periodicity of the lattice. The random nature of the pinning force results in a broad range of Fourier components. It is reasonable to expect that the Fourier components of the pinning potential with wavelengths close to the periodicity of the lattice have a different effect on the ensemble than that of the long wavelength components. The discrete symmetry of the perfect vortex lattice and its consequences for pinning is then accounted for, and can be shown to restore long range order. The details of this theory is beyond the scope of this thesis but a short account for the approach is given below.

Replica field theory and replica symmetry breaking

Consider a symmetric elastic Hamiltonian in three dimensions with identical moduli for shear, tilt and compression respectively

$$H_{el} = \frac{1}{2}C \int d^3x [\nabla u(x)]^2, \tag{8.85}$$

where $\nabla u(x)$ is the relative deformation costing elastic energy and x is a 3-dimensional vector. The pinning potential is described as a random Gaussian potential $V(x)$ which is slightly correlated in the transverse direction (with respect to the field applied along z) but not in the longitudinal direction described by

$$\overline{V(x)V(x')} = \Delta(r - r')\delta(z - z'), \tag{8.86}$$

where r and z are cylindrical coordinates. $\Delta(r)$ is assumed to be a short range function with a range of the order of the superconducting coherence length ξ_0 with Fourier transform $\Delta_q \perp$. Implementing the possibility of displacement the flux line density can be written as

$$\rho(x) = \sum_i \delta(r - R_i - u(R_i, z)) \tag{8.87}$$

where R_i is the flux line position in the perfect lattice and $u(R_i, z)$ is its displacement from this position. Including the potential pinning energy, the Hamiltonian can be written

$$H_{el} = \frac{1}{2}C \int d^3x [\nabla u(x)]^2 + \int d^3x V(x)\rho(x) \tag{8.88}$$

To be able to implement the existence of many metastable states and the fluctuation between them, it is favorable to *replicate* the Hamiltonian n times, simply introducing many copies of the system. The reason is that one can compute the free energy using the partition function for the full replicated Hamiltonian and take the limit $n \to 0$

$$F = \ln Z = \lim_{n \to 0} \frac{Z^n - 1}{n}. \tag{8.89}$$

Using this trick, it is possible to take all metastable states into account and calculate the true disorder average. GD introduced the replicated pinning Hamiltonian

$$H_{pin} = -\frac{1}{2T} \sum_{a,b} \int d^3x d^3x' \Delta(r - r')\delta(z - z')\rho^a(x)\rho^b(x') \tag{8.90}$$

where a and b are replica indices ranging from 1 to n and T is the temperature. The other important trick performed by GD was to express the flux line density in a form that is invariant under lattice translations, and hence respects the periodicity of the lattice and allowing for a more macroscopic treatment of the pinning potential. GD introduced a slowly varying auxiliary field

$$\phi(x) = r - u(\phi(r, z), z) \tag{8.91}$$

allowing for the flux line density to be approximated by an expression invariant under lattice translations

$$\rho(x) \simeq \rho_0 \left[1 - \partial_\alpha u_\alpha(\phi(x)) + \sum_{K \neq 0} e^{iKr} \rho_K(x) \right], \quad \text{where} \quad \rho_K(x) = e^{iK \cdot u(\phi(x))}. \tag{8.92}$$

This allows for a re-expression of the pinning energy term in which the Fourier components of the pinning potential with periodicity close to that of the lattice is separated from the long wavelength part of the pinning potential:

$$\begin{aligned} \int d^3x V(x)\rho(x) \quad &= \quad -\rho_0 \int d^3x V(x) \partial_\alpha u_\alpha + \rho_0 \int d^3x \sum_{K \neq 0} V_{-K} \rho_K(x), \\ &\text{where} \quad V_K(x) = V(x) e^{iKr}. \end{aligned} \tag{8.93}$$

The last term on the right hand side of equation 8.93 couples to the short scale spatial variations of the pinning potential and had been omitted in previous works. These short scale variations are indeed relevant. In the case of imperfections in the crystal lattice causing the pinning sites the scale of which the pinning site density varies are of the order of $10^{-10} - 10^{-9}$ m; two orders of magnitude less than the typical vortex lattice spacing. Since only the Fourier transform of the transverse part actually varies an effective replica Hamiltonian can be written as a function of the long wavelength transverse Fourier components of the pinning potential Δ_0 and the short wavelength components Δ_K

$$H_{eff} = \frac{C}{2} \int d^3x [\nabla u(x)]^2 - \int d^3x \sum_{a,b} \left[\frac{\rho_0^2 \Delta_0}{2T} \partial_\alpha u_\alpha^a \partial_\beta u_\beta^b + \sum_{K \neq 0} \frac{\rho_0^2 \Delta_K}{2T} \cos\left(K \cdot [u^a(x) - u^b(x)] \right) \right]. \tag{8.94}$$

This is the Hamiltonian used by GD to derive the Bragg glass correlation functions. They employed the same approach as Mezard and Parisi in [72]; applying variational theory using a general *trial replica Hamiltonian* of the form[8]

$$H_0 = \frac{1}{2} \int \frac{d^q}{(2\pi)^3} G_{ab}^{-1} u_a(q) \cdot u_b(-q), \tag{8.95}$$

where G_{ab} is the *replica field propagator* on the form

$$G_{ab} = \frac{1}{cq^2 \delta_{ab} - \sigma_{ab}}. \tag{8.96}$$

The form of the propagator G_{ab} is assumed to take the above form, where σ_{ab} is a self-energy, constant for a given set of replica indices. The problem is now to minimize the free energy

$$F_{var} = \langle H_{eff} - H_0 \rangle_{H_0}, \tag{8.97}$$

which - defining the *connected part* of the propagator as $G_c^{-1} = \sum_b G_{ab}^{-1}(q)$ - gives the saddle point equations

$$G_c(q) = \frac{1}{cq^2}, \quad \text{and} \quad \sigma_{a \neq b} \sum_K \frac{\Delta_K}{2T} K^2 e^{-K/2B_{ab}(0)}, \tag{8.98}$$

where ρ_0 has been absorbed into Δ_K, $\Delta_K \equiv \rho_0 \Delta_K$ and $B_{ab}(x)$ is a displacement correlator between replicas

$$B_{ab}(x) = \frac{1}{2} \langle [u_a(x) - u_b(0)]^2 \rangle. \tag{8.99}$$

[8] Mezard and Parisi considered a more general case of random manifold which has been simplified by GD

The displacement correlator in this framework is the *disorder average diagonal in replicas* which is the average of the diagonal $B_{aa}(x)$ denoted

$$\tilde{B}(x) = \frac{1}{2}\overline{\langle [u(x) - u(0)]^2 \rangle}. \tag{8.100}$$

using the density defined in equation 8.92 the translational correlator can be written as

$$C_K(x) = \overline{\langle \rho_K^*(x)\rho_K(0)\rangle}, \tag{8.101}$$

which in the above treatment of the Hamiltonian can be easily related to the displacement correlator by the expression

$$C_K(x) = e^{-\frac{K^2}{2}\tilde{B}(x)}, \tag{8.102}$$

The physics of this rather abstract theoretical framework lies in the *replica symmetry*. If one assumes replica symmetry - which implies that $G_a(q) = G_b(q)$ and $B_a(x) = B_b(x)$ for all a, b - one can solve the saddle point equations (equation 8.98) to yield the displacement correlator

$$\tilde{B}(x) \sim x, \tag{8.103}$$

which is the Larkin result for all distances. So if all replicas are exactly the same - meaning that the self-energy of all the propagators between replicas are the same - all replicas have the same energy and are in fact identical. In reality, there is *only one* stable state - namely the ground state. Therefore perturbation theory is a valid way of treating the problem and the Larkin result is naturally reproduced. In fact, GD argued that the replica symmetric solutions are *unstable* if the dimensionality d of the system is between 2 and 4; the modes of the interaction between replicas - the *replicons* - have negative eigenvalue. They argued that replica symmetry must be broken in the case of $2 < d < 4$. GD assumes in the case of $d = 3$ that replica symmetry is broken and constructs a hierarchy of replicas by a parametrization of the propagator between replicas $G_{ab}(x) = G(x, v)$ where $v \in [0 : 1]$. The self-energy between replicas is assumed to be an arbitrary function of v at low values up until a critical point v_c after which the self-energy is constant. GD focuses on the pairs of replicas with low self-energy and argues that these replicas determine the long-scale behavior of the disordered vortex lattice [74][9] - in fact they argued that the relevant scale L is determined by $L \propto T/v$. In the following, the predictions of the Bragg glass theory relevant for this experimental work are outlined leaving out the details.

8.4.4 Predictions of Bragg glass theory

Keeping only the $K = K_0$ terms in the pinning potential which can be argued to be appropriate at large distances, the asymptotic behavior of the disorder averaged displacement correlator can be shown to increase *logarithmically with distance*

$$\tilde{B}(x) = \frac{2}{K_0}\ln|x| \quad \text{yielding} \quad C_{K_0}(x) = |x|^{-1} \tag{8.104}$$

which is a very slowly increasing function leading to quasi-long-range order and a *power law decay* of the translational correlation function - $C_K(x) \propto |x|^{-\eta}$ with $\eta = 1$. This exponent is obtained using the variational method; in [74] GD also applied functional renormalization theory (not elaborated in this thesis) leading to a predicted exponent $\eta_{RG} = 1.1$. Simon Borgner, Thorsten Emig and Thomas Natterman predict a non-universal exponent $\eta_{BEN} \in [1.145 : 1.16]$, depending on the relationship between shear and compression moduli c_{66}/c_{11}, by taking all elastic modes of the lattice into account - not restricting themselves to $K \approx K_0$ [79] when treating order at long distances.

[9] page 1248 - section III.C.1

When keeping only the $K = K_0$ term in the Fourier expansion of the disorder potential, one ignores the higher harmonics of the interaction potential. Thus the part of the potential which varies on a spatial scale smaller than the lattice spacing is not taken into account. This is called the *single cosine model*, and the consequence of the simplification is that there are two regimes in the displacement correlator as a function of distance, the *Larkin* regime and the *asymptotic* regime with some crossover between the two occurring at a distance l. However, when one includes the higher harmonics of the potential the disorder can vary strongly between lattice spacing, resulting in a new regime at intermediate distances between the Larkin ($B(x) \sim x$) and asymptotic regime ($B(x) \sim \ln(x)$), the so-called *random manifold* regime. In this more complicated model, the crossover between the random manifold regime is supposed to occur at a length R_a much longer than a. In the present case with a three-dimensional condensate and a two-dimensional lattice vector one has

$$R_a = \frac{2a^4C^2}{2\pi^3\Delta} \quad \text{and} \quad v_{R_a} \sim \left(\frac{l_T}{a}\right)^2 \frac{a}{R_a}, \tag{8.105}$$

where Δ is $N_b\Delta_{K_0}$, N_b being the number of reciprocal lattice vectors with minimal norm. C is the elasticity constant from equation 8.85. The hierarchical placement of this length is v_{R_a} which is a function of the crossover length, the lattice spacing a, R_a and the Lindeman length l_T describing the fractional strength of the thermal fluctuations. v_{R_a} is much less than 1 which means that the crossover between random manifold regime and asymptotic regime belongs to the replica symmetry broken part of the replica pair self energy function $\sigma(v)$. GD derived the following form of the displacement correlator

$$\tilde{B}(r) \sim A_{d,m,\Omega}x^{2\nu} \quad A_{d,m,\Omega} \simeq 2.382 \quad \text{for} \quad \nu = \frac{1}{6} \tag{8.106}$$

where $A_{d,m,\Omega}$ is a constant depending on the dimensionality of the condensate d the lattice m and the volume of the unit cell Ω (which is actually a constant describing the symmetry of the lattice). For triangular symmetry, $d = 3$ and $m = 2$, ν is equal to $1/6$ and the displacement correlator grows as the cube root of r with an amplitude of approximately 2.382. This is of course under the assumption of an isotropic elasticity which will not hold in a realistic case, but the point is clear: In the Larkin regime, the displacement grows linearly with r, in the random manifold regime the displacement correlator slows down growing as a *power law* with an exponent less than 1, while at long distances the displacement correlation between flux lines has a very slow logarithmic increase with distance. Introducing this more complex pinning potential and hence the random manifold regime, while retaining the isotropic elasticity, leads to slight alterations in the translational correlator for long distances

$$C_{K_0}(x) = \frac{e^{-\gamma}R_a}{\eta|x|}, \tag{8.107}$$

where γ is the Euler constant $\gamma \simeq 0.577$.

An important point to underline when discussing the Bragg glass theory, is that the assumption that we have weak disorder acting on an elastic lattice needs to be valid. In practice this is equivalent to stating that the lattice needs to be mainly *dislocation free* in large areas. A dislocation is when a flux line in some given length interval δk along the field direction z completely wanders away from the lattice position $u(r, \delta l) > a$. This happens when the pinning is strong and the lattice is soft; the vortex line is able to explore the energy minima in a very large volume which dominates over the elastic energy of the lattice. It is clear that in the presence of a large fraction of dislocations the very assumption of 2D ordering breaks down, and elasticity theory becomes invalid. The lattice near a given flux line is defined by its nearest neighbors, so a dislocation free configuration amounts to stating that the displacement variation must be small - hence the displacement gradient $\overline{\langle(\Delta u)^2\rangle} \ll 1$. In the Bragg glass theory, the displacements are calculated,

and if these show a violent variation of displacements on small scales, the assumptions of the theory breaks down leading to a fundamental inconsistency. However, it can be shown that

$$\overline{\langle(\Delta u)^2\rangle} = \frac{8a}{2\pi^2 l} + \left(\frac{2\pi l_T}{\sqrt{3}a}\right)^2, \tag{8.108}$$

where l is the cross-over length to the asymptotic regime, a is the lattice constant and l_T is the Lindemann length. This is much less than 1 assuming that the onset of the asymptotic regime occurs at large distance and for a reasonable Lindeman length. If the LO theory holds, then dislocations would be preferred even at small scale beyond the Larkin length. GD argues, however, that this slow increase in displacements would result in very large dislocation free areas, which has actually been observed in decoration experiments [80, 81].

In [74, 82] the crossover length between the random random manifold regime and the asymptotic regime is calculated using a more realistic anisotropic elastic Hamiltonian suitable for the flux line lattice. R_a was shown to be proportional to the following expression containing the two elastic moduli c_{44} and c_{66}, the lattice constant a and the global vortex line density ρ_0

$$R_a \propto \frac{a^4 c_{66}^{3/2} c_{44}^{1/2}}{\rho_0^2}. \tag{8.109}$$

As the density of lines is proportional to $1/a^2$, ρ_0 must be proportional to the field density B following equation 8.59. Using the dispersionless versions of the expressions for the elastic moduli given in [74][10] the following holds

$$c_{44} \propto B^2 \quad \text{and} \quad c_{66} \propto B. \tag{8.110}$$

Using these expressions the rough dependency of the crossover length R_a on the magnetic field density is

$$R_a \propto \frac{B^{-2} B^{3/2} (B^2)^{1/2}}{B^2} = B^{-\frac{3}{2}} \tag{8.111}$$

As will be evident later on, one of the goals of using the Reverse Monte Carlo method in this thesis is to gain *direct access* to the correlation functions at different fields. A more experimentally reachable prediction can be achieved by taking advantage of the translational correlator. Since the Bragg glass theory does not describe systems with infinite correlation length, defining a structure factor for a unit cell and taking a lattice sum would be rather useless. Thus, the structure factor for the entire system is used. Returning to the expression for the structure factor in equation 3.56 and splitting up the reciprocal space coordinates into a discrete transverse part $k_\perp$ and a longitudinal continuous part k_z (along the field) gives the structure factor [79] averaged over dynamical disorder

$$S(\mathbf{q}) = \int_z \sum_r e^{iq_z z + iq_\perp \mathbf{r}_\perp} \overline{\langle e^{(iq_\perp[\mathbf{u}(\mathbf{r}_\perp, z) - \mathbf{u}(0,0)]}\rangle}. \tag{8.112}$$

This exposes the very useful form of the translational correlator and the reason for implementing it. In the vicinity of a reciprocal lattice vector $\mathbf{G}$, the structure factor in equation 8.112 can be expressed in terms of the translational correlator

$$S(\mathbf{q}) \simeq \int d^3 r e^{iq_z z + iq_\perp \mathbf{r}_\perp} C_{\mathbf{G}}(\mathbf{r}) \tag{8.113}$$

In [79] they showed a slight non-universal value of η, but only varying a few percent. Assuming a universal η the field dependency of the translational correlator can be estimated by collecting equations 8.111 and 8.107

$$C_{\mathbf{K}_0}(x) \propto \frac{B^{-3/2}}{\eta|x|} \quad \Rightarrow \quad S(\mathbf{K}_0) \propto B^{-3/2}. \tag{8.114}$$

[10] equation 4.26 on page 1257 - the expression for c_{44} given in [82] is erroneous.

Assuming a constant peak width this amounts to saying that the peak structure factor drops off as a power law with applied field with an exponent of 3/2. It should be noted that in principle η depends on the elastic moduli and hence the magnetic field. In spite of this, a quantitative but very imprecise agreement with this prediction was found by Klein et. al [83]

In this thesis, the experimental methods for examining the vortex lattice of superconducting Vanadium are magnetization measurements and small angle neutron scattering. Thus, the information extractable from the data are *global averages.* Therefore, individual dislocations can not be directly measured; only the magnetization and flux line order (assuming there is a signal). A vanishing signal in neutron scattering experiments indicates the disappearance of *static order*, but gives no information about the nature of the phase in question - be it either a static configuration full of dislocations (vortex glass) or a vortex liquid. Therefore, little effort is made in this text to describe these phases. However, several generic (H,T) phase diagrams have been proposed for type-II superconductors having weak random disorder. Some of these will be outlined in the following section.

8.4.5 Proposed phase diagrams

Once agreeing on the existence of a Bragg glass phase, the question remains under which conditions this phase is stable. GD argued that a good measure is the value of the displacement correlator for nearest neighbors [82]. For displacement larger than a certain value - well known as the Lindeman criterion c_L - the lattice breaks down and the assumptions underlying the Bragg glass theory no longer holds. The stability criterion can be written as follows

$$B(r = a) < c_L^2 a^2, \tag{8.115}$$

where a is the lattice spacing. GD used this criterion as a basis for estimating the melting phase line of the Bragg glass phase (see figure 71 right) in the (H, T)-phase diagram. The framework of GD says little about what the Bragg glass melts *into*, just that it is a disorder induced melting that causes the absence of Bragg peaks. In the work of Jan Kierfeld and Valerii Vinokur [84] a nice attempt to remedy this is made by expressing the free energy in terms of the *dislocation density* - ρ_D - which is inversely proportional to the spacing R_D between dislocations. In the Bragg glass, the free energy minimum is at $R_D = \infty \rightarrow \rho = 0$. Kierfeld distinguishes the *vortex glass* from the *vortex liquid* by pointing out that in the vortex liquid, all flux lines are dislocated on average ($R_D = a$) while the low temperature vortex glass is not saturated with dislocations and has $R_d = R_a$ where R_a is the crossover length to the logarithmic regime. Their vortex glass is thus a Bragg glass, but where the asymptotic regime providing the long range order and hence the Bragg peaks are disturbed by dislocations entangling the flux lines and destroying long range order.

Gautam I. Menon suggested that there is so-called *multi domain glass* phase separating the Bragg glass phase from the disordered liquid phase in *all of the (H, T)-phase diagram* [85]. Contrary to the suggestion of Kierfeld it is not possible directly to melt a Bragg glass into a liquid. He makes a conjecture that this multi domain glass has no long range order but a correlation length which is upper bounded by the crossover length to the asymptotic regime $R_D < R_a$. Thus he conjectures *domains* or *fractures* of finite size in which there is rigid order, the size of which would vary with the degree of disorder being smallest at large and small fields. Also, there should be a finite temperature interval in the vicinity of T_C in which there is no Bragg glass phase at all for any field.

This concludes the discussion of superconductivity, vortex lattices and the Bragg glass phase. As is evident the problem is immensely complicated, with a huge number of poorly understood adjustable variables and mechanisms. The Reverse Monte Carlo technique provides a flux line ensemble consistent with the data, that will serve as a source for extracting correlation functions.

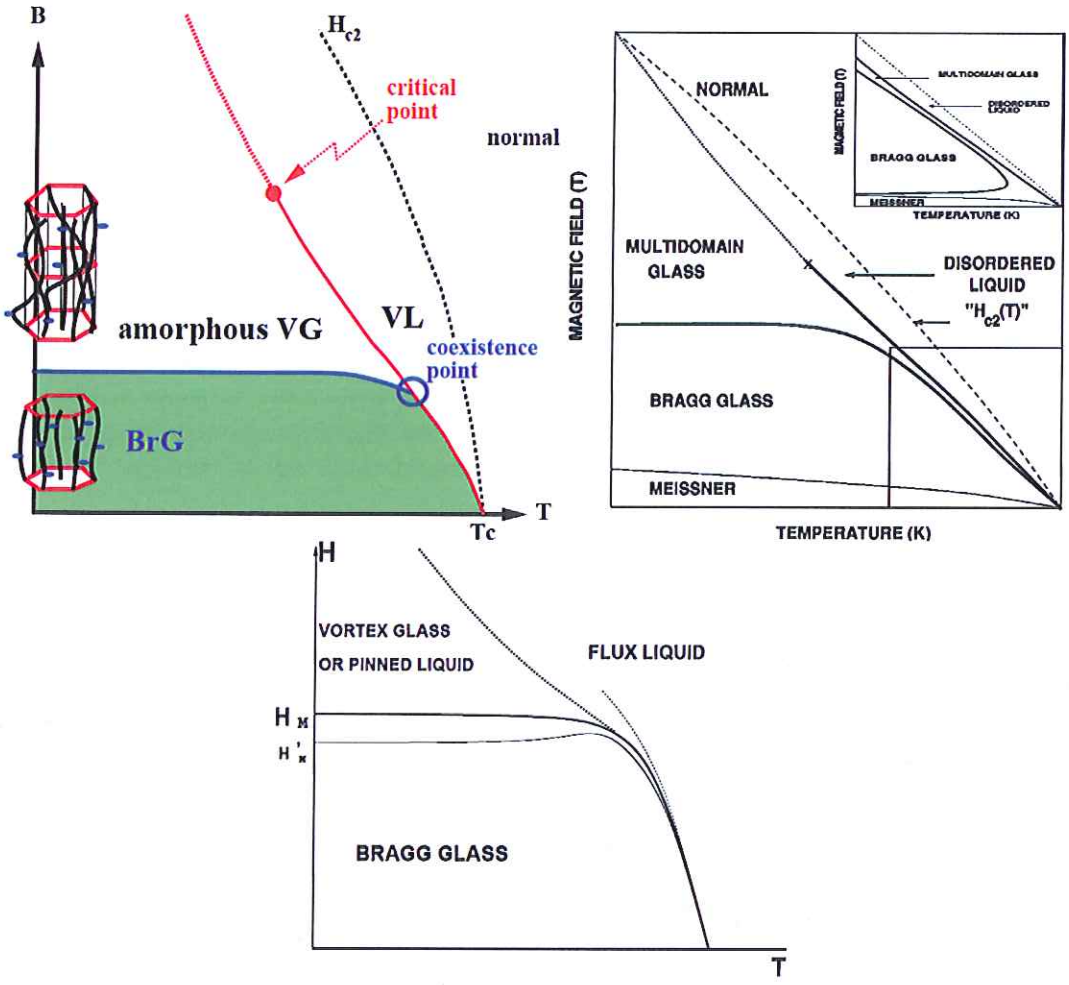

Figure 71: *Top Left:* Generic phase diagram modified from [84]. There is a low temperature, low field Bragg glass phase which undergoes a field induced 'melting' into the vortex glass, which itself can melt into a vortex liquid upon increasing the temperature. The phase line between the two disordered phases ends in a high field critical point and there is a co-existence point at low fields and high temperature. *Top Right:* Phase diagram proposed by Menon - the Bragg glass is surrounded by a multi domain glass. *Bottom:* The phase diagram proposed by Giarmarchi and Le Doussal, quite similar to the Kierfeld diagram. The rightmost dotted line corresponds to the melting line for a pure system without disorder and the leftmost line corresponds to a melting of the low-temperature phase lying quite close to that of the pure system.

These will - along with magnetization measurements and the intensity of neutron Bragg peaks - be compared to the Bragg glass predictions in the next chapter.

9 Reverse Monte Carlo simulation of the vortex lattice in superconducting Vanadium

In this part of the thesis, an attempt will be made to investigate the validity of the Bragg glass theory in superconducting Vanadium in a finite field- and temperature range by using Reverse Monte Carlo (RMC) refinement of SANS data with high angular resolution and by analyzing the field dependence of the integrated rocking curve intensity. The superconducting (H, T) phase diagram will be established for the Vanadium sample examined in this work using VSM magnetization data forming a framework for discussing the neutron scattering data. The magnetization data also reveal a rapid drop in the critical current close to H_{c2} where there is no measurable long range static order, as observed in our SANS experiments. A straightforward alteration of the RMC code is necessary to successfully fit the data: a slow decrease of the acceptance probability - called *simulated annealing* (SA) - increases the probability of reaching the global minimum in the χ^2 landscape. The results of the simulations will be discussed and interpreted in light of the Bragg glass theory, and cautious suggestions for the causes of the specific peak shapes observed in this sample - which are not explained by the Bragg glass theory - will be given. The work presented here is a continuation of the RMC work done by Mark Laver et. al. [86]; the code used for the simulations is written by him.

This chapter will start out with the experimental details. The form factor of a flux line and its dependency of field will be described. This is followed by a description of the crucial experimental geometry that enables an extraction of the correlation functions. A short description of the general principles behind Reverse Monte Carlo refinement and Simulated annealing is in order before outlining the structure of the RMC code. After this, the field dependency of the integrated intensities as recorded at 1.55 K will be analyzed and shown to be consistent with the Bragg glass prediction. This is succeeded by a presentation and analysis of the high statistics rocking curves recorded at 1.55 K and a presentation of the results of the SA simulations. The field dependency of the integrated intensity was measured at two additional temperatures ($T = 2.66$ K and $T = 3$ K), establishing the boundaries of static long range order in the phase diagram. A high statistics rocking curve was recorded near this phase boundary, which will be analyzed as well. Lastly, the VSM magnetization data will be presented along with a suggested phase diagram and a description of the phases.

9.1 Experimental details

The crystal structure of Vanadium is cubic with a space group $Im-3m$, and cell parameter 3.03 Å. Vanadium is one of the rare elements (along with niobium and technetium) which is intrinsically a Type-II superconductor. It is superconducting below 5.47 K and is only a marginal Type-II superconductor with $\kappa_{T=T_c} = 0.78$. In the clean limit, the coherence length is 46 nm and the London penetration depth is 37.4 nm at zero temperature. Two experiments were performed on a cylindrical sample of vanadium (with a length of 10 mm and a diameter of 5 mm) in 2008 and 2010 respectively. In this section the details necessary for an analysis of the rocking curves will be described along with the rather important experimental details. A description of the RMC and simulated annealing methods leads up to the section dealing with the results of the simulations.

9.1.1 Setup geometry

The small angle neutron scattering experiments were performed at the SANS-II instrument at the PSI. As mentioned in section 3.3.2, the SANS instruments accept a finite angular range and a finite range of wave vector lengths, so whenever rotating a Bragg peak into the scattering condition, the resolution ellipsoid needs to be taken into account to be able to model the angular distribution

of scattered neutron intensities. Since the attenuation slit near the velocity selector is a circular aperture, the size of the resolution ellipsoid has the same order of magnitude in the two directions perpendicular to the beam, providing the sample aperture is not completely one-dimensional. In the direction parallel to the beam, however, the resolution function of a SANS instrument is very narrow. The structure factor of the vortex lattice is not expected to resemble a delta function, but a peak shape with algebraically decaying tails. The sample has been chosen with this in mind; so the intrinsic peak shape of the vortex lattice is rather broad. If the width of the resolution function is comparable to the width of the peak in a scan, the poor resolution smears out all details of the rocking curve. Thus, one cannot probe the details of the structure factor since the broad resolution function smooths everything out; the resolution is low. If the width of the resolution function is much smaller than the peak width, however, the two distributions still need to be convoluted, but the recorded peak shape will reflect the structure factor, not the resolution function, and minor details will reflect the physics of the vortex lattice; the resolution will be high. To probe the structure factor of the vortex lattice with a high resolution the Bragg peak needs to be rotated in the direction parallel to the beam. This rotation can be about both a vertical and horizontal axis. However, since only horizontal magnets were available for the SANS-II instrument, the field was chosen to be horizontal and perpendicular to the beam, see figure 72.

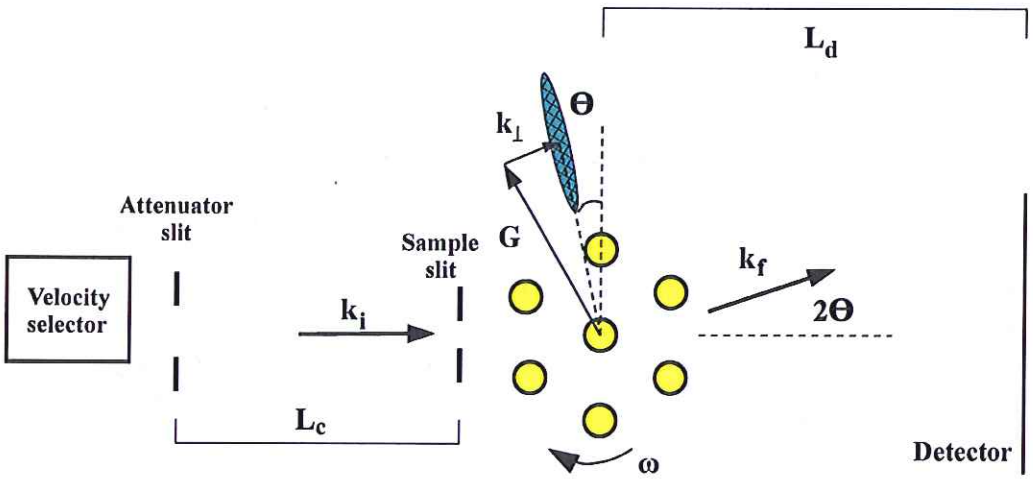

Figure 72: The setup used in the two SANS experiments. The field is perpendicular to the beam and horizontal. The reciprocal lattice vector G is shown artificially extended, and the angle ω marks the direction of rotation. The vector $\mathbf{k}_\perp$ denotes the scan direction in reciprocal space in a rocking curve. The cyan ellipse illustrates the rough cigar shape of the resolution function when projected onto the plane perpendicular to the present field direction. The resolution in the direction of rotation in this figure is determined by the size of and distance between the attenuator slit and the sample slit L_c as well as the sample-detector distance L_d. When rotating the sample - bringing G closer to the Bragg scattering condition - progressively shorter $\mathbf{k}_\perp$ are measured.

In the following, the angular FWHM of the resolution function in the direction of rotation ω is denoted by $W_\omega = 2.355\sigma_\omega$, where σ_ω is the standard deviation of the assumed Gaussian resolution function. W_ω is estimated in [87][11]. In the two experiments, circular attenuation apertures with diameters of $r_1 = 8$ and 16 mm was used, and the two relevant lengths in figure 72 were $L_c = 6450\ mm$ and $L_d = 6287\ mm$, respectively. The two angles referred to in [87] are almost identical

[11] formula 13 on page 324 using figure 2 a)

and the FWHM of the resolution function in the direction of rotation is thus

$$\begin{aligned} W_\omega \approx \frac{2r_1}{L_c} &\approx 0.078^\circ \quad \text{for} \quad r_1 = 4 \ mm, \quad \text{and} \\ W_\omega &\approx 0.16^\circ \quad \text{for} \quad r_1 = 8 \ mm. \end{aligned} \tag{9.1}$$

The structure factor of the disordered VL ensemble extends out in two dimensions centered at the scattering condition $\mathbf{G}$. When rotating the sample through the scattering condition ($\omega = \omega_0$) one performs a scan *perpendicular* to $\mathbf{G}$ for small angles so the resolution in reciprocal space is

$$k_\perp (\omega \sim 0) = \sin(\omega - \omega_0) |\mathbf{G}| \quad \Rightarrow \quad \frac{\Delta k_\perp}{G} \approx W_\omega[\text{rad.}] = 0.0014, \tag{9.2}$$

which is excellent. There is a disadvantage of using this setup. Since no vertical field cryomagnet was available, the cryostat itself needs to rotate about a *horizontal* axis. Such a rotation is usually limited by the geometry of the SANS setup. Obviously, there needs to be vacuum in both the collimation section and the detector tank in order to optimize flux, and the two vessel endpoints are close to the cryostat windows for the same reason. Therefore, there is little space to rotate the cryostat more than a few degrees. To remedy this, Asger B. Abrahamsen at Risø designed a brass sample mount which is able to rotate an arbitrary angle inside the cryostat. A rotatable rod is situated inside the sample stick with a thread in place on a cogwheel situated on the sample holder and with an electrical stepper motor mounted on the rod at the top of the sample stick. In this way, one is able to rotate the sample without moving the cryostat itself. The sample stick is shown in figure 73.

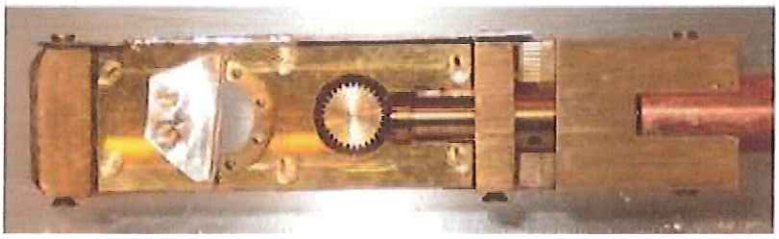

Figure 73: Brass sample stick used to mount and rotate the sample. The cogwheel in contact with the rod inside the sample stick is clearly visible. The disc on which to mount the sample is mounted on a second cogwheel which is connected with the aforementioned cogwheel below the mounted brass plate.

Such an unorthodox setup caused some problems during the two experiments which were the following:

- Due to the unavoidability of having a rod establishing direct thermal contact between a hot electric motor outside the cryostat and the sample holder, it is difficult to cool the sample down to 1.5 K. The only way to reach 1.5 K was to increase the exchange gas pressure until we flooded the sample space with liquid helium. This solution did not work in the 2010 experiment, since there was a leak in the 11T magnet, preventing an increase in the exchange gas pressure.

- It is difficult to use lubricants at 1.5 K, so the cogwheel contacts are metal on metal. Thus the sample holder can be expected to have a finite lifetime, simply due to scratches on the moving surfaces in contact. This happened in the 2010 experiment, when substantial polishing was necessary to get the sample mount rotating.

Using the definition of the structure factor given in 8.112, the scattering cross section is the Fourier transform of the field density distribution in the sample. This can be described by

$$\left(\frac{d\sigma}{d\Omega}\right) \propto S(\mathrm{q}) \times |F(\mathrm{q})|^2 \tag{9.3}$$

where $F(\mathrm{q})$ is the form factor for a single flux line. In fact, this only holds if the flux lines can be considered as isolated. Thus, aiming to evaluate the field dependency of the structure factor, knowledge of the form factor is needed. Calculating the form factor for a single flux line requires knowledge of the field distribution, which requires knowledge about both the coherence length and the penetration depth. These are temperature dependent parameters that are not the same for all vanadium samples - they depend on the impurity concentration. In the next two sections an attempt is made to obtain the form factor at all relevant fields and temperatures. First, an estimate of the impurity concentration is obtained using previous results found in literature. This is followed by a calculation of the form factor for an isolated flux line at the three relevant temperatures.

9.1.2 The vanadium sample used in this work

In order to evaluate the field dependency of the form factor correctly it is necessary to obtain information about the amount of impurities in the sample. The impurity dependence of the superconducting properties of vanadium was thoroughly examined by E. Moser, E. Seidl and H. W. Weber (MSW) in [88], where the characteristics of the purest vanadium-sample ever examined (with an electronic mean free path of as much as 2700 nm) are also reported. The clean limit $\kappa(T_c)$ of vanadium is 0.78 - which is only slightly over the limit for type-II superconductivity. The clean limit London penetration depth and GL coherence length are 37.4 nm and 46 nm, respectively at zero temperature. In [89][12], a useful expression can be found linking the electronic mean free path ℓ with the effective reduction in GL coherence length:

$$\xi(T) = \frac{0.74\xi_0}{\sqrt{\delta t}}\left(1+\frac{0.75\xi_0}{\ell}\right)^{-\frac{1}{2}}, \tag{9.4}$$

where $\delta t = (T_c - T)/T_c$. Using equation 9.4 and 8.53 an expression linking the upper critical field of a Vanadium sample to the mean free path:

$$\frac{H_{c2}^{this-work}}{H_{c2}^{MSW-clean}}(T) = \frac{\xi_{MSW-clean}^2}{\xi_{this-work}^2}(T) = 1+\frac{0.75\xi_0}{\ell}, \tag{9.5}$$

where the assumption $\ell_{clean} = \infty$ has been conveniently used. The upper critical field of the vanadium sample is extracted from magnetization measurements. VSM magnetization measurements have been performed on the sample, which will be presented in detail in section 9.3.9. In this section, an initial phase diagram for this sample is shown in figure 74 left. The values of H_{c2} are defined as the point where the hystersis loop shows no hysteresis and T_c is found by linear extrapolation of the H_{c2} phase boundary. When having obtained a good measure of the electronic mean free path, the penetration depth and coherence length can be calculated using equation 9.4 and the following expression for λ found in [89]:

$$\lambda(T) = \frac{\lambda_L(0)}{\sqrt{2\delta t}}\left(1+\frac{0.75\xi_0}{\ell}\right)^{\frac{1}{2}}. \tag{9.6}$$

Table 19 shows the calculated electronic mean free paths (which should be the same), the penetration depth and the coherence length for the three relevant temperatures in the sample used in this work.

[12] Page 49

T [K]	T/T_c	δt	$H_{c2}^{this-work}/H_{c2}^{MSW-clean}$	ℓ [nm]	λ [nm]	ξ [nm]
1.55	0.30	0.70	1.77	45	42.05	30.6
2.7	0.51	0.49	1.71	39	49.4	37.18
3.0	0.57	0.43	1.88	49	55.29	37.86

Table 19: Table of central GL parameters at the three relevant temperatures. The determined electronic mean free paths agree roughly within 10 percent of the average $\ell = 44$ nm

From magnetization measurements presented in succeeding sections, the critical temperature of the sample used in this work is roughly 5.25 K. Using the table given in [88][13], this value has a T_c of roughly the sample V23 presented in [88], which has roughly the same impurity concentration as the sample used in this work. Thus the critical temperature is consistent with the impurity concentration found using H_{c2} measurements. In conclusion, the characteristics of our sample fit the picture presented in [88] and will be used to calculate the form factor, as explained in the next section.

9.1.3 Magnetic form factor of a flux line

A simple model for the vortex core was given by J. R. Clem [90]. In convenient cylindrical coordinates he expressed the order parameter as $\Psi = (\rho/R)\exp(-i\phi)$, where $R = \sqrt{\rho^2 + \xi_v^2}$, ρ is the radial distance from the vortex core center and ϕ is the angle in the plane perpendicular to the vortex. He used ξ_v as a variational parameter minimizing the GL free energy equations, yielding results that were consistent with exact and numerical GL results within a few percent. The advantage of Clem's approach is that his model yields a simple expression for the Fourier transform $f(q)$ of the magnetic flux density of a single flux line $b_z(\rho)$, which is given as

$$\begin{aligned} f(q) &= \int d^2\rho b_z(\rho) exp(-i\mathbf{q}\cdot\rho) \\ &= \frac{\phi_0 K_1(Q\xi_v)}{Q\lambda K_1(\xi_v/\lambda)}, \quad \text{where} \quad Q = \sqrt{q^2 + \frac{1}{\lambda^2}}, \end{aligned} \tag{9.7}$$

where K_1 are the modified Bessel function of the second kind, q is the wave vector, λ is the penetration depth and ξ_v is the variational coherence length (the same as the GL coherence length within a few percent). Using the parameters in table 19, the form factor in the field range 50-300 mT has been plotted for the three relevant temperatures. These are shown in figure 74 along with the phase diagram of vanadium as determined from VSM measurements. In the high-κ limit the form factor effectively has power law dependence of applied field with an exponent of 1. In the low-κ limit the drop-off of the form factor is faster than a power law, especially at higher temperatures. Having calculated the form factor, what remains is to describe the method of RMC refinement used to fit the rocking curves that were recorded with high statistics. This is done in the following section.

9.2 Reverse Monte Carlo refinement

The goal of performing any experiments is getting data that are good enough to be able to compare different models of the system to the data and to conjure up new models based on the data. Having today's vast amounts of computer power at hand, it is possible to tackle many body problems in many ingenious and new ways. When examining disordered systems, computer power is very useful, since it is possible to deal with large ensembles of physical quantities in a random manner. One of

[13] page 592

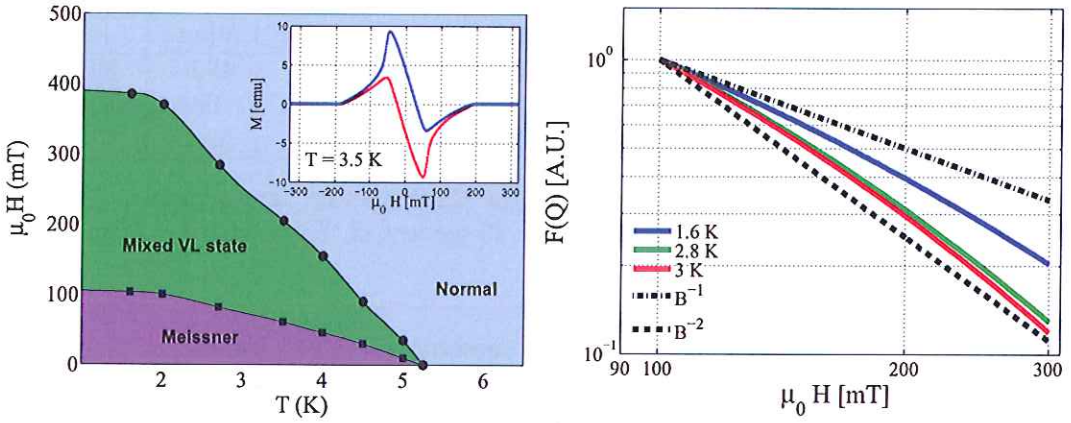

Figure 74: *Left:* Phase diagram of Vanadium as determined by VSM magnetization measurements. The insert shows a typical hystersis loop recorded to find H_{c1} and H_{c2}. *Right:* Magnetic form factor as a function of field at the three relevant temperatures in table 19 as a function of field in the range 100-300 mT. Two power law decays of B with exponents -1 and -2 have been plotted for reference. The form factor is shown to fall off quicker than the high κ power law for all temperatures.

the methods for fitting experimental data using a real physical ensemble is Reverse Monte Carlo modeling (a review is given in [91]).

The central idea of RMC is to create a large ensemble consisting of N units of the physical quantity examined possibly using periodic boundary conditions. No periodic boundary conditions can be employed in this work, since large scale disorder is examined and no unit cell can be defined. One then uses a data set to define a cost function of all the configuration variables $\mathcal{F}(\mathbf{C}) \rightarrow \chi^2$, where $\mathbf{C} = (c_1, c_2, ..., c_N)$ and c_i are the free variables for each unit. The goal is to minimize this function by randomly perturbing or moving random units within the ensemble enforcing useful physical constraints. The calculated experimental output of the two ensembles before and after the move is compared to the data by simply calculating χ^2 for both ensembles or *configurations*. If the move decreases χ^2 the move is accepted, but if the move *increases* χ^2 the move is accepted with the probability

$$P\,(\text{accept}) = \exp\left[-\frac{\Delta\chi^2}{p}\right]. \tag{9.8}$$

In usual RMC algorithms $p = 1/2$, but in the present case it is kept as a variable. The specific scheme applied to the flux line system is outlined in the flow chart in figure 76. Thus, the probability for accepting moves that increase cost is a decreasing exponential function of the cost increase, the decay rate of which is determined by p. A very high p facilitates an acceptance of almost every move regardless of the comparison with data, and the ensemble configuration becomes more and more random and disordered. In contrast, a very low p causes a rejection of every move increasing χ^2, and the configuration quickly converges towards whichever local minimum is nearest the initial configuration. This problem is known to anyone who has fiddled with simple versions of least squares fitting; a poor initial guess of the function parameters prevents a proper optimization, even when dealing with a few parameters.

The purpose of the RMC is to fit to the data using a large ensemble which is as unbiased as possible. The number of parameters is usually huge, so it is crucial not to be restrained to local minima, being a slave to the initial configuration. In order to be able to probe different minima and hopefully reach the global one, a value of p should be used which is high enough for the configuration to be able to escape local minima and low enough to actually fit the data and not just increase disorder until the end of time. In a way the acceptance probability is comparable

to a temperature of the ensemble in the sense that a high p promotes randomness, disorder and symmetry. After convergence, any finite p will naturally cause the configuration to oscillate between ensembles having some finite interval of χ^2 over the true global minimum. Thus, for any p there is a minimum χ^2 achievable simply due to the fluctuations between configurations facilitated by the finite acceptance probability. It is possible to employ a *cooling scheme*, starting out at a very high p and stepwise decreasing the 'temperature' while allowing the ensemble to achieve thermal equilibrium (a stable χ^2) at each step or temperature. Doing this allows the configuration to migrate far away from the initial configuration since the configuration is not initially subject to the local geometry of the cost function. This process is called *simulated annealing* (a review is given in [92]). An illustration of the different schemes is given in figure 75, where the process of rejecting every move increasing χ^2 is called simulated quenching (again using the temperature analogy).

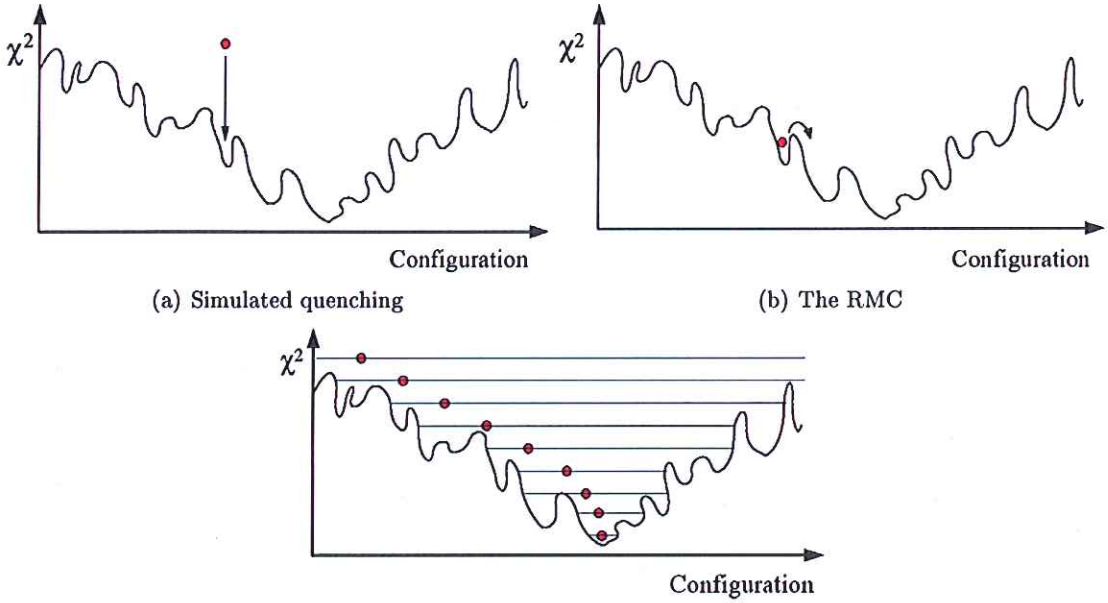

(a) Simulated quenching

(b) The RMC

(c) Simulated annealing

Figure 75: a) Simulated quenching immediately minimizes the cost function and the configuration goes to the nearest local minimum. b) Using the RMC algorithm several minima can be probed since an increase in cost function is accepted. c) In simulated annealing stable values of the cost function is reached at different temperatures allowing the configuration to migrate.

In the case of addressing the problem of a triangular lattice of vortices being perturbed by weak random forces, the RMC (and similar) approach seems appropriate, especially when probing the lattice using neutron scattering. This is for several reasons:

- The RMC algorithm is basically a process of introducing disorder in an ordered ensemble, while minimizing a cost function. The Bragg glass theory predict a large amount of disorder while still retaining quasi-long-range order. Therefore, introducing a certain amount of disorder is desirable.

- As described in chapter 3, neutron scattering actually just measures a sum of pair correlation functions. Describing pair correlations is a major result of Bragg glass theory, so neutron data is a well suited form of data to fit using an RMC approach to achieve an ensemble with realistic pair correlation functions.

- Using the RMC method on neutron data gives a way of interpreting neutron rocking curves

without enforcing any paradigms - one can simply achieve a model consistent with data without bias and test it against the Bragg glass hypothesis.

The last point in the above list can be reversed to a criticism of the RMC method, replacing the word bias with the word thought. In this work, an ensemble of roughly 10^5 VL's with 2 degrees of freedom each will be modified to fit a data set of maximum 70 points. Thus, the solution is hardly unique and we do not apply any physical criteria separating one well-fitting ensemble from another - who knows if we have the right one? This is a variant of the more general uniqueness critique dealt with by McGreevy in [91], the point is given here anyway. The uniqueness critique is in principle applicable to any many body problem subjected to experiment, the same applies in case of the refinements presented earlier in this work - not all peaks in reciprocal space have been measured, so any model conceived is simply only valid within the scope of the limited dataset. In this case, it is (mainly) the correlation functions that are interesting, and while there is no one to one correspondence between shapes of C_g and ensemble configurations, the degree of freedom of the correlation functions when subjected to the demands of the neutron data must be quite limited, as the rocking curve directly reflects C_g (this is essentially what is being measured). Precisely for this reason, emphasis has been laid on analyzing the simulated correlation functions and not the real space flux line ensembles, since these are subject to a uniqueness critique.

A much more relevant critique follows from the central assumption necessary to describe the flux lines using only two coordinates:

It is assumed that the flux lines are effectively almost straight rods and that contracting the longitudinal dimension into the discretely ordered XY-plane is a valid description

In principle, the validity of this assumption is up for debate - even though the existence of Bragg peaks suggests the existence of large dislocation free areas. In most cases, a 2D lattice is a very good describtion. However, one has to be careful when using RMC results to speculate on a transition to the vortex glass state, the RMC result shows how a *dislocation free* ensemble could be arranged to give the observed rocking curve. The vortex glass described by Kierfeld for instance can not be mimiced by the RMC.

9.2.1 The RMC code used for analyzing the high resolution rocking curves

The RMC code is written in standard C by Mark Laver. In this section, a short overview of the approach will be given. The code retrieves the data in ASCII-format in simple column form [$(\omega - \omega_0)$[deg.] Intensity Intensity Error], where $(\omega - \omega_0)$ denotes the angle relative to the peak center. In addition to the data, additional information needs to be given in an initialization file:

- **Size of vortex ensemble**
- **Magnetic field**
- **Number of initialization moves**
- **Number of accepted moves after which to stop**
- **Number of generated moves after which to print information on screen**
- **Number of generated moves after which to calculate correlation functions and save information to files**
- **Resolution FWHM**
- **Maximum move distance in units of lattice constants**

- **Boolean to indicate whether or not to implement a *minimum approach distance***
- **Value of minimum approach distance**
- **Boolean to indicate whether or not to implement *planarity constraint***
- **Acceptance probability**
- **Interval width in k-space within which to calculate the structure factor**
- **Step size in k-space with which to calculate the structure factor**

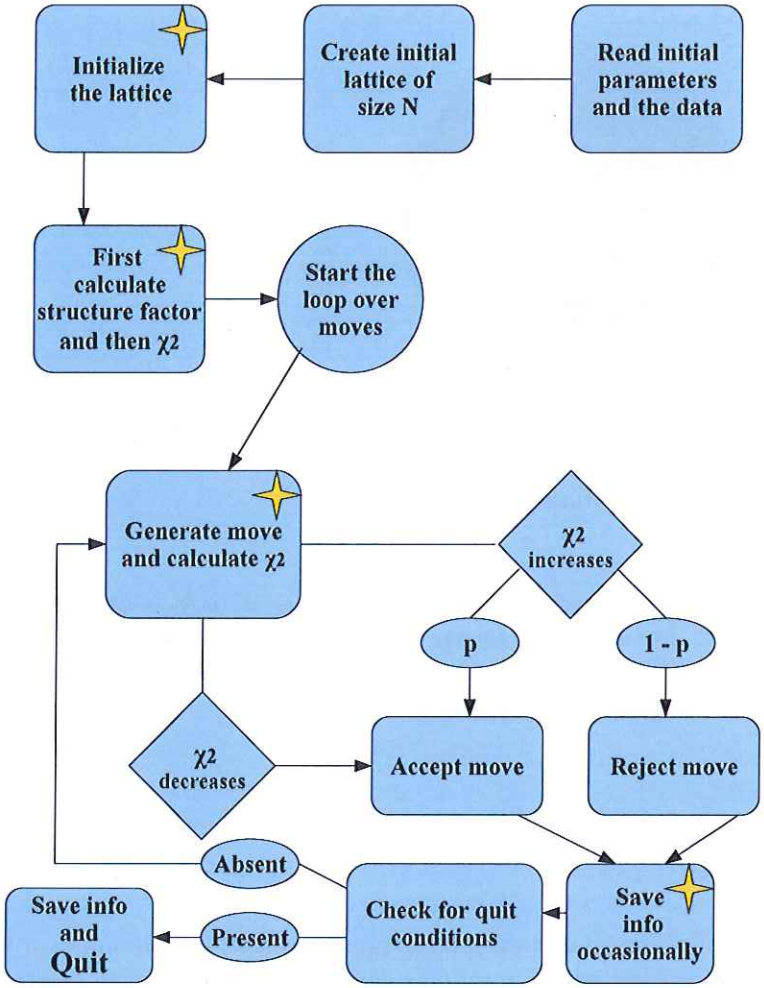

Figure 76: Flow chart describing the main features of the RMC code used in this work. The squares with a yellow star in the upper right corner mark actions that will be elaborated in the text below.

The main features of the RMC approach are outlined in the flow chart in figure 76. This simplification, however, leaves out some details that might be important in a discussion of the result, which will be elaborated in the following. The boxes in the flow chart marked with a star are explained below.

Initializing the lattice

Once the specified number of flux lines is retrieved, the two dimensional array of flux lines is arranged to form a circle. It is favorable and time-saving to start with some disorder in the system, since, to some extent, a disordered ensemble is what one wants to end up with. As will be evident later on, the minimum probed can depend on the starting conditions if the algorithm is not able to overcome all barriers in the configuration landscape. The reason for initializing the lattice is exactly this, to start out a little closer to the global minimum, but still without doing anything biased. Every flux line is simply moved the number of times specified in the initial file - n - resulting in the average initial displacement of $0.5\sqrt{n}r_{\max}$, where $r_{\max}$ is the maximum move displacement (assuming a random walk). An example of a initialized lattice before running the RMC loop is shown in figure 77. As evident, even after 10 random moves, the lattice is still close to perfect hexagonal.

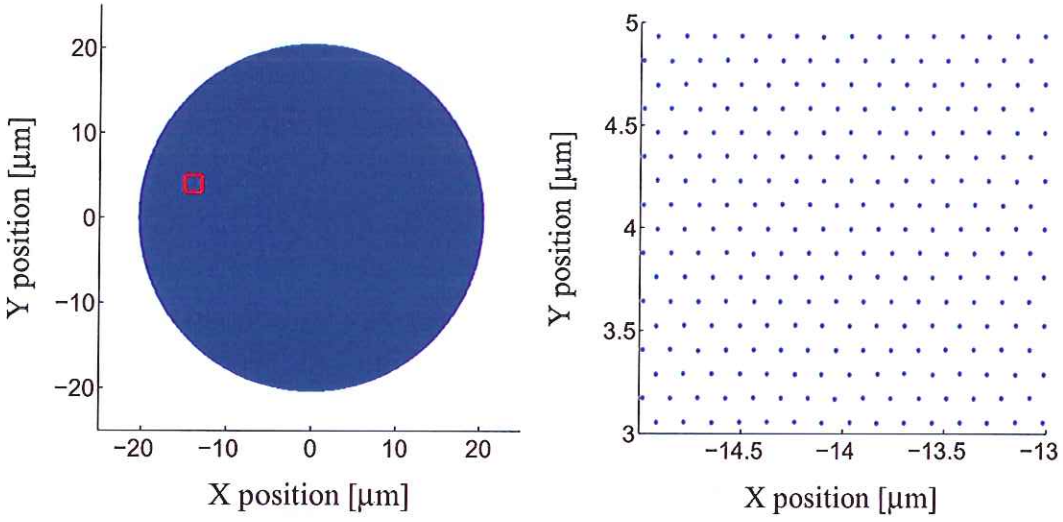

Figure 77: *Left:* Initialized ensemble of 80000 flux lines at $\mu_0 H = 130$ mT. The circular arrangement is near perfect. The small red square denotes the section shown to the right. *Right:* A small section of the ensemble after 10 initialization moves. As evident, the lattice is still near perfect illustrating the infinitesimal maximum move size.

Generating a move

The function *MoveGenerate* takes an integer input - specifying the index of the vortex line to be moved. If the input integer is -1, a random line will be chosen. The displacement vector of the move is determined by choosing a completely random angle between 0 and 2π and a random length in the interval specified in the initialization file (between 0 and the maximum). If the move brings the flux line nearer than the minimum approach distance of any other flux line, the disallow flag is set (if the minimum approach constraint is enabled). The same happens if the move brings the line out of planarity (if enabled). The planarity constraint is constraining the vortex line in question to the cage defined by its nearest neighbors (which are the same six flux lines throughout the simulations even though their positions change). Thus, planarity constraint prevents dislocations of entire flux lines (not segments) in the ensemble. If the disallow flag is set, another move will be attempted. If more moves than a given limit is disallowed, another flux line will be chosen.

Calculating the structure factor and χ^2

The structure factor is treated in different ways depending on the information needed - mainly to save time. After initializing the lattice, the whole structure factor needs to be calculated from scratch. This is done in the function *StrucCalcAll*, which has an integer input which is a set label denoting the sets before and after a move. For the set in question, there is a loop of every point in which to calculate the structure factor (the data point - or if one chooses - including artificial interspersed points). For each point, the sum over flux lines of both the imaginary and real part of the phase factor is saved, not only for the single point but for all points in the interval of k-vectors *parallel* to **G** defined in the initialization file. The saved structure factor is thus a four dimensional array [set, point, imaginary/real, KMag], where KMag is the index of scattering vectors parallel to G. Evidently, this is time-consuming.

In calculating the intensities, the resolution function needs to be taken into account. First of all, the amplitude is calculated for each point by summing the squares of the real and imaginary parts of the phase for all parallel k-vectors, KMag. Then the contribution from the neighboring points due to the resolution is calculated out to three times the resolution width and added to this value.

After moving a flux line, the function *StrucCalcMod* subtracts the phase factor for the given flux line before moving it - for all points and all k-vectors parallel to G - and adds the phase factor for the flux line as it is after the move. The result is saved in a new four dimensional array as the one created by *StrucCalcAll*, resulting in two arrays with phase factors before and after the move. Calculating the intensity for each set and renormalizing the structure factor allows one to compare the two values of χ^2 using the well-known definition:

$$\chi^2 = \sum_i \frac{\left(I_i^d - I_i^c\right)^2}{\sigma_i^2}, \tag{9.9}$$

where I^d and I^c are the measured and calculated intensities respectively and σ_i is the error of the measured intensity.

The information saved - calculating the correlation functions

After a given number of moves, the RMC code calculates and saves the correlation functions using the code given in CorrLib.c. The initial lattice is recreated, and the displacements are readily calculated for each VL index. Then a loop over all possible pairs in the ensemble is performed. The pairs are divided up into bins, one for each unit of lattice spacing between the pairs in the initial perfect lattice. For each bin the average displacement correlator and average translational correlator (averaged over all 6 reciprocal lattice vectors) is directly calculated. Thus, the large real space ensemble allows for a direct calculation of the two correlators as a function of distance between flux lines. This takes a lot of time due to the N^2 loops that need to be done, and should only be done when absolutely necessary.

9.3 The vortex lattice of superconducting Vanadium

In this section the experimental evidence for the existence of a Bragg glass phase and its extension in the phase diagram is presented. First, the field dependency of the integrated intensity will be analyzed and compared to the predictions of the Bragg glass theory. This is succeeded by an initial analysis of the raw high statistics rocking curves; effects near the peak center which are *not* consistent with Bragg glass theory will be shown, and analyzed using an (over)simplified model. Next, the correlation functions outputted from the RMC algorithm will be analyzed and shown to be in accordance with Bragg glass theory, at least for pair separations less than $80a_0$. This

is followed by an analysis of the field dependency of the intensity at 2.7 and 3 K, respectively, determining the boundaries of long range order in the phase diagram of the sample. Close to this boundary, a rocking curve with reasonable high statistics was recorded; it will be shown to be very wide - perhaps giving a little insight into the crossover to the more disordered part of the VL phase diagram. Lastly, an experimental phase diagram is presented along with a proposed interpretation. Both SANS experiments were performed on the SANS-II instrument at the PSI, using the 11 T horizontal field cryomagnet and the brass rotatable sample mount. The same cylindrical single crystal of Vanadium is used in both experiments having a diameter of 5 mm and a length of 10 mm. In both cases, the distance from the attenuator slit to the sample was 5800 mm, and the distance from the sample to the detector was 6290 mm. In both cases, the crystal was mounted with the crystallographic (111) direction parallel to the field, which was perpendicular to the beam and horizontal. In both experiments 10.6 Å neutrons were used, and therefore the beam stop was left out, having the direct beam hitting the detector. The detector array of the SANS-II instrument consists of a circular ensemble of pixels measuring 4.345×4.345 mm with a radius of 64 pixels.

The GRASP data analysis package

The GRASP package is an open source data analysis package developed at the ILL. It can be found and downloaded at the ILL homepage[14]. It is designed for visualizing the 2D data output of SANS instruments, and it has the specifics of most European SANS instruments as optional parameters, including the SANS-II instrument at the PSI. The instrument details of the SANS-II spectrometer can be found on the PSI web page[15]. The GRASP package offers an elegant way of extracting the rocking curves. At the applied field in question, a rocking curve is measured by recording 2D detector images with angular intervals and fixed monitor counts determined by the user. As derived in section 8.2.3, the lattice constant is a function of the applied field; which means that the Bragg reflection from the vortex lattice will hit the almost the same area of the detector for all angles in the rocking curve for any given field, at least at small angles with respect to the scattering vector. Therefore, the SANS detector images can be 'stacked' with the 'angle axis' perpendicular to the detector plane. Then, one can define an area encircling the spot of the Bragg reflection and plot the integrated intensity hitting that area as a function of rocking curve angle. The way this is done using GRASP is illustrated in figure 78

Using this convenient tool, obtaining the rocking curves directly from the raw data was an easy task. These rocking curves will be presented in the following.

9.3.1 The SANS-II experiment in May 2008

The first experiment performed on Vanadium was in May 2008. In that experiment - inspired by the results presented in [86] - as narrow a resolution function as possible was aimed for. Therefore, the attenuation slit (or source aperture) was set to a diameter of 8 mm - corresponding to a resolution angle of $\delta\beta = 0.079°$ (FWHM). This is a very narrow resolution as the rocking curves are several degrees wide. Throughout the experiment, the exchange gas pressure in the sample space was kept at a very high level in order to maintain a stable temperature of 1.55 K. Whenever a rocking curve was recorded, a field cool procedure was used: Warm up to 6.5 $K > T_C \rightarrow$ change field $\rightarrow$ cool to base temperature. In addition, the sample aperture was rectangular, measuring $4 \times 8 <;$ mm. The dimensions of the sample aperture was deliberately kept smaller than the sample size, to reduce effects from the demagnetization factor near the sample edge. The usable data recorded in this experiment consist of the following

[14] http://www.ill.eu/instruments-support/instruments-groups/groups/lss/grasp/home/
[15] http://kur.web.psi.ch/sans2/

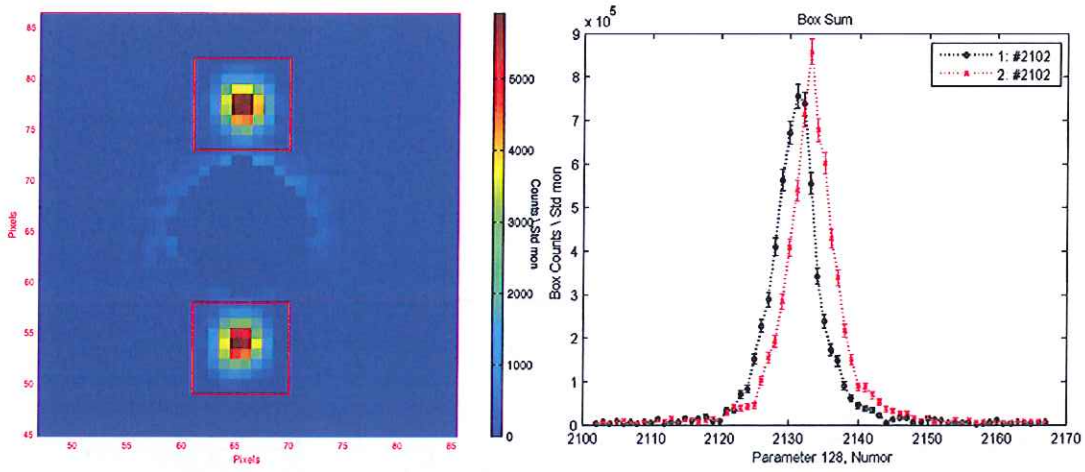

Figure 78: *Right:* The collected intensity from the entire rocking curve recorded at $\mu_0 H = 130\ mT$ projected onto the detector plane. A mask has been laid over the area where the direct beam hits the detector in order to be able to estimate the area where the Bragg spots hit the detector. The rectangular areas where intensity is collected are marked in the figure. *Left:* The extracted intensities as a function of rocking curve angle as determined by GRASP; the x-axis are file numbers each of which corresponds to angle intervals of 0.2 degrees. The center of the two rocking curves differs by an angle of 2θ as determined by $\lambda = 2d_{VL}\sin(\theta)$. Both figures are direct outputs from the GRASP package.

- Rocking curves with low statistics recorded at 80, 130, 200, 240, 260, 280 and 300 mT. This was done to determine the field dependency of the rocking curve integrated intensity. The angular step interval was 0.2° in all cases.
- Rocking curves with high statistics recorded at 115, 180 and 230 mT, respectively. These rocking curves ware recorded for the RMC simulations, and done in steps: The middle part of the curves was recorded with a narrow angular interval, and the outer part on both sides were recorded with a large angular interval in order to save time.

The collected intensity of the entire rocking curves as projected onto the detector plane, is shown in figure 79. As evident, the distance of the Bragg spots from the direct beam center (in the center of the frames) increases with field, but not in a linear manner. This is consistent with the $q \sim \sqrt{B}$ law. At somewhere between 280 and 300 mT, the Bragg spots disappear completely and no long range order can be detected by this experimental setup above this field.

Before starting the RMC refinement of the rocking curves with high statistics and discussing correlation functions, there is an important Bragg glass prediction to test - namely the prediction that near the rocking curve peak, the field dependency of the structure factor should fall off as a power-law with $S(\mathbf{K_0}) \propto B^{-3/2}$ as stated in equation 8.114. Figure 80 shows all the rocking curves obtained with low statistics as well as the middle part of the rocking curves recorded for RMC fitting. Before evaluating the field dependency of the peak intensity, the rocking curves need to be evaluated. As evident, the rocking curves obtained at 80 and 115 mT have tails extending far out in angle space. An obvious reason is that any given step in angle is a shorter step in reciprocal space at 80 mT than it is at 240 mT, due to the shorter lattice constant.

However, as evident on figure 81 (left), this is not enough to explain the increase in width. There are physical reasons for this as well. Close to H_{c1} the demagnetization factor is able to facilitate a phase separation between domains in the Meissner phase and domains in the Abrikosov vortex state, the *intermediate mixed state*. This would explain the large width as a finite size effect. If this

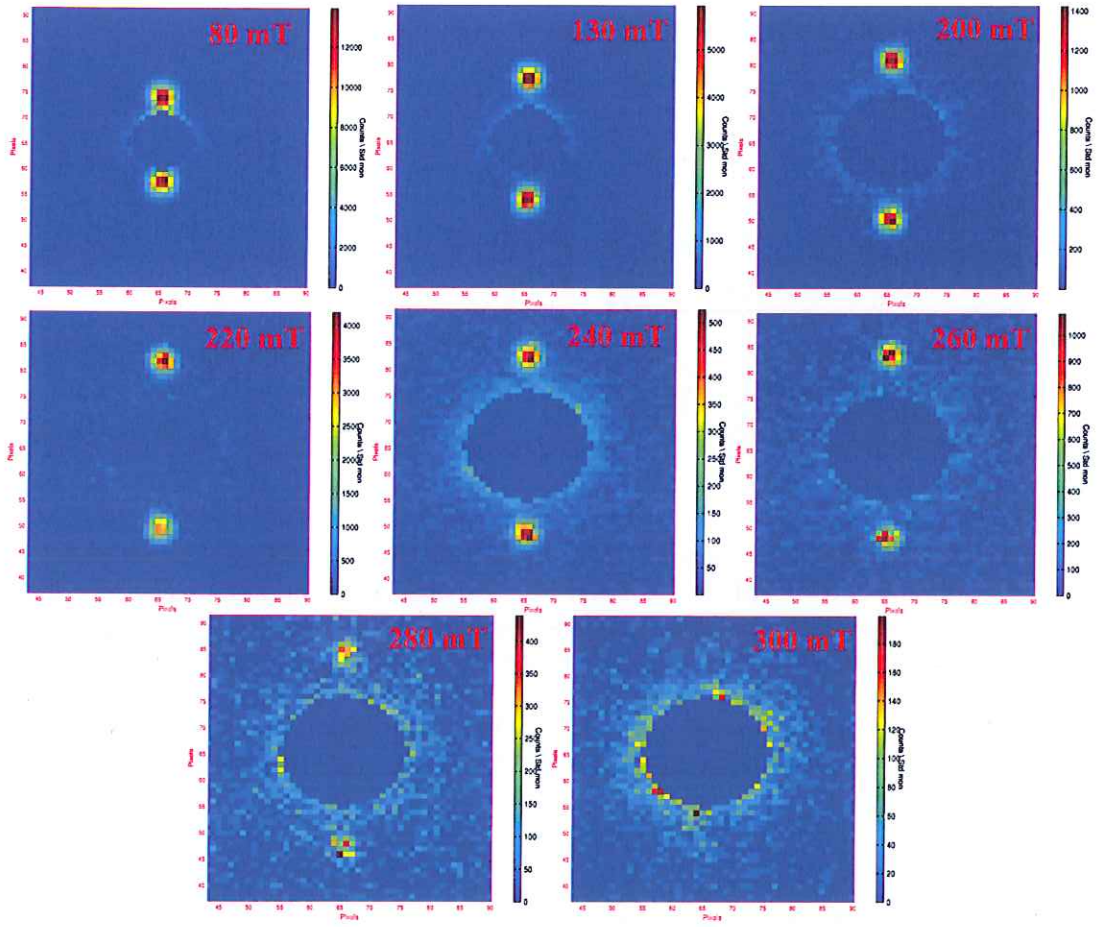

Figure 79: Collected intensity from the rocking curves recorded at T = 1.55 K with low statistics projected onto the detector plane. 80 mT is very near the Meissner phase (and possibly intermediate mixed state) at H_{c1} in the $(\mu_0 H, T)$ phase diagram and flux lines start to appear. As evident, the Bragg spots are very close to the direct beam. The scattering angle 2θ increases with field. At 280 mT, the Bragg spots are very weak; a reasonable rocking curve can not be obtained, and at 300 mT, there is no measurable intensity.

were the case, the total intensity of the ensemble would be lessened compared to what it would be if the entire sample volume was in the Abrikosov state, simply because there are less scatterers. If the width at low fields - in reciprocal space and not in angle space - is much higher than at slightly higher fields, the obtained integrated intensities will not be used for fitting the $I(H)$-curve.

The rocking curves depicted in figure 80 have been fitted to single Gaussian functions. It is clear that the rocking curves are not Gaussian, but varies in shape. However, one needs a basis for comparison. Fitting to a Voigt function for instance, leaves two free parameters which are coupled to the width of the rocking curve. When the curve shape is changing as a function of field, it is difficult to compare widths. As evident in figure 80, the integrated intensity is quite well determined at least for fields larger than 115 mT.

Another important feature of the rocking curves is that - as in [86] - there seems to be a flat plateau of slowly varying intensity at the peak center. According to the Bragg glass theory, the structure factor should have a power-law dependency of the intensity as a function of angle (or k but that does not make much difference at these small angles), diverging at the peak center. This divergence would, in a real experiment, be limited by the resolution function causing a smooth peak center.

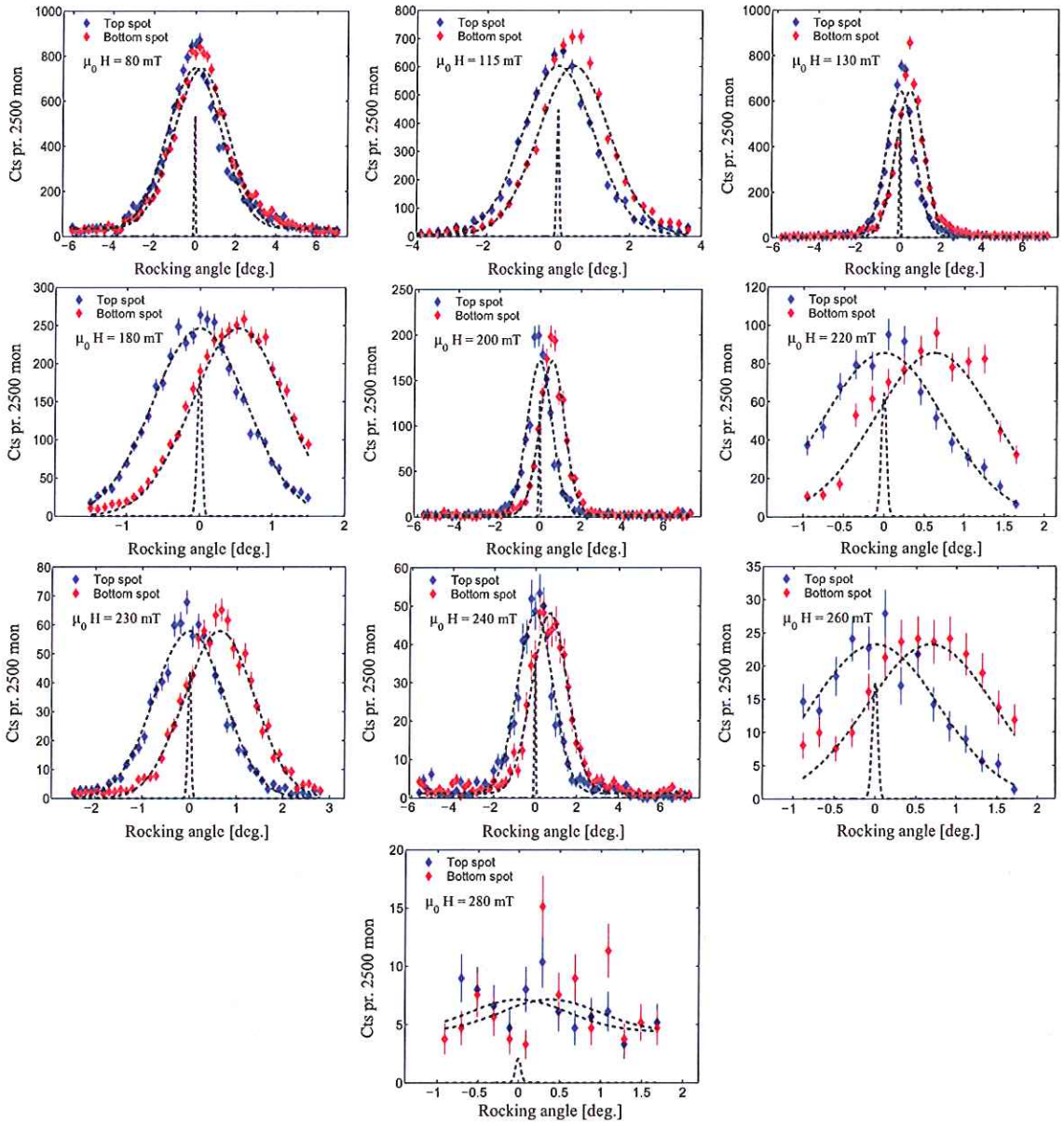

Figure 80: The rocking curves recorded in May 2008 fitted to single Gaussians. The curves obtained at 80, 130, 200, 220, 240, 260 and 280 mT are the curves obtained with low statistic with the purpose of obtaining a measure of the width and integrated intensity of the rocking curve. The curves at 115, 180 and 230 mT are the curves obtained with high statistics to be used for RMC fitting. Only the central part of these scans have been plotted and fitted (the Gaussian function does not fit the tail of the curves anyway). The zero point in angle has been chosen to be the center of the fit to the top spot data. The narrow peak in the center of the curves of the top spots, is a Gaussian representing the angular resolution width of the setup. The fits to the data recorded at 220 and 260 mT have been obtained by fixing the background to zero in order to avoid an unphysical negative background. The Bragg spots are far enough away from the direct beam for this to be reasonable. The data obtained at 280 mT do not really constitute a rocking curve (The peak was not measured using a broad enough angular interval), and should not be used for fitting. It should be underlined, however, that there *is* intensity at 280 mT as evident in figure 79.

The resolution width in this experimental setup is, however, much smaller than the angular range of the plateau at the peak centers in figure 80. This could be caused by a large mosaic spread in the vanadium crystal used, but this has been checked on the instrument ORION at the PSI, where the rocking curve width of the crystallographic (01-1) peak was not found to be significantly above the resolution width of 0.33 degrees. This suggests that the structure factor does *not* diverge at the peak center, and that the smoothing is due to the structure factor and not the resolution function. The may lead to the conclusion that the Bragg glass picture is not sufficient to describe the vortex lattice in this sample. Since the peak intensity is now not necessarily a good measure to test the Bragg glass hypothesis, the integrated intensity will be used. The prediction $S(\mathbf{K_0}) \propto B^{-3/2}$ was derived in section 8.4.4 for k-vectors near the Bragg peak center. Since the rocking curves (at least for fields larger than 115 mT) have a FWHM of only a couple of degrees, the assumption that the $B^{-3/2}$-dependency is valid for the entire rocking curve seems to be reasonable.

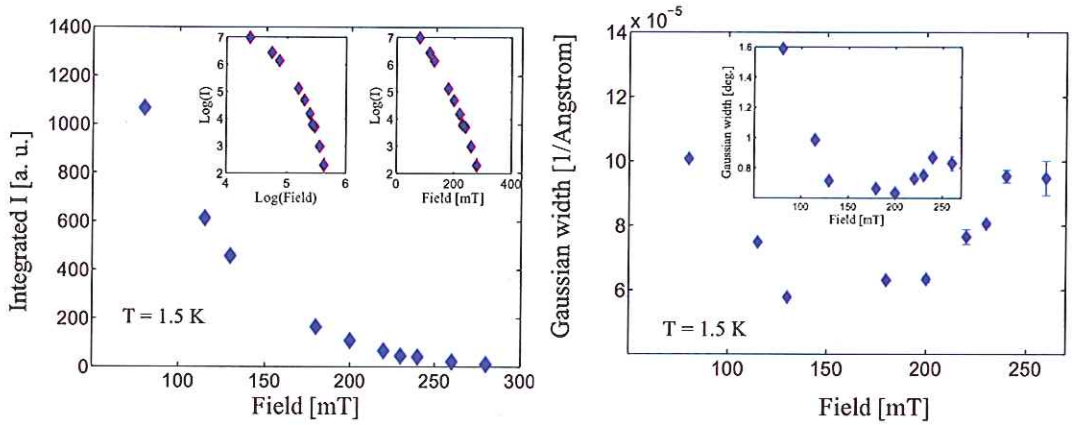

Figure 81: *Right:* Integrated intensity of the rocking curve as a function of field. The insets show $\log(I)$ vs $\log(\mu_0 H)$ and $\log(I)$ vs $\mu_0 H$. As evident, the intensity seems to drop off faster with field than a power law, most probably due to the form factor. *Left:* The Gaussian width of the rocking curves as a function of field. The widths have been converted to reciprocal space by $\sin(\sigma_\omega)|q_{10}(\mu_0 H)|$, where σ_ω is the width from the fits in figure 80 and $q_{10}(\mu_0 H)$ is the reciprocal lattice vector. As evident, the peak width decreases strongly with field until it reaches a plateau at $130mT < \mu_0 H < 220mT$ after which the width starts increasing again. The insert shows the rocking curve widths in angles.

Figure 81 (left) shows the integrated intensity of the rocking curves as a function of field - with the insets showing double logarithmic and single logarithmic plots respectively. The plots point to a power law or exponential decay of the intensity versus field, with a slight preference towards an exponential decay. This could be due to the form factor which in case of a low κ superconductor falls off faster than a power-law. It could also be caused by the intensity actually being zero as some finite angle - which would cause an otherwise power law decay not to be a straight line on a log-log-plot. The Gaussian peak width as a function of field is plotted in figure 81 (right). The widths are relatively high at low fields and drop to a minimum at 130 mT. Between 130 and 200 mT the peak width is relatively constant, after which the width increases as a function of field until the point where the rocking curves become unmeasurable above 260 mT. The wide rocking curves at low fields may (or may not) be attributed to finite size effects caused by the system being in the intermediate mixed state. Close to H_{c1} the demagnetization factor is expected to have significance anyhow. Since this is a possibility the intensities at 80 and 115 mT are discarded. The width is increasing at fields larger than 200 mT. However, since the entire sample is expected to be in the Abrikosov state, and since the full integrated intensity is used these intensities will be accepted. A derivation of the reflectivity analogous to that given in 3.3.7 can be done in case of a 2D lattice.

The form factor is constant in equation 3.81 and is therefore not contained in that equation. This is not the case for flux line lattices where the form factor strongly depends on applied field. The reflectivity from a flux line lattice is given in [23] as

$$I_{VL} = 2\pi \left(\frac{\gamma}{4\Phi_0}\right)^2 \frac{L}{A_\mu^2} \frac{\lambda^2}{\tau \cos(\eta_\tau)} |F(\boldsymbol{\tau})|^2 \int S(\omega) d\omega, \tag{9.10}$$

where γ is the gyromagnetic ratio, L is the length of the sample parallel to the field, A_μ is the area of the unit cell, τ is the length of the reciprocal lattice vector, η_τ is the angle between the scattering vector and the axis of rotation, $|F(\boldsymbol{\tau})|$ is the flux line form factor and $S(\omega)$ is the structure factor as a function of angle. Notice that the structure factor is not squared; this is due to the slightly different definition of the structure factor from that defined for crystallographic magnetic structures. Removing all the factors which are roughly constant in all scans made in this work, the integrated intensity is proportional to three factors: A *geometrical factor*, the *form factor* and the *structure factor integrated over the rocking curve*:

$$I_{VL} \propto \frac{1}{\tau A_\mu^2} \cdot |F(\boldsymbol{\tau})|^2 \cdot \int S(\omega) d\omega \propto B^{3/2} \cdot |F(\boldsymbol{\tau})|^2 \cdot \int S(\omega) d\omega \tag{9.11}$$

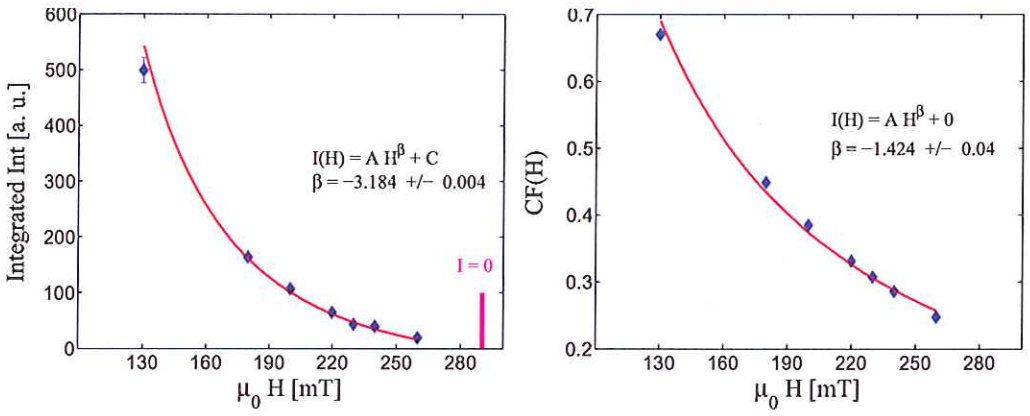

Figure 82: *Left:* The uncorrected intensity as directly extracted from the fits - fitted to a power law with *unfixed* background (A and C are free parameters). *Right:* The correction factor as calculated using Clems form factor and the geometrical factor - fitted to a power law with the background fixed to 0.

The calculated form factor from section 9.1.3 needs to be multiplied with the geometrical $B^{3/2}$ dependence in order to obtain the true correction factor - $CF(H) = H^{3/2} \cdot |F(\boldsymbol{\tau}(H))|^2$. After correcting for these factors, the exponent needs to be fitted, which can be done in several ways. Due to the fact that at some finite field below H_{c2}, the order becomes unmeasurable on the instrument, the fitting function needs to intersect the field axis. The increasing rocking curve width points to the fact that there is a gradual transition to a disordered phase, but the crossover has not been measured well due to the weak scattering cross section. However, the magnetization measurements presented in 9.3.9 hint to the fact that nothing drastic happens at 290 mT. Furthermore, the peak value of the finite intensity at 280 mT (see figure 80) is roughly half the value at 260 mT, which indicates a slow decrease of intensity close to the zero-point field. Therefore, a 'business-as-usual' function has been fitted to the data - a power-law decay - $I(H) = AH^\beta + C$ - only with a finite (and negative) background facilitating the necessary intersection with the field axis where the measurable intensity goes to zero. Other functions facilitating a slow and gradual intensity falloff - for instance $AH^\beta \cdot \tanh(1 - H/H_0)$ - give the same exponents as the power law with background. On the other

hand, functions with a rapid drop of intensity - $AH^{\beta} \cdot \sqrt{1 - H/H_0}$ - gives poor fits if the field of zero intensity H_0 is forced to be between 290 and 300 mT. The uncorrected intensities and the calculated correction factor using the Clem form factor are shown in figure 82.

As evident in figure 82, the uncorrected intensities fall off with an exponent of roughly -3, and the correction factor with an exponent of roughly -3/2. The fit to the correction factor has been done with a fixed background of 0, since the correction factor is well defined to arbitrary large field values with the field axis as an asymptote. The intensity can be directly corrected for geometrical effects as well as the form factor as calculated in the Clem approximation to obtain the structure factor integrated over the rocking curve as a function of field. This is shown in figure 83.

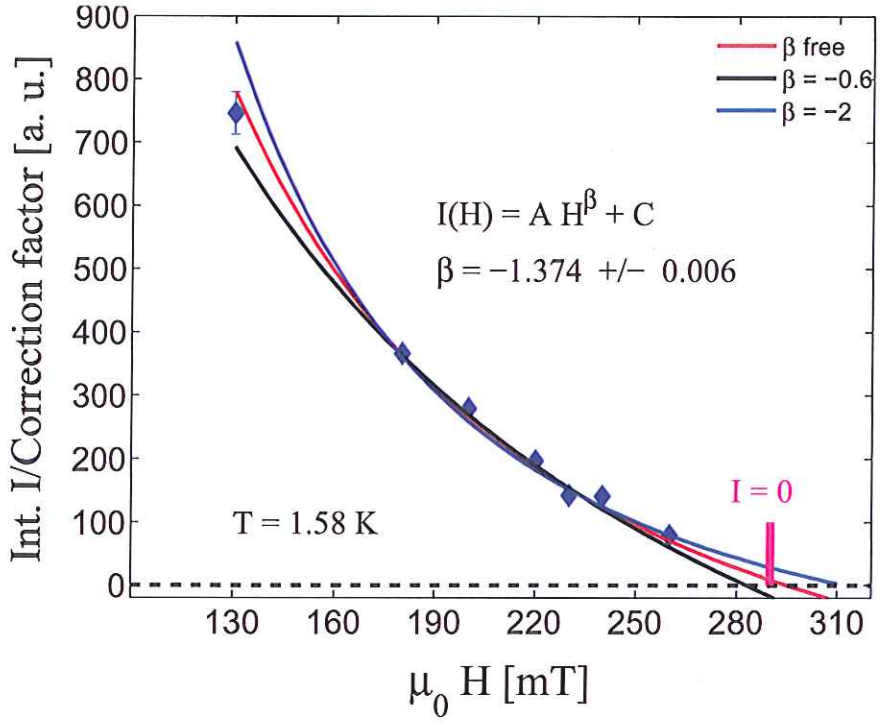

Figure 83: Corrected integrated intensity as a function of field fitted to a power law - $I(H) = AH^{\beta} + C$ - with *variable background* C. The exponent is roughly -1.4 which is quite close to the Bragg glass prediction. The statistical error of the exponent is unreasonably low. The re-evaluated error is explained in the text. However, the extrapolation of the fitted curve to higher fields is consistent with the observation of very little intensity at 280 mT and the lack of intensity at 300 mT.

These corrected intensities have been fitted to a power law with variable background, and an exponent of $\beta = -1.374(6)$ is obtained. It is the author's opinion that this statistical error does not reflect the true uncertainty at all. Figure 83 shows - in addition to the fit with all parameters free - two fits to power-laws with *fixed* exponents -2 and -0.6, respectively. These curves fit the data reasonably well, although they are not consistent with the observation of intensity at 280 mT and the lack thereof at 300 mT. The truth is that removing just a single point from the data to be fitted has quite a large effect on the determined exponent β. The reason for this is that the exponent and the necessary background are quite coupled in the fitting function, especially with sparse data near the point of zero intensity. Removing the point at 130 mT results in an exponent of -2.16, for instance, while removing the data point at 230 mT gives an exponent of -1.04. In this work, the determined exponent is decided to be the average exponent of 8 fits - one with all data points and 7 fits each with a different point removed from the set - with the uncertainty given as $\sigma/\sqrt{8}$,

where sigma is the standard deviation of the set of exponents. Thus, the power-law exponent of the integrated structure factor versus field is determined as

$$I \propto H^{\beta}, \quad \text{where} \quad \beta = -1.42 \pm 0.12. \tag{9.12}$$

This value lies quite close to the predicted value of $\beta = -1.5$. The uncertainty should still be regarded as a minimum. This determined exponent is consistent with the Bragg glass paradigm, but it should by no means be regarded as a solid proof of the theory. The sensitivity of the determined exponent to the slightest data reduction is one thing, but there have been made several assumptions that might be flawed. They are the following:

- The assumption that the $\beta = -1.5$ result holds for the entire rocking curve - and not just the peak of the curve - might not be true.

- The fact that the structure factors seems not to diverge at the peak center, as predicted, could point to the fact that the Bragg glass scenario might not be sufficient to describe the vortex ensemble. If this is the case - a consistency of the exponents might just be a coincidence. The $\beta = -3/2$ prediction is a consequence of an algebraically diverging structure factor, which is directly observed not to be the case entirely.

- The form factor derived by Clem is for an *isolated* flux line. Especially in low-κ Vanadium, the field distributions from the flux lines are overlapping - the lattice parameter is between 95-135 nm while the penetration depth is 40 nm. The difference between minimum and maximum magnetic field in the ensemble - which in some sense is proportional to the form factor - *cannot be expected to be constant as a function of field.* Furthermore, due to field dependency of the overlap of flux line field distribution - the Clem solution for the field density might not in itself be true. Thus, the form factor might be expected to fall off even quicker than predicted by Clem.

- The only field-dependent parameter in the Clem form factor is $q \propto sqrtB$. However, if the superconducting order parameter has decreased significantly in the field regime investigated, the *amplitude* of the field distribution from an isolated flux line could decrease as well, resulting in a form factor smaller than that described by Clem at high fields. The last valid intensity was recorded at 260 mT, where the lattice constant is $a_0^{260} \approx 96nm \approx 3\xi_{T=1.55K}$. So this effect could also diminish the form factor as compared to the Clem result.

These objections being stated, the fact that there are Bragg peaks - and hence long range order - and that the overall corrected intensity drops off roughly as predicted, within error, shows that the Bragg glass theory might be a good starting point for describing the flux line ensemble. Setting the details aside - the predicted $\beta = -1.5$ exponent is roughly a prediction of how quickly the order of the ensemble decays as a function of field. In this work, the decay of order must be said to have been proven to be consistent with Bragg glass theory, at least at 1.55 K. The decay of intensity with field is a very indirect way of confirming the Bragg glass hypothesis, especially in this work. If the effects listed above have significance, the observed decay of intensity is actually *slower* than predicted. There is no quick answer to how one can account for the effects above; it is the author's opinion that when fitting to only 7 data points, any theoretical suggestion cannot be backed up by the data presented here anyway. To it would be grossly overestimating the data if one claims this drop off to be a proof of the Bragg glass theory. The shape of the rocking curve however, is *directly* proportional to $S(\tau)$; and an analysis of these rocking curves could provide much more reliable insight into the nature of the flux line order. This analysis is described in the following section.

9.3.2 Initial analysis of the rocking curves with high statistics

The rocking curves with high statistics were done at 115, 180 and 230 mT. When revisiting the low statistics data, it is clear that the 130 mT data actually contain very good statistics. When evaluating the measurement of the intensity versus field, the 115 mT data were discarded as having been recorded at a field to close to H_{c1}. Therefore, this rocking curve will initially not be considered valid. In doing RMC simulations, it is important to have data as free of statistical error as possible especially in the tails, as these tails will form the experimental basis for determining the exponent of the expected power law dropoff. Therefore, in order to obtain rocking curves with as high statistics as possible, the average of the rocking curves from top and bottom spot is taken. This is done by re-setting the angular zero-point of each curve to center of the curve as obtained from a Gaussian fit (as long as the peak is symmetric around the center, this center will be properly determined), and simply adding the counts using the same angular binning as in the rocking curve scan. Before employing the powerful tool of RMC fitting, an initial analysis of these high statistics rocking curves is in order, and will be given in the following section.

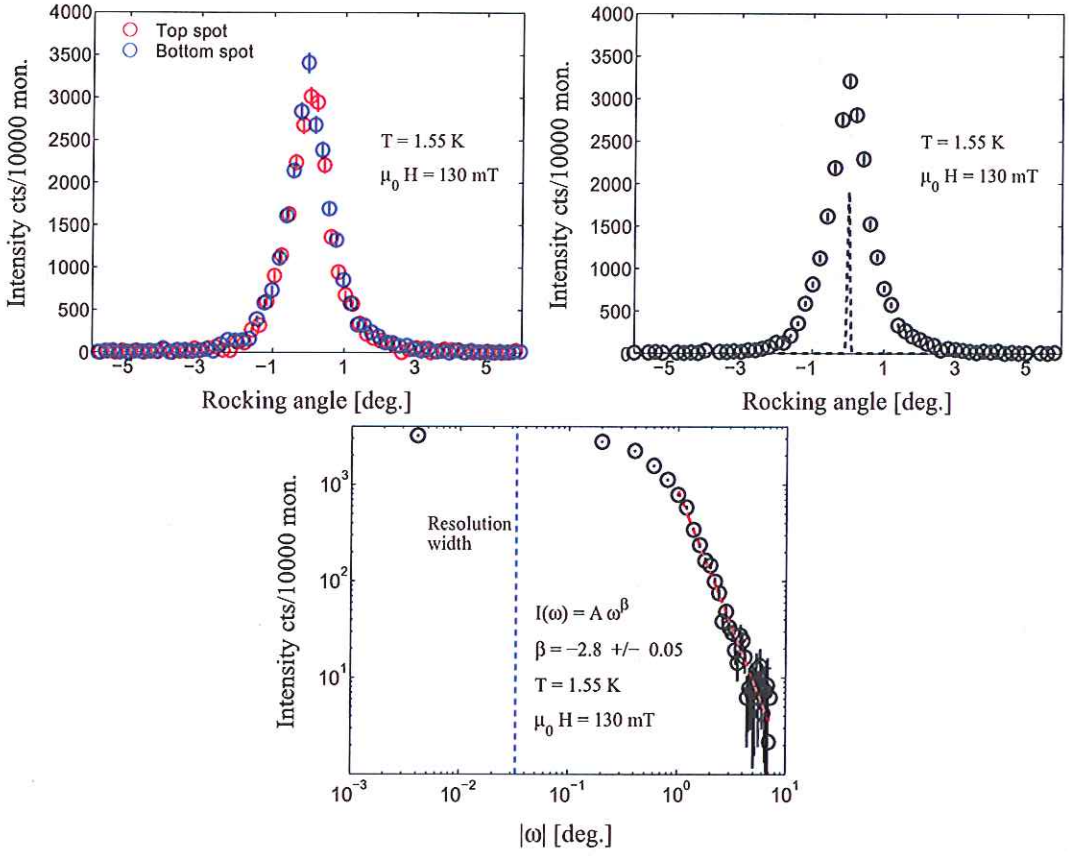

Figure 84: *Top Left:* The rocking curves as extracted from the top and bottom Bragg spot on the 2D detector, respectively. As expected, the two curves are very similar. *Top Right:* The average of the top and bottom rocking curve. The curve is much more smooth as the errors are smaller, and very useful for RMC fitting. The dashed line represents the Gaussian width of the resolution function. *Bottom:* The average observed intensity as a function of *absolute* angle plotted on a double logarithmic scale. As evident, the tails of the rocking curves decay as a power law. However - as observed in [86] - the intensity starts to smooth to a constant value at an angle much higher than the angular width of the resolution function.

The rocking curve at 130 mT

Figure 84 (top left) shows the rocking curves obtained at 130 mT, and the resulting average rocking curve (top right). The bottom part of figure 84 shows the observed intensity as a function of angular deviation from the peak center ($|\omega - \omega_0| = |\omega|$ as $\omega_0 \equiv 0$) on a double logarithmic plot. As evident the intensity drops off as a power law indeed, but only for angles larger than 1°. This is exactly as what was observed by Laver *et. al.* in [86], where a *fractured* Bragg glass was conjectured from the RMC results. A possible reason is that the power law dependence of the two point translational correlator only holds up until a certain pair separation distance, above which the flux lines start to de-couple faster than predicted by the Bragg law. This results in large domains of the Bragg glass which are decoupled from each other to a larger extent than as predicted by Bragg glass theory. Since the rocking curve *directly* reflects the two-point translational correlator this must be a reasonable interpretation.

Setting aside the smoothing of the power law intensity dependence at angles larger than expected, the high angle power law dependence of the intensity versus angle is a very uplifting result. The power law form of the structure factor is yet another Bragg glass prediction that stands the test of experiment.

The rocking curve at 180 and 230 mT

Figure 85 shows the high intensity rocking curves recorded at 180 and 230 mT, plotted in a similar way as for the curves at 130 mT. Notice that the angular steps in these rocking curves are smaller than at 130 mT. It is evident that the rocking curves at 230 mT (which took almost a full day to record at SANS-II), start to show substantial statistical deviations. The monotonic behavior evident in the 130 mT data is not always there at 230 or 180 mT due to statistical fluctuations. Even so, the same trends as in the case of 130 mT are clearly evident. Again, there is a nice power law dependence of the intensity at high angles, and a smooth transition to a constant intensity at angles far above what is dictated by the resolution function. It is thus directly shown experimentally that the structure factors display a high angle power law dependency in a *field interval* of at least 100 mT, in which the structure factor drops off as a power law with $S \propto B^{-\frac{3}{2}}$. It is very interesting that the *exponent* of the power law drop off is lower at 130 mT than at both 180 and 230 mT. It should be noted that the rocking curves at 180 mT and 230 mT can be successfully fitted to Gaussians as well. It is difficult, however, to put too much weight into whether or not the structure factor drops off exponentially or as a power law, unless the statistics are good enough to unambiguously distinguish between the two. This is what the RMC hopefully will resolve later on. The intensities as a function of reciprocal Ångstroems are shown in figure 86.

As previously mentioned, the power law exponent is significantly less at 130 mT than at 180 and 230 mT. Furthermore, the cutoff angle - where the power law ceases to hold - seems to increase as a function of field. But so does the length reciprocal lattice vectors. This suggests that the critical quantity is the *number of flux lines* in a domain, and not the absolute size of the domain. That at all fields, there is a critical number of flux lines in each domain, above which the correlations start to decrease rapidly. Perhaps the high field increase in rocking curve width is caused by a reduction in domain size until the point where long range order ceases to exist. This cutoff is difficult to determine by fitting; but an attempt can be made. First of all fitting the rocking curve to a Voigt function makes little sense as the parameters cannot be directly interpreted. One needs a function incorporating a high angle power law and a low angle smoothed cutoff to a low angle pseudo-constant behavior. To do this the following simplified function is considered:

$$\Gamma(\omega) = \begin{cases} \left(A\omega_c^{-\beta}\right)\omega^{\beta} & \text{if } |\omega| > \omega_c \\ A & \text{if } |\omega| < \omega_c \end{cases} \tag{9.13}$$

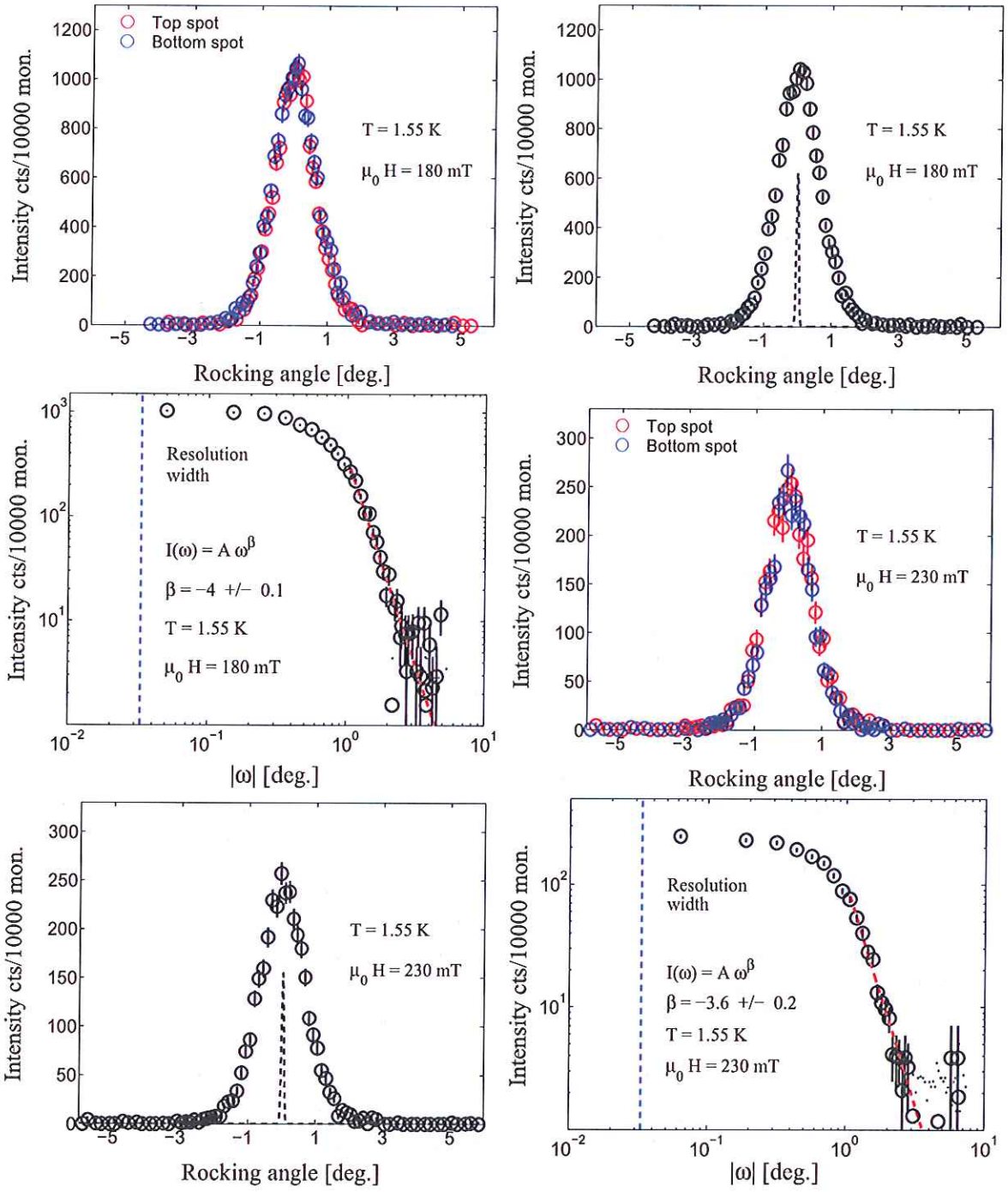

Figure 85: The rocking curves at 180 mT and 230 mT respectively, plotted along with the calculated average rocking curve. As evident even the average rocking curve at 230 mT displays substantial statistical fluctuations. In this case - since these rocking curves were meant for RMC fitting, the angle interval in the high intensity area is smaller than at 130 mT. As evident on the plots of the intensities as a function of absolute angle, the power-law divergence at the peak center - which should only be limited by the resolution function - is terminated at angle well above what the resolution function dictates. At higher angles, however, the intensity falls off as a power law in both cases, with comparable exponents.

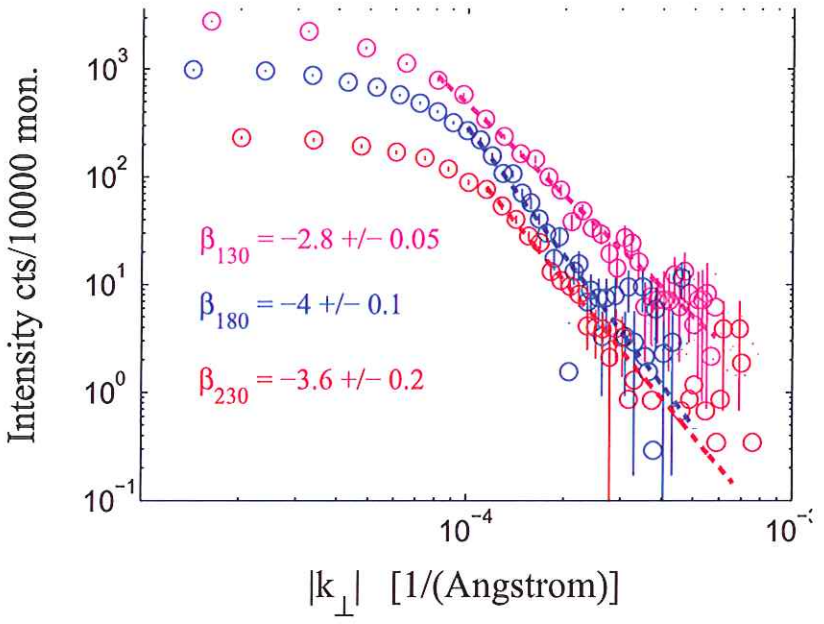

Figure 86: Intensity as a function of $|k_\perp|$ at 130, 180 and 230 mT respectively. The fall off exponent of the power law fits is comparable at 180 and 230 mT, but significantly lower at 130 mT. It seems that the cutoff point at which the power law seems to hold increases with field (but only in reciprocal space). This could be because of the larger unit cell; perhaps the cutoff length in real space is a constant multiple of the lattice constant.

which is simply a constant function up to a critical angle ω_c, where the intensity decreases as a power law. This transition from the constant peak value to the high angle power law decay is not smooth, which would fit badly to the observed rocking curves. In order to smooth over the transition between the constant regime and the power law regime (not necessarily only due to the resolution function), the function 9.13 is convoluted with a Gaussian of unity amplitude, a center at zero but *keeping the width as a free variable* - $G_\sigma(\omega) = e^{-\omega^2/2\sigma_g^2}$. Thus, the function used to fit the intensity is on the form

$$I(\omega) = (\Gamma \star G_\sigma)(\omega). \tag{9.14}$$

The width is kept as a variable since other effects that have nothing to do with the resolution function can cause a smooth transition between the power law and constant regimes. Whatever the reason, it is assumed to be able to incorporate into the width of the Gaussian with which the function 9.13 is to be convoluted. So the variable parameters in the fitting function is the amplitude A, the cutoff angle ω_c, the exponent β, the Gaussian convolution width σ_g and the background. In the fitting function 9.14, there are three parameters determining the behavior of the curve at small angles - A, ω_c and σ_g. As A can be easily determined from the curve by eye, it is kept fixed to try to minimize the errors of the fitted ω_c and σ_g coefficients. Fixing the peak center to be 0, this leaves only a reasonable four fitting parameters including the peak center. The convolution has been done numerically in Matlab (The code is presented without further elaboration in Appendix A. Since $|k_\perp| = \sin(\omega)|q_{10}|$, the intensity plotted as a function of rocking angle is already normalized to reciprocal lattice units. Therefore, the critical angle can be used to find a critical length in units of a_0 - $\ell_c/a_0 = 1/\sin(\omega_c)$. Figure 87 shows the fits to the three rocking curves using the fitting function described above (top), and the extracted values of coefficients (excluding the background) as a function of field.

As evident in figure 87 bottom left, the critical angle is roughly constant as a function of field. The Gaussian smoothing width is very large and *increases* as a function of field. The smoothing widths

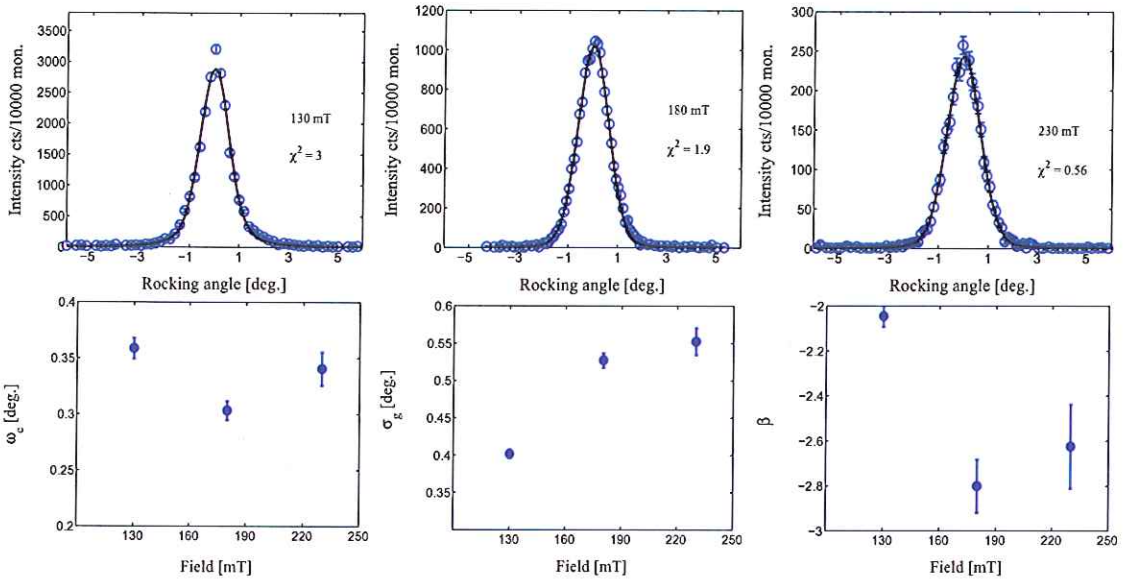

Figure 87: *Top:* The fits to the rocking curves using the function described in the text. The fits and the χ^2's are reasonable. *Bottom left:* The extracted cutoff angles as a function of field which are roughly constant within errors. *Bottom middle:* The smoothing widths σ_g as a function of field which shows an increase as a function of field. *Bottom right:* The fitted exponents as a function of field. These are larger than those determined from merely fitting the tails of the rocking curves.

exceed the critical angles, this underlines that the power law cut off is not a sharp effect but very gradual. This is also directly visible from the rocking curves. A bold interpretation would be that $\ell_c/a_0 = 1/\sin(\omega_c)$ represents the average pair separation distance above which the power law decay of the translational correlator ceases to hold. Then, $\ell_{min}/a_0 \approx 1/\sin(\omega_c + \sigma_g)$ would represent the minimum pair separation distance (on average) at which this becomes relevant and starts to alter the Bragg glass behavior. Using these simple interpretations, the length scales are

$$\begin{aligned} \ell_c &\approx 173\, a_0 \quad \text{for all fields} \\ \ell_{\text{min}}^{130} &\approx 76\, a_0 \\ \ell_{\text{min}}^{180} &\approx 70\, a_0 \\ \ell_{\text{min}}^{230} &\approx 63\, a_0 \end{aligned} \tag{9.15}$$

It should be noted that using this fitting function might not be justified at all, it is just the author's way of extracting interpretable parameters from the near-peak part of the rocking curve - the part that does not fit the predictions of the Bragg glass theory. The author can think of two distinct physical situations that could cause this high-separation-drop-off of the translational correlator.

- **There are dislocations at all fields** with some distribution of separations around a mean value (ℓ_c?). As the field increases, the flux line tension energy decreases, allowing the flux lines to bend around conforming to the pinning landscape. At some field the density of dislocations start to slowly increase - widening the rocking curves and decreasing the range of order - slowly decreasing the intensity. This is the picture given by Kierfeld. Dislocations are shown to be excluded from the Bragg glass picture as mentioned in section 8.4.4. Furthermore, an increase in dislocation density should be accompanied by an increase in the average pinning, as the flux lines are more easily able to conform to pinning sites. This may have an effect on the critical current at higher fields, if the change in dislocation density is large and occurs rapidly.

The RMC offers no information (and can even be misleading) about such dislocations as they are assumed not to occur in the algorithm.

- **There are large dislocation free fractures of Bragg glass** with some distribution of fracture sizes distributed around some mean value (ℓ_c?). The correlations between these fractures are significantly smaller than those within the fractures which decay as a power law. This would cause the translational correlator to show a more rapid drop-off at pair separations larger than the fracture size. This increase in drop-off exponent would probably be gradual, judging by the rocking curves. In principle, the RMC should be able to mimic this scenario, which is more or less the proposal of Menon.

In general, the RMC is only suited to mimic the fractured Bragg glass scenario, and even if a nice fractured ensemble came out, one could always object that this is only hold under the assumption of the absence of dislocations. It would just be an answer to how a 2D-ensemble would fit the data and not how an ensemble full of dislocations would look.

The exponents of the fits using this very simplified model differ from those obtained from merely fitting the tail to a power law. It therefore seems that the fitted exponents of the rocking curves are dependent of the model one chooses to use for the rocking curve as a whole. As the power law exponents of the translational correlator are one of the central parameters to determine, this is unfortunate. The RMC, however, is able to give an *unbiased* fit to the data resulting in a real space flux line ensemble from which the translational correlator can be directly calculated. The results of the RMC/SA simulation will be presented in the following sections, starting with a description of the problems that occurred during the simulation work.

9.3.3 Problems with the simulations - Simulated Annealing

Fitting the recorded rocking curves using the RMC code was not an easy task. Upon realizing that the first try failed, there are several parameters which can be reasonably varied quite a lot to remedy the situation. The simulations were run on a multi node server called *Sauron* - which had 16 independent processors available. So dozens of simulations were ran in parallel for several months (each simulation took from 1 to 3 days), in the process of solving various plentiful problems. To give a full and detailed account of all the simulations and considerations would be unfruitful, and uninformative. In this section, two central problems are described as these are fundamental and very important for future studies.

When recording the data the attenuation slit was set to only 8 mm in order to make the resolution function as narrow as possible. The point of this was to - in the case that a cutoff was observed - better be able to extract information from the peak center. When the RMC evaluates the structure factor in a given point, it includes the contribution from all adjacent points within 3 times the angular width of the resolution function. However, the calculated width of the resolution function is $\sigma_r \approx 0.034°$, which is roughly one third of the *minimum* rocking curve angular step of 0.1° (in the 130 mT data the step is 0.2°). Due to the fact that the width of the resolution function is much smaller than the angular steps in the rocking curve, each point is virtually decoupled from its nearest neighbors in the rocking curve. The RMC simply does not need to take the neighboring point into account when fitting the curve to one particular point; there is almost complete local freedom to adjust the structure factor in any arbitrary way to fit the point in question. This has severe consequences for the results, as evident in figure 88.

Figure 88 shows the results of RMC simulations with the ensemble size of 40000 with varying move acceptance probability, and simulations with different ensemble sizes, done with the same very high acceptance probability of χ^2 increasing moves. The data are shown along with the calculated structure factor (red curve) after RMC convergence along with the calculated rocking

curve obtained after convoluting the structure factor with the resolution function (blue curve). The three simulations done with a 40000 flux line ensemble all show unphysical variation on short angular scales that are not dictated by the data. The extent and frequency of these variations decrease with increasing move acceptance probability.

The intrinsic width of the SINQ function $(sin(N * \omega)/(N\omega)$ describing the sum and product of phase factors for a finite ensemble of N isotropic scatterers is $1/\sqrt{N}$. When the simulation is done

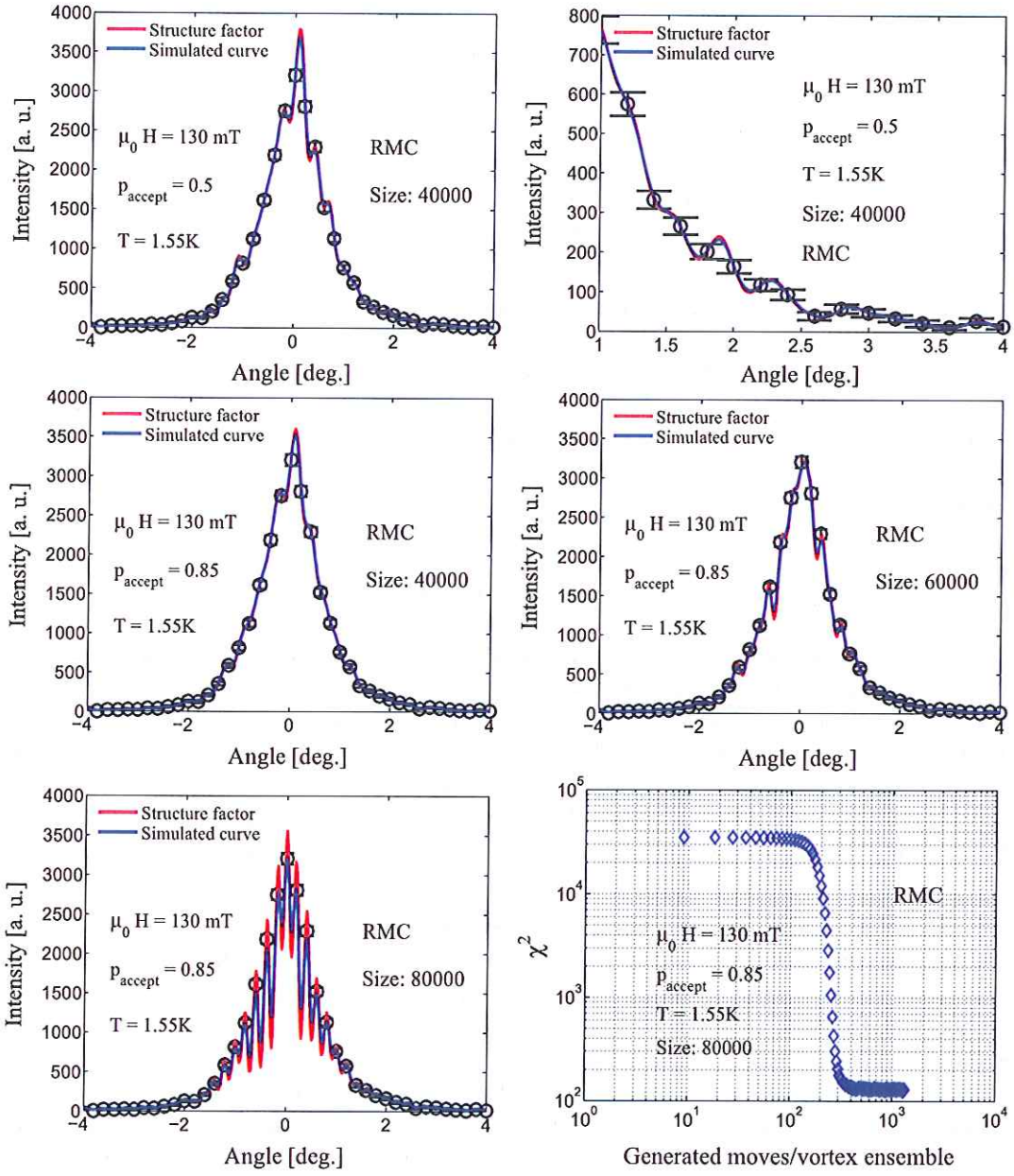

Figure 88: *Top plots and middle left:* The RMC structure factor (red line) and rocking curve (blue line) as outputted from the RMC algorithm for two different acceptance probabilities for an ensemble of 40000 flux lines. Substantial local variations are evident decreasing with acceptance probability. *Middle right and bottom plots:* The RMC fitting of the 130 mT data for ensemble sizes of 40000, 60000, and 80000 respectively. There is a natural increase of local fluctuations with ensemble size. The evolution of χ^2 as a function of normalized number of moves is shown as well.

with a very high acceptable probability, the RMC attempts to fit the curve while introducing a very high degree of randomness or disorder. Increasing the disorder of the ensemble will serve to smooth the curve as peaks in the structure factor widen with disorder. However, even when accepting 85 % of the moves increasing χ^2 the rocking curve obtained using a 40000 flux line ensemble still shows irregularities. The results shown in figure 88 for $P_{accept} = 0.85$ for different ensemble sizes can be said to be the smoothest curves obtainable using the RMC code with the calculated resolution function. As evident, there are variations in the structure factor which is not at all dictated by the data due to this lack of inter-point coupling. As the ensemble size increases to 80000 - and thereby the angular interval within which the structure factor is able to change - these variations increase to a point when they are comparable with the difference between the background and the peak amplitude. As evident on the evolution of the χ^2 curve for the high-p simulations, the χ^2 value stabilizes at around 130, which is quite a lot. This is due to the very large degree of unphysical randomness that is maintained by accepting virtually every move even though convergence has been reached. Such high values of χ^2 should not be accepted; as the ensemble is hovering at a high χ^2 fluctuating between configurations with this particular χ^2 value.

Similar unphysical variations were observed in the simulations of 180 mT and 230 mT curves. Simply decreasing the ensemble size until these variations cannot occur, is not a viable option. The intrinsic peak width of an 20000 flux line ensemble is roughly 0.4° compared to 0.2° for an 80000 flux line ensemble. Since physical effects are causing an increased curve width of roughly 0.5°, it makes little sense to use an ensemble size where this curve width is an intrinsic property.

The first attempt to fit the 130 mT data using an ensemble size of 80000 flux lines, was using the simulating annealing technique described previously in the text. Starting at a very high acceptance probability and slowly 'cooling' the ensemble might serve to smooth the structure factor even more and perhaps reach the global (and hopefully physical) minimum of the χ^2 function. Even though this gave considerably lower χ^2 values, it did not solve the problem with the fluctuations. Perhaps this is caused by the RMC algorithm lowering the χ^2 values by simply creating different ordered minor ensembles within the larger one, orientationally displaced from each other such that a peak in the structure factor is created at or between *each data point in the rocking curve.* This would enable the algorithm to minimize the χ^2 to very low values, so perhaps the global minimum for the cost function is this unphysical 'sharks teeth' curve. If this is true, it is no fault of the algorithm; if adding 'sharks teeth' costs no energy (or χ^2) the algorithm cannot be expected to avoid them.

The only way to solve this was by using a brute force method. Interpolated points - using the spline interpolation method - are simply but in between the real data points, with an equal weight. This does not pose as big a problem as one might think; the interpolation point(s) placed between two data points are placed well within the area spanned by the two error bar endpoints. It is the authors opinion that the error introduced by this method is un-biased and introduces less systematic error than the statistical errors already caused by the counting statistics. The interpolated point used for the 130 mT curve - which is the curve with the best statistics - is shown in figure 89.

In summary, the two most important steps undertaken to achieve converging simulations with reasonably low values of χ^2 while achieving physically acceptable rocking curves were the following:

- The method of *simulated annealing* was used. One starts out with a very high χ^2-increasing move acceptance probability, after which one slowly decreases said probability at well defined points in the simulation. This is a process of slowly cooling the ensemble and probably the best way of reaching the global minimum.
- However, due to the very narrow resolution function, the algorithm does not need to take the adjacent points into consideration when fitting the structure factor to any given point. Therefore, the algorithm can just make peaks in the structure factor between any two points and adjusting the peak characteristics until the curve fits perfectly. The possibility of doing this increases with simulation ensemble size. This actually means that *the global minimum in*

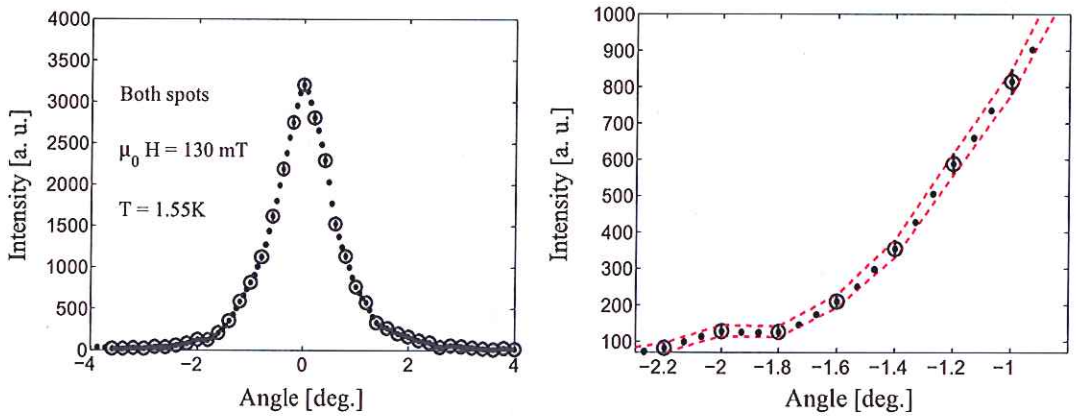

Figure 89: *Left:* The 130 mT data (circles) plotted along with the interpolated points (dots) *Right:* A zoom on the left hand tail of the rocking curve plotted along with the area spanned by the error bar ends (red dashed lines). As evident, the interpolated points are well within the rocking curve statistics - which are quite good to begin with.

configuration space is unphysical. The only way to remedy this is to introduce artificial points as described in the text. The errors of doing this are arguably smaller than the statistical errors introduced by the counting statistics.

9.3.4 The intrinsic finite size problem

Due to computational limitations, the ensemble size to be fitted to the data is much smaller than the ensemble created in the SANS experiments - figure 77 shows an ensemble radius of 20 μm for 80000 flux line ensemble which is 1/1000 of the sample radius. Since no obvious periodic boundary conditions can be enforced; as no unit cell can be defined - the should be no translational symmetry in the ensemble after convergence. The similarity between the simulated ensemble and the real one only holds when the flux line pair (from which to calculate the correlation) is far away from the ensemble edge. This is illustrated in figure 90.

The displacement correlator calculated from the ensembles returned from the RMC/SA algorithm after convergence showed a drop at pair separation distances larger than roughly half the ensemble radius. The following is a possible explanation given in retrospect. In order for a pair correlation between two flux lines separated by d to mimic the pair correlation for an infinite ensemble, both flux lines need to have surroundings resembling those for an infinite ensemble at distances up to d. Thus, the joined width of the blue and green circles needs to be smaller than the radius of the ensemble - which means that $3d < 2R \Rightarrow d < 2/3R$. Even if this was the case, the only flux line pairs - out of the N^2 possible pairs - that mimic the correlations in an infinite ensemble are those on the circle $|\vec{P}| = d/2 = R/3$, where $\vec{O}$ is a vector from O to any flux line at P. When $d < 2/3R$, this circle becomes a shell of width $2R - 3d$ containing the possible pairs separated by d, which is described by $2d - R < |\vec{P}| < R - d$. It is proposed that this shell needs to constitute a substantial fraction of the ensemble area in order for the two-point correlation functions extracted to be free of finite size effects. This can hardly be said to be the case for separations $d = 2/3R$. However, as the pair separations become smaller than $R/2$, the number of pairs having identical surroundings resembling those for an infinite ensemble starts to grow rapidly (as evident in figure 90). The ensemble size used in the RMC simulations presented in this work, is $N = 80000$. The radius of the ensemble expressed in lattice units is thus $R = \sqrt{\sqrt{3}N/(2\pi)} \approx 150a_0$, using $A = N\Phi_0/B$ and $a = \sqrt{2\Phi_0/(\sqrt{3}B)}$. Here, A is the unit cell area and a is the lattice constant. Thus, for an ensemble

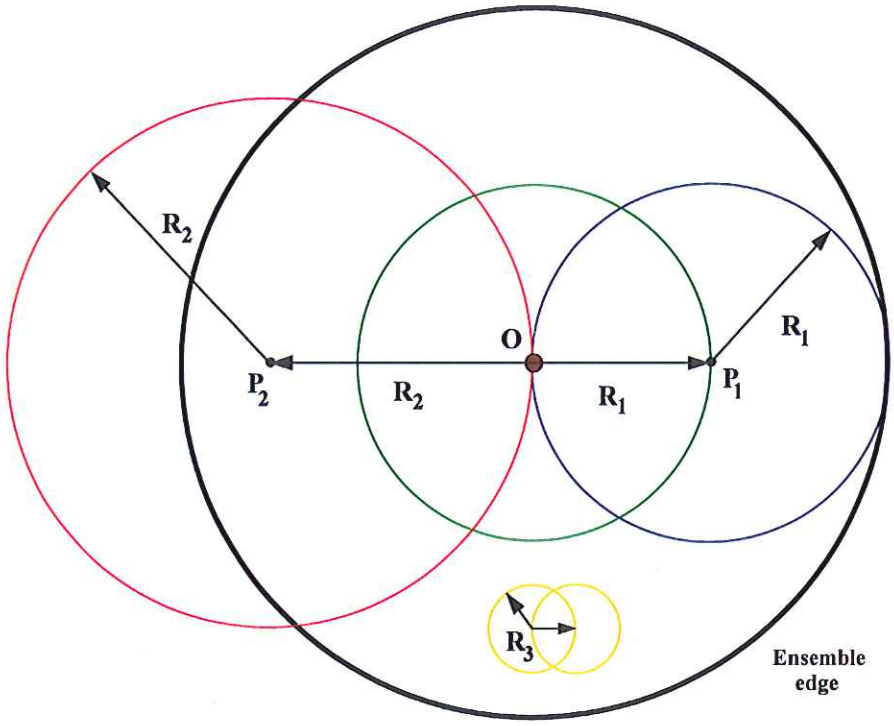

Figure 90: Illustration of the proposed finite ensemble effect. The black circle centered at O represents the circular array of flux lines. Two flux lines positioned at O and a distance $|P_1| = R_1 = R/2$ from O (where R is the ensemble radius) both have surroundings resembling that for an infinitely large ensemble for distances smaller than R_1. Thus, for pair separations of R_1 all correlations between pairs in the green circle mimic those for an infinite ensemble. Two flux lines at O and P_2 do *not* have identical surroundings at distances R_2. The only flux line pairs separated by R_2 having similar surroundings which are valid to an infinite ensemble are those on the circular shell $2R_2 - R < |P| < R - R_2$ all of which further than R_2 from the ensemble edge - as explained in the text. The number of flux line pairs separated by R_3 that are further than R_3 from the edge - and hence mimic correlations in an infinite ensemble - is very large.

size of 80000 flux lines, the RMC/SA algorithm is only expected to give credible results for pair separations larger than roughly 80 a_0. This is a bit unfortunate, as the rocking curve analysis 9.3.2 suggests effects at these exact separations. But since the computation time scales with N^2 it was difficult to redo the simulations in the limited time available, once this was realized. In the next sections, the results of the RMC/SA simulations are presented. It will be evident that the displacement correlator starts to drop for pair separations larger than roughly 80 a_0 - which is unphysical.

9.3.5 Results of the simulations

In this section, the results of the simulated annealing runs performed on the rocking curves - with interpolated points as described previously - will be presented. The simulations have been done enforcing neither planarity constraint nor minimum approach distance, in order to put as few constraint as possible on the algorithm. Similar results as those presented here were obtained enforcing these constraints. The calculated structure factors and rocking curves will be presented with the actual data, and an analysis of the correlation functions is given. Fitting the correlation function has to be done using several regimes, and in order to do that some rather circumstantial

functions need to be used.

As described in section 8.4.4, the displacement correlator has three regimes: The Larkin regime ($B(x) \sim x$), the random manifold regime ($B(x) \sim x^{1/3}$) and the asymptotic regime ($B(x) \sim log(x)$). If one assumes the crossover between two regimes to occur over just a few lattice spacings, one needs functions going from 0 to 1 and vice versa in just a few lattice spacings in order to describe said crossover in a reasonable way. The function $f(x) = 1/2 \pm 1/2 \cdot \tanh(x - x_0)$ does exactly that, as described in [86]. An appropriate function for describing all three regimes is the following function which is denoted as a $B(x)$ three piece function:

$$\begin{aligned} B(x) &= p_1 + (p_2 x) \cdot x_-^1(x) + \left(p_3 x^\beta\right) \cdot x_+^1(x) x_-^2(x) + (p_4 \log(x) + p_5) \cdot x_+^2(x), \\ \text{where } x_\pm^1(x) &= \frac{1}{2} \pm \frac{1}{2} \cdot \tanh(x - x_{rm}) \quad \text{and} \\ x_\pm^2(x) &= \frac{1}{2} \pm \frac{1}{2} \cdot \tanh(x - x_{asymp}). \end{aligned} \tag{9.16}$$

The background parameter in the function above is unphysical since $B(0) = 0$. The three-piece function is to be viewed as an attempt to fit three regimes to the data. It should be noted that when the RMC calculates the structure factor, it normalizes the intensities. Therefore, it is the shape of the correlators that are fitted to the data and not the absolute size of the displacements. In this fit, the parameters x_{rm} and x_{asymp} are interesting. However, the displacement correlator might not be able to be obviously divided into three regimes. Therefore, it might be interesting to collect the Larkin and random manifold regime into one power law with variable exponent for comparison, denoted as a two piece function in this work:

$$B(x) = p_1 + \left(p_2 x^\beta\right) \cdot x_-^2(x) + (p_3 \log(x) + p_4) \cdot x_+^2(x), \tag{9.17}$$

with $x_+^2(x)$ and $x_-^2(x)$ defined as in equation 9.16. It is very important to analyze the decay of the translational correlator with distance. For that purpose, the translational correlator can be fitted to the following three- and two-piece functions which are direct consequences of equations 9.16

$$C_g(x) = p_1 \exp(-x) \cdot x_-^1(x) + p_2 \exp\left(-\frac{x^{2\zeta}}{\xi_c}\right) \cdot x_+^1(x) x_-^2(x) + p_3 \left(x^{-\eta}\right) \cdot x_+^2(x) \tag{9.18}$$

$$C_g(x) = p_1 \exp\left(-\frac{x^{2\zeta}}{\xi_c}\right) \cdot x_-^2(x) + p_2 \left(x^{-\eta}\right) \cdot x_+^2(x), \tag{9.19}$$

also with $x_+^2(x)$ and $x_-^2(x)$ defined as in equation 9.16. These are the functions used to evaluate the correlation functions that are the main output of the SA algorithm.

Rocking curve at 130 mT

Using the recorded SANS data at 130 mT (both spots) including interpolated points, the simulated annealing algorithm converged nicely. The calculated structure factor, rocking curve and the actual data are shown in figure 91 along with the evolution of χ^2 and the fitted correlation functions.

As can be seen in figure 91, the rocking curve is fitted very well and the structure factor is monotonic on each side of the peak and shows no rapid variations. The χ^2 starts out at a very high value where it stays up until each flux line has been moved roughly 200 times, after which it starts to drop rapidly. After roughly 600 moves χ^2 starts to be stable after which it decreases in jumps when the acceptance probability is lowered. The displacement correlator (see figure 91 bottom left) has been fitted to both a two-piece and a three-piece function, and there is not much difference; they both show a very good agreement with a logarithmic rise of the displacement correlator at large distances and reproduce the short distance behavior rather well. However, when looking at the

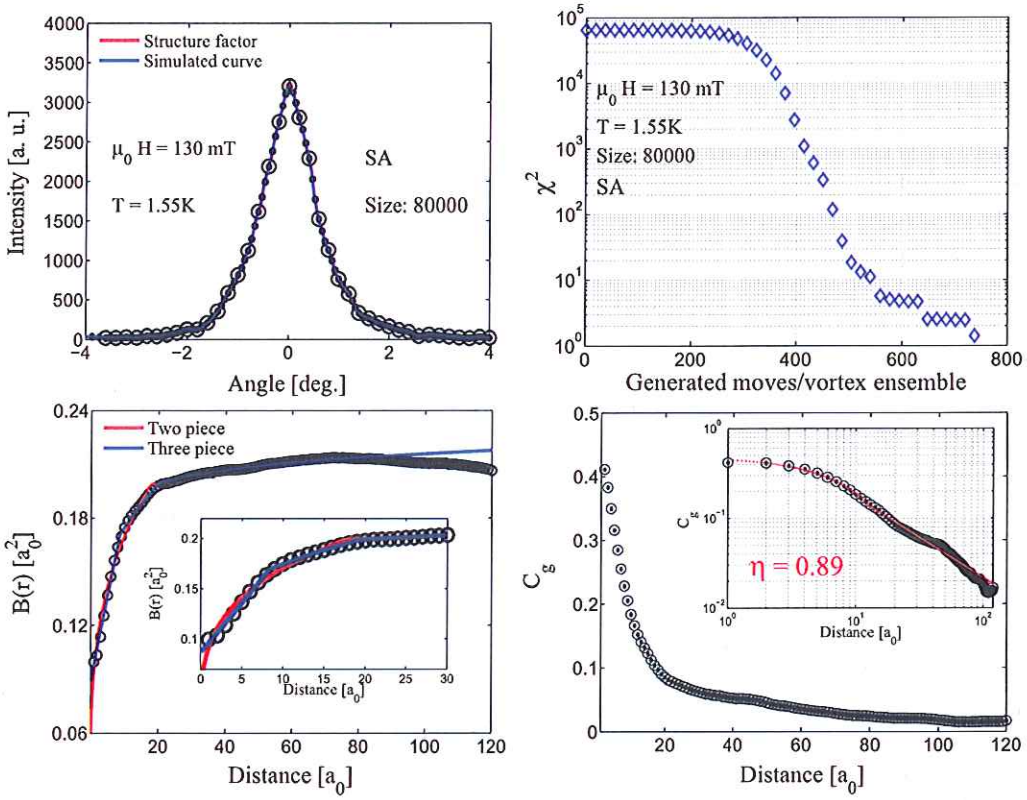

Figure 91: *Top left:* The fitted structure factor (red line), the calculated rocking curve (blue line), the actual data (hollow circles) and the interpolated data points (black dots). The ensemble size is 80000 flux lines. As evident, the rocking curve is fitted as well as reasonably expected. *Top right:* The evolution of χ^2 as function of number of moves pr. flux line. After 200 moves with high acceptance probability, the fit starts to converge rapidly. After 500 moves pr. flux line, the χ^2 is simply determined by the acceptance probability - or the temperature. *Bottom Left:* The displacement correlator $B(r)$ as a function of distance between flux lines in units of a_0. The points have been fitted to both a two piece (red) and a three piece (blue) function. The two are almost identical, but zooming in on short distances two kinks are slightly evident. The logarithmic rise at large distances is clearly evident though. At distances larger than $80a_0$, the displacement correlator starts to drop. *Bottom right:* The translational correlator $C_g(r)$, fitted only to a two-piece function (inset). A power law at large distances is clearly evident with a fitted exponent of $\eta = 0.9$.

inset of the figure, two very slight kinks are evident at $r = 8a_0$ and $r = 18a_0$ both fitted very well by the three-piece function. It looks like there are separable linear and power law regimes at short distances. The cross-over lengths and the fitted power law exponent are

$$x_{rm} \approx 8a_0 \quad x_{asymp} \approx 18a_0 \quad \beta \approx 0.37. \tag{9.20}$$

The value of β is very close to the predicted value of 0.33 as stated in equation 8.106. However, other values of β can easily fit the correlation functions rather well with only minor changes in regime boundaries x_{rm} and x_{asymp}. The power law exponent of the two-piece fit is $\beta = 0.27$, which is also rather close to the random manifold prediction.

The lower right part of figure 91 shows the translational correlator on both linear and double logarithmic scale. As is somewhat suggested by the almost equivalency of the two-piece and three-piece fits to the displacement correlator, only two regimes are directly evident on this plot. Therefore, the two-piece fitting function for the translational correlator has been used. At distances larger

than roughly $10a_0$, the drop off of the translational correlator exhibits a power law behavior up to a distance $100a_0$ as evident on the double logarithmic inset. The fitted exponent is:

$$\eta_{130} \approx 0.9 \tag{9.21}$$

Which is at least 10 % less than any of the predicted falloff exponents between 1 and 1.18 from section 8.4.4, but definitely in the same ball-park.

Field	Rocking angle span [deg.]	Angular Step [deg.]	Number of curves recorded	Monitor	File-numbers
180 mT	[3.0:5.0]	0.25	2	2500	2718-2735
180 mT	[5.25:8.75]	0.1	1	2500	2736-2771
180 mT	[9.0:12.0]	0.25	2	2500	2772-2797
180 mT	[5.25:8.25]	0.1	2	2500	3223-3284

Table 20: List of scans performed at 180 mT in the 2008 SANS-II experiment.

Rocking curve at 180 mT

During the course of the 2008 experiment, an attempt was made to get as many RMC-worthy rocking curves as possible at different fields. During this process the rocking curves were recorded several times with low statistics to be added together later on in order to get a rocking curve with high statistics. Furthermore, the goal was both to measure the rather long tail with good enough statistics to properly measure the background and at the same time measure the peak with small enough steps to have a hope of resolving the effects near the peak center. Therefore, several scans were made with large angular steps in the tail and small steps near the peak center. In the case of the 180 mT curve, a total of 8 scans comprises the final curve. The nature of these scans are listed in table 20.

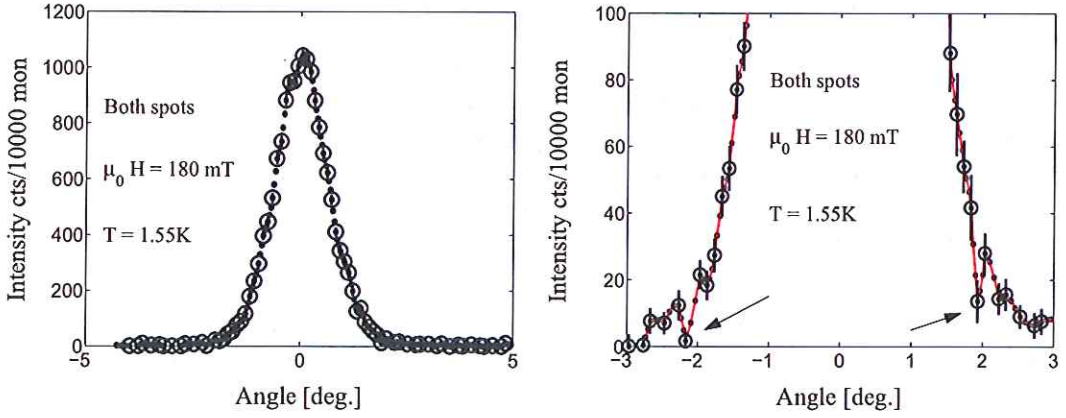

Figure 92: *Left:* The full rocking curve as obtained from the scans (circle) including the interpolated points (dots). *Right:* Zooming in on the tails, the two deviating points with low statistics are clearly evident.

If one looks closely at table 20, it can be seen that a clear error has been done in the choice of scans. The interval [5.25 : 8.25] has been measured with 7500 monitor ($3 \cdot 2500$), while the interval [8.25 : 8.75] has only been measured with 2500 monitor. In addition, the interval [5.0 : 5.25] has not been measured at all. This would be fine if these intervals were far out in the tails, but they

are exactly where the intensity starts to rise. Figure 92 shows the rocking curve with interpolated points both at full scale and zoomed in on the tail. The count rate just where the intensity starts to rise is as low as 5 counts pr. 2500 monitor, which is too low a count rate for the count to be considered equal to the high statistics counts. This switch of statistics facilitated two points with very low counts in the middle of the tails as evident in figure 92 (right). These two low points will have significant consequences for the SA output, as they are at the same angular distance from the peak center. The algorithm can and will fit to *any* point regardless of the error, due to the vast number of free parameters. Thus, there would be a substantial reduction in the translational correlator at specific distances, changing the fitted exponent. Since there is a clear reason for these low counts, and since they are so clearly deviating from the rest of the curve, they have been removed. The SA output for the unaltered rocking curve can be found in appendix B. The SA output after the removal of these low statistics points is shown in figure 93.

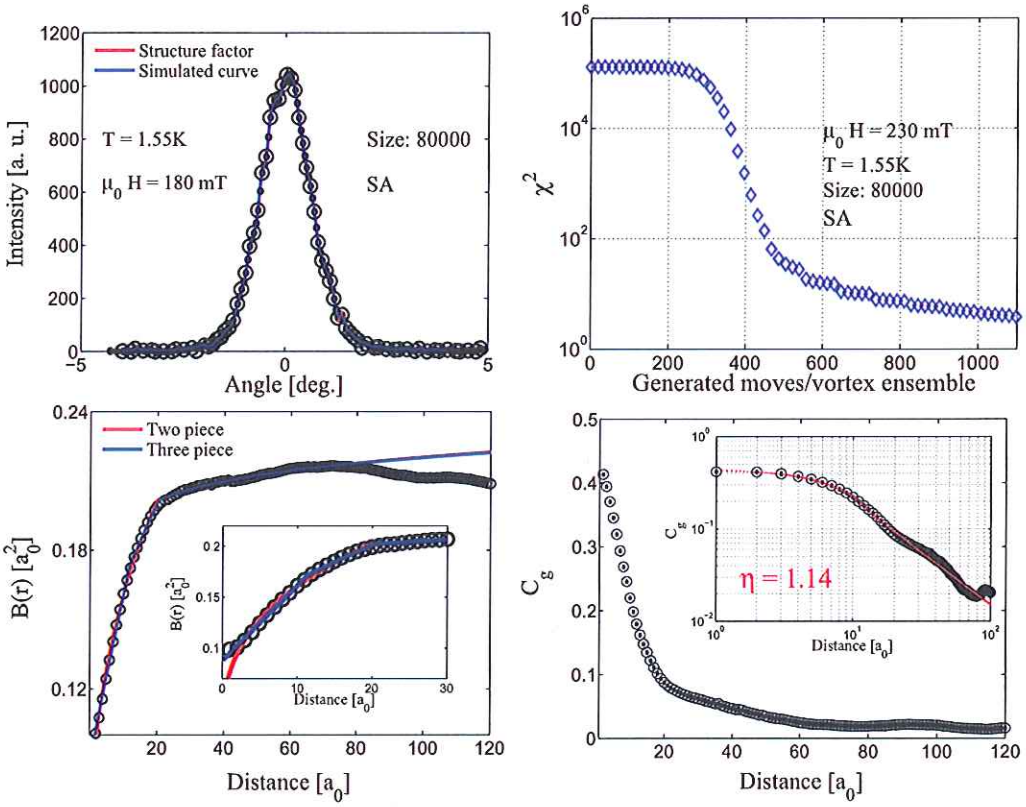

Figure 93: *Top left:* The fitted structure factor (red line), the calculated rocking curve (blue line), the actual data (hollow circles) and the interpolated data points (black dots). *Top right:* The evolution of χ^2 as function of number of moves pr. flux line. Convergence is reached after roughly 800 moves pr. flux line. *Bottom Left:* The displacement correlator $B(r)$ as function of distance between flux lines in units of a_0. The points have been fitted to both a two piece (red) and a three piece (blue) function. Again, a logarithmic rise up to $80a_0$ is evident. *Bottom right:* The translational correlator $C_g(r)$, fitted only to a two-piece function (inset). A power law at large distances is clearly evident with a fitted exponent of $\eta = 1.14$. The translational correlator exhibits a bump at roughly $90a_0$. The ensemble size is 80000 flux lines.

As in the case at 130 mT the fit converges nicely. The χ^2 starts to converge after roughly 200 moves, and goes from roughly 160000 to 5 after 1000 moves pr flux line. The displacement correlator $B(r)$ shows the same features as at 130 mT including a gradual decrease at distances large than $80a_0$. It has been fitted to both a two- and three-piece function again with almost complete similarity.

The three piece function gives the following parameters:

$$x_{rm} \approx 11 \quad x_{asymp} \approx 20 \quad \beta \approx 0.54, \tag{9.22}$$

while the two piece function gives $x_{asymp} \approx 19$ and $\beta \approx 0.33$. There is quite a difference in the RM exponent of the two fits, where the exponent of the second fit matches perfectly the predicted value of 0.33. The translational correlator has a clear power law falloff for distances between $10a_0$ and $80a_0$. At roughly $90a_0$ there is a bump (on a logarithmic scale), but this is after the displacement correlator has started to drop. The translational correlator has been fitted to a two-piece function for distances between $a_0 - 80a_0$ as in all cases and the exponent is

$$\eta_{180} \approx 1.14, \tag{9.23}$$

which is on the lower edge of Borgner, Emig and Nattermans prediction taking the anisotropic elasticity into account, the *non-universal exponents* obtained from renormalization group theory.

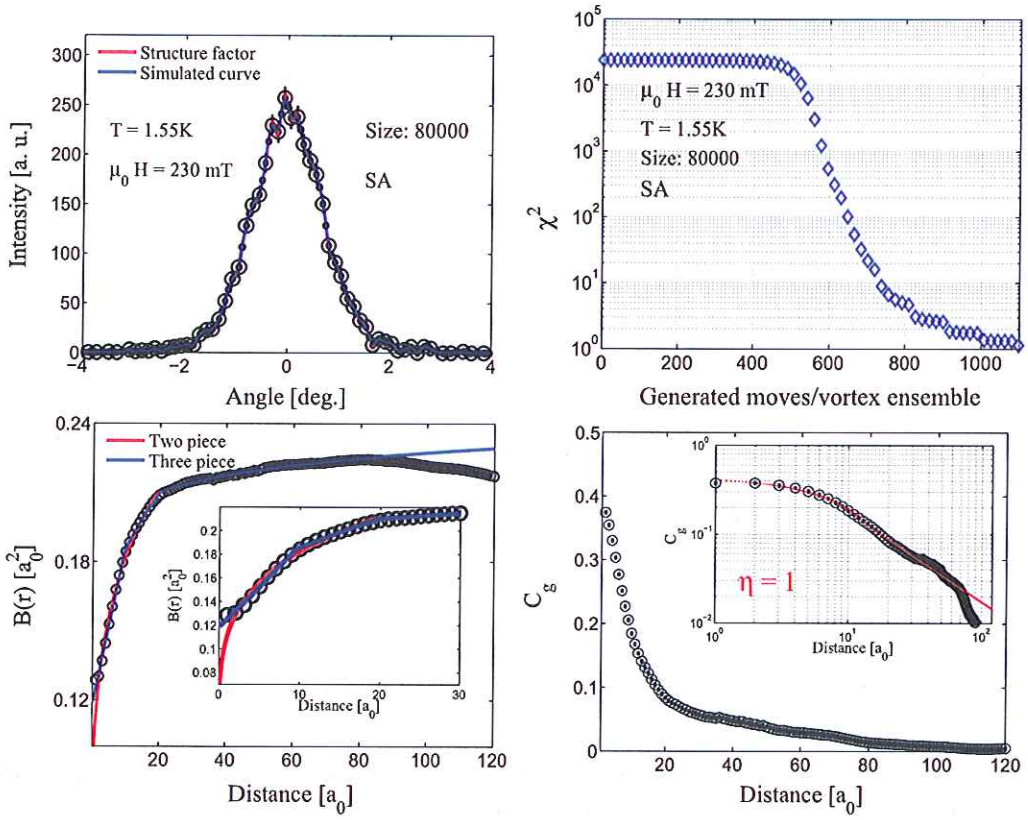

Figure 94: *Top left:* The fitted structure factor (red line), the calculated rocking curve (blue line), the actual data (hollow circles) and the interpolated data points (black dots) at 230 mT. *Top right:* The evolution of χ^2 as function of number of moves pr. flux line. After 400 moves with high acceptance probability, the fit starts to converge rapidly. *Bottom Left:* The displacement correlator $B(r)$ as a function of distance between flux lines in units of a_0. The points have been fitted to both a two piece (red) and a three piece (blue) function, which are almost identical. The logarithmic rise at large distances is clearly evident though until it starts to drop at $80a_0$. *Bottom right:* The translational correlator $C_g(r)$, fitted only to a two-piece function (inset), with an exponent of $\eta = 1$. The translational correlator exhibits a rapid drop at only $65a_0$.

Rocking curve at 230 mT

Using the rocking curve for both spots obtained at 230 mT including interpolated points, the SA algorithm was able to converge nicely - starting out with a χ^2 increasing move acceptance probability of 99 % and ending at roughly 40 %. The simulated structure factor and rocking curve are presented along with the χ^2 evolution and the correlation functions in figure 94.

The fit is very acceptable as in the previous cases, and the χ^2 evolution resembles those for 130 and 180 mT, respectively. The displacement correlator shows the exact same dependency on distance as in the case of 130 mT. The displacements start to drop around $80a_0$ as in the other two cases. The displacement correlator has been fitted to both a two-piece and a three-piece function. The three-piece function yields the following parameters:

$$x_{rm} \approx 9 \quad x_{asymp} \approx 20 \quad \beta \approx 0.44, \tag{9.24}$$

while the two piece function yields $x_{asymp} \approx 19$ and $\beta \approx 0.22$. So once again, the two functions agree on the crossover distance to the asymptotic regime (which is also clearly evident by eye), but disagree on the random manifold exponent. They are both still somewhat close to the predicted value.

The translational correlator drops off as a power law between $10a_0$ and $65a_0$ after which is drops rapidly. This could be due to an onset of fracture size effects or an increase of dislocation density introducing a fast drop off of the translational correlator at large distances. It could also just be a consequence of variations near the peak center due to counting statistics. It is peculiar, however, that the existence of this drop-off below $80a_0$ fits the picture given in equations 9.15. The translational correlator has been fitted to a two-piece function between a_0 and $80a_0$ yielding an exponent

$$\eta_{230} \approx 1.02, \tag{9.25}$$

which is also close to the predicted values. There is some degree of uncertainty on this number which is difficult to evaluate. But since the power law is quite clear and without too many variation, the exponent of around 1 seems reasonable. This exponent is in the middle between the exponents at 130 and 180 mT, which is also suggested by the fitted exponent of the rocking curve power laws.

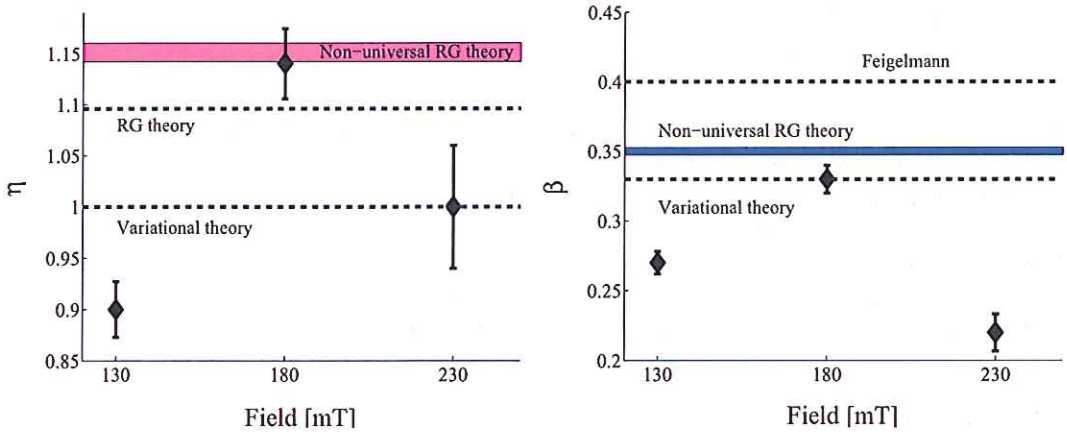

Figure 95: *Left:* Fitted power law exponents η for $C_g(r)$. The values suggested in literature - explained in the text - are shown as well. *Right:* Fitted RM exponents β compared to values suggested in literature.

Comparison of exponents

Since three regimes cannot be distinguished on the plots of the translational correlator and since the two- and three-piece fits of the displacement correlator are very similar - the two piece function being the simplest - the two piece function has been chosen as the basis for comparing random manifold exponents, β. The Bragg glass power law decay of the translational correlator leaves little doubt about the fitted exponent η. There are, of course, errors in the determination of exponents but they are difficult to evaluate properly. However, for the power law exponent an obvious candidate for an error is the same fractional error of the determined exponent as in figure 86. These are the errors used both for the RM exponent determined from $B(r)$ and the power law C_g exponents. Figure 95 shows these determined exponents from the SA simulated compared to suggested exponents in the literature.

The basic origins of the suggested exponents are briefly evaluated below:

- **Feigel'man et al.** Modified the LO collective pinning theory, recognizing the existence of metastable states and predicted a power law increase of the displacement correlator for all distances with an exponent of 0.4 [78]. The power law prediction can be directly compared to the short distance behavior of the displacement correlator as outputted from the SA algorithm. The predicted exponent seems to be too large.

- **Giamarchi and Doussal used variational theory** as an initial way of making predictions about the nature of the correlations in the Bragg glass phase. They found an exponent of $\beta = 1/3$ and $\eta = 1$ for the short distance power law increase of the displacement correlator and the long distance power law decay of the translational correlator [74]. The 180 mT simulation gives exactly $\beta = 0.33$ and the 230 mT simulation gives $\eta = 1$

- **Giamarchi and Doussal also used renormalization group theory** to make predictions about the nature of the correlations in the Bragg glass phase. They found an exponent of $\eta = 1.097$ for the long distance power law decay of the translational correlator, which is close to both the 180 mT and the 230 mT result.

- **Bogner, Emig and Natterman (BEN) found non-universal** exponents both for the case of the RM exponent β and the Bragg glass exponent η [79]. The exponent intervals are $\beta \in [0.3474 : 0.3526]$ and $\eta \in [1.144 : 1.16]$. The 180 mT simulation curve has a power law decay of the translational correlator that is just what BEN predicted. Actually, BEN predicted a field dependence of the exponent but given the limited range of their prediction, this would be unfeasible to test.

The 130 mT simulation shows an translational correlator decay with an exponent of $\eta = 0.9$, which is below the predicted values. However, if all the exponents are to be taken at face value, there is a rather large angular interval of which the power law decay of the translational correlator lies within predicted values. The random manifold exponents are below the predicted values except at 180 mT where the exponent is just what was predicted using variational theory. In spite of this, since the long range behavior is so close to what was predicted using quite general models, the ordered VL phase between 130 mT and 230 mT can be called a Bragg glass phase in the author's opinion.

9.3.6 The SANS-II experiment in December 2010

The second experiment on Vanadium was performed in December 2010. The purpose of the experiment was to get more rocking curves with better statistics at high fields. In this experiment the resolution was chosen to be a little more relaxed than in 2008; the attenuation slit was set to a diameter of 16 mm resulting in a resolution angle of $\delta\beta = 0.158°$. This experiment experienced

severe problems with controlling the temperature. Since at the time of the experiment, the 11 T SANS-magnet to which the custom sample stick was designed had a leak; the exchange gas pressure could not exceed a certain limit which was naturally set rather low. Due to this leak, it was not possible to increase the exchange gas pressure in order to maintain a stable temperature of 1.6 K. The minimum temperature reached was 2.6 K; this was simply due to the thermal contact between the top of the sample stick (and the electrical stepper motor) and the sample itself which was facilitated by the rod supposed to turn the cogwheels on the sample holder. In addition, the brass parts of the sample holder were worn down to some extent - there were scratches which prevented the cogwheels from turning smoothly. Therefore, the order of business of the experiment naturally changed to examining the field dependence of the integrated intensity at temperatures higher than the base temperature, namely 2.67 K and 3 K. Even though this agenda was not intended at all, it should provide a basis for a phase diagram of the vortex lattice in the vanadium sample in this work.

9.3.7 Field dependence of the rocking curve intensities at higher temperatures

The lowest temperature in the sample space reachable was a floating variable throughout the experiment, since a lot of work was done to remedy and optimize the situation (such as changing exchange gas pressure, adjusting the PID settings and even removing the sample and try to improve the thermal isolation). The temperatures at which the rocking curve intensities have been measured are therefore rather arbitrary; they reflect the minimum temperature reachable at that particular point in time where the data were recorded. At the beginning of the experiment, the minimum temperature was 2.55 K.

Over a little less than a day, a collection of rocking curves was measured using the tilt of the sample table and *not* the rotatable sample stick for fields between 50 and 210 mT. The cooling was always done in field just as in the 2008 experiment. Due to the poor coupling between the exchange and the sample, the sample temperature drifted from 2.55 to 3.0 K during the tilt. This is around 10 percent of the temperature span of the entire $(\mu_0 H, T)$ phase diagram which is completely unacceptable. However, the entire rocking curve is not necessarily needed for a credible determination of the integrated intensity. The rocking curves were reduced in the following way: An average temperature was calculated from the first three points of the scan. Any point where the measuring temperature exceeds 0.2 K above that mean is discarded. The temperature variation in the peak is thus around 3 % which is much better. The reduced rocking curves and the corresponding Gaussian fits are shown in figure 96. Only the rocking curves obtained for fields above 80 mT are shown. The rocking curves between 50 mT and 80 mT had an increased width and were discarded using the same arguments as in the 1.55 K case.

As evident in figure 96, the Gaussian fits to the reduced data are reasonable. They all have comparable widths, and the amplitude is well determined. At 2.7 K the penetration depth and coherence length are different from those at 1.55 K (see table 19), resulting in a steeper field dependency of the form factor. In order to correct the measured intensities for the geometrical factor and the form factor, the exact same method is used as in the 1.55 K case. The result is shown and fitted to various power laws in figure 97. As in the 1.55 K case the error of the fitted exponent does not reflect the real error. So just as previously, the determined exponent is decided to be the average exponent of 9 fits - one with all data points and 8 fits each with a different point removed from the set - with the uncertainty given as $\sigma/3$, where σ is the standard deviation of the set of exponents. Using this method, the determined exponent is

$$I_{T=2.66K} \propto H^{\beta}, \quad \text{where} \quad \beta = -1.7 \pm 0.065. \tag{9.26}$$

Again, the error of this estimate is to be regarded as an absolute minimum. This value is quite close to -3/2; it cannot be said to be significantly less than -3/2 in any case. This determined exponent is

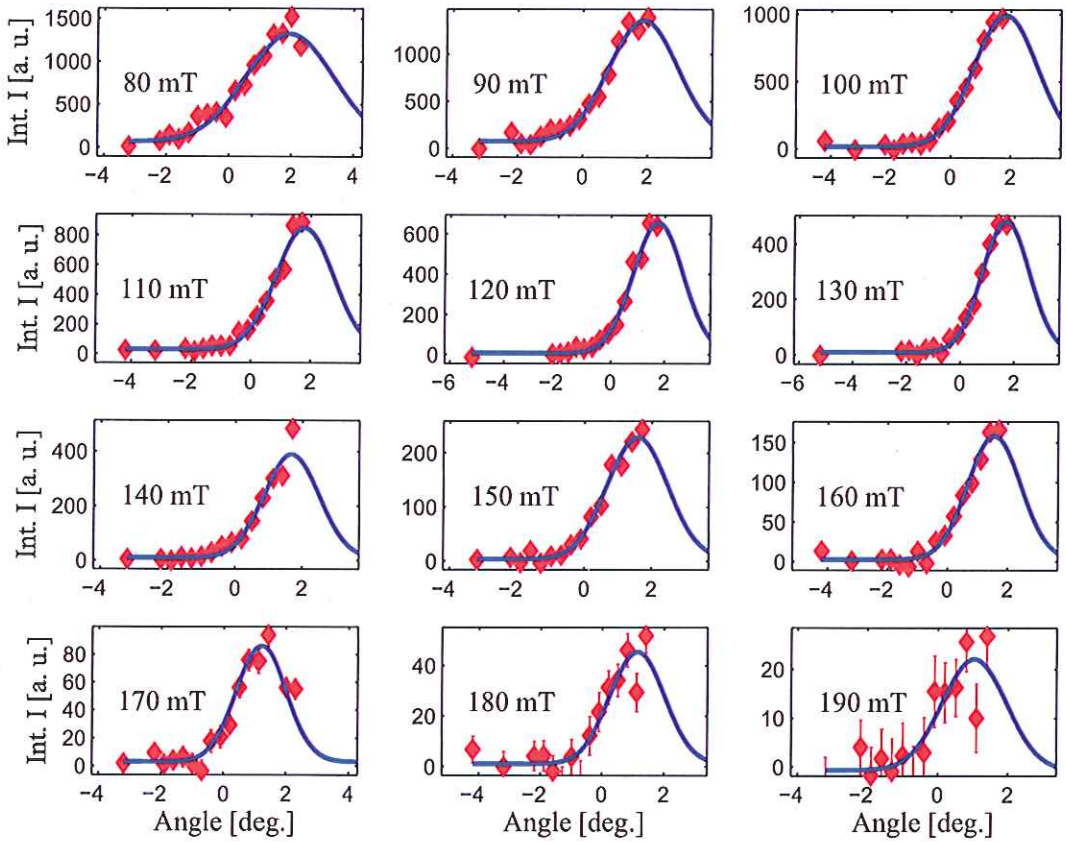

Figure 96: Rocking curves obtained at an average of 2.66 K using the reduction scheme described in the text. No intensity was found above 190 mT. An accurate determination of the peak width and amplitude is possible; the blue lines represent the Gaussian fits which converged nicely. The counts have been normalized to 2500 monitor

not to be regarded as a proof of the Bragg glass theory - as argued previously. However, the decay of order with field is again consistent with Bragg glass theory. Thus, one can cautiously say that this decay of order is as predicted in *a finite area of the phase diagram.* One could assume that this is the area of the phase diagram where correlation functions like the ones determined by the RMC in the previous section hold - to some extent at least. Thus, a Bragg glass-like phase has been determined at low temperatures which decays into a phase without static order upon increasing the field.

As the experiment progressed, the minimum reachable temperature continued to climb. Due to this fact, another set of intensities was measured as a function of field at 3 K. The rocking curves obtained at various fields are shown in figure 98. The magnetic form factor was calculated using suitable parameters from table 19, and the intensities were corrected for both the form factor and the geometrical factor. The results are shown in figure 99 fitted to various gaussians. The exponent is much higher than those obtained at 1.55 K and 2.66 K, respectively. The data points are far more irregular though. Employing the same point removal scheme as described in the previous cases, the average exponent is -1.96 with a standard deviation of 1.3. Therefore, this data set is too incoherent to produce a credible exponent (this can be due to the lack of counting statistics). For the sake of completeness the exponent is

$$I_{T=3.0K} \propto H^{\beta}, \quad \text{where} \quad \beta = -1.96 \pm 0.43. \tag{9.27}$$

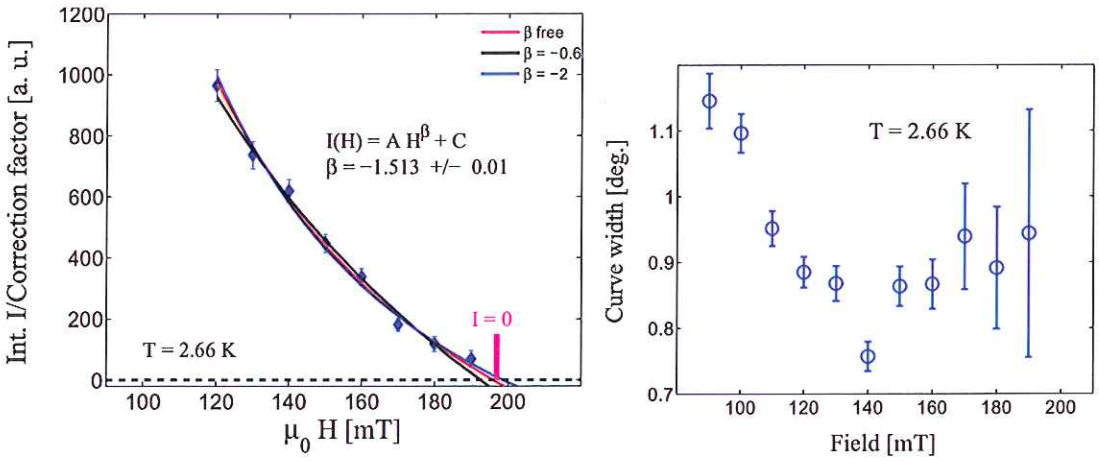

Figure 97: *Left:* Corrected integrated intensity as a function of field fitted to a power law - $I(H) = AH^{\beta} + C$ - with *variable background* at 2.66 K. The exponent determined by the fit is -1.5. *Right:* The rocking curve widths as determined by Gaussian fits.

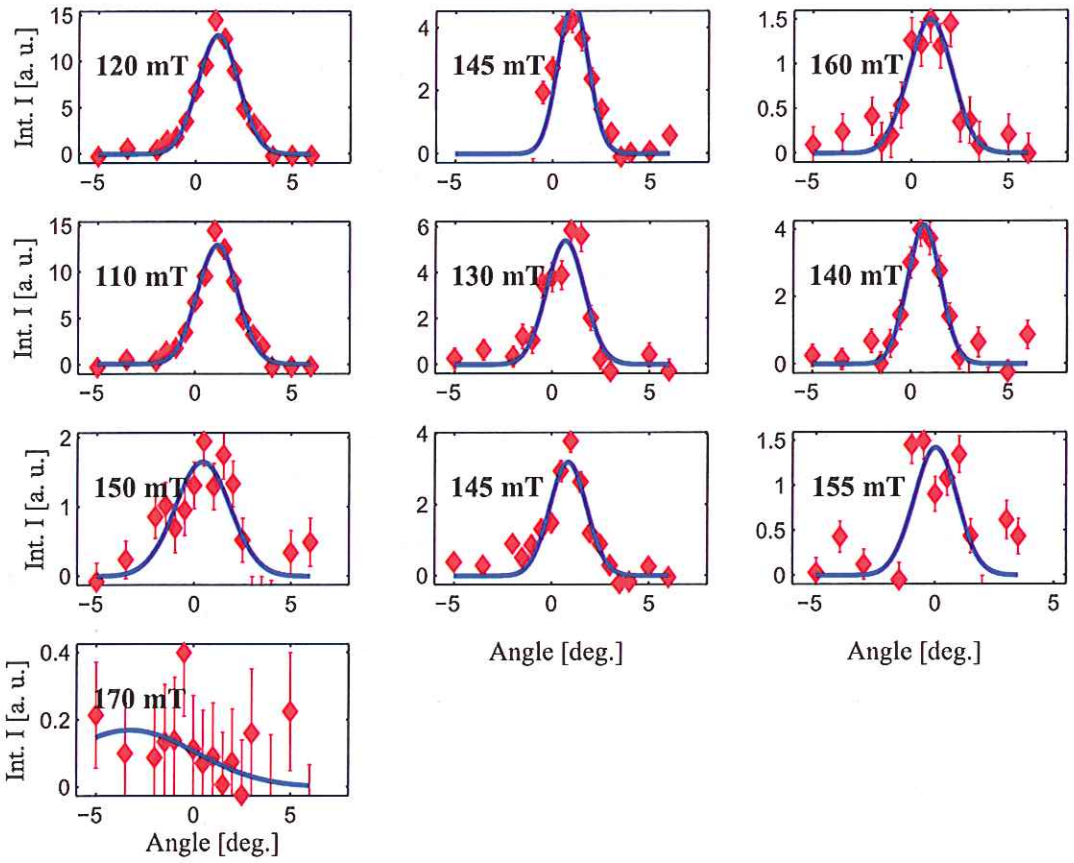

Figure 98: Rocking curves obtained at an average of 3.0 K. No intensity was found at 170 mT. The blue lines represent the Gaussian fits.

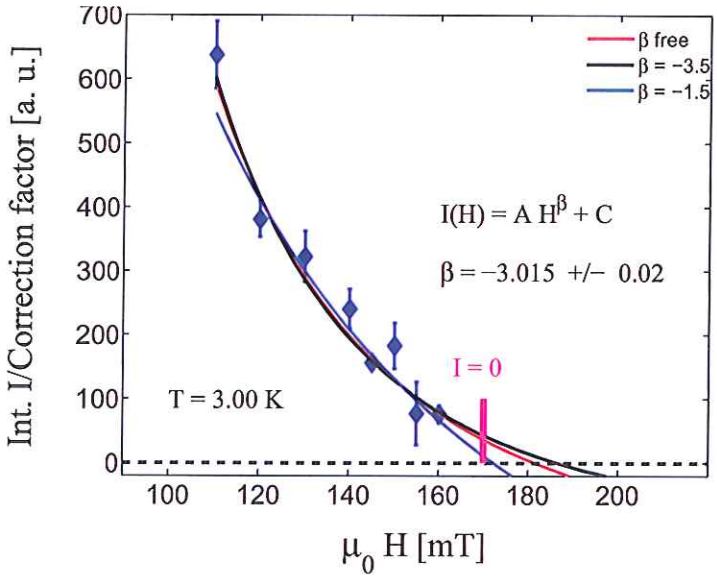

Figure 99: Corrected integrated intensity as a function of field fitted to a powerlaw - $I(H) = AH^{\beta} + C$ - with *variable background* at 3.0 K. The exponent determined by the fit is -2.6. These data are more irregular than at 1.55 and 2.66 K, and removing just a single point has a large impact on the exponent.

It should be mentioned that no intensity was observed at 170 mT at 3 K where $H_{c2} = 250$ from magnetization measurements. Therefore, the fitted exponent of -2.5 can be said to be an absolute minimum. The trend of the exponent as a function of temperature can be said to be slightly decreasing if one ignores the errors. However, within errors, the exponent might as well be constant. A significantly increasing exponent is improbable though. Since the determination of the drop-off exponents is doubtful, the most important result at these two temperatures is the determination of the critical field where long range order becomes unmeasurable.

9.3.8 The high statistics rocking curve at high field and high temperature

At the end of the 2010 experiment the sample stick was removed, the brass cogwheels were polished and the rotatable sample holder was working again. Upon re-inserting the sample stick and adjusting the PID settings for the cryomagnet the minimum reachable temperature was 2.66 K. At this temperature - with the retrieved 4π rotation option - an attempt was made to record a RMC curve just below the critical field above which there is no observable order. This should be in a region where the rocking curve width has increased considerably, but where the scattering intensity is still high enough for reasonable statistics. Two days were used to record the rocking curve, as background measurements were necessary to achieve good statistics. The two rocking curves obtained and the calculated average are shown in figure 100.

Figure 100 shows some irregularities in the rocking curves especially in the top spot data. Since the background was irregular at the peak angles, this could be a probable cause. However, since there is no particular reason for discarding these irregular points, these will be kept for fitting. The combined rocking curve looks acceptable, though not as nice as the ones obtained at 1.55 K. The peak center is very interesting in this curve, since it can not be well fitted by neither a Voigt nor a Gaussian. Only the function described earlier - a powerlaw with a low angle cutoff convoluted with a Gaussian of variable width - fits the peak center well. The fits and the χ^2's are shown directly in figure 100 (bottom left). Fitting the rocking curve to this power law with a cutoff (keeping the

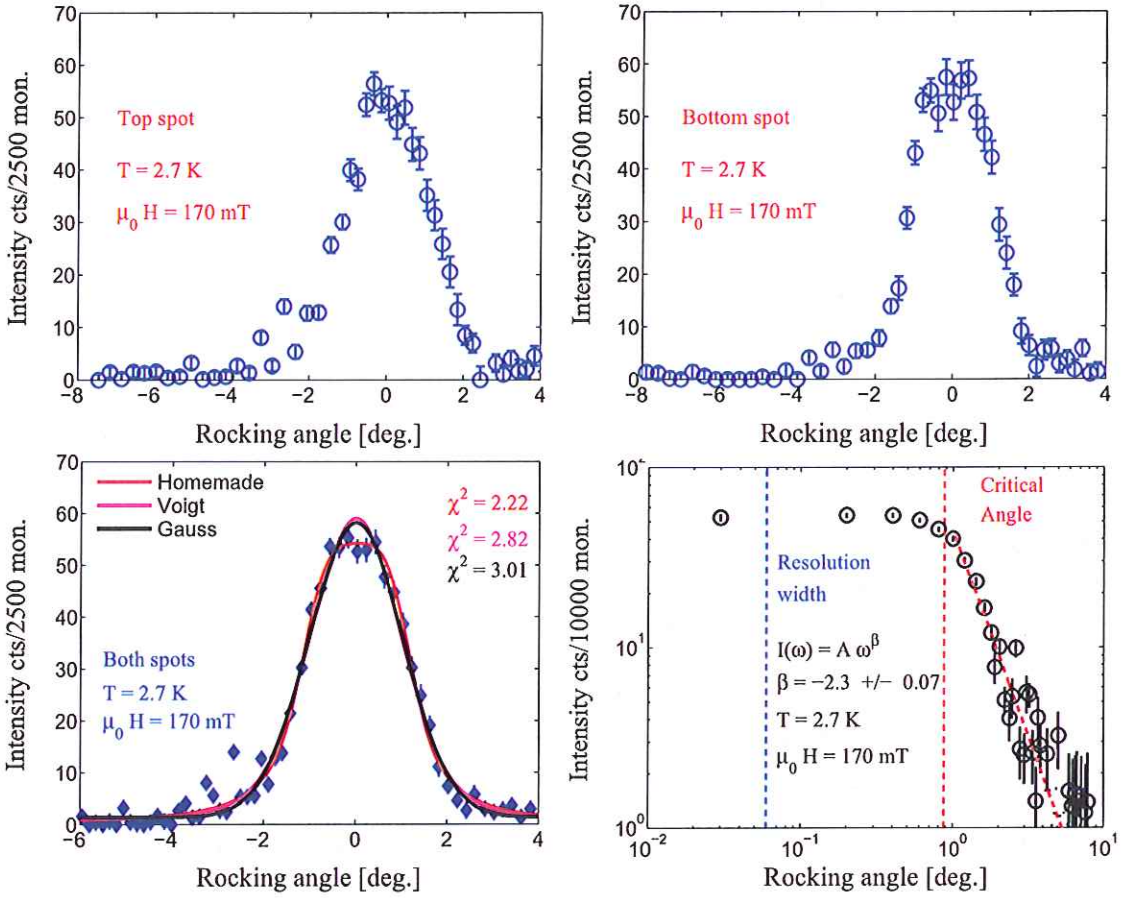

Figure 100: *Top:* The rocking curves of the top and bottom spot respectively as recorded at 2.7 K and 170 mT after background subtraction. Some counts ended up being less than zero after background subtraction; those have been manually set to be zero. *Bottom left:* The rocking curve obtained after combining the rocking curves from the top and bottom spot. The rocking curve has been fitted to a Voigt, a Gaussian and to the function described in section 9.3.2, denoted as homemade. It is clear that all function fit the tail of the rocking curve equally well, but that both the Gaussian and the voigt fail to fit the peak center. However, the homemade powerlaw with a cutoff fits this peak center nicely. *Bottom right:* Intensity as a function of absolute angle, fitted in the same way as previously described. As in all rocking curve the critical angle exceeds the resolution. However, the critical angle is much larger than the ones determined at 1.55 K.

power law exponent fixed as described earlier) yields a cutoff angle considerably higher than those found at 1.55 K - namely $\omega_c = 0.9°$ with a smoothing width $\sigma_g = 0.32$. The determined values of ℓ_c and ℓ_{min} are

$$\begin{aligned} \ell_c^{3K-170} &\approx 65\, a_0 \\ \ell_{\min}^{3K-170} &\approx 48\, a_0 \end{aligned} \tag{9.28}$$

Thus, the power law dependency of the translational correlator should cease to hold at roughly $50a_0$. Perhaps the cause for the increase in rocking curve width at high fields is that the fracture size starts to decrease (or the dislocation density starts to rise), decreasing what could be called *a maximum Bragg glass correlation distance.* If this is true, the fracture size would continue to decrease with field causing the maximum correlation length to decrease up to the point where it becomes comparable to the random manifold cross-over length, after which static long range order

ceases to exist and the system is well into the fractured vortex glass state (or just the vortex glass if dislocations are the cause of the plateau). With regard to RMC simulations, since the data in the tail is quite irregular in this rocking curve, emphasis was laid on the low temperature rocking curves. In the following section the VSM magnetization data performed on the sample is presented.

9.3.9 VSM magnetization measurements

To determine the field dependency of the critical current, VSM magnetization measurements were performed at the CFMS magnetization system at Risø. The field was applied along the crystallographic (111) axis just as in the neutron experiments. The main goal of these measurements was to determine H_{c1} and H_{c2} as a function of temperature using *bulk* measurements. Thus, the bulk properties - or phase diagram - serve as a nice framework in which the neutron data can be interpreted. There was also a hope that some sign was to be seen of the transition between the Bragg glass phase and the phase without static order - in this work called vortex glass.

As mentioned previously in this work, the amount of flux line pinning in a type-II superconductor directly influences the critical current. The easiest way of estimating the critical current is actually via the magnetization curve. Using the so-called Bean model - which is explained in [59] - it can be shown that the critical current J_c is actually proportional to the difference in magnetization ΔM in a hysteresis loop

$$J_c(H) \propto \Delta M(H) \tag{9.29}$$

So when performing magnetization measurements on a bulk 0.2 cm^3 superconducting sample, the signal is quite large, and even small changes in the critical current should be resolvable, which would ultimately give an idea of the amount of flux line pinning as a function of field. This is assuming that the demagnetization factor does not cause an inhomogeneous field throughout the bulk sample cause any sharp effects to be smeared out. The sample was placed in the cryostat and the field increased to the maximum chosen value which is well above H_{c2}. The hystersis loop is then the magnetization curve upon slowly reversing the field from this maximum to the same value in the opposite direction and back again. The raw data are shown in figure 101.

As evident on all the hysteresis curves, the critical current is almost constant at small fields. This makes perfect sense since the Meissner-phase is defined by its perfect diamagnetic response - $M = 0$ at low fields. This changes when entering the vortex lattice phase (at around 90 mT at 1.6 K) where the gap between the two curves closes in rapidly as a function of field. Figure 102 (top left) show the obtained critical current as a function of field at 1.6 K (obtained merely by dividing the hystersis curve into suitable bins and taking the difference in magnetization between decreasing and increasing field), plotted on a double logarithmic scale. The onsets of static order, onset of constant width and absence of order as determined by neutron scattering at 1.55 K are marked on the plot. The critical current is plotted on a linear scale as well for the sake of completeness.

The critical current drops rapidly not at a specific field but in an entire field region around H_{c1}. This may suggest that the process of going from the Meissner state into the vortex state is a rather gradual process and perhaps occurs via an intermediate mixed state. This is also indicated by the quite wide rocking curves obtained at 80 and 115 mT at this temperature. Note that there is some degree of static order measurable with neutrons already at 80 mT which is well below the point where the rapid drop in critical current sets in at 1.6 K. This means that there is coexistence of bulk diamagnetism and statically ordered flux lines. After the rapid drop in the H_{c1} region, the critical current falls off as a power law with field up until 340 mT at 1.6 K. At this field, the critical current exhibits a very rapid drop in a finite field region to zero. When examining the hysteresis curve at these high fields, an anomaly is clearly evident (see figure 102 bottom left). It is quite clear from the hysteresis curve why the critical current drops rapidly; there is a kink in the magnetization curve for both decreasing and increasing fields after which the gap closes in very rapidly. The definite kink and the characteristic way in which the δM gap closes - the same is observed at all

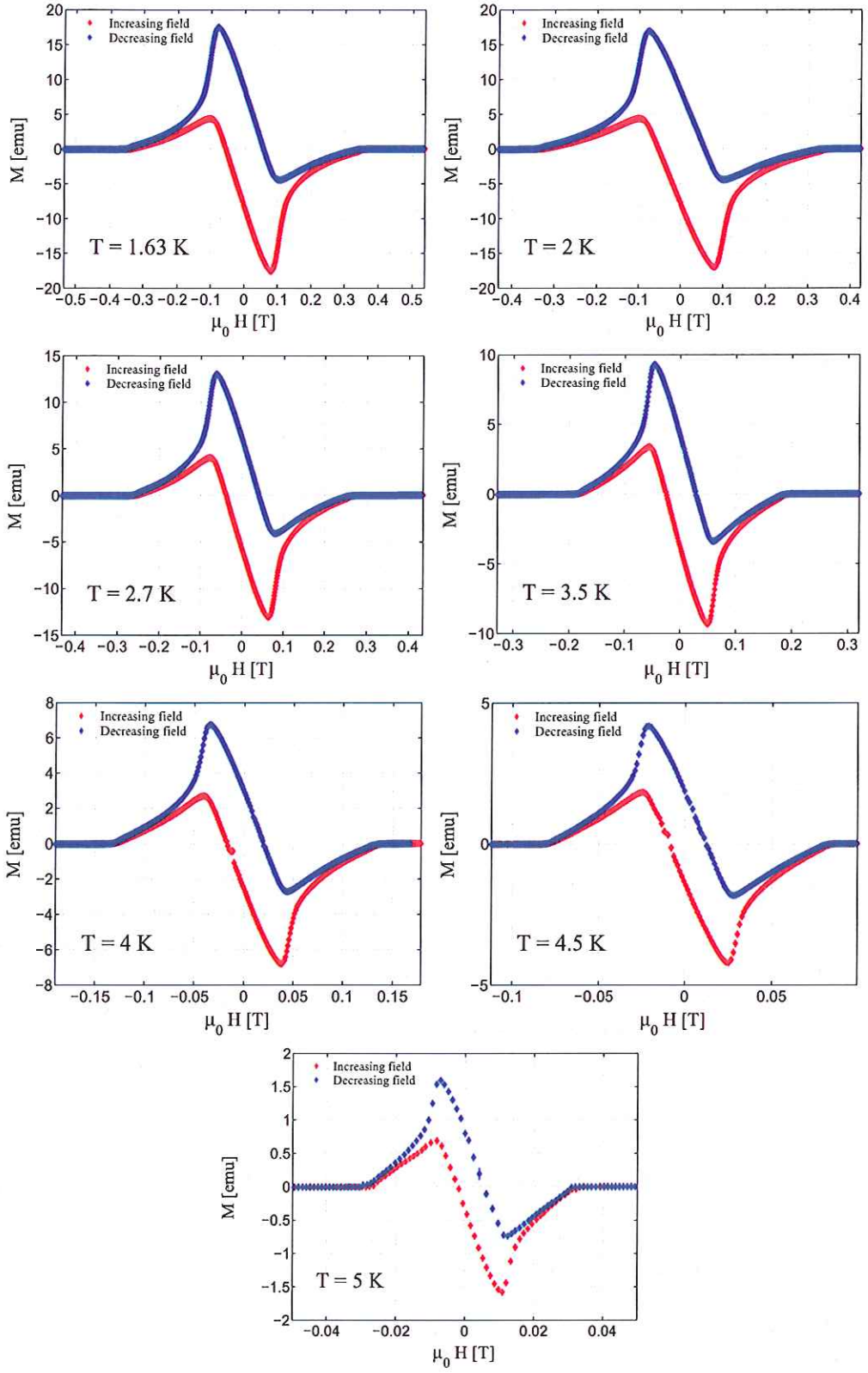

Figure 101: Raw magnetization measurements for both increasing and decreasing field applied along (111) at various temperatures. It is clear that ΔM is roughly constant at low fields, and that it starts to decrease heavily upon entering the vortex state at H_{c1}.

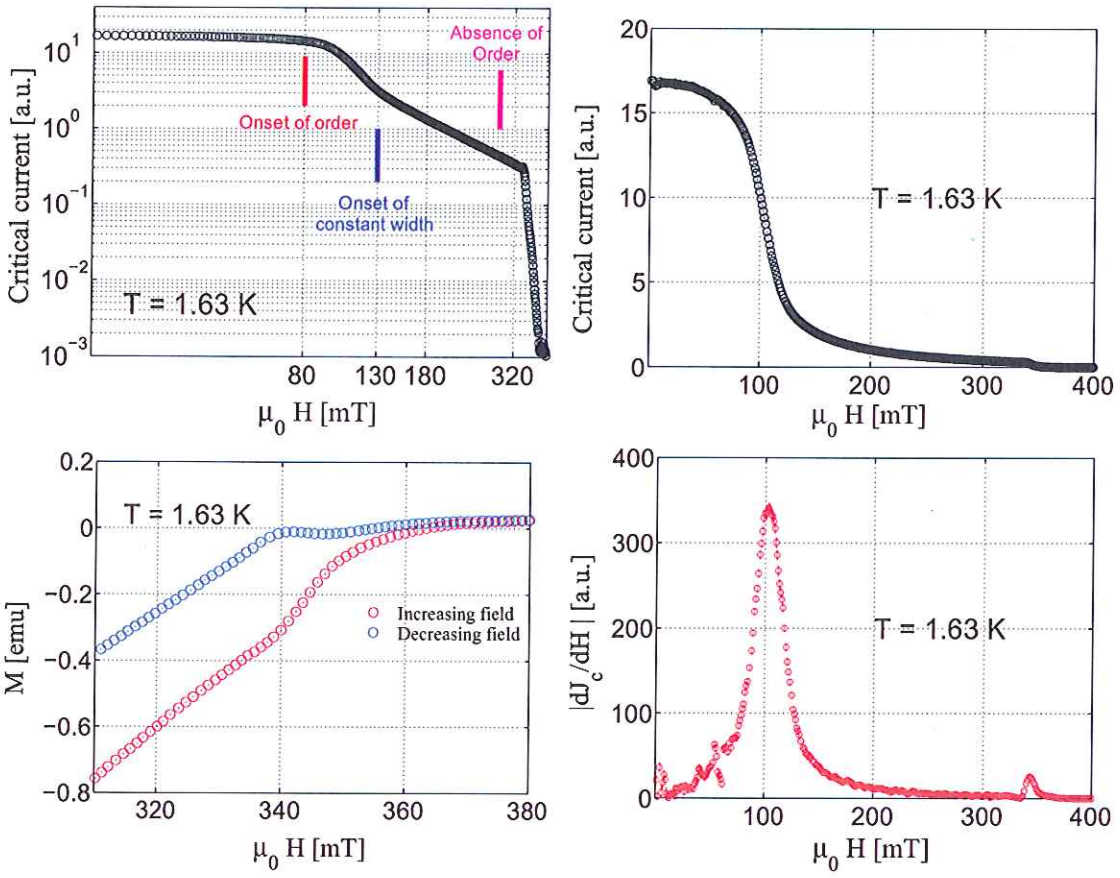

Figure 102: *Top left:* The critical current as directly extracted from ΔM on the magnetization curves, plotted with a logarithmic y-axis. At low fields the critical current drops heavily over a substantial field range, after which it drops off exponentially. At roughly 340 mT - which is significantly above the field where detectable order ceases to exist at 1.6 K - the critical current drops very rapidly to zero. *Top right:* The critical current plotted on a linear scale. *Bottom left:* The hystersis loop at high fields. The rapid drop in ΔM is clearly evident in the magnetization where there is an anomalous kink for both increasing and decreasing fields. Note that detectable hysteresis - and hence superconductivity - exists for fields above this anomaly *Bottom right:* The differential critical current. Two peaks are evident, one at H_{c1} and one at high fields. The transition from the Meissner phase to the vortex phase can be said to occur in a critical region rather than a specific field.

temperatures but 5 K - point to the suggestion that in the field range with a rapid drop the flux line system is in a very different phase than at lower fields. Since the critical current - and thereby the pinning - is heavily affected in this phase could be called a *de-pinned glass.* The effects of pinning at large fields are greatly diminished with the order parameter. As evident in figure 102 (top left), the disappearing of static order as observed by means of neutron scattering cannot be observed in the magnetization measurements, neither by a kink in the curve or a change of the drop off exponent. As mentioned previously, this could be due to the suggested gradual transition to high field phase without long range order. The falloff exponent of the critical current is also the same in the Bragg glass phase and the vortex glass phase. Figure 102 (bottom right) shows the differential critical current as a function of field, supposed to form a basis for determination of phase boundaries. In this work H_{c1} is defined as the maximum slope of the critical current. The phase boundary into the 'de-pinned glass' phase H_{cl} is defined as the onset of the high field rapid

drop and H_{c2} is defined as the point where the critical current reaches zero. This concludes the description of the magnetization measurements performed in this work.

9.3.10 Interpretation of the flux line phase diagram

The phase diagram as determined from VSM measurements is shown in figure 103 along with the suggested boundaries of the Bragg glass phase.

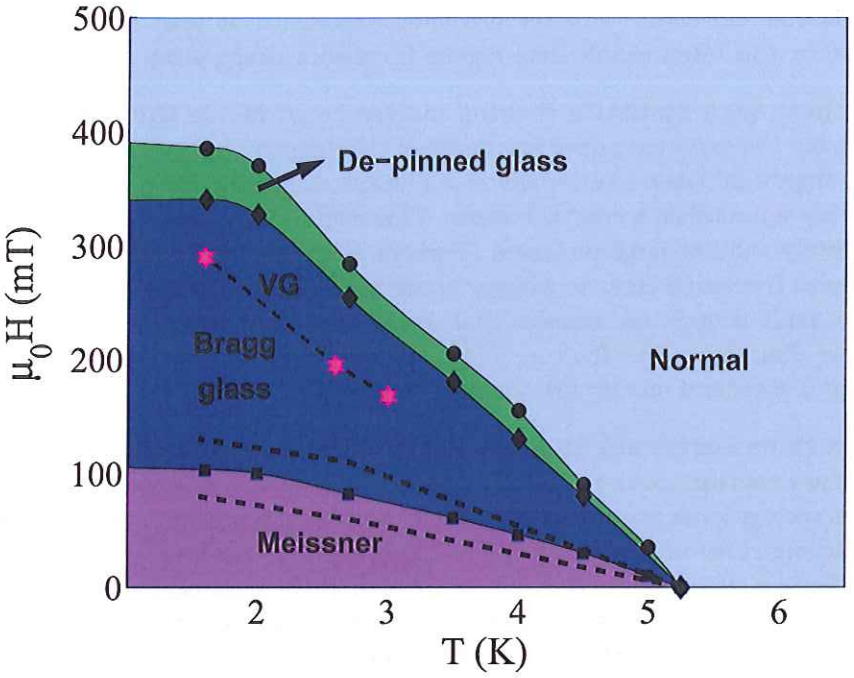

Figure 103: The phase diagram of the Vanadium sample used in this work determined using magnetization and neutron measurements. The black circles represent H_{c2} - the point of zero critical current as determined from VSM measurements. The black diamonds represent the onset of the rapid drop in the critical current - the anomalous kink in the VSM measurements. The pink stars are the points where the neutrons scattering intensity drops to zero and long range order ceases to exist. Above these fields, the phase is called a vortex glass (VG). The black squares represent H_{c1} - the peak in differential critical current - while the stapled black lines denote the possible boundaries for an intermediate mixed state as suggested by the low fields neutron rocking curve widths.

A summary of the suggested phases and their justification in experiment is given below:

- **The phase transition between the Meissner phase and the Abrikosov vortex phase** is found to occur gradually in a field region. At both 1.55 K and 2.66 K, wide rocking curves were recorded at low fields where the sample is still largely diamagnetic. A cautious suggestion might be that in the field interval where the rocking curve width drops to a stable value there is a coexistence of Meissner phase and long range ordered Abrikosov phase, the so-called *intermediate mixed state*. It is also important to underline the fact that in the neutron scattering experiment, the sample was *field cooled* to the temperature at which the rocking curve was recorded. When looking at the phase diagram in figure 103, it is evident that upon cooling to 1.5 K at 80 mT, the sample is cooled into the Meissner state from at mixed phase. Upon cooling into the Meissner phase, the sample should expel the flux lines, but this is only

in the absence of pinning. One could image that pinning forces hold the flux line in place even when cooling to 1.5 K, and perhaps this the cause of the wide rocking curves at low fields. That being said, the tails of these rocking curves still strongly suggest a finite size broadening.

- **Long range flux line order** occurs in a finite intermediate field area at low temperatures. The sum of two point pair correlations is found to drop off as a power law with roughly the predicted exponent used Bragg glass theory in this area. At 1.55 K SA simulations were performed in the field range 130-230 mT all with a long distance power law decay of the translational correlator with the predicted exponents, at least in the interval 180-230 mT. Therefore, this intermediate field regime is called a Bragg glass.

- **The three high statistics rocking curves recorded in the field range 130-230 mT** all display the expected power law decay of the intensity in the tail. However, at angles much larger than what the resolution function dictates away from the peak center, the rocking curve smoothly approaches a constant value. This could mean that the Bragg glass picture is not completely valid at large distances. Perhaps there are large domains or *fractures* which are decoupled from each other to a larger extent than within the fractures themselves, facilitating a more rapid drop in the translational correlator at pair separation distances larger than the fracture diameter. This fracture effect has also been seen in Niobium [86], so perhaps this picture is a general one for low κ superconductors.

- **The rocking curves are found to increase in width just before the neutron scattering cross section goes to zero**, suggesting a change in the nature of the pair correlations. This is very gradual and not al all evident in the magnetization measurements. A high statistics rocking curve at 170 mT at 2.7 K which just below the zero intensity field. This rocking curve had an almost flat and very wide plateau at the peak center. Perhaps the rocking curve width increases because the domain sizes get smaller and more decoupled, as the system enters the vortex state where long range order ceases to exist.

- **The kink in the magnetization measurements** - facilitating a very rapid drop in the critical current suggests that the nature of the vortex lattice has changed and the average flux line pinning is drastically reduced. This rapid decrease of average pinning very close to H_{c2} - is called a *de-pinned glass.*

10 Concluding remarks

This concludes the work done during the project. This section will shortly summarize the results obtained in both parts of the thesis.

10.1 Magnetic structures of the lithium orthophosphates

The work done on the lithium-ortho-phosphates can be summed up as follows:

- **The incommensurate magnetic structure of $LiNiPO_4$ in strong applied magnetic fields** has been shown to consist of three distinct phases for $13.5 < \mu_0 H < 17.3$ T, all propagating along the crystallographic b-axis. At high temperatures close to T_N the structure is linearly polarized along c with a slight canting along a. Upon further cooling, the structure undergoes a second-order phase transition to a canted IC spiral polarized in the ac plane. At these low temperatures, increasing the field decreases the real-space modulation of the spiral until $\mu_0 H > 16$ T where the spiral conforms to a pseudo-commensurate quintupling of the unit cell. The spin-waves measured in the spiral phase has been shown to be pseudo-Goldstone-modes in near perfect agreement with the calculations done by Jens Jensen. The two IC magnetic order parameters present in the IC phase are unlikely to produce a ME-effect.

- **The structure in the spin-flopped phase of $LiMnPO_4$** has been determined. The phase diagram has been measured, focusing on the bicritical point, where the two antiferromagnetic phases join with the paramagnetic phase. A paramagnetic wedge has been found in the phase diagram which is in accordance with theoretical predictions. The critical scattering *intensity* has been found to be significantly increased at the flop field, with no significant increase in the correlation length along c. This could be caused by an increase in the volume fraction of the domains with short range order.

- **The magnetic structure in $LiCoPO_4$** has been found to be collinear in zero field and rotated away from the high symmetry b axis towards the a axis, indicating a lower structural symmetry than *Pnma*. Upon applying field along a the field induced ferromagnetic component has been found to cause a large *antiferromagnetic* component along the c direction, suggesting a very strong DM interaction. This is in accordance with the calculations of Jens Jensen, suggesting a very large orbital contribution to the pseudo-quenched ground state. If some of the symmetries are broken in zero field, this DM interaction can be shown to cause a magneto-electric effect by preferring a polarization in an applied field. An attempt to determine the phase diagram has resulted in plenty of open questions, subject to further study.

10.2 The study of the Bragg glass phase of vortex matter

The properties of the vortex lattice as found in the particular Vanadium sample used in this work, has been thoroughly examined in the course of two neutron scattering experiments and magnetization measurements. The field dependence of the structure factor as integrated over the full rocking curve was measured at three different temperatures. At low fields, the rocking curves are wide, suggesting some finite size effect - either due to the demagnetization factor or the existence of an intermediate mixed state. The field dependence of the integrated intensity roughly follows the $S(\mathrm{q}) \propto B^{-3/2}$ dependence predicted by Bragg glass theory. However, the data are quite sparse and many objections are valid upon using this as an indication of a Bragg glass. At higher fields, the rocking curves start to widen before the intensity drops to zero - or an unmeasurably low value - at some finite field well below H_{c2}.

Three rocking curves were recorded with enough statistics and in the right field range, to perform relevant Simulated Annealing (SA) simulations of the structure factor. They all show the expected power law decay of intensity at large angles from the peak center. However, they also show a crossover to a constant angular dependency near the peak center at much larger angles than what the resolution function dictates. This perhaps suggests that the power law decay of the translational correlator ceases to hold at some finite pair separation. After implementing the necessary interpolated points, the algorithm was successfully able to fit all three curves. The displacement correlator was in all three cases found to rise as a power law for low pair separations, crossing over to the predicted logarithmic increase for large separations. This logarithmic increase is a major result of Bragg glass theory, and explains the existence of quasi long range order - and hence the observed Bragg peaks - in the vortex lattice. The translational correlators - which is what is measured in these neutron scattering experiments - all show the predicted power law decays at large pair separations, with exponents $\eta_{130} \approx 0.9$, $\eta_{130} \approx 1.14$ and $\eta_{230} \approx 1$. The 130 mT exponent is lower than any predicted values, while the two other exponents are exactly as predicted, even though the two predictions are results from two different methods of calculation. Even so, the author chooses to call the low temperature intermediate field phase a Bragg glass.

VSM magnetization measurements have been performed on the same sample used in the neutron scattering experiments, in order to get a phase diagram and search for bulk signs of phase transitions. At 1.55 K, very broad Bragg peaks were observed at only 80 mT where the magnetization measurements show that the sample is mainly diamagnetic. This could be due to either the demagnetization factor or the existence of an intermediate mixed state. There was no sign of change at all near the field where the measurable static order vanishes. This suggests that in this particular Vanadium sample, the phase transition from a Bragg glass to a vortex glass is very gradual and results in no increase of critical current. At fields close to H_{c2} however, the magnetization exhibits a kink for both increasing and decreasing field, and the critical current drops rapidly to zero. In spite of the limited evidence available, a high field liquid state is cautiously suggested. This is to be taken with a grain of salt, since no direct evidence for the lack of even short range order exists.

11 References

[1] R. P. Santoro, D. J. Segal, and R. E. Newnham. Magnetic properties of $LiCoPO_4$ and $LiNiPO_4$. *J. Phys. Chem. Solids.*, 27:1192, 1966.

[2] A. Ait-Salaha, J. Doddb, A. Maugerc, R. Yazamib, F. Gendrona, , and C. M. Juliena. Structural and magnetic properties of $LiFePO_4$ and lithium extraction effects. *Z. Anorg. Allg. Chem.*, 632:1598–1605, 2006.

[3] Werner S. Weiglhofer and Akhlesh Lakhtakia. *Introduction to complex mediums for optics and electromagnetics.* SPIE - The International Society for Optical Engineering, 2003.

[4] T. B. S. Jensen, N. B. Christensen, M. Kenzelmann, H. M. Rønnow, C. Niedermayer, N. H. Andersen, K. Lefmann, J. Schefer, M. v. Zimmermann, J. Li, J. L. Zarestky, and D. Vaknin. Field-induced magnetic phases and electric polarization in $LiNiPO_4$. *Phys. Rev. B*, 79:092412, 2009.

[5] Richard L. Liboff. *Introductory quantum mechanics.* Addison-Wesley, 2003.

[6] J. J. Sakurai. *Modern Quantum Mechanics.* Addison-Wesley, 1994.

[7] B.H. Bransden and C. J. Joachain. *Physics of atoms and molecules.* Pearson Education Limited, 1983.

[8] Stephen Blundell. *Magnetism in condensed matter.* Oxford University Press, 2001.

[9] K. Yosida. *Theory of Magnetism.* Springer, 1996.

[10] P.W.Anderson. New approach to the theory of superexchange interactions. *Physics Letters*, 115:2–12, 1959.

[11] Toru Moriya. Anisotropic superexchange interaction and weak ferromagnetism. *Physical Review*, 120:91, 1960.

[12] S. Geller and J. L. Durand. Refinement of the structure of $LiMnPO_4$. *Acta Cryst.*, 13, 325, 1960.

[13] Redman M.J. Newnham R.E. Crystallographic data for $LiMnPO_4$, $LiCoPO_4$ and$LiNiPO_4$. *Journal of the American Ceramic Society*, 48, 10, 1965.

[14] R.P Santoro andNewnham R.E. Antiferromagnetism in $LiFePO_4$. *Acta Cryst.*, 22, 344, 1967.

[15] Thomas Bagger Stibius Jensen. *Magnetic structures, phase diagram and spin waves of magneto-electric LiNiPO4.* PhD thesis, RisÃ¸ National Laboratory, DTU, 2007.

[16] R. E. Newnham, R. P. Santoro, and M. J. Redman. Neutron diffraction study og $LiNiPO_4$. *J. Phys. Chem. Solids.*, 26:445, 1964.

[17] G. L. Squires. *Introduction to the theory of thermal neutron scattering.* Dover Publications, 1997.

[18] D. F Johnston. On the theory of the electron orbital contribution to the scattering of neutrons by magnetic ions in crystals. *Proceedings of the Physical Society*, 88:37, 1966.

[19] Jens Als Nielsen and Des McMorrow. *Elements of Modern X-ray Physics.* Wiley and Sons Ltd., 2001.

[20] G. Shirane, Stephen M. Shapiro, and John M. Tranquada. *Neutron scattering with a triple-axis spectrometer: basic techniques.* Cambridge University Press, 2002.

[21] Yu.A. Izyumov, V.E. Naish, and R.P. Ozerov. *Neutron diffraction of magnetic materials.* Consultants Bureau, 1991.

[22] Kim Lefmann. *Neutron Scattering: Theory, Instrumentation and Simulation.* Lecture Notes, 2007.

[23] Asger Bech Abrahamsen. *Possible magnetism in vortex cores of superconducting TmNi2B2C studied by small angle neutron scattering.* PhD thesis, RisÃ¸ National Laboratory, 2003.

[24] Edited by Albert-Jose Dianoux and Geery Lander. *Neutron Data Booklet.*

[25] T. B. S. Jensen, N. B. Christensen, M. Kenzelmann, H. M. RÃ¸nnow, C. Niedermayer, N. H. Andersen, K. Lefmann, M. Jimenez-Ruiz, F. Demmel, J. Li, J. L. Zarestky, and D. Vaknin. Anomalous spin waves and the commensurate-incommensurate magnetic phase transition in $LiNiPO_4$. *Phys. Rev. B*, 78, 184429, 2008.

[26] D. Vaknin, J. L. Zarestky, J. P. Rivera, and H. Schmid. Commensurate-incommensurate magnetic phase transition in magnetoelectric single crystal $LiNiPO_4$. *Phys. Rev. Lett.*, 92:207201, 2004.

[27] V. M. Khrustalyov, V .N. Savitsky, and N. F. Kharchenko. Multi-step-like magnetization of $LiNiPO_4$ in a pulsed magnetic field. *Czech. J. Phys.*, 54:Suppl. D, 27, 2004.

[28] Yu. N. Kharchenko, N. F. Kharcheno, M. Baran, and R. Szymczak. Weak ferromagnetism and an intermediate incommensurate antiferromagnetic phase in $LiNiPO_4$. *Low Temp. Phys.*, 24:579, 2003.

[29] Jens Jensen and Allan R. Mackintosh. *Rare Earth Magnetism: Structures and Excitations.* Clarendon Press, Oxford, 1991.

[30] I. Kornev, M. Bichurin, J.-P. Rivera, S. Gentil, H. Schmid, A. G. M. Jansen, and P. Wyder. Magnetoelectric properties of $LiCoPO_4$ and $LiNiPO_4$. *Physical Review B*, 62:12247, 2000.

[31] G. Lawes, A. B. Harris, T. Kimura, N. Rogado, R. J. Cava, A. Aharony, O. Entin-Wohlman, T. Yildirim, M. Kenzelmann, C. Broholm, and A. P. Ramirez. Magnetically driven ferroelectric order in $Ni_3V_2O_8$. *Physical Review Letters*, 95:087205, 2005.

[32] M. Kenzelmann, A. B. Harris, S. Jonas, C. Broholm, J. Schefer, S. B. Kim, C. L. Zhang, S.-W. Cheong, O. P. Vajk, and J.W. Lynn. Magnetic inversion symmetry breaking and ferroelectricity in $TbMnO_3$. *Physical Review Letters*, 95:087206, 2005.

[33] Jiying Li, Wei Tian, Ying Chen, Jerel L. Zarestky, Jeffrey W. Lynn, and David Vaknin. Antiferromagnetism in the magnetoelectric effect single crystal $LiMnPO_4$. *Phys. Rev. B*, 79,144410, 2009.

[34] J. H. Ranicar and P. R. Elliston. Spin-flopping in $LiMnPO_4$ and Cr_2BeO_4. *Physics Letters*, 25A:720, 1967.

[35] H. Rohrer and H. Thomas. Phase transitions in the uniaxial antiferromagnet. *J. Appl. Phys*, 40:1025, 1969.

[36] Keith W. Blazey, Heinrich Rohrer, and Ronald Webster. Magnetocaloric effects and the angular variation of the magnetic phase diagram of antiferromagnetic $GdAlO_3$. *Phys. Rev. B*, 4:2287, 1971.

[37] J. A. J. Basten, E. Frikke, and W. J. M. de Jonge. Neutron-scattering studies of bicritical behaviour in $CsMnBr_3 \cdot 2D_2O$. *Phys. Rev. B*, 22:1429, 1980.

[38] Michael E. Fisher. Scaling axes and the spin-flop bicritical phase boundaries. *Phys. Rev. Lett.*, 34:1634, 1975.

[39] Michael E. Fisher and David R. Nelson. Spin flop, supersolids, and bicritical and tetracritical points. *Phys. Rev. Lett.*, 32:1350, 1974.

[40] David R. Nelson, J. M. Kosterlitz, and Michael E. Fisher. Renormalization-group analysis of bicritical and tetracritical points. *Phys. Rev. Lett.*, 33:813, 1974.

[41] H. Rohrer. Properties of $GdAl0_3$ near the spin-flop bicritical point. *Phys. Rev. Lett.*, 34:1638, 1975.

[42] Jr. N.F. Oliveira, A. Paduan Filho, and S. R. Salinas. Magnetic phase boundaries of $NiCl_2 \cdot 6$ H_2O near the biciritcal point. *Physics Letters*, 55A:293, 1975.

[43] J. M. Kosterlitz and D. J. Thouless. Ordering, metastability and phase transitions in two-dimensional systems. *J. Phys. C: Solid State Phys.*, 6:1973.

[44] Michel Mercier. *Etude de l'effect magnetoelectrique sur des composes de type olivine, perovskite et granat.* PhD thesis, L'Univesite de Grenoble, 1969.

[45] Wei Tian, Jiying Li, Jeffrey W. Lynn, Jerel L. Zarestky, and David Vaknin. Spin dynamics in the magnetoelectric effect compound $LiCoPO_4$. *Phys. Rev. B*, 78, 184429, 2008.

[46] D. Vaknin, J. L. Zarestky, L. L. Miller, J.-P. Rivera, and H. Schmid. Weakly coupled antiferromagnetic planes in single-crystal $LiCoPO_4$. *Phys. Rev. B*, 65, 224414, 2002.

[47] Yu. Kharchenko, N. Kharchenko, M. Baran, and R. Szymczak. Weak ferromagnetism in $LiCoPO_4$ and $LiNiPO_4$. *arXiv: cond-mat/0310156.*

[48] H. Wiegelmann. *Magnetoelectric Effects in Strong Magnetic Fields.* PhD thesis, University of Konstanz, 1995.

[49] N. F. Kharchenko, V. M. Khrustalev, and V. N. Savitski. Magnetic field induced spin reorientation in the strongly anisotropic antiferromagnetic crystal $LiCoPO_4$. *Low Temperature Physics*, 36:558, 2010.

[50] A. Szewczyk, M. U. Gutowska, J. Wieckowski, A. Wisniewski, R. Puzniak, R. Diduszko, Yu. Kharchenko, M. F. Kharchenko, and H. Schmid. Phase transitions in single-crystalline magnetoelectric $LiCoPO_4$. *Physical Review B*, 84(104419), 2011.

[51] J. File and R. G. Mills. Observation of persistent current in a superconducting solenoid. *Physical Review Letters*, 10, 3:93–96, 1963.

[52] H. K. Onnes. The resistance of pure mercury at helium temperatures. *Commun. Phys. Lab. Univ. Leiden.*, 12, 120, 1911.

[53] Norman E. Phillips. Heat capacity of aluminum between 0.1 k and 4.0 k. *Physical Review*, 114:676–685, 1959.

[54] Neil W. Ashcroft and N. David Mermin. *Solid State Physics.* Brooks/Cole, 1976.

[55] W. Meissner and R. Ochsenfeld. Ein neuer effekt bei eintritt der supraleitfahigkeit. *Naturwiss.*, 21 (44):787â788, 1933.

[56] L. N. Cooper J. Bardeen and J. R Schrieffer. Theory of superconductivity. *Physical Review*, 108, 5:1175–1204, 1957.

[57] Michael E. Peskin and Daniel V. Schroeder. *An introduction to Quantum Field Theory.* Addison-Wesley Advanced Book Programme, 1995.

[58] Charles Kittel. *Introduction to solid state physics.* Wiley and Sons, Inc., 1996.

[59] Kristian Fossheim and Asle Sudbø. *Superconductivity: Physics and Applications.* John Wiley and Sons Inc., 2004.

[60] V. L. Ginzburg and L. D. Landau. *Zh. Eksperim. i. Teor. Fiz.*, 20:1064, 1950.

[61] L. P Gor'kov. *Zh. Eksperim. i. Teor. Fiz.*, 36:1918, 1959.

[62] Michael Tinkham. *Introduction to superconductivity.* McGraw Hill Inc., 1996.

[63] P. G. de Gennes. *Superconductivity of metals and alloys.* Perseus Books Publishing,, 1966.

[64] W. H. Kleiner, L. M. Roth, and S. H. Autler. *Phys. Rev.*, 133:A1226, 1964.

[65] Dingping Li and Baruch Rosenstein. Lowest landau level approximation in strongly type-ii superconductors. *Physical Review B*, 60:9704, 1999.

[66] Ernst Helmut Brandt and Mukunda P. Das. Attractive vortex interaction and the intermediate-mixed state of superconductors. *ArXiv.org*, arXiv:1007.1107v1, 2010.

[67] U. Essman. Intermediate state of superconducting niobium. *Physics Letters*, 41A/5:477, 1972.

[68] A. I. Larkin and Yu. N. Ovchinnikov. Pinning in type ii superconductors. *J. Low. Temp. Phys*, 34:409, 1979.

[69] Yoseph Imry and Shang-Keng Ma. Random-field instability of the ordered state of continuous symmetry. *Phys. Rev. Lett.*, 35:1399, 1975.

[70] A. I. Larkin. *Zh. Eksp. Teor. Fiz.*, 58, 1970.

[71] A. I. Larkin and Yu. N. Ovchinnikov. *Zh. Eksp. Teor. Fiz.*, 65:1704, 1973.

[72] Marc Mezard and Giorgio Parisi. Replica field theory for random manifolds. *Journal de Physique I*, 1:809–836, 1991.

[73] Thierry Giamarchi and Pierre Le Doussal. Elastic theory of pinned flux lattices. *Physical Review Letters*, 72:1530, 1994.

[74] Thierry Giamarchi and Pierre Le Doussal. Elastic theory of flux lattices in the presence of weak disorder. *Physical Review B*, 52:1242, 1995.

[75] Thomas Natterman. Scaling approach to pinning: Charge-density waves and giant flux creep in superconductors. *Physical Review Letters*, 64:2454, 1990.

[76] Jean-Phillipe Bouchaud, Marc Mezard, and Jonathan S. Yedidia. Variational theory for disordered vortex lattices. *Physical Review Letters*, 67:3840, 1991.

[77] Jean-Phillipe Bouchaud, Marc Mezard, and Jonathan S. Yedidia. Variational theory for the pinning of vortex lattices by impurities. *Physical Review B*, 46:14686, 1992.

[78] M. V. Feigelâman, V. B. Geshkenbein, A. I. Larkin, and V. M. Vinokur. Theory of collective flux creep. *Physical Review Letters*, 63:2303–2306, 1989.

[79] Simon Bogner, Thorsten Emig, and Thomas Natterman. Non-universal correlations and crossover effects in the bragg-glass phase of impure superconductors. *Physical Review B*, 63, 2001.

[80] D. G. Grier, C. A. Murray, C. A. Bolle, P. L. Gammel, D. J. Bishop, D. B. Mitzi, and A. Kapitulnik. Translational and bond-orientational order in the vortex lattice of the high T_c superconductor $Bi_{2.1}Sr_{1.0}Ca_{0.9}Cu_2O_{8+d}$. *Physical Review Letters*, 66, 1991.

[81] Zhen Yao Philip Kim, Cristian A. Bolle, and Charles M. Lieber. Structure of flux line lattices with weak disorder at large length scales. *Phys. Rev. B*, 6(18):R12589, 1999.

[82] T. Giarmarchi and P. Le Doussal. Phase diagrams of flux lattice with disorder. *Physical Review B*, 55, 1997.

[83] T. Klein, I. Joumard, S. Blanchard, J. Marcus, R. Cubitt, T. Giamarchi, and P. Le Doussal. A bragg glass phase in the vortex lattice of a type ii superconductor. *Letters To Nature*, 413:404, 2001.

[84] Jan Kierfeld and Valerii Vinokur. Dislocations and the critical endpoint of the melting line of vortex line lattices. *Physical Review B*, 61, 2000.

[85] Guatam I. Menon. Phase behavior of type-ii superconductors with quenched point pinning disorder: A phenomenological proposal. *Physical Review B*, 65, 2002.

[86] M. Laver, E. M. Forgan, A. B. Abrahamsen, C. Bowell, Th. Geue, and R. Cubitt. Uncovering flux line correlations in superconductors by reverse monte carlo refinement of neutron scattering data. *Physical Review Letters*, 100:107001, 2008.

[87] Jan Skov Pedersen, Dorthe Posselt, and Keld Mortensen. Analytical treatment of the resolution function for small-angle scattering. *J. Appl. Cryst.*, 23:321–333, 1990.

[88] E. Seidl E. Moser and H. W. Weber. Superconductive properties of vanadium and their impurity dependence. *J. of Low Temp. Phys.*, 49:585, 1982s.

[89] J. R. Waldram. *Superconductivity of Metals and Cuprates.* Imstitute of Physics Publishing Bristol and Philadelphia, 1996.

[90] John R. Clem. Simple model for the vortex core in a type-ii superconductor. *Journal of low temperature physics*, 18, 1975.

[91] R. I. McGreevy. Reverse monte carlo modelling. *J. Phys. Condens. Matter*, 13:R877, 2001.

[92] S. Kirkpatrick, C. D. Gelatt, and M. P. Vecchi. Optimization by simulated annealing. *Science, New Series*, 220:671, 1983.

12 List of publications - Rasmus Toft-Petersen

- R. Toft-Petersen, J. Jensen, T. B. S. Jensen, N. H. Andersen, N. B. Christensen, C. Niedermayer, M. Kenzelmann, M. Skoulatos, M. Duc Le, K. Lefmann, S. R. Hansen, J. Li, J. L. Zarestky and D. Vaknin *High-field magnetic phase transitions and spin excitations in magnetoelectric $LiNiPO_4$* PRB, 84, 054408 (2011) [10 pages].

- S. E. Dutton, M. Kumar, M Mourigal, J. Wen, N. H. Andersen, R. Toft-Petersen, Q. Huang, Z. G. Soos, C. L. Broholm and R. J. Cava *Field driven quantum critical transition in $LiCuSbO_4$, an S=1/2 1D frustrated chain magnet*, submitted to PRL.

- R. Toft-Petersen, N. H. Andersen, T. B. S. Jensen, C. Niedermayer, M. Laver, O. Zaharko, N. Aliouane, J. Li, J. L. Zarestky and D. Vaknin *Field induced spin canting in magnetoelectric $LiCoPO_4$ (tentative)*, in preparation

- R. Toft-Petersen, N. H. Andersen, Haifeng Li, T. B. S. Jensen, C. Niedermayer, M, Laver, O. Zaharko, J. Li, J. L. Zarestky and D. Vaknin *Continuous spin flop transition and bicriticality in magnetoelectric $LiMnPO_4$ (tentative)*, in preparation

- R. Toft-Petersen, M. Laver, A. B. Abrahamsen, S. Balog, E. M. Forgan *Flux line correlations in superconducting Vanadium investigated by simulated annealing refinement of neutron scattering data (tentative)*, in preparation

A Selected MATLAB-scripts

A.1 Rocking curve convoluted fitting function

The following is the 'homemade' function used to fit the RMC rocking curves. It does a numerical convolution between the function 'powercut' and a standard gaussian.

```
function [y, name, pnames, pin]=realpowergauss(x,p,flag)
% glconv    : Numerical convolution of a gaussian and a simple powerlaw with a variable
% exponent. Includes a cutoff to account for finite size effects
% function [y, name, pnames, pin]=glconv(x,p)
%
% p = [  Amplitude Centre q_0 Sigma_g exp bg]

% Author:  Rasmus Toft-Petersen


if nargin==2;
xint = (max(x)-min(x))/2;
xcen = min(x) + xint;
mini = min(x) - xint;
maxi = max(x) + xint;
sumstep = (max(x) - min(x))/(length(x)*8);
d = mini:sumstep:maxi;

AMP = 1/sqrt(2*pi*p(3)*p(3));
   for i = 1:length(x)
   d2 = d -x(i);
   ypow = feval('powercut', d, [p(1) p(2) p(3) p(5)]);
   ygauss = feval('gauss', d2, [AMP, 0, p(4), 0]);
   glnew = ypow.*ygauss;
   y(i) = trapz(d, glnew) + p(6);
   end
y = y';
end
```

The following is the function 'powercut' which is simply the powerlaw with a cut-off - $\Gamma(\omega)$ - as decribed in equation 9.13

```
function [y, name, pnames, pin]=powercut(x,p,flag)
% powercut    : Clean powerlaw with a cutoff.
% function [y, name, pnames, pin]=(x,p)
%
% p = [Amplitude Centre Cutoff Exp]

% Author:  Rasmus Toft-Petersen


if nargin==2;
mini = 2*min(x);
maxi = 2*max(x);
```

```
sumstep = (max(x) - min(x))/(length(x)*30);
d = mini:sumstep:maxi;
a = p(1)*p(3)^(-p(4));

   for i = 1:length(x)
if abs(x(i) - p(2)) <= p(3)
   y(i) = p(1);
end
if abs(x(i) - p(2)) > p(3)
   y(i) = (abs(x(i) - p(2))^p(4))*a;
end
   end
end
```

B SA results for the unaltered 180 mT rocking curve

In section 9.3.5 it was described how an unfornate recording scheme for the 180 mT rocking curve resulted in important parts of the rocking curve being recorded with a much lower monitor-rate than the rest of the curve. The consequence of this was two points in the middle of the tails which had a much lower intensity than a monotonic curve would have. These points were discarded, simply because they were explainable and unphysical. However, strictly peaking, there is no predominant reason for these points not to be taken at face value. Figure 104 shows the results of the simulation annealing algorithm for the 180 mT rocking curve *without* removing any points, presented in the same way as in section 9.3.5.

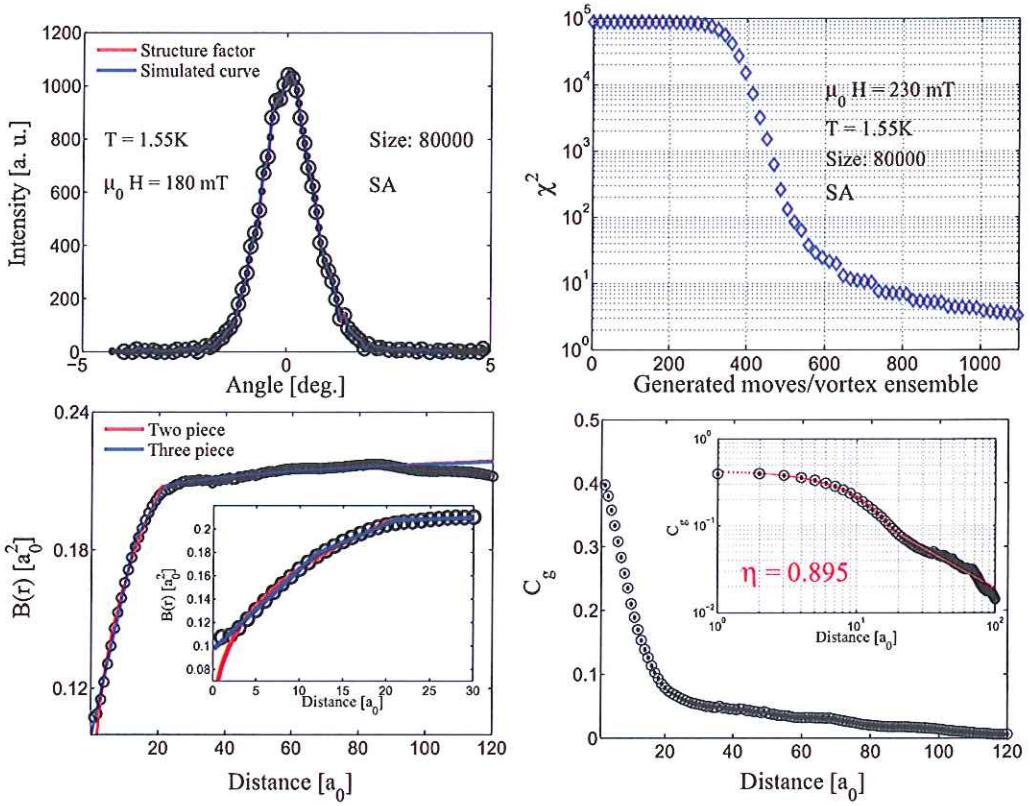

Figure 104: *Top left:* The fitted structure factor (red line), the calculated rocking curve (blue line), the actual data (hollow circles) and the interpolated data points (black dots) for the case of the *unaltered* 180 mT rocking curve. *Top right:* The evolution of χ^2 as function of number of moves pr. flux line. Convergence is reached after roughly 1000 moves pr. flux line. *Bottom Left:* The displacement correlator $B(r)$ as a function of distance between flux lines in units of a_0. The points have been fitted to both a two piece (red) and a three piece (blue) function. Again, a logarithmic rise up to $80a_0$ is evident. Inaddition there is a small bump at 25 a_0 *Bottom right:* The translational correlator $C_g(r)$, fitted only to a two-piece function (inset). A power law is evident with a fitted exponent of $\eta = 0.9$. The translational correlator exhibits a downward bump at roughly $25a_0$ - which is suggested to be caused by the two low-intensity points. The power law dropoff exponents is much lower than when removing the points (1.14) indicated that they are significant. The ensemble size is 80000 flux lines in this cases.

As evident in both the displacement correlator and the translational correlator there is a bump at roughly $25a_0$. An explanation could be that the two low-intensity points - which are both close to 2 degrees from the peak center - causes an unphysically low translational correlator at 25 a_0.

To support this, the determined drop-off exponent is similar to the exponent obtained from the simulation of the 130 mT data - namely 0.9. As evident in figure 86, these exponents are *not* the same in the rocking curves.

List of Figures

1 An illustration of the nomenclature of multiferroics and magnetoelectrics. True multiferroics exhibits both a spontaneous magnetization and spontaneous electric polarization. The magnetoelectrics on the other hand are defined by the *coupling* between the two order parameters; the spontaneous presence of any of the order parameters is thus not a necessary condition. 3

2 The spatial distribution of an electron in the orbitals possible with principal quantum number (n = 3). Picture from http://www.sci.uidaho.edu/Chem101/Links.htm . . 6

3 The splitting of the principal multi-electron atomic states. The perturbation accounted for in the Hamiltonian is shown below. Picture modified from [7]. 10

4 a) Examples of charge distribution of the d-shell transition metal electrons surrounded by p-shell electrons from the four oxygen atoms in the same plane. b) The actual position of the transition metal ion (brown) slightly displaced within an oxygen (red) octahedron. c) Example of crystal field splitting of an $(3d)^6$ state of an Fe^{2+}-ion. 12

5 The structure of the lithium orthophosphates as determined from powder x-ray experiments ([12, 13, 14]). 20

6 An illustration of the concept of irreducible representations. 25

7 Four of the twelve commensurate irreducible basis structures related to the three AFM symmetry classes (A, G and C) and the ferromagnetic class (F). Only one of the three possible polarizations (x, y, z) is shown for each one of the four different classes. 26

8 (a) The scattering triangle in reciprocal space fulfilling the scattering condition. The yellow circles are reciprocal space lattice points and 2θ is the neutron scattering angle. (b) Braggs law visually expressed in terms of in-going and out-going waves and the interference between them caused by diffraction from the crystal planes. . 44

9 (a) Layout of the principle of neutron diffractometry. (b) The TriCS spectrometer at the PSI. There are two different monochromators and possibility of using a 2D detector array. 47

10 (a) Layout of a conventional neutron triple-axis spectrometer (IN14 at ILL). (b) The unique analyzer setup of the RITA-II spectrometer at the PSI. A 2D-detector is also called a position sensitive detector. Ω_A denotes the collective rotation of all 7 analyzer blades and $2\theta_A$ denotes the scattering angle of the middle blade. 48

11 (a) The general layout of a small angle neutron scattering instrument. (b) A velocity selector cylinder with dimension $d \times R$ rotating with angular velocity ω. The blades are separated by a distance d, and tilted an angle α away from horizontal. Pictures from [23]. 50

12 Calculated magnetic form factors for the four magnetic ions Ni^{2+}, Co^{2+}, Mn^{2+} and Fe^{2+}, using equation 3.77. 51

13 *Left:* Phase transitions in $LiNiPO_4$ measured by pulsed magnetization. The large peak at 120 kOe shows the increase in magnetization due to the C-IC transition. A minor peak is evident at 160 kOe. *Right:* The phase diagram of $LiNiPO_4$ up to 14.7 T as determined by T. B. S. Jensen *et. al.* [4] 53

14 *Left:* The anomalous dispersion as measured in [25] *Right:* The five exchange interactions in $LiNiPO_4$, from [25]. 54

15 *Left:* Spin canting in zero field and in applied field along c [4]. *Right:* The linearly polarized IC spin structure proposed in [4]. Pictures from [15]. 54

16 a)-b) Neutron-diffraction scans through the $(1, k_{\mathrm{ic}}, 0)$ and the $(1, 2 + k_{\mathrm{ic}}, 0)$ peaks at 14.7 T applied along the c axis at temperatures close to the transition temperature at 17.7 K. The two peaks reflect, respectively, the A_z (neglecting A_y as discussed in the text) and the weighted sum of the A_z and A_x components of the spiral structure. The A_z component disappears above 17.7 K while the A_x component persists. c) Integrated intensities of $(0, 1 + k_{\mathrm{ic}}, 0)$, $(1, k_{\mathrm{ic}}, 0)$ and $(1, 2 + k_{\mathrm{ic}}, 0)$ as functions of temperature at 14.7 T applied along the c axis. The integrated intensity from the $(1, k_{\mathrm{ic}}, 0)$ and the $(1, 2 + k_{\mathrm{ic}}, 0)$ peaks have been multiplied by a factor of 140 and 170, respectively. The onset of an additional order parameter below 17.7 K is evident. 56

17 $\theta - 2\theta$ scan before and after removal of points lying more than 4σ way from initial fit. On this scan only the encircled point is affected, and green points are not used for fitting. There is a small shift in the determined peak center. It is important to emphasize that even though the uncertainty of the physical A4 position is probably larger than the shift presented above, assuming a statistical error in A4, the error in peak position of en entire scan will still be well below this shift. 58

18 *Left:* $(0\ 1+q\ 0)$ and $(0\ 1-q\ 0)+(0\ 0.4\ 0)$ plotted together so a comparison between the symmetry connected peaks is possible. Similar behavior of the two peaks is clearly evident, which is as it should be. *Right:* $\mathrm{k_{ic}}$ as obtained from formula 4.4 as a function of applied field along c at 2 K. It is clear that the modulation stabilizes at $\mathrm{k_{ic}} = 0.2$ for fields larger than 16 T. 58

19 *Top left:* $(0\ 1+q\ 0)$ and $(0\ 1-q\ 0)+(0\ 0.4\ 0)$ plotted as a function of temperature at $\mu_0 H = 17.3T$. The position of the two symmetry connected peaks has substantial systematic variations but the sign and size of the shift from $Q = 0.2$ are comparable below 10 K. Thus the difference between τ_+ and τ_- has a stable value of 0.4 below 10 K. *Top right:* The integrated intensities of $(0\ 1-q\ 0)$ and $(0\ 1+q\ 0)$ as a function of temperature. They are both very irregular but still display the expected power law. *Bottom left:* $|\mathrm{k_{ic}}|$ as a function of temperature at 17.3 T. The commensurate quintupling of the unit cell persists until incommensurability sets in at $T = 10\ K$. *Bottom right:* The average integrated intensity of the symmetry connected $(0\ 1+q\ 0)$ and $(0\ 1-q\ 0)$ peaks. A power law is evident within errors. 59

20 k-scans of the (1, k_{ic}, 0)-peak at $T = 2K$ (left) and $T = 16K$ (right). These scans were made before the alignment issue was resolved, so the intensities are not correct. The binary results that the peaks are there, of course, holds. 60

21 The three magnetic IC structures shown by stacking six unit cells along b. Only the four magnetic Ni^{2+} ions are shown in each unit cell. a) Magnetic IC spiral at 2 K and $\mu_0 H = 13$ T applied along c. The circles around the lower left ion marks the rotation plane of the spins and the black line marks the spiral itself. b) Lock-in commensurable spiral $\mu_0 H > 16$ T and $T < 10$ K. The 1/5 modulation is evident by comparing the 1st and the 6th unit cell. c) Linearly polarized IC structure; the line marks the sinusoidal modulation. In the phase diagram for fields along c, shown in Fig. 26, the three structures are denoted as $\mathrm{IC_{ac}}$, 1/5-C and $\mathrm{IC_c}$, respectively. . . . 61

22 The magnetization in $\frac{\mu_B}{\text{Ni-atom}\cdot T}$ at 1 and 16 tesla applied along b. The Curie tail is evident at 1 tesla but not at 16 tesla. 62

23 *Left:* Field scans at $T = 5\ K$ for all three crystallographic directions. The magnetization curves for fields applied along a and b are almost linear with a slightly decreasing susceptibility. For field along c the susceptibility is much lower than along the other two directions, and there is a clear jump at the $C \rightarrow IC$ transition. The inset shows the hysteresis loop. *Right:* A field scan at 13 K. The inset shows the differential magnetization allowing for a precise determination of the critical field. . 63

24 *Left:* Temperature scan at $\mu_0 H = 16\ T$ applied along b. T_N can be determined with low precision from the small peak in differential susceptibility preceding the larger peak that reflects T_{NC} *Right:* The temperature dependence of the magnetization at 12.5 T applied along the c axis. Two clear jumps in magnetization indicates the commensurate ordering temperature and the re-entrance into the IC phase upon cooling. The insets show the differential magnetization upon cooling with an additional focus on the kink at T_N. 63

25 *Left:* Magnetization as a function of temperature at 16 tesla. A kink is clearly evident at 17.3 K. The inset shows the differential magnetization where a peak is very clear at 17.3 K *Right:* A temperature scan at 14 T. No kink is directly evident but the differential magnetization (inset) facilitates a determination of the phase boundary. 64

26 $(\mu_0 H, T)$ phase diagram of $LiNiPO_4$ for $\mu_0 H > 10$ T applied along the c axis. The black circles mark the C–IC phase boundary as found using magnetization data, supported by neutron diffraction data taken from [4] (stars). The diamonds mark the lock-in phase boundaries found using V2/FLEX data. The squares mark the boundary of the IC spiral phase found at RITA-II (below 15 T) and V2/FLEX (above 15 T), while the two right-pointing triangles indicate the phase boundary detected by VSM measurements. The linearly polarized IC ordering temperatures are taken from [4] (up-pointing triangles) supported by a measurement from V2/FLEX (down-pointing triangle). The errors on the VSM measurements are much smaller than the markers, while the error bars on the neutron-diffraction measurements are comparable to the marker size if not explicitly given. IC_c denotes the IC structure linearly polarized mainly along c, while IC_{ac} denotes the IC spiral in the ac-plane. . 65

27 Phase diagram for $\mu_0 H || b$ as determined from magnetization measurements. The zero field transition temperatures seem to extent almost vertically upwards up to 16 T. The phase diagram for fields applied along a is identical within error. 66

28 A single energy scan as measured by all 7 analyzer blades along $(0, 1+q, o)$. The resolution in q is very good along k, which allows for thorough measurements of the dispersion along k. 67

29 Dispersion measured along $(0, 1+K, 0)$ for 13.5 tesla applied along c. *Top:* The peak values from Gaussian fits such as those depicted in figure 28. The purple line represents the RPA calculation. *Bottom left:* Calculated spin wave intensities along K. *Bottom right:* Color plot representing the measured spin wave intensities. An excellent agreement is clearly evident. 68

30 Spin-wave dispersions in the IC-phase at 2 K and 13 T along $(H, 1+k_{ic}, 0)$ and $(H, 1, 0)$. 68

31 Spin flopping in $LiMnPO_4$. *Right:* The low field spin structure of $LiMnPO_4$. The spins are colinear and pointing along a. *Right:* The flopped spin state. The AFM spin configuration is probably a C-type polarized along c as expected from the anisotropy constants. This state is easy to magnetize by simply canting the spins along the field; which gains Zeeman energy on all four spins. This canting is resisted by the exchange interaction. 71

32 The instrumental setup in the TriCS experiment on $LiMnPO_4$. The magnetic field is vertical and parallel to the a axis. The detector can be tilted out of the scattering plane to reach reflections out of said plane. 72

33 *Left:* Integrated intensity of (010) as a function of field. The intensity is constant over the entire field range within errors.*Right:* A3 scans of (012) at 0 and 4.5 tesla. A drastic drop in intensity is evident. 74

34 *Top left:* Peak intensity of (012) as a function of field at various temperatures; these are the scans used for phase boundary determination. *Bottom left:* Integrated intensities of the (010), (012) and (230) peaks as a function of field. The data are consistent with a C-type flop of polarization from a to c, using table 10. *Top right:* Peak intensity of (012) as a function of both increasing an decreasing field - no hysteresis is evident *Bottom right:* Slope of the intensity vs. field curve for increasing field as given above, used for determination of critical field. 74

35 *Left:* Erroneous peak shape with a very irregular shape *Middle:* The strong (010) reflection. *Right:* The (032) reflection. All plots have been normalized to 50000 monitor which corresponds roughly to 2 seconds of measurement time at maximum source flux. 76

36 *Top:* Integrated intensity of all peaks accepted by the author and FullProf as valid magnetic peaks plotted along with the calculated values. *Bottom:* Difference between observed and calculated intensities. There are significant deviations but not enough to doubt the $C_z + F_x$ structure in the author's opinion. 77

37 *Left:* Magnetization as a function of temperature at 4.5 T applied along a. At roughly 33 K the magnetization decreases sharply with almost a discontinuous jump in differential magnetization (inset). Upon further cooling $LiMnPO_4$ enters the flopped phase and the magnetization rises. *Right:* Magnetization as a function of field applied along a at 2 K. At low fields, $LiMnPO_4$ is difficult to magnetize. At 4 T however, the spin flop occurs followed by a heavily increased susceptibility. . . 78

38 *Left:* The susceptibility for $T = 2 - 300\ K$ as measured by VSM in a DC field of 0.1 T *Right:* Magnetization as a function of temperature at $\mu_0 H = 5\ T$ which is above the spin flop field at all temperatures. 79

39 Sub-lattice magnetization as a function of temperature near T_N at 0 T (*left*), 4.7 T (*middle*) and 12 T (*right*). The data have been fitted to the function in equation 5.6 with a fixed background of 0. As evident, the critical temperature at the flop field is significantly lower than that in zero field, but the critical exponent is the same. 80

40 Phase diagram of $LiMnPO_4$ for fields applied along a. The up-pointing orange triangles represent the critical fields as measured by VSM magnetization measurements. The down-pointing purple triangles are the critical fields as determined by the TriCS measurements of the (012) reflection, and the purple diamonds represent the critical fields as determined by the RITA-II measurement of the (001) reflection as a function of field. The black circles represent the ordering temperature as found from power-law fits to the integrated intensity of the (010) reflection as measured on RITA-II. The spin flop boundary has a modest slope with the critical field increasing with temperature. The inset shows that phase boundary close to the bi-critical point. The low-field AFM phase boundaries merge with the spin flop phase boundary *tangentially* and the ordering temperature seems slightly suppressed at the critical field. 81

41 *Left:* Universal phase diagram for a spin flop system given in [38]. The two scaling field axes $\tilde{g} = 0$ and $\tilde{t} = 0$ are explained in the text. *Right:* The phase diagram of $LiMnPO_4$ with the asymptotes and points as described in the text. 82

42 *Left:* Long L-scans at 4 different temperatures above $T_N = 33.4$ at zero field *Right:* Long L-scans at 4 different temperatures above $T_b = 32.75\ K$ at $H_b = 4.5\ T$. The logarithmic intensity scale tones it down a little bit, but there is a substantial increase in critical scattering at the bicritical field. 83

43 *Left:* Integrated intensity of the long (010) L-scans as those presented in figure 42 as a function of $T - T_N$ at 0 T, 4.7 T and 10 T respectively *Right:* The domain correlation length along the crystallographic c-axis as a function of temperature at 0 T, 4.7 T and 10 T respectively. There is a clear increase of critical scattering intensity at the flop field which is not there at neither 0 T nor 10 T. The correlation length along c as a function of temperature, however, remains the same at all three fields within errors. 84

44 *Left:* The proposed zero field case - small volumes of order is embedded in a disordered bulk material. *Right:* The density of such domains is allowed to increase a lot more at the critical field before long range order is established. 84

45 *Left:* Energy scan at (010). There are two dispersions of which the authors have only used the high energy branch to fit the exchange parameters. The data are from SPINS at NIST with a resolution of 0.28 meV. *Middle and right:* Dispersions of the high energy branches as measured by the BT7 thermal spectrometer at NIST with a resolution of 1 meV. The solid lines mark the fit and the dashed lines the calculated second dispersion. 87

46 *Left:* Field induced phase transitions in $LiCoPO_4$ measured by pulsed magnetization. Two distinct peaks are evident followed by a constant plateau with a relatively high susceptibility. *Right:* Magnetization as a function of field. These magnetization measurements should be estimated with caution since thermal equilibrium is not reached and the field is strongly time-dependent. Results from [49]. 88

47 Spin wave calculations done by Jens Jensen assuming the exchange an anisotropy parameters reported in [45]. 89

48 The definitions of angles in the 4-circle setup, which are explained in the text. . . 90

49 The reflections (300), (120), (110) and (310) - central for ruling out the A and G type components - as measured at 6.5 K and 35 K respectively. The plots show the difference between the two integrated intensities - ΔI - and the calculated structure and polarization factors in terms of the irreducible representations. Notice the low background of 2 counts pr. 50000 monitor, compared to 30 counts in the $LiMnPO_4$ experiment. 91

50 The reflections (001) and (003) central for estimating the experimental precision. The plots show the omega scan measuring the integrated intensity, the difference between the two integrated intensities - ΔI - and the calculated structure and polarization factors in terms of the irreducible representations. 92

51 Observed and calculated structure factors for the refinement of the nuclear structure. The solid red line shows the $F_{obs} = F_{calc}$ line and the two stapled lines denote a 10 percent increase and decrease in structure factor, respectively 93

52 *Top left:* Integrated intensity of all peaks accepted by the author and FullProf as valid magnetic peaks plotted along with the calculated values for a $C_y + C_x$ refinement. *Bottom left:* Difference between observed and calculated intensities. *Right:* The zero field magnetic structure of $LiCoPO_4$. The angle of collinear spin rotation towards the a-axis has been exaggerated for the sake of illustration. . . . 94

53 The integrated intensity of the (021) and (041) reflections at zero field and 13 tesla respectively. The finite nuclear background recorded at 35 K in zero field is plotted for comparison. These two reflections reflect the same magnetic symmetries and they both show a significant increase in intensity - ΔI_H - upon applying field along a. The zero field magnetic intensity ΔI_T is shown as well. 95

54 The integrated intensity of the (001), (032) and (050) reflections at zero field and 13 tesla applied along a respectively. The nuclear background has only been measured on the (032) peak. As evident the (001) reflection rules out G_x and G_y components, while the (032) and (050) rule out any C-type components. There is a small increase of intensity in the (050) peak, but nowhere near enough to be comparable to the field induced signal in the (041) reflection which has a comparable magnetic form factor. 96

55 *Left:* Peak intensity of the (021) reflection as function of field at T = 2 K. The curve has been fitted to the polynomial $I = H^2 + I_0$ - the fit is quite acceptable *Right:* Peak intensity of the 021 reflection as a function of temperature at $\mu_0 H = 13.5T$. The curve has been fitted to an AFM Curie-Weiss (CW) law *squared* $M^2_{CW} = I_0 + \left(\frac{A}{(T_N+T)}\right)^2$ as well as a CW law for comparison. In both cases, the background and Neel temperature was fixed to observed values, $I_0 = 250$ and $T_N = 16$ K. As evident, the squared CW law gives the best fit, in agreement to the fact that the neutron scattering cross section is proportional to the square of the moment. 96

56 *Left:* Spin structure projected onto the ab-plane showing the C_y, C_x and F_x components. *Right:* Projection of the spin structure onto the bc-plane showing the C_y and the G_z components. 97

57 *Top Left:* Peak (not integrated) intensity of the (301) reflection as a function of field applied along b. As evident, the intensity drops over a substantial field range at roughly 10.3 tesla. There is a substantial hystersis of 1 tesla. *Top Right:* Omega scans of the (301) reflection in zero field at 2 and 60 K respectively. *Bottom Left:* The (301) peak at 13.5 tesla at 2 and 60 K respectively. There is a remnant of magnetic intensity of roughly 1/3 of the zero field intensity.*Bottom Right:* Integrated magnetic intensity of the (301) peak as a function of temperature at 13.5 tesla. The intensity drops off as a power law with a critical temperature of 6 K. 108

58 *Left:*The range in reciprocal space reachable using 5, 7, 10, 15 and 20 meV neutrons on RITA-II with the horizontal field SANS cryomagnet mounted. *Right:* Integrated intensity of the (032) peak as a function of both increasing and decreasing field at 1.5 and 8 K, respectively. It is evident that the hysteretic behavior only exists in the low temperature phase. 109

59 The phase diagram obtained after performing temperature- and field scans of the (301) reflection. The black circles denote the phase boundaries found using the commensurate (301), and the red triangles denote the phase boundaries found from the remnant (301) intensity. The commensurate phase boundary shows a flat plateau at low temperatures, and a gradual decrease in critical field at high temperatures. The critical temperature for the 'remnant' phase remains constant at fields between 10 and 13.5 tesla. The red pentagrams mark the ordering phase boundary as found by specific heat measurements in [50]. 110

60 *Left:* The resistance of mercury near the superconducting transition temperature as measured by H. K. Onnes in 1911 [52] *Right:* The heat capacity of aluminum in the normal state and in the superconducting state - with $T_c = 1.1$ K [53]. 113

61 *Left:* The field penetrating the material in its normal state. *Right:* The Meissner effect: The superconductor expels all magnetic field from its interior when cooled through the superconducting transition. (Illustration from http://www.cm.ph.bham.ac.uk) 114

62 *Left:* Feynman diagram of an elastic electron-electron scattering event conserving spin. The timely axis is the vertical one while the spatial axis is horizontal. The propagator or matrix element is denoted by the dashed line. *Right:* The impact of the propagator residue on the momentum distribution is to lessen the discontinuity at the Fermi surface. Picture from [59]. 116

63 Feynman diagrams of phonon emission (*right*) and absorption (*left*) by electrons. The strength of the interaction is given by $M_{\mathbf{q}}$. Picture from [59]. 119

64 *Left:* The realistic sum of the phonon-mediated and the photon-mediated electron-electron interaction at fixed $\mathbf{q}$. *Right:* The crude BCS simplification of the total electron-electron interaction for low energies. Picture from [59]. 120

65 *Left:* The case of non anti parallel wave vectors under the assumption that the thin shell requirement is fulfilled for one of the electrons *Right:* The only case where all four considered electron states are within a thin shell of the Fermi surface. Picture from [59]. 120

66 A one-dimensional illustration of the relevant region near an interface between the superconducting state and the normal state (a domain wall), in the two cases where $\lambda \gg \xi$ ($\kappa \gg 1$ - right) and $\lambda \ll \xi$ ($\kappa \ll 1$ - left) 126

67 The hexagonal close-packed vortex lattice for an applied field of $130mT$ 129

68 Radial dependency of both the superconducting order parameter ξ and the magnetic field h taken from the center of the flux line for $\kappa \approx 8$. Picture from [62]. 131

69 Intermediate mixed state in niobium as observed in [67]. 133

70 *Top left:* Compression - an applied force changes the lattice constant. *Top right:* Two forces of opposite direction acting on two different z-coordinates tilt the flux lines at the cost of flux line energy. *Bottom:* An illustration of shear - a displacement of one chain of flux lines from its neighboring chain. Picture from [59]. 135

71 *Top Left:* Generic phase diagram modified from [84]. There is a low temperature, low field Bragg glass phase which undergoes a field induced 'melting' into the vortex glass, which itself can melt into a vortex liquid upon increasing the temperature. The phase line between the two disordered phases ends in a high field critical point and there is a co-existence point at low fields and high temperature. *Top Right:* Phase diagram proposed by Menon - the Bragg glass is surrounded by a multi domain glass. *Bottom:* The phase diagram proposed by Giarmarchi and Le Doussal, quite similar to the Kierfeld diagram. The rightmost dotted line corresponds to the melting line for a pure system without disorder and the leftmost line corresponds to a melting of the low-temperature phase lying quite close to that of the pure system. 144

72 The setup used in the two SANS experiments. The field is perpendicular to the beam and horizontal. The reciprocal lattice vector $\mathbf{G}$ is shown artificially extended, and the angle ω marks the direction of rotation. The vector $\mathbf{k}_\perp$ denotes the scan direction in reciprocal space in a rocking curve. The cyan ellipse illustrates the rough cigar shape of the resolution function when projected onto the plane perpendicular to the present field direction. The resolution in the direction of rotation in this figure is determined by the size of and distance between the attenuator slit and the sample slit L_c as well as the sample-detector distance L_d. When rotating the sample - bringing $\mathbf{G}$ closer to the Bragg scattering condition - progressively shorter $\mathbf{k}_\perp$ are measured. 146

73 Brass sample stick used to mount and rotate the sample. The cogwheel in contact with the rod inside the sample stick is clearly visible. The disc on which to mount the sample is mounted on a second cogwheel which is connected with the aforementioned cogwheel below the mounted brass plate. 147

74 *Left:* Phase diagram of Vanadium as determined by VSM magnetization measurements. The insert shows a typical hystersis loop recorded to find H_{c1} and H_{c2}. *Right:* Magnetic form factor as a function of field at the three relevant temperatures in table 19 as a function of field in the range 100-300 mT. Two power law decays of B with exponents -1 and -2 have been plotted for reference. The form factor is shown to fall off quicker than the high κ power law for all temperatures. 150

75 a) Simulated quenching immediately minimizes the cost function and the configuration goes to the nearest local minimum. b) Using the RMC algorithm several minima can be probed since an increase in cost function is accepted. c) In simulated annealing stable values of the cost function is reached at different temperatures allowing the configuration to migrate. 151

76 Flow chart describing the main features of the RMC code used in this work. The squares with a yellow star in the upper right corner mark actions that will be elaborated in the text below. 153

77 *Left:* Initialized ensemble of 80000 flux lines at $\mu_0 H = 130$ mT. The circular arrangement is near perfect. The small red square denotes the section shown to the right. *Right:* A small section of the ensemble after 10 initialization moves. As evident, the lattice is still near perfect illustrating the infinitesimal maximum move size. 154

78 *Right:* The collected intensity from the entire rocking curve recorded at $\mu_0 H = 130\ mT$ projected onto the detector plane. A mask has been laid over the area where the direct beam hits the detector in order to be able to estimate the area where the Bragg spots hit the detector. The rectangular areas where intensity is collected are marked in the figure. *Left:* The extracted intensities as a function of rocking curve angle as determined by GRASP; the x-axis are file numbers each of which corresponds to angle intervals of 0.2 degrees. The center of the two rocking curves differs by an angle of 2θ as determined by $\lambda = 2d_{VL}\sin(\theta)$. Both figures are direct outputs from the GRASP package. 157

79 Collected intensity from the rocking curves recorded at T = 1.55 K with low statistics projected onto the detector plane. 80 mT is very near the Meissner phase (and possibly intermediate mixed state) at H_{c1} in the $(\mu_0 H, T)$ phase diagram and flux lines start to appear. As evident, the Bragg spots are very close to the direct beam. The scattering angle 2θ increases with field. At 280 mT, the Bragg spots are very weak; a reasonable rocking curve can not be obtained, and at 300 mT, there is no measurable intensity. 158

80 The rocking curves recorded in May 2008 fitted to single Gaussians. The curves obtained at 80, 130, 200, 220, 240, 260 and 280 mT are the curves obtained with low statistic with the purpose of obtaining a measure of the width and integrated intensity of the rocking curve. The curves at 115, 180 and 230 mT are the curves obtained with high statistics to be used for RMC fitting. Only the central part of these scans have been plotted and fitted (the Gaussian function does not fit the tail of the curves anyway). The zero point in angle has been chosen to be the center of the fit to the top spot data. The narrow peak in the center of the curves of the top spots, is a Gaussian representing the angular resolution width of the setup. The fits to the data recorded at 220 and 260 mT have been obtained by fixing the background to zero in order to avoid an unphysical negative background. The Bragg spots are far enough away from the direct beam for this to be reasonable. The data obtained at 280 mT do not really constitute a rocking curve (The peak was not measured using a broad enough angular interval), and should not be used for fitting. It should be underlined, however, that there *is* intensity at 280 mT as evident in figure 79. . 159

81 *Right:* Integrated intensity of the rocking curve as a function of field. The insets show $\log(I)$ vs $\log(\mu_0 H)$ and $\log(I)$ vs $\mu_0 H$. As evident, the intensity seems to drop off faster with field than a power law, most probably due to the form factor. *Left:* The Gaussian width of the rocking curves as a function of field. The widths have been converted to reciprocal space by $\sin(\sigma_\omega)|q_{10}(\mu_0 H)|$, where σ_ω is the width from the fits in figure 80 and $q_{10}(\mu_0 H)$ is the reciprocal lattice vector. As evident, the peak width decreases strongly with field until it reaches a plateau at $130mT < \mu_0 H < 220mT$ after which the width starts increasing again. The insert shows the rocking curve widths in angles. 160

82 *Left:* The uncorrected intensity as directly extracted from the fits - fitted to a power law with *unfixed* background (A and C are free parameters). *Right:* The correction factor as calculated using Clems form factor and the geometrical factor - fitted to a power law with the background fixed to 0. 161

83 Corrected integrated intensity as a function of field fitted to a power law - $I(H) = AH^\beta + C$ - with *variable background* C. The exponent is roughly -1.4 which is quite close to the Bragg glass prediction. The statistical error of the exponent is unreasonably low. The re-evaluated error is explained in the text. However, the extrapolation of the fitted curve to higher fields is consistent with the observation of very little intensity at 280 mT and the lack of intensity at 300 mT. 162

84 *Top Left:* The rocking curves as extracted from the top and bottom Bragg spot on the 2D detector, respectively. As expected, the two curves are very similar. *Top Right:* The average of the top and bottom rocking curve. The curve is much more smooth as the errors are smaller, and very useful for RMC fitting. The dashed line represents the Gaussian width of the resolution function. *Bottom:* The average observed intensity as a function of *absolute* angle plotted on a double logarithmic scale. As evident, the tails of the rocking curves decay as a power law. However - as observed in [86] - the intensity starts to smooth to a constant value at an angle much higher than the angular width of the resolution function. 164

85 The rocking curves at 180 mT and 230 mT respectively, plotted along with the calculated average rocking curve. As evident even the average rocking curve at 230 mT displays substantial statistical fluctuations. In this case - since these rocking curves were meant for RMC fitting, the angle interval in the high intensity area is smaller than at 130 mT. As evident on the plots of the intensities as a function of absolute angle, the power-law divergence at the peak center - which should only be limited by the resolution function - is terminated at angle well above what the resolution function dictates. At higher angles, however, the intensity falls off as a power law in both cases, with comparable exponents. 166

86 Intensity as a function of $|k_\perp|$ at 130, 180 and 230 mT respectively. The fall off exponent of the power law fits is comparable at 180 and 230 mT, but significantly lower at 130 mT. It seems that the cutoff point at which the power law seems to hold increases with field (but only in reciprocal space). This could be because of the larger unit cell; perhaps the cutoff length in real space is a constant multiple of the lattice constant. 167

87 *Top:* The fits to the rocking curves using the function described in the text. The fits and the χ^2's are reasonable. *Bottom left:* The extracted cutoff angles as a function of field which are roughly constant within errors. *Bottom middle:* The smoothing widths σ_g as a function of field which shows an increase as a function of field. *Bottom right:* The fitted exponents as a function of field. These are larger than those determined from merely fitting the tails of the rocking curves. 168

88 *Top plots and middle left:* The RMC structure factor (red line) and rocking curve (blue line) as outputted from the RMC algorithm for two different acceptance probabilities for an ensemble of 40000 flux lines. Substantial local variations are evident decreasing with acceptance probability. *Middle right and bottom plots:* The RMC fitting of the 130 mT data for ensemble sizes of 40000, 60000, and 80000 respectively. There is a natural increase of local fluctuations with ensemble size. The evolution of χ^2 as a function of normalized number of moves is shown as well. 170

89 *Left:* The 130 mT data (circles) plotted along with the interpolated points (dots) *Right:* A zoom on the left hand tail of the rocking curve plotted along with the area spanned by the error bar ends (red dashed lines). As evident, the interpolated points are well within the rocking curve statistics - which are quite good to begin with. . . 172

90 Illustration of the proposed finite ensemble effect. The black circle centered at O represents the circular array of flux lines. Two flux lines positioned at O and a distance $|P_1| = R_1 = R/2$ from O (where R is the ensemble radius) both have surroundings resembling that for an infinitely large ensemble for distances smaller than R_1. Thus, for pair separations of R_1 all correlations between pairs in the green circle mimic those for an infinite ensemble. Two flux lines at O and P_2 do *not* have identical surroundings at distances R_2. The only flux line pairs separated by R_2 having similar surroundings which are valid to an infinite ensemble are those on the circular shell $2R_2 - R < |P| < R - R_2$ all of which further than R_2 from the ensemble edge - as explained in the text. The number of flux line pairs separated by R_3 that are further than R_3 from the edge - and hence mimic correlations in an infinite ensemble - is very large. 173

91 *Top left:* The fitted structure factor (red line), the calculated rocking curve (blue line), the actual data (hollow circles) and the interpolated data points (black dots). The ensemble size is 80000 flux lines. As evident, the rocking curve is fitted as well as reasonably expected. *Top right:* The evolution of χ^2 as function of number of moves pr. flux line. After 200 moves with high acceptance probability, the fit starts to converge rapidly. After 500 moves pr. flux line, the χ^2 is simply determined by the acceptance probability - or the temperature. *Bottom Left:* The displacement correlator $B(r)$ as a function of distance between flux lines in units of a_0. The points have been fitted to both a two piece (red) and a three piece (blue) function. The two are almost identical, but zooming in on short distances two kinks are slightly evident. The logarithmic rise at large distances is clearly evident though. At distances larger than $80a_0$, the displacement correlator starts to drop. *Bottom right:* The translational correlator $C_g(r)$, fitted only to a two-piece function (inset). A power law at large distances is clearly evident with a fitted exponent of $\eta = 0.9$. . 175

92 *Left:* The full rocking curve as obtained from the scans (circle) including the interpolated points (dots). *Right:* Zooming in on the tails, the two deviating points with low statistics are clearly evident. 176

93 *Top left:* The fitted structure factor (red line), the calculated rocking curve (blue line), the actual data (hollow circles) and the interpolated data points (black dots). *Top right:* The evolution of χ^2 as function of number of moves pr. flux line. Convergence is reached after roughly 800 moves pr. flux line. *Bottom Left:* The displacement correlator $B(r)$ as function of distance between flux lines in units of a_0. The points have been fitted to both a two piece (red) and a three piece (blue) function. Again, a logarithmic rise up to $80a_0$ is evident. *Bottom right:* The translational correlator $C_g(r)$, fitted only to a two-piece function (inset). A power law at large distances is clearly evident with a fitted exponent of $\eta = 1.14$. The translational correlator exhibits a bump at roughly $90a_0$. The ensemble size is 80000 flux lines. . 177

94 *Top left:* The fitted structure factor (red line), the calculated rocking curve (blue line), the actual data (hollow circles) and the interpolated data points (black dots) at 230 mT. *Top right:* The evolution of χ^2 as function of number of moves pr. flux line. After 400 moves with high acceptance probability, the fit starts to converge rapidly. *Bottom Left:* The displacement correlator $B(r)$ as a function of distance between flux lines in units of a_0. The points have been fitted to both a two piece (red) and a three piece (blue) function, which are almost identical. The logarithmic rise at large distances is clearly evident though until it starts to drop at $80a_0$. *Bottom right:* The translational correlator $C_g(r)$, fitted only to a two-piece function (inset), with an exponent of $\eta = 1$. The translational correlator exhibits a rapid drop at only $65a_0$. 178

95 *Left:* Fitted power law exponents η for $C_g(r)$. The values suggested in literature - explained in the text - are shown as well. *Right:* Fitted RM exponents β compared to values suggested in literature. 179

96 Rocking curves obtained at an average of 2.66 K using the reduction scheme described in the text. No intensity was found above 190 mT. An accurate determination of the peak width and amplitude is possible; the blue lines represent the Gaussian fits which converged nicely. The counts have been normalized to 2500 monitor 182

97 *Left:* Corrected integrated intensity as a function of field fitted to a power law - $I(H) = AH^\beta + C$ - with *variable background* at 2.66 K. The exponent determined by the fit is -1.5. *Right:* The rocking curve widths as determined by Gaussian fits. 183

98 Rocking curves obtained at an average of 3.0 K. No intensity was found at 170 mT. The blue lines represent the Gaussian fits. 183

99 Corrected integrated intensity as a function of field fitted to a powerlaw - $I(H) = AH^{\beta} + C$ - with *variable background* at 3.0 K. The exponent determined by the fit is -2.6. These data are more irregular than at 1.55 and 2.66 K, and removing just a single point has a large impact on the exponent. 184

100 *Top:* The rocking curves of the top and bottom spot respectively as recorded at 2.7 K and 170 mT after background subtraction. Some counts ended up being less than zero after background subtraction; those have been manually set to be zero. *Bottom left:* The rocking curve obtained after combining the rocking curves from the top and bottom spot. The rocking curve has been fitted to a Voigt, a Gaussian and to the function described in section 9.3.2, denoted as homemade. It is clear that all function fit the tail of the rocking curve equally well, but that both the Gaussian and the voigt fail to fit the peak center. However, the homemade powerlaw with a cutoff fits this peak center nicely. *Bottom right:* Intensity as a function of absolute angle, fitted in the same way as previously described. As in all rocking curve the critical angle exceeds the resolution. However, the critical angle is much larger than the ones determined at 1.55 K. 185

101 Raw magnetization measurements for both increasing and decreasing field applied along (111) at various temperatures. It is clear that ΔM is roughly constant at low fields, and that it starts to decrease heavily upon entering the vortex state at H_{c1}. 187

102 *Top left:* The critical current as directly extracted from ΔM on the magnetization curves, plotted with a logarithmic y-axis. At low fields the critical current drops heavily over a substantial field range, after which it drops off exponentially. At roughly 340 mT - which is significantly above the field where detectable order ceases to exist at 1.6 K - the critical current drops very rapidly to zero. *Top right:* The critical current plotted on a linear scale. *Bottom left:* The hystersis loop at high fields. The rapid drop in ΔM is clearly evident in the magnetization where there is an anomalous kink for both increasing and decreasing fields. Note that detectable hysteresis - and hence superconductivity - exists for fields above this anomaly *Bottom right:* The differential critical current. Two peaks are evident, one at H_{c1} and one at high fields. The transition from the Meissner phase to the vortex phase can be said to occur in a critical region rather than a specific field. 188

103 The phase diagram of the Vanadium sample used in this work determined using magnetization and neutron measurements. The black circles represent H_{c2} - the point of zero critical current as determined from VSM measurements. The black diamonds represent the onset of the rapid drop in the critical current - the anomalous kink in the VSM measurements. The pink stars are the points where the neutrons scattering intensity drops to zero and long range order ceases to exist. Above these fields, the phase is called a vortex glass (VG). The black squares represent H_{c1} - the peak in differential critical current - while the stapled black lines denote the possible boundaries for an intermediate mixed state as suggested by the low fields neutron rocking curve widths. 189

104 *Top left:* The fitted structure factor (red line), the calculated rocking curve (blue line), the actual data (hollow circles) and the interpolated data points (black dots) for the case of the *unaltered* 180 mT rocking curve. *Top right:* The evolution of χ^2 as function of number of moves pr. flux line. Convergence is reached after roughly 1000 moves pr. flux line. *Bottom Left:* The displacement correlator $B(r)$ as a function of distance between flux lines in units of a_0. The points have been fitted to both a two piece (red) and a three piece (blue) function. Again, a logarithmic rise up to $80a_0$ is evident. Inaddition there is a small bump at 25 a_0 *Bottom right:* The translational correlator $C_g(r)$, fitted only to a two-piece function (inset). A power law is evident with a fitted exponent of $\eta = 0.9$. The translational correlator exhibits a downward bump at roughly $25a_0$ - which is suggested to be caused by the two low-intensity points. The power law dropoff exponents is much lower than when removing the points (1.14) indicated that they are significant. The ensemble size is 80000 flux lines in this cases. 201

List of Tables

1 Characteristics of the magnetic ions in the three lithium ortho-phosphates examined in this thesis. The spin and orbital quantum numbers are found using Hund's rules without taking the crystal surroundings into account. The spin orientations are found in the literature [1, 2]. $\Delta g/g$ determines the strength of higher-order exchange couplings induced by the spin-orbit coupling - explained in the text. The maximum strengths of the ME-effect are found in [3]. 4

2 Shell- and sub shell names. 8

3 The eight irreducible representations of the symmetry group excluding translations in the lithium orthophosphates and how they transform under the symmetry operations of G. The basis vectors for the representation space of each irreducible representation is given as well. 26

4 The four irreducible representations of the little group $G_{\mathbf{k}_{ic}}$ in the lithium orthophosphates and how they transform under the symmetry operations of $G_{\mathbf{k}_{ic}}$. The basis vectors for the representation space of each irreducible representation is given. . . . 27

5 Transformation properties of the magnetic ions in the lithium orthophosphates and their spin under the symmetry operations of the *Pnma* space group. 28

6 The exchange interactions and single ion anisotropies as given in [25]. All units are in meV 53

7 Squared structure (F) and polarization (P) factors for the three IC peaks used to establish the spiral structure in terms of the irreducible representations. The structure factors are normalized to unit spin lengths of the spin components. $k_{\mathrm{ic}} = 0.18$ rlu have been used, but note that small changes of k_{ic} have no effect on our conclusions. 56

8 How the four irreducible representations and the three polarization vectors transform under the symmetry operations of $G_{\mathbf{k}_{ic}}$. 69

9 The exchange interactions and anisotropies in $LiMnPO_4$ as given in [33]. All units are in meV 71

10 Squared structure (F) and polarization (P) factors for the three peaks used to establish the flopped structure in terms of the irreducible representations. The structure factors are normalized to unit spin lengths of the components. The structure factor of the strongest nuclear peaks is 4000 for comparison. 73

11 Refinement parameters and goodness-of-fit parameters for three different spin structure vectors. As evident, the most physical refinement is the one with the low reduced χ^2. 77

12 The exchange interactions and anisotropies in $LiCoPO_4$ as given in [45]. All units are in meV. The very large uncertainties on most of the parameters should be noted. 88

13 Refinement parameters and goodness-of-fit parameters for three different spin structure vectors. As evident, the $C_y + C_x$ structure gives the lowest reduced χ^2. 93

14 Transformation properties of the magnetic ions in the lithium orthophosphates and their spin under the symmetry operations of the *Pnma* space group. 99

15 Transformation table for the *transformed* pseudo vector components (D^i_{14}) of the *untransformed* ionic sites 1 and 4 - $RD^i_{14}R^\dagger$ - and the *untransformed* eigenvector components on the *transformed* sites $D^i_{R(1)R^\dagger R(4)R^\dagger}$. For a DM term to be invariant the two quantities have to be equal. 100

16 Transformation table for the *transformed* pseudo vector components (D^i_{14}) of the *untransformed* ionic sites 1 and 2 - $RD^i_{12}R^\dagger$ - and the *untransformed* pseudo vector components on the *transformed* sites $D^i_{R(1)R^\dagger R(2)R^\dagger}$. For a DM term to be invariant the two quantities have to be equal. 100

17 Transformation table for the *transformed* pseudo vector components (D^i_{14}) of the *untransformed* ionic sites 1 and 3 - $RD^i_{13}R^\dagger$ - and the *untransformed* pseudo vector components on the *transformed* sites $D^i_{R(1)R^\dagger R(3)R^\dagger}$. For a DM term to be invariant the two quantities have to be equal. 101

18 Structure factors evaluated in the (301) reflection for the zero field structure C_y, the proposed ferrimagnetic structure $1/3F_y + 2/3C_y$ and a ferromagnetic commensurate magnetization $1/3F_y$. 107

19 Table of central GL parameters at the three relevant temperatures. The determined electronic mean free paths agree roughly within 10 percent of the average $\ell = 44$ nm 149

20 List of scans performed at 180 mT in the 2008 SANS-II experiment. 176